Robust Quantum Information Processing using Quantum Spin Networks

Abdulsalam Alsulami

Doctor of Philosophy

University of York

School of Physics, Engineering and Technology

February, 2024

Abstract

Future quantum devices are powerful devices that will generally generate, manipulate, and store quantum information using qubits. A linear array of solid-state types of qubits (known as spin chains) have been thoroughly investigated. It has demonstrated its usefulness for short-range quantum communication and computation, and entanglement generation. In this thesis, we design complex Spin Network (SN) systems by coupling together spin chain systems using a novel unitary transformation method. The richer topology involved in our SN systems gives wider application than spin chains and enables the generation of various quantum information processing without the need to re-engineer the SN parameters, such as coupling interactions, for each unique task. We have used the SN for routing quantum information, generating various types of entangled states, and for quantum sensing purposes. All these applications have been investigated against different types of disorder and show very good robustness for practical levels of disorder. Investigation of the scalability of the SN by increasing the number of qubits or by increasing the number of spin chains that form the SN have also been considered. As the SN description and approach are widely applicable to a range of physical realisations, our work demonstrates the feasibility of realising these quantum information systems as practical devices.

Contents

List of Figures

Acknowledgements

Praise be to Allah who taught with the pen, taught humanity what it did not know, and peace be upon the best of mankind and the Seal of the Prophets, our Prophet Muhammad, the most knowledgeable among us. I thank Allah Almighty who has given me many blessings and who has provided me with reasons and people to achieve what I have achieved.

People who have made my PhD journey pleasant and exciting are my supervisors, Tim, Irene, and Marta. I am profoundly grateful to them for their consistent support, help, and guidance throughout the four years of my PhD. I really enjoyed our weekly supervision meetings, where they taught me with dedication and kindness. May they receive Allah's abundant blessings.

I would also like to express my deepest gratitude to my father for his unconditional support and for funding my PhD. Without his assistance, I would not have reached this point. Equally, I am immensely grateful to my mother for her prayers and everything she has done for me; she is one of the greatest blessings Allah has bestowed upon me. May Allah shower them with blessings and protection.

Another great blessing in my life is my wife, whom I am deeply grateful to, for her encouragement, patience, and sacrifices throughout this journey. Her constant support and understanding have been pillars of strength for me, enabling me to focus on my studies with determination. The arrival of our little one filled our home with laughter, love, and inspiration, enriching each day of my PhD journey.

I extend my gratitude to everyone I got to know through my journey. Special thanks to Georgia for her unwavering assistance whenever I reached out for help. Additionally, I express my gratitude to my colleagues, Rupesh, Jenny, and Ayan, for their collaboration on a small project that we anticipate will result in a publication.

Declaration of Authorship

I declare that this thesis is a presentation of original work and I am the sole author. This work has not previously been presented for a degree or other qualification at this University or elsewhere. All sources are acknowledged as references. Part of the work in this thesis have been published in [1,2], with myself as the first author. Another part of the work in this thesis is in preparation for another publication. AI tools have been used to improve English (i.e., correcting typos and grammatical errors).

List of Abbreviations

- **QIP**: Quantum Information Processing
- **QST**: Quantum State Transfer
- **SN**: Spin Network
- **QKD**: Quantum Key Distribution
- **PST**: Perfect State Transfer
- **USC**: Uncoupled Spin Chains
- **EOF**: Entanglement of Formation
- **TWS**: Tripartite W-type State
- **MWS**: Multipartite W-type State

List of Symbols

- N: Number of qubits/sites
- H_{XY}: Spin chain Hamiltonian
- $\mathcal{H}_{XY}$: Spin network Hamiltonian
- t_m: Mirroring time
- $J_{i,i+1}$: Coupling interaction
- J_{max}: Maximum constraint on the couplings
- T_c: Coherence time
- ϵ_i: On-site energy
- $\mathcal{I}$: Identity of the appropriate dimension for the system being discussed.
- $\mathcal{N}$: Number of excitations
- λ_j: Eigenvalues
- $|\varphi_j\rangle$: Eigenvectors
- $F(t)$: Fidelity
- $\overline{F}(t)$: Averaged fidelity
- $\overline{EOF}$: Averaged EOF
- d_i: random number
- E: Error strength
- $t_{d,\xi}$: Time delay in the application of a phase
- $t_{d,|+\rangle}$: Time delay in the injection of a state
- ξ_D: Error in the applied phase angle
- D: Scale of the delay

Publications

During the course of this PhD, two papers have been published and third one is in preparation:

1. Abdulsalam H. Alsulami, Irene D'Amico, Marta P. Estarellas, and Timothy P. Spiller. Unitary design of quantum spin networks for robust routing, entanglement generation, and phase sensing. *Advanced Quantum Technologies*, 5(8):2200013, 2022.

2. Abdulsalam H. Alsulami, Irene D'Amico, Marta P. Estarellas, and Timothy P. Spiller. Scalable quantum spin networks from unitary construction, *Advanced Quantum Technologies*, 2300238, 2023.

3. Abdulsalam H. Alsulami, Irene D'Amico, Marta P. Estarellas, and Timothy P. Spiller. Generation and investigation of cluster states in quantum spin networks. In preparation.

The work was also presented at various events:

1. Abdulsalam H. Alsulami, Irene D'Amico, Marta P. Estarellas, and Timothy P. Spiller. Robust Quantum Information Processing using Quantum Spin Networks. *Poster session presented at PHOTON2022, Nottingham, UK*, 2022, 8.

2. Abdulsalam H. Alsulami, Irene D'Amico, Marta P. Estarellas, and Timothy P. Spiller. Robust Quantum Information Processing using Quantum Spin Networks. *Oral presentation, Northern Quantum Meeting, Manchester, UK*, 2022, 9.

3. Abdulsalam H. Alsulami, Irene D'Amico, Marta P. Estarellas, and Timothy P. Spiller. Robust Quantum Information Processing using Quantum Spin Networks. *Oral presentation at Quantum Group research group, Sheffield, UK*, 2022, 11.

In The Name of Allah, The Most Beneficent, The Most Merciful

Chapter 1

Introduction

"Curiosity - the rover and the concept - is what science is all about: the quest to reveal the unknown."

Ahmed Zewail

Quantum mechanics is a theory that describes how the world works at the microscopic level, and it has been shown to be very accurate in its predictions. Understanding quantum mechanics has already changed our life in the sense that almost all electronic technology we have contains a transistor, a semiconductor device that relies on the concept of band structure of a material, which is a quantum mechanical concept. However, the building blocks of our current technology are nevertheless based on the laws of classical physics, because they manipulate information according to classical Boolean logic.

The power of classical computers is limited to how large a computational task is. As a case in point, the amount of information embodied in the spin degrees of freedom of 20 electrons is given by 2^{20} and this could be simulated using classical computers. But when it comes to simulating a real physical system, where the number of particles could be on the order of 10^{20}, the amount of information that needs to be stored and processed outweighs the capabilities of ordinary computers. Even with approximation methods (e.g., perturbation theory) or advanced hardware architectures, no classical computer has provided efficient and accurate solutions for such problems. Therefore, it has become clear that simulating a real physical system requires a computer that is much more powerful than ordinary/classical computers that are used in everyday life.

Feynman realised this difficulty and suggested a quantum simulation that can be performed by a quantum computer (rather than classical computers) to overcome certain classes of problems [3]. It has subsequently been shown that problems

that cannot be solved efficiently by classical computers can be solved by quantum computers. For example, factoring large numbers can be solved by using the Shor algorithm [4], which provides an exponential speedup over its classical counterpart. Many other quantum algorithms have also been proposed for various problems [5]. However, building a quantum computer is not a simple task, and could even be the hardest task scientists ever faced. Therefore, scientists have been studying quantum systems, mostly of small system size due to the limitation of current classical computers.

Advanced tools have been used to emulate quantum systems, such as experiments with ultracold atoms [6] and photonic simulation [7]. A great amount of effort has been made in exploring the quantum computing field to realise a quantum computer. In fact, cutting-edge quantum technology devices with a number of qubits ranging from 50 to 100 have already been built and have achieved quantum supremacy, which means that they outperformed the most powerful classical supercomputers for solving certain mathematical tasks [8, 9].

In addition to using quantum mechanics for quantum computing, it can also be used for secure communication [10] and quantum communication [11]. Moreover, quantum mechanics can be used to improve the accuracy of physical measurements, and a new field is emerging from this known as quantum sensing [12].

These developments bring us to what is known as Quantum Information Processing (QIP), which is concerned with transferring and manipulating quantum information. Therefore, QIP can be used to contribute to all the applications we have mentioned above: quantum communication, quantum computation, and quantum sensing. In this thesis, we contribute to the field of QIP by proposing a novel design for scalable and robust quantum spin networks and show how they can be used for transferring and manipulating quantum information.

1.1 Quantum Information Processing

In this section we will introduce the basic ingredients and definitions of QIP; qubits, quantum states, entanglement, measurement, decoherence, unitary operators, and quantum gates. Then, DiVincenzo requirements for quantum devices will be discussed. Finally, a discussion of the physical implementations of QIP will be presented.

1.1.1 Basic definitions

Qubits

Classical computers and communications run on bits, where there are just two possible outcomes; either 0 or 1 (i.e. mathematically: 1 is where a wire has a current and 0 represents no current passing). The quantum analogy of classical bits is that of quantum bits, which are also known as qubits. Although the bit state can only be 0 or 1, the qubit state can be 0 and 1 simultaneously, which is a fundamental feature of quantum mechanics and known as *superposition*. Furthermore, each of the qubit states, 0 and 1, can be expressed in a two-dimensional vector space as $|0\rangle = \begin{pmatrix} 0 \\ 1 \end{pmatrix}$ and $|1\rangle = \begin{pmatrix} 1 \\ 0 \end{pmatrix}$, respectively. The notations $|0\rangle$ and $|1\rangle$ are known as the *computational basis states*. Note that the definitions of the basis $|0\rangle$ and $|1\rangle$, given here, are opposite to the definition most commonly (but not exclusively) used in the quantum information literature.

There are various notations that can be used to denote the basis of a qubit, such as $|+\rangle$ and $|-\rangle$ or $|\downarrow\rangle$ and $|\uparrow\rangle$ or sometimes letters. In this work, we will stick to the notation basis $|0\rangle$ and $|1\rangle$. Therefore, a single qubit state can be expressed as a linear combination of the basis states as

$$|\psi\rangle = \alpha\,|0\rangle + \beta\,|1\rangle\,, \tag{1.1}$$

where α and β are complex number coefficients, the probability of finding the qubit in $|0\rangle$ state or $|1\rangle$ state is $|\alpha|^2$ and $|\beta|^2$ respectively. Furthermore, any qubit must satisfy the normalisation condition $|\alpha|^2 + |\beta|^2 = 1$. The plus and minus notations are usually used to denote a specific example of a single-qubit superposition $|\pm\rangle = \frac{1}{\sqrt{2}}(|0\rangle \pm |1\rangle)$.

Quantum states

The first postulate of quantum mechanics is that the state of a closed quantum system can be represented as a complex state vector that belongs to a complex Hilbert space [13]. The Hilbert space is spanned by a complete basis set, and it contains all the possible configurations that the system can have. Take as an example the single qubit state mentioned above, where the Hilbert space bases are $|0\rangle$ and $|1\rangle$. These bases are said to be orthonormal (i.e., orthogonal to each other and normalised).

A system composed of two subsystems, $|0_1\rangle$ and $|1_2\rangle$, is described by taking the tensor product of the two subsystems (i.e., $|0_1\rangle \otimes |1_2\rangle$). For convenience, this is simplified as $|01\rangle$. Therefore, the quantum state of a system composed of two qubits, $|\psi_1\rangle = c_1 |0\rangle + c_2 |1\rangle$ with Hilbert space $\mathcal{H}_1$ and $|\psi_2\rangle = c_3 |0\rangle + c_4 |1\rangle$ with Hilbert space $\mathcal{H}_2$, can be represented as

$$|\Psi\rangle = |\psi_1\rangle \otimes |\psi_2\rangle = c_1 c_3 |00\rangle + c_1 c_4 |01\rangle + c_2 c_3 |10\rangle + c_2 c_4 |11\rangle . \tag{1.2}$$

Generalising this for N qubits, we can write the product state of the system as a tensor product of all the qubits $|\Psi\rangle = |\psi_1\rangle \otimes |\psi_2\rangle \otimes \ldots |\psi_N\rangle$. This tensor product results in 2^N basis states $|\kappa_i\rangle$, and therefore any quantum state of such system can be represented as a linear combination of these basis states

$$|\Psi\rangle = \sum_{i=1}^{2^N} c_i |\kappa_i\rangle , \tag{1.3}$$

with the normalisation condition $\sum_{i=1}^{2^N} |c_i|^2 = 1$. The basis states $|\kappa_i\rangle$ achieve the orthonormality condition, as they are orthogonal $\langle \kappa_i | \kappa_j \rangle = 0$ for $i \neq j$ and normalised $\langle \kappa_i | \kappa_i \rangle = 1$.

As will be discussed in the following, the vector representation of the quantum state cannot describe any type of quantum state. An equivalent method for representing a quantum state is the representation known as the density operator (also called the density matrix). A general density matrix can include classical uncertainty (lack of classical knowledge about the system) and quantum uncertainty associated with superposition. Therefore, any quantum state can be described using the density matrix ρ as

$$\rho = \sum_i p_i |\psi_i\rangle \langle \psi_i| , \tag{1.4}$$

where p_i represents the probability to find the system in the pure state $|\psi_i\rangle$ and all the probabilities sums up to unity, $\sum_i p_i = 1$. The trace of the density matrix is always equal to one, $Tr(\rho) = 1$. The density matrix applies to an ensemble of quantum systems, or one system used many times with repeated preparation.

- Pure states

  Pure states represent quantum states that are well known. For instance, if a device is used to fire an electron and, each time the device fires an electron,

we find that the spin of the electron is in a spin-up state, then the system state is a pure state. Similarly, if the electron spin is found to be in the same superposition state each time the device fires the electron, then the system state is a pure state. This is also true with a system composed of many particles; as long as the state of the system is always well known, then the state is said to be in a pure state.

Pure states can be described using either the vector state representation $|\Psi\rangle$ or the density matrix representation ρ. Since the pure state is well known, its density matrix representation is given by $\rho = |\Psi\rangle\langle\Psi|$. Furthermore, the trace of the square density matrix of pure states is equal to one, $Tr(\rho^2) = 1$. As this thesis work is mainly focused on pure states, we will generally use the vector state representation $|\Psi\rangle$.

- Mixed states

  While pure states can be described using the vector state representation $|\Psi\rangle$ or the density matrix ρ, mixed states can only be described using the density matrix ρ. A mixed state ensemble of quantum systems can be described as a probabilistic sum over pure state $|\psi_i\rangle$ projectors, each with probability p_i, so $\rho = \sum_i p_i |\psi_i\rangle\langle\psi_i|$. For example, if a spin-$\frac{1}{2}$ ensemble is prepared as 30% "up" in z, 20% "down" in z, and 50% in the $|+\rangle$ state, it is decomposed as

$$\begin{aligned}\rho &= 0.3\,|1\rangle\langle 1| + 0.2\,|0\rangle\langle 0| + 0.5\,|+\rangle\langle +| \\ &= 0.3\,|1\rangle\langle 1| + 0.2\,|0\rangle\langle 0| + 0.25\,(|0\rangle\langle 0| + |0\rangle\langle 1| + |1\rangle\langle 0| + |1\rangle\langle 1|)\,.\end{aligned} \tag{1.5}$$

  Therefore, a z-basis measurement on the ensemble will reveal "up" with probability 0.55 and "down" with probability 0.45. As ρ can also be decomposed as

$$\begin{aligned}\rho = {} & 0.15\,(|+\rangle\langle +| - |+\rangle\langle -| - |-\rangle\langle +| + |-\rangle\langle -|) \\ & + 0.1\,(|+\rangle\langle +| + |+\rangle\langle -| + |-\rangle\langle +| + |-\rangle\langle -|) \\ & + 0.5\,|+\rangle\langle +|\,,\end{aligned} \tag{1.6}$$

  a x-basis measurement on the ensemble would reveal "+" with probability 0.75 and "-" with probability 0.25.

  Frequent measurements on a mixed state ensemble provide probabilistic outcomes and such uncertainty does not only come from the quantum superposition uncertainty but also from classical uncertainty, as the state is a proba-

bilistic ensemble of pure states. Quantifying the closeness between two mixed states (known as fidelity measure) can be achieved using the Uhlmann–Jozsa measure [14–16]. Furthermore, the trace of the squared density matrix of mixed states is less than one, $Tr(\rho^2) < 1$.

Entanglement

Entanglement is a fundamental feature of quantum mechanics and has counter-intuitive behavior. It is when two quantum particles (each in a superposition) are strongly correlated in a sense that observing the state of one particle instantaneously reveals the state of the other particle to that observer, even if they are separated by millions of meters.

As we discussed above, a composed physical system is represented by taking a tensor product between them – but this is only true if they are separable, meaning that observing one particle does not affect the other particle. An example of a separable state is a system of two photons given as $|\Psi\rangle = \frac{1}{\sqrt{2}}(|HV\rangle + |HH\rangle)$, where H and V denote the horizontal and vertical polarisations of the photon, respectively. This state shows that the first photon is always horizontally polarised and so the state of these two photons can be factorised as a product state between the two photons as $|\Psi\rangle = |H_1\rangle \otimes \frac{1}{\sqrt{2}}(|V_2\rangle + |H_2\rangle)$. On the other hand, when the state of the composed physical system is an entangled state, then it cannot be represented as a product state of the components of the system.

- Examples:

  Take, as an example, the case where two photons are entangled, which can be represented as $|\Psi\rangle = \frac{1}{\sqrt{2}}(|HV\rangle + |VH\rangle)$. This is clearly a unique state and cannot be factorised such that each qubit is represented alone, which is because it is an entangled state and not a separable state. The entanglement can be generated experimentally using different protocols, such as coincident detection of two fibre-based infrared photons [17], a spontaneous emission-based protocol [18,19] or a parametric down-conversion in a non-linear crystal [20].

  The type of entangled state given as $|\Psi\rangle = \frac{1}{\sqrt{2}}(|01\rangle + |10\rangle$ tells us that whenever we observe one particle's state to be in the $|0\rangle$ state, we know that the other particle's state must be in the $|1\rangle$ state and vice versa. However, this is not the only way to represent the entanglement between two qubits.

We show below all the cases that can represent the entanglement of two qubits and these are known as Bell states:

$$\begin{aligned} |\Psi^+\rangle &= \frac{1}{\sqrt{2}}(|01\rangle + |10\rangle) & |\Psi^-\rangle &= \frac{1}{\sqrt{2}}(|01\rangle - |10\rangle) \\ |\Phi^+\rangle &= \frac{1}{\sqrt{2}}(|00\rangle + |11\rangle) & |\Phi^-\rangle &= \frac{1}{\sqrt{2}}(|00\rangle - |11\rangle) \end{aligned} \tag{1.7}$$

- Quantifying entanglement

  To quantify whether a state is entangled or not, we can use the Entanglement of Formation (EOF) method [21]. EOF is a quantity that can measure the degree of entanglement between any arbitrary pair of qubits, regardless of whether they are in a pure or mixed state. A detailed discussion on this method of quantifying the entanglement will be given in Chapter 2.

  We note that when dealing with pure states, a simpler quantity known as concurrence [21] can be used to quantify the degree of entanglement. The concurrence formula for an arbitrary two qubits pure state $|\Psi\rangle = c_1|00\rangle + c_2|01\rangle + c_3|10\rangle + c_4|11\rangle$ is given by

$$\mathcal{C} = 2|c_1c_4 - c_2c_3|, \tag{1.8}$$

  where the concurrence $\mathcal{C} \in \{0, 1\}$, and when $\mathcal{C} = 1$ the state is maximally entangled.

  We use the EOF to quantify the degree of entanglement between two qubits, although the state of the overall system is a pure state. This is because when the system is traced out to leave only the two sites in which we are interested, the state of these remaining two sites could be a mixed state. In the case of pure states, there is a relationship between the concurrence and the EOF [21].

- EPR and Bell inequality

  "I like to think the moon is there even if I am not looking at it."

  Albert Einstein

  The fact that observing one particle state reveals the other particle state instantaneously regardless of how far they are from each other contradicts

the locality principle. Furthermore, the superposition nature of the entanglement suggests that, before performing the measurement, the two particles are not in a definite state, which contradicts the principle of realism. This casts doubt on the completeness of quantum mechanics as highlighted in the famous Einstein–Podolsky–Rosen (EPR) paper [22]. In this paper, the authors suggested that there may be hidden variables that contribute to the measurement results and that we just do not have access to yet.

The EPR argument was then settled in 1964 when John S. Bell laid out what is known as Bell's inequality. Bell shows theoretically that common-sense-based physical theory (i.e., locality and realism) cannot support the predictions of quantum mechanics because the correlations between entangled particles violate Bell's inequality [23]. The first experimental result that confirms that quantum mechanics violates Bell's inequality was done in 1972 by John F Clauser and Stuart J Freedman [24]. A more advanced experiment was performed by Alain Apsect in 1982 and confirmed the violation of Bell's inequality [25]. Furthermore, the loopholes [26] in Bell's inequality tests have been resolved [27, 28]. The 2022 Nobel prize was awarded to John Clauser, Alain Aspect and Anton Zeilinger for their pioneering work on Bell inequality.

- Entanglement for quantum technology
  In the field of quantum technology, quantum entanglement plays an important role, and it will be an essential ingredient of any future quantum device. This is because quantum entanglement can be used for various protocols in QIP. For instance, in quantum secure communications tasks, entanglement is a key element in Quantum Key Distribution (QKD) [10, 29–32]. Furthermore, entanglement can be used for teleportation protocols [33–37], which is the process of transmitting a qubit state using a pre-shared maximally entangled Bell state and a classical communication channel.

Measurement

Quantum measurement is one of the most fundamental challenges in quantum information technology. In classical physics, measurement provides information about what is being measured in the system, while in quantum physics, measurement affects the observable being measured and results in a state that may not be the actual state prior to measurement. This is because the actual state before

measurement is not necessarily a definite state, as it could be a pure superposition state, or a mixed state comprising a probabilistic distribution of pure states. But as soon as the quantum state is measured, the initial state is projected into one of the eigenstates of the observable that is being measured. The probability of measuring an outcome k can be represented as $\mathcal{P}(k) = \langle\Psi| M_k^\dagger M_k |\Psi\rangle$, where M_k is the measurement projection operator. The state of the system after this measurement will be given by

$$|\Psi'\rangle = \frac{M_k |\Psi\rangle}{\sqrt{\langle\Psi| M_k^\dagger M_k |\Psi\rangle}}. \tag{1.9}$$

For example, suppose that an electron is in a spin-up $|1\rangle$ or spin-down $|0\rangle$ state, along the z-axis and a measurement of the electron spin is performed along the x-axis, then we will get one of the eigenstates $|+\rangle$ or $|-\rangle$ of the x-axis spin observable (σ^x). Information about the spin of the electron along any other axis will be indeterminate. The operators that represent the spin components along the three Cartesian axes are known as Pauli operators and they are given by 2×2 matrices as

$$\sigma^x = \begin{pmatrix} 0 & 1 \\ 1 & 0 \end{pmatrix}, \qquad \sigma^y = \begin{pmatrix} 0 & -i \\ i & 0 \end{pmatrix}, \qquad \sigma^z = \begin{pmatrix} 1 & 0 \\ 0 & -1 \end{pmatrix} \tag{1.10}$$

As we shall see in Chapter 2, the state of the system after measurement will remain in the eigenstate of the observable being measured and no longer in a superposition of all the eigenstates. This means that measuring the spin along x-axis again will still give the same eigenstate, unless measurement on another observable (e.g., along y or z-axis) is taken place, which will bring the system back to its undetermined state with respect to its x-axis spin.

Decoherence

Coherence is a property in quantum mechanics where different amplitudes for the components in a pure superposition state have well-defined relative phases, which allows quantum phenomena, such as interference, to occur. Generally, quantum systems suffer from the loss of coherence in the system; in a phenomenon known as decoherence. This could be due to the system's interaction with the environment. An example of the effect of decoherence would be when a system of one qubit is prepared in a pure state, and the environment interaction with the qubit makes it partially entangled with the environment, which in turn results in the state of

the system alone being a mixed state. In this case, the evolution of a specific quantum information task should be treated as an open evolution, and hence as a non-unitary evolution of just the system, which is described using a master equation for the density matrix evolution. Furthermore, preferred bases can arise by environmental decoherence when the interaction of the environment and the system effectively results in a measurement performed on a specific basis. Unless other Hamiltonian terms continue to act, such an environment interaction alone will evolve the system density matrix to being diagonal in this preferred basis..

The presence of decoherence in the system is not only attributed to the interaction of the environment with the system, but could also be due to manufacturing errors with stochastic nature in the system itself. Here, our investigations of decoherence focus on errors in the establishment of the time-independent Hamiltonian (manufacturing defects). We note that other effects may lead to different forms of decoherence, but our studies apply best to systems where manufacturing defects dominate. Thus, assuming that the decoherence effect (interaction with environment) in our model is sufficiently weak over the relevant time scales of operation, our investigation will focus on closed systems. In this case, the evolution of a single realisation of a specific quantum information task is a unitary evolution that is engineered to exhibit periodic behaviour, and which can be described using Schrodinger's equation. However, the average over an ensemble of realisations evolves as a mixed state, due to the averaging of different realisations which have different periodicities, or amplitudes, or both. A detailed discussion on this will be given in Section 2.3.

As will be seen in Section 1.1.2, one of the important requirements for a reliable quantum device is that the time required for a quantum information task to be carried out needs to be performed faster than the decoherence time of the relevant system. Otherwise, the information of the quantum system will be lost due to decoherence before a useful operation is performed. Therefore, in order to put our results in a realistic context, we have tested our device performance against this requirement, as given in Section 6.5.

Unitary operators

Quantum operations are generally reversible and the mathematical tool used to represent an operator that is reversible is the unitary operator. Unlike a measurement operator, the action of a unitary operator on a system state will give a

different state, $U|\Psi\rangle = |\Psi'\rangle$. The reversibility of this operation is achieved by applying $U^\dagger$. The unitary has the property $UU^\dagger = U^\dagger U = \mathcal{I}$, where $\mathcal{I}$ is the identity operator. As a result, the reversibility in quantum mechanics can be expressed by unitary operators as

$$U^\dagger[U|\Psi\rangle] = U^\dagger[|\Psi'\rangle] = |\Psi\rangle\,. \tag{1.11}$$

Closed quantum systems have a specific type of unitary known as a time evolution operator. Reversibility in the time evolution operator can be simply seen when the system in an initial state evolves to a certain state and allowed to evolve again so that the system retains its initial state. A detailed discussion of that will be given in Chapter 2.

Quantum gates

Classical computation requires circuits for a computation to be done. Circuits are a sequence of gates, where the information is changed and manipulated (such as magnifying or stopping current, etc.). Gates can be realised using components such as transistors, diodes, and vacuum tubes. Logic gates implement a Boolean function, or logical operation, performed on one or more inputs of binary, and produce an output binary. In general, this is not reversible.

Similarly, quantum computation requires quantum circuits, where information is manipulated through a sequence of quantum gates or through the natural time evolution of the system, which can be thought of (abstractly) as a gate. Quantum gates can be expressed as unitary matrices. Therefore, since the unitary operators have inverse, all quantum gates are reversible. The action of a quantum gate (unitary operator) on a particular quantum state produces a new quantum state, $Q|\Psi\rangle = |\Psi'\rangle$, where Q represents the quantum gate, $|\Psi\rangle$ represents the quantum state, and $|\Psi'\rangle$ is the new quantum state resulting from the application of the quantum gate.

For example, when the quantum NOT gate acts on a single qubit state $|\psi\rangle = \alpha|0\rangle + \beta|1\rangle$, it will simply flip the state $|0\rangle$ to $|1\rangle$ and vice versa. Therefore, the output state is a new quantum state $|\psi'\rangle = \alpha|1\rangle + \beta|0\rangle$. It is clear that the NOT quantum gate acts linearly [13]. This NOT gate can be represented by a 2x2 unitary matrix, which happens to be the σ^x operator

$$X = \sigma^x = \begin{pmatrix} 0 & 1 \\ 1 & 0 \end{pmatrix} \tag{1.12}$$

Another example of a single qubit gate is the *Hadamard* gate,

$$U_H = \frac{1}{\sqrt{2}} \begin{pmatrix} 1 & 1 \\ 1 & -1 \end{pmatrix} \tag{1.13}$$

which transforms the state $|0\rangle$ to superposition state $\frac{|1\rangle - |0\rangle}{\sqrt{2}}$ and the state $|1\rangle$ to superposition state $\frac{|1\rangle + |0\rangle}{\sqrt{2}}$.

On the other hand, two-qubit or multiple-qubit gates are necessary for quantum information processing [13]. A common example of a two-qubit gate is the controlled NOT gate (or CNOT or CX). The CNOT gate has a controlled qubit $|C\rangle$ and a targeted qubit $|T\rangle$. For example, in this state $|01\rangle$, the controlled qubit is the first qubit $|0\rangle$ and the target qubit is the second qubit $|1\rangle$. When this gate acts on a two-qubit state, it flips the target qubit if the control qubit is $|1\rangle$, and it does nothing if the control qubit is $|0\rangle$. For instance, $\text{CX}|00\rangle = |00\rangle$, $\text{CX}|01\rangle = |01\rangle$, $\text{CX}|10\rangle = |11\rangle$, and $\text{CX}|11\rangle = |10\rangle$. Therefore, a CNOT gate can be represented as a 4x4 matrix.

$$\text{CNOT} = \begin{pmatrix} 0 & 1 & 0 & 0 \\ 1 & 0 & 0 & 0 \\ 0 & 0 & 1 & 0 \\ 0 & 0 & 0 & 1 \end{pmatrix} \tag{1.14}$$

The CNOT gate can be used to produce a maximally entangled state (Bell state) out of a product state. Consider, for example, the two-qubit state $\frac{1}{\sqrt{2}}(|0\rangle + |1\rangle)_{q1} \otimes |1\rangle_{q2}$, which can be written as $\frac{1}{\sqrt{2}}(|01\rangle + |11\rangle)$, applying the CNOT gate here will produce the entangled state $|\Psi^+\rangle = \frac{1}{\sqrt{2}}(|01\rangle + |10\rangle)$. The first implementation of a CNOT quantum gate was performed using trapped ions [38].

If a set of gates can be used to perform any computation, then this set of gates is said to be a universal set of gates. In classical computation, these sets of gates are: AND, OR, NOT gates. In quantum computation, any arbitrary operation can be performed using single-qubit gates and any two-qubit gate (e.g., CNOT) that is capable of producing entanglement [13, 39].

1.1.2 DiVincenzo requirements for quantum devices

A couple of decades ago, DiVincenzo established seven requirements that must be satisfied to build a reliable quantum device [40]. The first five requirements are necessary for quantum computation, and the remaining two are necessary for

quantum communication or distributed quantum computing.

1. *The physical system must be scalable and its qubits must be well characterised.*

   The qubit is the building block of quantum technology and so it is necessary to be well defined. The problem is that when the number of qubits increases, the system becomes more difficult to handle, as there are various parameters that have to be controlled. The physical parameters include the interaction between qubits, the coupling of state correlations, and the interaction of qubits with external parameters that might be used to control or manipulate the qubits. Therefore, well-characterised qubits mean that all these parameters are well defined regardless of the number of qubits [40]. There are different methods used to realise qubits and it will be demonstrated in Section 1.1.3.

2. *The system should have the ability to initialise the qubit state to a desirable state.*

   This requirement is raised for two reasons. First, registers need to be initialised to a known state before the computation starts. Second, a continuous supply of ground-state qubits (i.e. $|0\rangle$) is needed for quantum error correction. The process of initialisation can be performed by either naturally cooling the system down to its ground state or by a measurement that projects the system to a desired state. The latter may involve additional operation, for example, if the measurement results in a state $|1\rangle$, while the initialisation requires a state $|0\rangle$, then we apply a bit-flip operation on the $|1\rangle$ state to get the desired state. The important parameter here is the time it takes for the initialisation process to complete, which should be less than the decoherence time [40].

3. *The relevant decoherence time needs to be longer than the gate operation time.*

   Decoherence as defined in Section 1.1.1 is the loss of quantum coherence. It is when, for example, a qubit state $|\psi\rangle = \alpha|0\rangle + \beta|1\rangle$ is transformed into a mixture state as

   $$\rho = |\alpha|^2 |0\rangle\langle 0| + |\beta|^2 |1\rangle\langle 1| . \tag{1.15}$$

   Decoherence times describe the dynamics of a quantum system in contact with an external reservoir, or, in other words, being in contact with its

environment. For a quantum computation, it is necessary that the relevant decoherence time remains long enough so that the computation operation takes place. The word "relevant" decoherence times indicates that there are many decoherence times for a quantum particle. The relevant time is determined by the choice of the basis states of the qubit $|0\rangle$ and $|1\rangle$. For example, if these two states describe identical orbital states but different spin states, then the spin coherence time is relevant, while the orbital coherence is not [40]. Quantum error correction can correct for the decoherence of computational qubits by using additional (ancilla) qubits to redundantly encode the computational states into a greater number of qubits.

4. *A universal set of quantum gates.*

   A set of quantum gates is called universal if any computation can be performed using a sequence of that set of gates. A two-qubit gate, such as a CNOT gate that is capable of generating entanglement, allows for any multiple-qubit operation [41], (see Section 1.1.1 for a discussion on quantum gates). However, random errors are likely to occur in the implemented Hamiltonian and therefore quantum gates cannot be perfectly achieved [40].

5. *The ability to measure a specific qubit.*

   As it is essential for quantum computation to acquire an initial state input (as discussed in requirement 2), the output of a computation needs to be read out as well. Therefore, measurement of a specific qubit is required to read the computation result. An ideal measurement on a particular qubit state should not change the states of the other qubits. Such an ideal measurement is said to have 100% quantum efficiency. However, in real measurement, the quantum efficiency is always less. However, such measurement efficiency can be improved by averaging a large number of realisations (e.g. 1000) of the same computation [40].

6. *The ability to interconvert stationary qubits and flying qubits.*

   Quantum devices hardware will be made with solid state qubits (e.g., quantum dots or trapped ions). Our spin network system that will be introduced in Chapter 3 is a generic example of a network of solid-state qubits. These are usually well suited for short-range quantum communication. However, for long-range quantum communication, the state of such qubits must be

encoded into flying qubits (photons). Photons are well suited for long-range quantum communication, and therefore the quantum device needs to have the ability to exchange information from solid-state qubits to photons [40]. This interface between light and matter has been achieved experimentally [42–44]. It may also require frequency-conversion of the photons to telecom wavelengths in order for these to be transmitted via optical fibres.

7. *Faithful transmission of flying qubits between specific locations.*

   During transmission, the information encoded in the photonic states is susceptible to disorder. Therefore, there must be a way to ensure that the information is preserved to enable a reliable quantum communication to be performed. There are many protocols that can be used to meet these requirements [45, 46].

1.1.3 Quantum information processing platforms

There are various physical systems that can be used to achieve various QIP protocols. Basically, any effective two-level system that can be isolated within a larger system and follows the DiVincenzo criteria can be regarded as a qubit and information is encoded in the qubits. We will discuss a few examples below and a detailed discussion will be given in Section 1.2.4.

An example of a two-level quantum system is a photon, where qubits in this case can be encoded in the polarisation of photons, as discussed in Section 1.1.1. Photons have been used to generate entangled states that are necessary for QIP protocols, and such entangled states can be generated using the spontaneous emission-based protocol [18, 19] or coincident detection of two fibre-based infrared photons [17] or parametric down conversion. Using photons as information carriers plays a crucial role in long-range QIP [47, 48]. Photons are particularly well suited for quantum communication protocols, such as fibre-based QKD [49–52] or satellite-based QKD [32, 53, 54].

Other examples of two-level quantum systems are the solid-state-based or matter-based systems, such as trapped ions [55–57], superconducting qubits [8, 58–60], quantum dots [61–63], and Rydberg atoms [64–66]. These systems compared to photon-based systems are suitable for short-range QIP protocols or as memories. This is because it may be possible to then avoid conversion to photons and back [67–71]. A detailed discussion of solid-state-based and matter-based

systems will be given in Section 1.2.4.

1.2 Spin Networks

Spin-1/2

It is the nature of quantum mechanics that subatomic particles exhibit strange behaviours. For example, a strange effect has been illustrated in the Stern-Gerlach experiment [72], which shows that when a beam is sent through an inhomogeneous magnetic field, the beam splits into two as shown in Fig.1.1. This was known as an intrinsic angular momentum (distinguishable from the orbital angular momentum), which is now known as "spin".

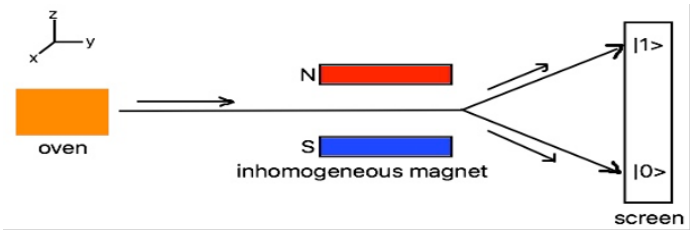

Figure 1.1: This figure demonstrates the apparatus used in Stern-Gerlach experiment for a spin-$\frac{1}{2}$ particle, where $|1\rangle$ denotes spin-up and $|0\rangle$ denotes spin down.

The spin-$\frac{1}{2}$ particle can be described using the three 2×2 Pauli matrices (see Section 1.1.1). These Pauli operators are especially useful mathematical tools for working with two-level quantum systems. As the spin-$\frac{1}{2}$ particle is a two-level quantum system (qubit), it can be utilised to be for use in QIP. The following section will introduce the model that describes a system composed of many spin-$\frac{1}{2}$ particles coupled to each other that can be used for QIP.

1.2.1 Model

A one-dimensional array of spin-$\frac{1}{2}$ particles (or equivalent) coupled to each other is known as a spin chain system or a linear Spin Network (SN) system. There are different Hamiltonians that can be used to represent a spin chain system. A general representation of the Hamiltonian of a spin chain system with nearest-neighbour interactions and open boundary conditions is given by

$$\mathscr{H} = \frac{1}{2}\sum_{i=1}^{N-1} J_{i,i+1}[(1+\Omega)\sigma_i^x\sigma_{i+1}^x + (1-\Omega)\sigma_i^y\sigma_{i+1}^y + \Gamma\sigma_i^z\sigma_{i+1}^z] + \sum_{i=1}^{N}\epsilon_i\sigma_i^z \quad (1.16)$$

This Hamiltonian is a general Heisenberg Hamiltonian [73]. The nearest-neighbour coupling interactions $J_{i,i+1}$ and the on-site energies ϵ_i are homogeneous if they are site-independent. The symmetry of the coupling interaction is specified depending on the anisotropy parameters Ω and Γ. For instance, when $\Omega = 0$ and $\Gamma = 1$, we attain the original Heisenberg model, called the XXX model. Another model known as the XXZ model is obtained when $\Omega = 0$ and $\Gamma \neq 1$. A special case of this model is obtained when $\Omega = 0$ and $\Gamma = 0$ and is called the XX model (also known as the XY model). This is the model used in this thesis and will be discussed in detail in Chapter 2. Finally, a model known as XYZ can be obtained with $\Omega \neq 0$ and $\Gamma \neq \{0, 1\}$, and another model known as the Ising model can be obtained with $\Omega \pm 1$ and $\Gamma = 0$. These models can be realised in different physical systems when the parameters can be set as such in that system.

1.2.2 Spin networks for quantum communication

Quantum communication is the process of transferring quantum information, a transfer that is based on the laws of quantum mechanics. It is a broad field ranging from short-range communications (for example, communication between registers inside a quantum processing or computing) to long-range communications (e.g., satellite-based communications [32, 53, 54]).

In this thesis, we are concerned with the short-range quantum communication that can be achieved using spin-$\frac{1}{2}$ based systems without conversion to photons and back [67–71]. As discussed in Section 1.1.3, unlike photon-based systems that are suitable for long-distance quantum communication, solid-state-based or matter-based systems are well suited when it comes to short-range quantum communication performed, for example, inside a quantum computer. This is due to the fact that the solid-state entities (spin-$\frac{1}{2}$ qubits) within a quantum device can interact, for example, through Coulomb interaction, facilitating the transfer of quantum information between qubits with minimal external control. This eliminates the need to move the qubits or utilize a flying qubit to perform such a task, which could involve interfacing between photons and stationary spins [11, 73]. Moreover, as will be seen in Section 1.2.4, solid-state-based or matter-based systems can be implemented through different physical platforms.

The first study of quantum communication using linear SN systems was proposed by Bose in 2003 [11, 74]. This opened up a new research field that focuses on using spin chains or SN systems to transfer quantum information. Bose considered

a ferromagnetic Heisenberg chain where all sites have a spin-down $|0\rangle$ state, and where the couplings are homogeneous. The information transfer in this spin chain is performed as follows: Alice (the sender) places an excitation (encoded as a spin-up $|1\rangle$) at one end of the spin chain, and Bob (the receiver) receives it at the other end of the spin chain at a later time τ. The importance of the spin chain system for Quantum State Transfer (QST) is that, unlike other quantum implementation systems [75, 76], it does not require a switching on or off between qubits, which may cause decoherence, in order for a transfer process to occur. When such an operation is performed without the need to control the system (i.e., simply by injecting excitation and waiting until it evolves to the desired location), we say that it is achieved by the natural dynamics of the system. In addition to one-to-one communication, spin chains can also be used for communication between multiple users by connecting multiple users to the ends of the spin chain and with the appropriate tuning of the Hamiltonian parameters [77].

Such systems form an example of non-linear SN systems that involves more complex topologies (e.g., a two-dimensional SN). Non-linear SN systems have also been used for QST [1, 60, 78–82]. The advantage of SN systems over spin chain systems with respect to QST is that SN systems offer wider opportunities for QST and may require local operations on part of the SN in order for QST to occur. Moreover, as will be discussed in Chapter 3, the richer topology that SN systems have gives them the potential for wider applications such as multipartite entanglement generation and quantum sensing [1, 12, 83].

In order to quantify how well the QST operation is performed, the fidelity measure is used (see Section 2.2.1 for a discussion of fidelity). The useful QST requires fidelity above the threshold of $\frac{2}{3}$, which is the maximum value of classical transmission of a quantum state for $N \leq 80$ [73]. However, higher fidelities are also desirable. In fact, QST with high fidelity has been achieved in spin chains (and spin networks) through various methods. Examples include the application of local magnetic fields near the sender and receiver qubits [84], or through local operations on the receiving qubit [85], or by using adiabatic techniques [86]. These methods enabled QST, and are scalable, with high fidelities but still not perfect (fidelity < 1). When the fidelity of the QST is 1, then we say that the transfer operation is perfect, a process known as Perfect State Transfer (PST).

It has been shown that PST can be achieved in spin chains with homogeneous nearest-neighbour interactions, $J_{i,i+1} = 1$, as long as the chain length is $N \leq 3$

[11, 87]. In order for the PST to be achieved independently of the chain length, there are various strategies that can be used. Examples include pre-engineering the nearest-neighbour interactions [87–89], using a specific encoding method such as dual rail encoding [90,91] or wavepacket encoding [92,93]. A detailed discussion of the PST protocols will be given in Chapter 2.

Various experimental realizations of high-fidelity QST and PST have been achieved through various physical systems. High-fidelity QST has been enabled through superconducting qubits by the application of an on-site potential as well as modulation of couplings strength [94] or via a cavity bus [95]. High-fidelity QST has also been realised in a system of electrons confined in Penning traps [96]. PST on the other hand has been achieved experimentally using a liquid nuclear magnetic resonance system for an XY type spin chain of $N = 3$ [97]. Moreover, using superconducting qubits, PST has been achieved via a tunable coupling technique [98] that relies on a parametric modulation of the qubits such that the coupling strengths fulfill the symmetric ratio of the couplings [87–89] required for PST.

1.2.3 Spin networks for entanglement generation

Quantum entanglement is necessary for various QIP protocols, as discussed in Section 1.1.1. SN systems can be used to generate, manipulate, and transfer different types of entangled states. Here, we will discuss generation of entangled states in SN systems and recent advances in this field.

One way to generate a bipartite entangled state (i.e., two-qubit entanglement) between the ends of a linear SN system is via the injection of a single-excitation in the middle of the chain with some couplings being weakly coupled to the chain, known as a dimerised chain [99,100]. Another way is to use a linear SN of Y shape (i.e., one end of the chain has two outputs) which will results in entanglement between these two outputs, when a single-excitation is evolved from the other end of the chain [101]. In this Y-shaped SN, the generated entangled state can be frozen by applying a phase flip (-1) to one of the entangled qubits, which will result in an eigenstate, and such a frozen entangled state is a useful quantum resource [101]. In a complex non-linear SN system, generation of a bipartite entanglement between the ends of the SN can be achieved by injecting a single-excitation at the middle of the SN or by injecting the excitation at one end of the SN with the application of a local phase factor into another part of the SN [2].

Transferring an entangled state is achieved through the natural dynamics of linear SN systems. If, for example, a Bell state of the form $|\Psi^+\rangle = \frac{1}{\sqrt{2}}(|01\rangle + |10\rangle$ is generated on the first two qubits of the chain, then the evolution of the system will transfer this entangled state so that it will be between the last two qubits of the chain [11, 89]. This happens because the PST system is set up to give perfect mirroring of any input state to the mirror image (about the chain centre).

Entanglement shared between multiple qubits (multipartite entanglement) can also be achieved in SN systems. For example, the W-type entanglement (i.e., entanglement shared equally between N qubits) [102, 103] can be achieved in the XY-type spin chain via the application of a transverse magnetic field [104] or via the branching at one end of the chain [105]. It can also be generated in complex SN systems by applying an appropriate phase factor as well as the natural evolution of the dynamics [2]. Generation of another multipartite entanglement such as GHZ entanglement, which is given by $|GHZ\rangle = \frac{|00...0_N\rangle + |11...1_N\rangle}{\sqrt{N}}$, has also been achieved in linear SN systems via Hamiltonian evolution as well as single-qubit rotations [106]. Such entangled states are not only useful for investigation of quantum non-locality [107] but also have wider applications in QIP, such as superdense coding [108], quantum teleportation [109], and quantum secure direct communication [110].

1.2.4 Physical implementation of spin networks

The SN systems we discuss here can be realised experimentally using various physical systems. Specifically, systems that are of spin-$\frac{1}{2}$ equivalent. Optical systems, such as photons, are not considered here because they lack an important feature of SN systems, which is direct and deterministic interaction between photons. Therefore, it is not possible to prepare a chain of static photons, with static couplings between them, to act as a spin chain. It is possible to envisage all-optical quantum computing [111,112], but here the photon qubits move constantly through the computer. Static solid-state-based or matter-based systems, on the other hand, can be used to transfer information between qubits, as they can interact directly [73]. In the following, we discuss these two-level solid-state-based and matter-based quantum systems that are capable of realising the XY model, which is the generic system of study in this thesis.

As will be demonstrated in this thesis, the characteristic device operation time will relate to the inverse of the coupling and it is clearly desirable for this to be

significantly smaller than any coherence time. Note that the coherence time of a single-qubit is usually longer than the coherence time of a two-qubit system, as in the two-qubit case, interactions and additional sources of decoherence can arise, which makes the coherence time shorter. Therefore, the coherence times we use in the following hardware are the coherence times relevant to two-qubit operations. This is important in order for the comparison of a two-qubit gate time against the coherence time to be fair. A comparison table for implementations will be presented in Section 6.5.

Quantum dots

Quantum dots are a two-level quantum state and can therefore be used to realise a SN system [61]. The types of quantum dots are determined by encoded information, such as exciton quantum dots [113] or electron quantum dots [61,88]. For example, the exciton quantum dot encodes the state of the qubit in the presence or absence of the exciton ground state as the logical $|1\rangle$ or $|0\rangle$, respectively [113,114]. When initialized to their ground state, the quantum dots remain in their ground state as long as there is no external applied field, and can be excited with the application of electromagnetic radiation. Quantum dots have already been used for QIP protocols, such as QST and entanglement [88, 115]. Recent advances in quantum dots allow for efficient control of many quantum dots and pave the way for the scalability of quantum dots [63].

The Hamiltonian model given in Eq.(1.16) has two parameters: the nearest-neighbour coupling interaction $J_{i,i+1}$ and the on-site energy ϵ_i. The physical nature of these parameters in a quantum dot, where the qubits are excitons, will be of dipole-dipole interaction for $J_{i,i+1}$, whereas ϵ_i will be the energy band gap between the conduction and the valence bands of a quantum dot, which can be controlled by an external field [113].

A typical characteristic value of the coupling interaction $J_{i,i+1}$ in silicon quantum dots is $J_{i,i+1} \approx 900$ MHz [62] and the coherence time, T_c, for a two-qubit operation is of the order of $T_c = 8.3$ μs [116]. Note that both references given here use the same system (silicon quantum dots). A comprehensive discussion can be found in [117].

Trapped ions

Another two-level matter-based quantum system is trapped ions. Trapped ions are charged particles or ionised atoms confined in a complex combination of electric and magnetic fields. The qubit of a trapped ion is its two internal states; the ground state $|g\rangle = |0\rangle$ and the excited state $|e\rangle = |1\rangle$ [38, 55, 118]. Initialisation can be done by cooling the system down to its ground state using lasers. Individual manipulation of a trapped ion can be achieved via the application of a laser on the ion [38].

Trapped ions have many advantages, such as exceptionally long coherence times, high-fidelity quantum gates, and straightforward state preparation/readout. On the other hand, the main disadvantage of using trapped ions is scalability, as the ability to increase the number of qubits remains a challenge [119]. However, a recent study has paved the way for scalability by preparing bilayer crystal configurations of well-defined layers that involve hundreds of ions using Penning traps [57].

In trapped ions, the coupling interaction parameter $J_{i,i+1}$ in the Hamiltonian model given in Eq.(1.16) will be of Coulomb repulsion type, while the on-site energy parameter ϵ_i will be the energy required to excite a trapped ion from the ground state $|g\rangle$ to the excited state $|e\rangle$ [38].

A typical characteristic value of the coupling interaction $J_{i,i+1}$ in trapped $^{171}YB^{+}$ ions is $J_{i,i+1} \approx 0.6$ kHz [120] with long coherence time of around $T_c = 0.5$ s [56]. For an in-depth review, see [117].

Superconducting qubits

Superconducting qubits are also a two-level solid-state quantum system that can be used to realise SN systems. There are three types of superconducting qubits: charge qubits, flux qubits, and phase qubits. In charge qubits, the two-level quantum state can be represented as the presence or absence of a cooper pair on a superconducting island. Flux qubits states are the magnetic flux pointing up and down. Phase qubit states are encoded in the conductance wavefunction as the change of the phase amplitudes of the oscillation across a Josephson Junction [58, 121].

Quantum technology based on superconducting qubits has gained interest in recent years for it features. In fact, great progress in quantum technology (quantum supremacy) has been made recently in superconducting loops [8]. Moreover, the superconductors coherence and Josephson effect are used as a nonlinear resource for making artificial atoms [122]. Experimental implementation of a two-dimensional

spin network has been achieved in superconducting qubits [60].

In superconducting flux qubits, the coupling interaction parameter $J_{i,i+1}$, of the Hamiltonian Eq.1.16, between two neighbouring qubits will be achieved by modulating the frequency of a tunable coupler that is attached to both qubits. The on-site energy ϵ_i can be manipulated by an external magnetic field [123].

A typical characteristic value of the exchange coupling $J_{i,i+1}$ in superconducting qubits is $J_{i,i+1} \approx 50$ MHz [59]. The relaxation and dephasing times of such qubits are $T_1 \approx 50 - 85\mu$s and $T_2 \approx 10 - 50\mu$s, respectively [59]. Therefore, we take the shortest of these times as the coherence time, $T_c = 10$ μs. See [58, 117] for a detailed discussion.

Rydberg atoms

A system of Rydberg atoms is also an interesting platform that can be used to implement our SN experimentally. Such atoms are realised when outer electrons of the atoms are in a highly excited state. The two-level qubit states in Rydberg atom can be encoded in the ground state $|g\rangle = |0\rangle$ and the excited state $|e\rangle = |1\rangle$. Laser can be used in Rydberg atoms to control the transition states or to initialise atoms in a desired state. Such platform is promising in terms of scalability and is feasible to realise in two or three dimensions [64, 65, 124–127].

The typical characteristic value of the coupling interaction $J_{i,i+1}$ between two atoms, in the blockade regime, is given as $J_{i,i+1} \approx 685$ MHz [66] and the coherence time is found to be $T_c \approx 1.3$ μs [66].

NMR-based processors

Another interesting platform for realising SN systems is Nuclear Magnetic Resonance (NMR) systems. The qubit states in NMR are the spin up $|1\rangle$ and spin down $|0\rangle$ states of the nucleus of a molecule. Initialisation can be performed via optical pumping or by polarisation of dynamic nuclear [128]. NMR processors can be of the solid-state form or the liquid-state form. Implementation of liquid samples of NMR allows the realisation of PST for a chain of $N = 3$ [97] and universal control on up to 12 spin qubits [129]. Solid-state NMR, on the other hand, provides stronger couplings and therefore allows for faster gates [73].

In solid-state-based NMR processors, the Hamiltonian interaction parameter $J_{i,i+1}$ will be dominated by a magnetic dipole-dipole interaction [130]. In liquid-based NMR, the inhomogeneous chemical properties of the environment around

each spin results in magnetically distinct spins in each molecule. The interaction between these spins, $J_{i,i+1}$, is a weak interaction mediated by the molecular orbital between nuclei that forms by the electrons [130].

1.3 Thesis outline

The present thesis contains 5 chapters in addition to the introduction chapter. We start in Chapter 2 by introducing the Hamiltonian of our system and describing various techniques, measurement tools, and perturbations used in this thesis. The contribution in this thesis is shown in the following chapters. Chapter 3 will introduce the design of our SN system and demonstrate the applications of the SN by focusing on a specific structure of the SN (which we call two-chain spin networks). Another structure of the SN with wider applications is proposed in Chapter 4. Until now we would have only discussed the work considering the single-excitation subspace. Therefore, Chapter 5 will discuss the usage of our SN when considering higher excitations subspace. Finally, the conclusion of the thesis is given in Chapter 6.

Chapter 2

Method

The research presented in this thesis is mainly based on computational methods, and Python programming is used to investigate and produce all the results of this thesis. To ensure the accuracy of our numerical methods and simulations, we have reproduced some existing results found in the literature. Furthermore, analytical calculations were also used for simple systems to ensure that our numerical simulations are correct.

This chapter presents the techniques and tools used to produce and analyse the results. First, we start by introducing a linear spin network (SN) Hamiltonian. From now on, we will use the wording "spin chain" systems to refer to "linear SN" systems. We also introduce a non-linear SN Hamiltonian used to represent a 2D SN system. Then, we discuss Schrödinger equations that govern the time evolution of the dynamics of the system. We also demonstrate the encoding methods used as well as the techniques used to set the initial conditions of the system. In addition, we present the measurement tools used to assess how well a particular operation has performed. Finally, we illustrate different types of disorder that might arise in real-world practical systems.

2.1 Techniques

2.1.1 Hamiltonian

As discussed in the previous chapter (Section 1.2.1), there are various Hamiltonian models that can be used to describe SN systems. However, we will focus on the time-independent XY-Hamiltonian since there are different physical systems that can be modelled using this Hamiltonian [96, 98]. Note that this model can be obtained from the familiar Heisenberg model (e.g., describing coupled semiconductor spin qubits [73,75]) by removing the coupling between the z spin components. The

time-independent XY-Hamiltonian for a spin chain system is given by

$$H_{XY} = \frac{1}{2}\sum_{i,i+1}^{N-1} J_{i,i+1}(\sigma_i^x\sigma_{i+1}^x + \sigma_i^y\sigma_{i+1}^y) + \sum_{i=1}^{N}\frac{\epsilon_i}{2}(\sigma_i^z), \tag{2.1}$$

where N is the total number of sites/spins and $J_{i,i+1}$ denotes the nearest-neighbour coupling interaction between sites i and $i+1$. The x, y, and z spin components are represented using Pauli operators σ^x, σ^y, σ^z, respectively, that have already been introduced in Section 1.2.

The second term in Eq. (2.1) represents the on-site energy (i.e., the energy cost to excite site i from a spin down state $|0\rangle$ to a spin up state $|1\rangle$). For simplicity, we set $\epsilon_i = 0$ in the ideal case. However, when examining the impact of diagonal disorder on the system, noise variation in ϵ_i must be taken into account.

The number of excitations $\mathcal{N} = \sum_{i=1}^{N}\frac{1}{2}(\sigma_i^z + \mathcal{I}_i)$, where $\mathcal{I}$ is the relevant identity, is conserved. This is because the total z-component of the spin network commutes with the Hamiltonian $[\mathcal{N}, H_{XY}] = 0$. This holds for any values of the couplings $J_{i,i+1}$ and the on-site energies ϵ_i. As a result, the different excitation-number subspaces decouple, meaning that if you initialise the system in an $\mathcal{N}$-excitation subspace ($\mathcal{N}$ could be 1 or 2 or more) the system will evolve only in this $\mathcal{N}$-excitation subspace.

As will be clear in Chapter 3, we use the spin chain Hamiltonian Eq. (2.1) to build systems of spin chains that are not coupled to each other, referred to as Uncoupled Spin Chains (USC). An example of a two USC system is shown in Fig.3.3. Once we prepare the USC, we couple them together via unitary transformation to form a 2D SN system. The 2D SN system is then used to perform various quantum information processing. The Hamiltonian $\mathcal{H}_{XY}$ of a 2D SN can be represented by

$$\mathcal{H}_{XY} = \frac{1}{2}\sum_{i,j} J_{i,j}(\sigma_i^x\sigma_j^x + \sigma_i^y\sigma_j^y) + \sum_{i=1}^{N}\frac{\epsilon_i}{2}(\sigma_i^z). \tag{2.2}$$

There are still N sites in the system. $J_{i,j}$ represents the coupling interaction between sites i and j, which are not necessarily nearest neighbour sites, and ϵ_i, as defined above, is set to zero for simplicity unless we consider the effect of diagonal disorder. Off-diagonal disorder (affecting $J_{i,j}$) is also considered (see Section 2.3.2). Both diagonal and off-diagonal disorder preserves the number of excitations, because $\mathcal{H}_{XY}$ and $\mathcal{N}$ commute for any choice of couplings and on-site energy values. Note that other types of disorder not considered here (e.g.,

uncorrelated noise in the xx and yy couplings) can mix subspaces with different $\mathcal{N}$ values; these are not considered in this thesis.

2.1.2 Time evolution

The Schrödinger equation is an essential tool in quantum mechanics and can be used to calculate the evolution of a quantum state with time [131, 132]. A time-dependent Schrödinger equation can be used to solve a quantum system for which the Hamiltonian is either time-dependent or time-independent. The time-dependent Schrödinger equation is given by

$$i\hbar\frac{\partial}{\partial t}\left|\Psi(t)\right\rangle = \hat{H}(t)\left|\Psi(t)\right\rangle . \tag{2.3}$$

We are considering the time-independent Hamiltonian that describes a closed quantum system which is assumed to not interact with its environment, and therefore its total energy is conserved. This is because, as discussed in Chapter 1, our investigations of decoherence focus on errors in the physical implementation of the time-independent Hamiltonian and therefore for each realisation of the system we consider a closed dynamic. Thus, the Schrödinger equation can be reduced to its time-independent form and it is given by

$$E\left|\Psi\right\rangle = \hat{H}\left|\Psi\right\rangle . \tag{2.4}$$

By diagonalising the observable $\hat{H}$, a complete basis set known as eigenstates $|\varphi_j\rangle$ can be obtained and for each eigenstate there is a real eigenvalue λ_j associated to it. Therefore, any state can be written as a linear combination of the eigenstates

$$\left|\Psi(t)\right\rangle = \sum_j c_j(t)\left|\varphi_j\right\rangle , \tag{2.5}$$

where $c_j(t) = \langle\varphi_j|\Psi(t)\rangle$.

By projecting the eigenstates $|\varphi_j\rangle$ into the time-dependent Schrödinger equation Eq. (2.3) and with a simple re-arranging and integration, we can find an expression for $c_j(t)$ given as $c_j(t) = c_j(0)e^{-i\lambda_j t/\hbar}$. Therefore, the state at any time, expanded in terms of the eigenstates, is given by

$$\left|\Psi(t)\right\rangle = \sum_j c_j(0)e^{-i\lambda_j t/\hbar}\left|\varphi_j\right\rangle , \tag{2.6}$$

with $c_j(0) = \langle \varphi_j | \Psi(0) \rangle$.

The state evolution can be written in another form. If we set the Hamiltonian term, $\hat{H}(t)$, in Eq. (2.3) to be time-independent, $\hat{H}$, and re-arrange and integrate the equation, the state evolution can be given by

$$|\Psi(t)\rangle = e^{-i\hat{H}t/\hbar} |\Psi(0)\rangle \tag{2.7}$$

2.1.3 State encoding

The chosen basis for our system is the site basis $|0_i\rangle$ and $|1_i\rangle$. The $|0_i\rangle$ state represents a spin down state at site i, while $|1_i\rangle$ state represents a spin up state at site i. Each site of the SN system represents a qubit which can be in a spin up state ($|1\rangle$) or in a spin down state ($|0\rangle$) or in a superposition of these two states ($\alpha |0\rangle + \beta |1\rangle$). From now on, when we refer to a site that has an excitation, we mean that its state is a spin up state $|1\rangle$.

In order to study the dynamics of the system, we start by initialising the system so that all sites have a spin down state. This is represented as $|000\ldots\rangle$. We note that there are other protocols that do not require state initialisation [133]. When the system is initialised to a known pure state where all sites have a spin down state, we can then start injecting excitations and investigate the dynamics. Note that the injection of excitations needs to be performed on a timescale that is very fast compared to the natural dynamical timescale for the SN. Injecting a single-excitation at a site can be represented as flipping the spin of the desired site to be in a spin up state. For example, in a spin chain of size $N = 3$, when a single-excitation is injected at site 1, the state of the system will be given by

$$|\Psi\rangle = |1_1\rangle \otimes |0_2\rangle \otimes |0_3\rangle \,, \tag{2.8}$$

which can be written in a simplified version as $|\Psi\rangle = |100\rangle$. Let's define a notation, $|r_i\rangle$, that represents a state where a single-excitation is injected at site i. Therefore, using this notation for our example above, $|100\rangle = |r_1\rangle$ or generally $|00\ldots1_i00\ldots\rangle = |r_i\rangle$. Similarly, if there are excitations at sites 1 and 3, then we represent this as $|\Psi\rangle = |r_{1,3}\rangle$. If there are no excitation at any sites, then we represent this as $|\Psi\rangle = |r_0\rangle$. Other types of injection include for example injecting a superposition state (e.g., $|+\rangle = \frac{1}{\sqrt{2}}(|0\rangle + |1\rangle)$) at site i. The state of the system in this case is given by $|\Psi\rangle = \frac{1}{\sqrt{2}}(|000\ldots\rangle + |001_i00\ldots\rangle)$. Using our notation above, $|\Psi\rangle = \frac{1}{\sqrt{2}}(|r_0\rangle + |r_i\rangle)$.

The site basis $|r_i\rangle$ of the SN systems forms a complete basis set for the single-excitation subspace, and the dimension of the site basis depends on the choice of the subspace with which we work. Particularly, when we restrict ourselves to the single-excitation subspace, the vectors of site basis we need are only those which involve a spin up state at a site and spin down states at the remaining sites. The dimension of the site basis in the single-excitation subspace is equal to the number of sites N. Taking as an example $N = 3$, the site bases in this case are $|001\rangle$, $|010\rangle$, and $|100\rangle$.

In the case where we are not restricted to a subspace (e.g., considering the full Hilbert space of the system) the dimension of site basis grows as 2^N and for our example above, we would have 8 site bases given as $|000\rangle$, $|001\rangle$, $|010\rangle$, $|011\rangle$, $|100\rangle$, $|101\rangle$, $|110\rangle$, and $|111\rangle$.

2.1.4 Building the Hamiltonian matrix

As we have seen above, the Hamiltonian operator consists of Pauli operators and the action of Pauli operators (see Section 1.2) on a spin state is given by

$$\begin{aligned} \sigma^x|0\rangle &= |1\rangle & \sigma^y|0\rangle &= -i|1\rangle & \sigma^z|0\rangle &= -|0\rangle \\ \sigma^x|1\rangle &= |0\rangle & \sigma^y|1\rangle &= i|0\rangle & \sigma^z|1\rangle &= |1\rangle \end{aligned} \tag{2.9}$$

Therefore, the action of the Hamiltonian operator H_{XY} on a vector, for example $|10\rangle$, is given by

$$\begin{aligned} H_{XY}|10\rangle &= \frac{J_{1,2}}{2}[\sigma_1^x\sigma_2^x|10\rangle + \sigma_1^y\sigma_2^y|10\rangle] \\ &= \frac{J_{1,2}}{2}[|01\rangle + (-i)(i)|01\rangle] \\ &= J_{1,2}|01\rangle, \end{aligned} \tag{2.10}$$

and this shows that our Hamiltonian induces a hopping between nearest neighbouring sites.

In order to build the Hamiltonian matrix, we need the site basis of our system, which will be used to find the matrix elements. For a spin network system of size N, there are 2^N vectors in the site basis that can be used to find all the matrix elements to construct the Hamiltonian matrix. But if we are restricted to a specific subspace (e.g., single-excitation subspace) we can then just use the basis vectors of that specific subspace to construct the matrix Hamiltonian (e.g., single-excitation

site basis).

For example, for $N = 3$, taking matrix elements in the single-excitation site basis, the Hamiltonian matrix is given by

$$H_{XY} = \begin{pmatrix} 0 & J & 0 \\ J & 0 & J \\ 0 & J & 0 \end{pmatrix}, \tag{2.11}$$

where $H_{XY,ij}$ is given by $\langle r_i | H_{XY} | r_j \rangle$ and we assumed the coupling is constant $J_{i,i+1} = J$ and $\epsilon_i = 0$. This Hamiltonian matrix represents an XY-type spin chain system.

Consider now a system that is constituted of two separate XY-type spin chains (two USC system), each of 3-site. We have proposed a method that can be used to form a complex 2D SN system out of the two USC system. Our method is based on a unitary transformation of the Hamiltonian of the two USC system, a transformation that conserves the eigenvalues but changes the eigenstates. A detailed discussion about applying an appropriate unitary transformation to the Hamiltonian of the two USC to form a new Hamiltonian that describes a 2D SN will be presented in Chapter 3. Our unitary transformation method is also used to construct a more complex 2D SN out of multiple USC as will be shown in Chapter 4. A general form of such a unitary transformation is proposed in Chapter 5. This is useful when working with higher-excitation subspaces.

2.1.5 Perfect state transfer

As discussed in Chapter 1, achieving QST with high fidelity is desirable, but it is even better to achieve Perfect State Transfer (PST). Therefore, it is vital that our 2D SN system exhibits PST for the excitation transfer in an error-free case. There are various proposals that can be used in order for the state transfer to exhibit PST. Details of these proposals will be discussed below.

An approach to enable PST uses a specific encoding method such as dual rail encoding [90, 91] or wavepacket encoding [92, 93]. Another common approach to achieve PST over arbitrarily long distances is based on pre-engineering of the coupling parameters of the spin system. As mentioned in Chapter 1, the issue with homogeneous coupling interactions ($J_{i,i+1} = 1$) is that it does not allow PST to occur for chains of length $N > 3$ [11,74,87]. Therefore, various protocols that involve engineering the spin-spin interactions have been proposed in order to overcome

this issue. For example, a protocol relies on controlling each coupling parameter, $J_{i,i+1}$, to achieve PST, [134–136]. Another protocol depends on controlling only the boundary couplings, $J_{1,2}$ and $J_{N-1,N}$ to achieve near-PST [137–140].

In this thesis, we use a special type of coupling engineering protocol that sets the coupling parameters $J_{i,i+1}$ to be symmetric around the centre of the spin chain, which has been shown to allow PST to occur for any chain length [87–89]. The coupling interaction $J_{i,i+1}$ in this protocol is defined as

$$J_{i,i+1} = J_0\sqrt{i(N-i)}. \tag{2.12}$$

For any spin chain system, there is a maximum coupling, J_{max}, which depends on the physical realisation of the system [141]. This maximum coupling occurs in the middle of the chain and increases with N. In order to address such a practical constraint, we define dimensionless coupling units such that $J_{max} = 1$ (unless otherwise stated) for any N. This enables systems of different sizes to be compared, as the maximum coupling will always be the same, independent of N. Thus, J_{max} is our energy unit. Since the maximum coupling occurs in the middle of the chain, J_0 in Eq. (2.12) can be derived as following:

- For an even length spin chain, the maximum coupling occurs in the middle of the chain, $\frac{N}{2}$ as shown in Fig.2.1b, which is substituted in Eq. (2.12) as $J_{max} = J_0\sqrt{\frac{N}{2}(N-\frac{N}{2})}$ and therefore, $J_0 = 2J_{max}/N$.

- For an odd length spin chain, the maximum coupling occurs in the middle of the chain, sharing two couplings between $(\frac{N}{2}-\frac{1}{2})$ and $(\frac{N}{2}+\frac{1}{2})$ sites, and $(\frac{N}{2}+\frac{1}{2})$ and $(\frac{N}{2}+\frac{3}{2})$ sites, as shown in Fig.2.1a.
  Thus, $J_{max} = J_0\sqrt{(\frac{N}{2}-\frac{1}{2})\left[N-(\frac{N}{2}-\frac{1}{2})\right]}$ and therefore, $J_0 = J_{max}/\sqrt{\frac{N^2}{4}-\frac{1}{4}}$.

The symmetric distribution of the coupling interactions $J_{i,i+1}$ are given as: $J_{1,2} = J_{N-1,N}$, $J_{2,3} = J_{N-2,N-1}$, $\ldots$,$J_{i,i+1} = J_{N-i,N-i+1}$. This is illustrated in Fig.2.1 for both even and odd chains.

Engineering the couplings parameter of each spin chain of the USC systems will ensure that our 2D SN system that is built from these USC also exhibits PST, as will be shown in Chapter 3.

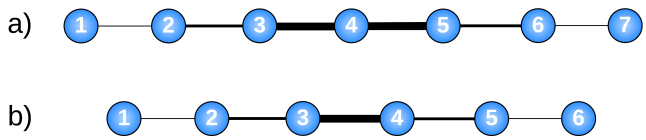

Figure 2.1: Demonstration of the coupling being symmetric around the centre of the chain, Eq. (2.12). Higher thickness means stronger coupling. a) represents odd chain of $N = 7$ where the maximum coupling is two couplings in the middle of the chain. b) represents even chain of $N = 6$ where the maximum coupling is in the middle of the chain.

2.2 Measurement tools

When a quantum system undertakes a specific operation, such as QST or entanglement distribution, then there are different figures of merit that can be used to assess or measure the performance of such an operation. Examples of measurement tools will be discussed below.

2.2.1 Fidelity

Fidelity is a tool that measures how close a desirable state is to the state of the system, and its value ranges from 0 to 1. If the fidelity $F(t) = 1$, this means that there is a complete overlap between the desirable state and the state of the system (i.e. the desirable state is the same as the state of the system up to a global phase). However, if the fidelity $F(t) = 0$, the state of the system and the desirable state are orthogonal to each other. The fidelity is significant in quantum communication and quantum information as it measures the efficiency of transferring a quantum state from one region of the SN to another chosen region. It is defined as

$$F(t) = |\langle\Psi_{des}| \exp(-i\mathcal{H}_{XY}t) |\Psi(0)\rangle|^2, \tag{2.13}$$

where $|\Psi_{des}\rangle$ is the desirable state. We set the reduced plank constant $\hbar = 1$ from now on.

Using this fidelity tool, we can check the efficiency of a quantum state to be transferred from one end of SN ($site_1$) to the other end ($site_N$) (e.g., from an initial state $|1000\rangle$ to a desirable state $|0001\rangle$). The corresponding fidelity is therefore $F(t) = |\langle 0001| \exp(i\mathcal{H}_{XY}t) |1000\rangle|^2$. PST is achieved when the fidelity is 1. However, when manufacturing errors are considered or any other environmental noise is considered, PST will no longer be observed. In addition, the effect of the

error depends on the type and scale of the error applied to the system.

As will be discussed in Chapter 3, in order to describe practical systems, errors must be considered. Therefore, we use ensembles of systems described by Hamiltonians containing independent random errors. For such ensembles, the average fidelity can be calculated as

$$\overline{F}(t) = Tr(\rho(t) \left|\Psi_{des}\right\rangle \left\langle\Psi_{des}\right|), \tag{2.14}$$

where $\rho(t) = \frac{1}{K}\sum_{i=1}^{K} \left|\Psi_i(t)\right\rangle \left\langle\Psi_i(t)\right|$ is the ensemble density matrix, K is the number of systems in the ensemble, and $\left|\Psi_i(t)\right\rangle$ represents a pure state at a time t for the i-th member of the ensemble, evolved with Hamiltonian $\mathcal{H}_{XY,i}$ that contains the i-th independent realisation of the noise/errors.

2.2.2 Entanglement of Formation (EOF)

Quantifying whether a state is entangled or not can be achieved using the Von Neumann entropy. This is a mathematical tool that allows us to determine whether a state ρ is pure or mixed, and it is given by

$$S(\rho) \equiv -tr(\rho \log \rho). \tag{2.15}$$

When $S(\rho) = 0$, the state is pure; otherwise it is a mixed state. Using this entropy, one can determine whether subsystems q_1 and q_2 are entangled or not by tracing out subsystem q_1 from the density matrix (i.e., $\rho_{q_2} = tr_{q1}\rho$). If $S(\rho_{q_2}) \neq 0$ and the combined state of q_1 and q_2 is pure, then there is entanglement [142].

When dealing with mixed states, using Von Neumann entropy for entanglement measure might not be appropriate, as it mixes both quantum and classical correlations [143]. Therefore, another suitable measure, known as the Entanglement of Formation (EOF) can be used in this case. EOF provides the degree of entanglement between a pair of qubits $q1$ and $q2$ regardless of whether they are in a pure or mixed state. The EOF for the case of two qubits is defined as [21]

$$EOF_{q1,q2} = -x \log_2 x - (1-x) \log_2 (1-x) \tag{2.16}$$

where $x = \frac{1+\sqrt{1-\tau}}{2}$, $\tau = [max(\lambda_1 - \lambda_2 - \lambda_3 - \lambda_4, 0)]^2$, $\lambda_i = \sqrt{\varepsilon_i}$, and ε_i are the eigenvalues of the matrix $\rho_{q1,q2}\overline{\rho_{q1,q2}}$. Here $\rho_{q1,q2}$ is the reduced density matrix of sites $q1$ and $q2$, and $\overline{\rho_{q1,q2}}$ is the spin-flipped $\rho_{q1,q2}$, so $\overline{\rho_{q1,q2}} = (\sigma_y^{q1} \otimes \sigma_y^{q2}) \rho^*_{q1,q2} (\sigma_y^{q1} \otimes$

σ_y^{q2}).

Note that fidelity (see Section 2.2.1) can also be used to quantify the entanglement between two qubits by measuring the closeness of the system state with a desirable entangled state. However, it is advisable to avoid using the fidelity as a figure of merit to quantify the degree of entanglement between two qubits. This is because high fidelities do not always guarantee a high degree of entanglement [144]. However, fidelity is a useful additional check of the closeness of a desired entangled state with the system state. In fact, being given knowledge of the EOF alone is not useful in some protocols, such as teleportation [109], where it is necessary to know the state of the system.

When we consider the practical situations where the system has random errors, the average of many realizations of EOF is calculated as

$$\overline{EOF} = \frac{1}{K}\sum_{i=1}^{K} EOF_i, \tag{2.17}$$

where EOF_i is calculated from the reduced density matrix of the two relevant sites for a single randomly generated example of disorder. Since the error we consider is random, the value of EOF_i for each independent realisation of the Hamiltonian can be different. Therefore, the average procedure we use (Eq. (2.17)) is important as it gives the average performance of the system against such random errors.

2.3 Perturbations

Indeed, quantum systems are susceptible to errors, for example fabrication errors or uncontrolled noise from the system itself [145]. Fabrication errors could be due to the device not being engineered exactly as required, while uncontrolled noise could be due to an unwanted magnetic field. In principle, both couplings and on-site energies may be fixed as part of the manufacturing process of the qubits (e.g. if these are quantum dots or devices of a specific size, placed a specific distance from their neighbour). In other systems, both the couplings and on-site energies may be tuneable with a local magnetic or electric field. Thus, both couplings or on-site energies could be susceptible to either form of disorder – it depends on the realisation.

This work considers the effect of static errors introduced in the fabrication of the quantum devices, so the parameters in the actual system Hamiltonian (the

on-site energies and the couplings) deviate from those specified in the ideal device design, which are set to produce PST, or satisfy the chosen application.

In a current experimental setting, likely only one device at a time would be considered (or even available), and this work reflects this experimental setting by considering, for each device realisation, the closed evolution of the system subject to a static Hamiltonian which deviates from the ideal one. This models the static fabrication error set-up.

Further, to understand, on average, how damaging fabrication errors can be, we consider a number of realisations, which we refer to as 'an ensemble of devices'. The Hamiltonian of each realisation contains errors generated randomly according to a set error distribution. Each member of the ensemble is evolved according to its particular (closed) Hamiltonian evolution, so the averaged projector over the ensemble will effectively evolve as a mixed state, due to the different (closed) Hamiltonian evolution of each ensemble member. Therefore, modelling the ensemble will demonstrate decay of quantities such as PST fidelity, or entanglement between two chosen sites. In these instances, the ensemble modelling results provide a guide to and understanding of device performance, because if the modelled ensemble results produce the desired application (such as PST) with high fidelity at a given error rate, then the expectation is that – on average – an individual device from that ensemble will operate with high fidelity. Note that even though we consider a closed quantum system, the average procedure we employ leads to a decay in time with the quantity of interest (e.g., fidelity), mimicking the behaviour of an open quantum system (see Section 6.4 for a detailed discussion).

We also consider errors that are not due to fabrication errors, but arise in the protocols used to perform a desired operation. These are the time delay errors or phase angle errors. A detailed discussion on this is given below.

2.3.1 Diagonal disorder

Diagonal disorder is the error on the on-site energy and contributes to the diagonal elements of the Hamiltonian matrix. In the ideal case, the on-site energies ϵ_i are set to zero for simplicity. Now, we will consider noise variation on the on-site energy. Therefore, the term ϵ_i given in Eq. 2.2 will now be given as $\epsilon_i = Ed_iJ_{max}$, where E is the error strength given in units of J_{max}, and d_i represents a random number that depends on a particular distribution and is chosen independently for each site i. The maximum coupling J_{max}, as defined in Chapter 2, sets the perturbation

units and is set equal to unity, $J_{max} = 1$.

For the random number d_i, two physically reasonable distributions (Gaussian and uniform distribution), each with zero mean value are considered. The normalised uniform (or flat) distribution of random numbers is chosen to be of unit weight within the window [-0.5 , 0.5]. For zero mean, the normalised Gaussian distribution with a standard deviation of w takes the form $f(d) = \frac{1}{w\sqrt{2\pi}} \exp\left(-d^2/2w^2\right)$. As the standard deviation of our chosen flat distribution is $w = \frac{1}{2\sqrt{3}}$, we use this value of w in the Gaussian distribution to model Gaussian errors equivalent to the flat case. As will be seen, our disorder modelling is essentially independent of the *form* of the random distribution used (flat or Gaussian), until the regime of very large disorder is reached. For error regimes of interest for useful devices, no dependence on the form of the error distribution used will be significant.

2.3.2 Off-diagonal disorder

The disorder in the coupling interaction between nearby sites is known as off-diagonal disorder (also called coupling disorder). As will be seen, our SN systems are more sensitive to off-diagonal disorder, than diagonal disorder. This is attributed to the fact that the energy levels, under off-diagonal disorder, are distributed on a larger energy scale when compared to the energy levels under diagonal disorder. A detailed discussion of this will be given in Chapter 3.

The coupling disorder is represented by adding it to the off-diagonal elements of the Hamiltonian matrix. Thus, the coupling interaction in Eq. (2.2), will now be given by

$$J_{i,j}^{perturbed} = J_{i,j} + J_{i,j}^{'} \ , \tag{2.18}$$

where $J_{i,j}^{'} = E d_{i,j} J_{max}$. The symbols E and J_{max} have the same definitions as above. $d_{i,j}$ is a random number that depends on a particular distribution and is chosen independently for each coupling $\{i, j\}$.

Another way to represent the off-diagonal disorder is given in [146] as $J_{i,j}^{perturbed} = J_{i,j}(1 + \epsilon)$. However, this expression means that the error is re-scaled for each individual coupling parameter. This may be true in systems where the error is a fraction of the energy/coupling at that site, but we feel that it is a more widely applicable approach to consider the error as a fraction of J_{max}. Therefore, we will adopt the expression given in Eq. (2.18).

2.3.3 Time delays

Some of the quantum information processing protocols involve sudden application of a phase or injection of an excitation at a specific time. The time delay error is considered when such operations are not performed at exactly the right time.

One way of modelling time delay error is in protocols that involve the application of a phase $e^{i\xi}$ at a specific site at a specific time $t = t_p$. The time t_p is the phase application time of the relevant chain of the SN. Thus, in a case where the phase is not applied at t_p, but at a slightly different time specified by a delay strength D. The time delay on the application of the phase is given by

$$t_{d,\xi} = t_p + Dt_p, \tag{2.19}$$

where D is the scale of the delay ($-0.2 \leq D \leq 0.2$). We set the range of the timing error to have a maximum error of 0.2 because the timing error with larger values of D results in the calculated quantity (fidelity or EOF) being very low. Furthermore, any experimental realisation would be expected to have a timing accuracy of $D \ll 1$, or else use of the system for practical injection and extraction of states to undergo PST would not be possible. Taking this into account, $D = 0.2$ is a suitable upper bound for timing error. t_p is the phase application time of the relevant chain of the SN. Note, our results are independent on whether the time error is $D > 0$ (delayed operation) or $D < 0$ (earlier operation).

The second approach to modelling time delay errors is found in protocols where we start with simultaneous injection of two states at two sites at $t = 0$. Specifically, the protocol for the generation of a cluster state, as shown in Chapter 5, requires injecting two plus states (a plus state is given by $|+\rangle = \frac{1}{\sqrt{2}}(|0\rangle + |1\rangle)$), simultaneously at two different sites at $t = 0$. In this case, we consider a scenario in which the injection of the initial $|+\rangle$ states is performed in an asynchronous way. In other words, there is a time delay in the injection of one of the two $|+\rangle$ states such that they are not injected simultaneously. The time delay in the injection of the $|+\rangle$ state is represented as

$$t_{d,|+\rangle} = t_0 + Dt_p, \tag{2.20}$$

where $t_0 = 0$ is the $|+\rangle$ states injection time, D and t_p have the same definitions as above.

Another possible error we consider is the measurement-time error. This is the

case where the fidelity (or EOF) of a desired operation is measured at a different time from the ideal measurement time. The scale of the error here is again the parameter D with the same constraint ($-0.2 \leq D \leq 0.2$).

2.3.4 Phase disorder

Another possible error that can be considered is an error that is due to the applied phase not being the exact required phase. For example, in a protocol that involves application of a phase of $e^{i\xi}$, the error on the phase means that the angle of this phase is now disordered

$$\xi_D = e^{i(\xi + D\xi)} \tag{2.21}$$

where D has the same constraint as above.

Chapter 3

Two-chain spin networks

In this chapter, we propose a SN system designed via the transformation of two USC - hence its name, two-chain SN - and show how it can be used for various QIP protocols and investigate its robustness against different types of disorder. We then demonstrate another structure of the SN system designed via transformation of two USC, each of different length - hence its name, SN of unequal chains - and show how to use this for various QIP protocols and investigate its robustness against various types of disorder. Finally, we examine the scalability of such SN systems by designing larger SN systems and show how they can be used for longer-range QIP protocols, as well as investigate their robustness against disorder.

Part of the work in this chapter has been published in [1], and another part of this chapter results has been published in [2].

Spin networks can be defined as systems made up of nodes and edges. The physical representation of nodes are spins, where the edge between a pair of spins represents the coupling interaction. There has been considerable advancement in the field of quantum spin networks for QIP protocols [1,2,73,82]. Usually such SN systems are known as graphs, a simple example of which is the linear graph (spin chain) system.

Non-linear SN systems can be transformed into a spin chain system using partitioned graph theory [82, 147]. This is the process of simplifying the complexity of a graph by reducing its dimensionality so that it becomes a simple linear SN system (spin chain). On the other hand, the opposite operation, which expands a spin chain system such that it involves more topology and becomes a non-linear SN system, is also possible [1]. These methods of simplifying or expanding SN systems can also be thought of as unitary transformations of the Hamiltonian of such a system [82]. Under such a transformation, the overall spectrum of the system (eigenvalues) do not change, while the eigenstates, on the other hand, do.

In this chapter, we propose a Hadamard-based transformation method that can be used to form a complex SN system out of two uncoupled spin chain systems (two USC). These two USC are coupled together via the Hadamard-based transformation method, which results in a complex non-linear SN system. A detailed discussion will be given below.

3.1 Spin chains and mirror symmetry

Before we introduce our SN system, let us first discuss the building blocks of the SN, the spin chain system. Consider an XY-type spin chain of 3 sites as shown in Fig.3.1. The nearest-neighbour coupling interactions are set to satisfy the formula given in Eq. (2.12) which is required for PST. Note that since the number of sites in this spin chain is three, the couplings are homogeneous, $J_{i,i+1} = J$, but for a longer spin chain, the couplings will not be uniform.

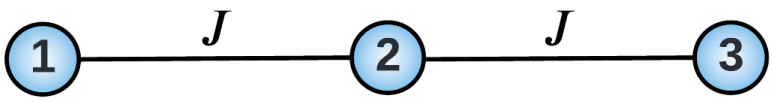

Figure 3.1: Diagram of a spin chain of 3 sites.

Let us assume that the spin chain is initialised so that all sites have spin down state, $|000\rangle$. This is an eigenstate of the Hamiltonian H_{XY} of the system, and will not evolve with time, and the system will just acquire a global phase evolution (i.e., $\exp\{-iH_{XY}t\}\,|000\rangle = e^{\zeta}\,|000\rangle$).

If, in the error-free case, a single excitation is injected at the first site, $|100\rangle$, and the system is left to evolve, then at a time known as the *mirroring time* t_m, the excitation will be completely transferred to the other end of the chain, $|001\rangle$, demonstrating PST. The name mirroring time stems from the fact that the excitation has evolved from the initial state, $|100\rangle$, to its reflected state, $|001\rangle$, and is given as $t_m = \pi/(2J_0)$. Further evolution of the system shows that the excitation evolves back to its initial state, $|100\rangle$, at $2t_m$, and therefore will continue to evolve between the ends of the chain, as shown in Fig.3.2.

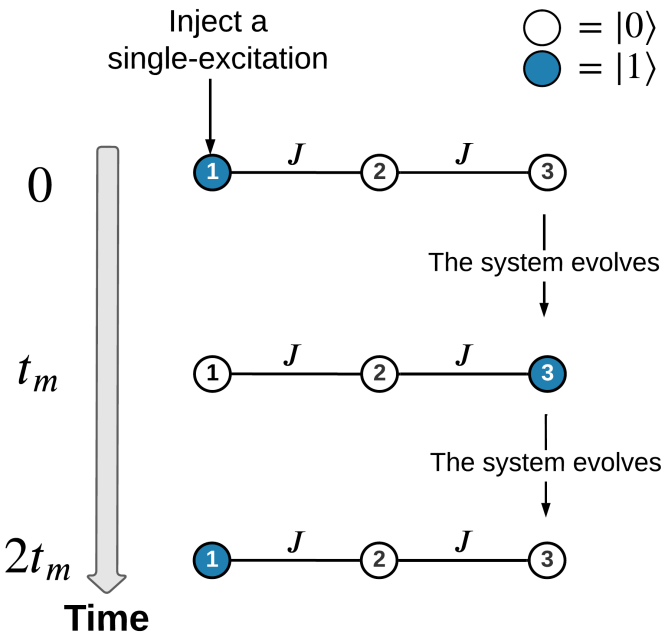

Figure 3.2: Demonstration of the single-excitation evolution in the spin chain.

3.2 Design and realization of our spin network

We can be seen above, the spin chain system exhibits PST between the ends of the chain. Let us call such a chain a PST chain. We are interested in building a SN out of two USC, each of which is a PST chain. Therefore, the building blocks of our SN are the two USC shown in Fig.3.3.

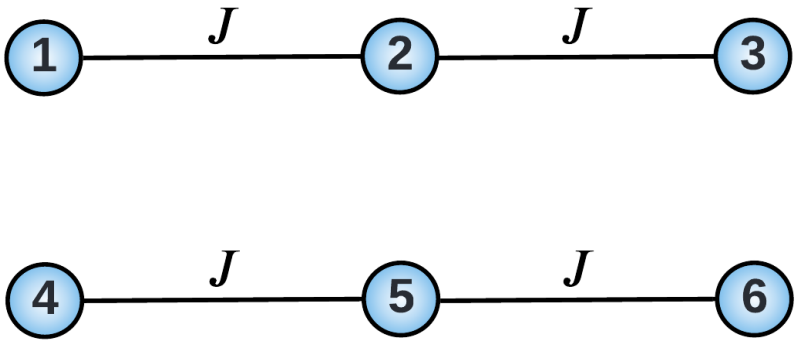

Figure 3.3: Two uncoupled trimers.

The Hamiltonian for these two USC, for the single-excitation site basis is given

as

$$H_{XY} = \begin{pmatrix} 0 & J & 0 & 0 & 0 & 0 \\ J & 0 & J & 0 & 0 & 0 \\ 0 & J & 0 & 0 & 0 & 0 \\ 0 & 0 & 0 & 0 & J & 0 \\ 0 & 0 & 0 & J & 0 & J \\ 0 & 0 & 0 & 0 & J & 0 \end{pmatrix} \tag{3.1}$$

The two USC shown in Fig.3.3 can be coupled together to form a non-linear SN system. In order to do so, we propose a unitary transformation that can be applied to the USC Hamiltonian, H_{XY}, which results in a new Hamiltonian that describes a non-linear SN. The unitary transformation is a Hadamard-like unitary that superposes sites 3 and 4, and is given as

$$U = \begin{pmatrix} 1 & 0 & 0 & 0 & 0 & 0 \\ 0 & 1 & 0 & 0 & 0 & 0 \\ 0 & 0 & \frac{1}{\sqrt{2}} & \frac{1}{\sqrt{2}} & 0 & 0 \\ 0 & 0 & \frac{1}{\sqrt{2}} & -\frac{1}{\sqrt{2}} & 0 & 0 \\ 0 & 0 & 0 & 0 & 1 & 0 \\ 0 & 0 & 0 & 0 & 0 & 1 \end{pmatrix} \tag{3.2}$$

Here, $U^\dagger = U$.

A crucial point to make is that this unitary transformation is not implemented as a physical operation on the physical realisation of the USC, but rather is merely a mathematical tool used to design a non-linear SN out of the USC. Applying this unitary on the USC Hamiltonian, H_{XY}, will transform the Hamiltonian, resulting in a new Hamiltonian that can be given as

$$\mathcal{H}_{XY} = UH_{XY}U^\dagger = \begin{pmatrix} 0 & J & 0 & 0 & 0 & 0 \\ J & 0 & \frac{J}{\sqrt{2}} & \frac{J}{\sqrt{2}} & 0 & 0 \\ 0 & \frac{J}{\sqrt{2}} & 0 & 0 & \frac{J}{\sqrt{2}} & 0 \\ 0 & \frac{J}{\sqrt{2}} & 0 & 0 & -\frac{J}{\sqrt{2}} & 0 \\ 0 & 0 & \frac{J}{\sqrt{2}} & -\frac{J}{\sqrt{2}} & 0 & J \\ 0 & 0 & 0 & 0 & J & 0 \end{pmatrix} \tag{3.3}$$

It is important to note that this new Hamiltonian $\mathcal{H}_{XY}$ has the same eigenvalues

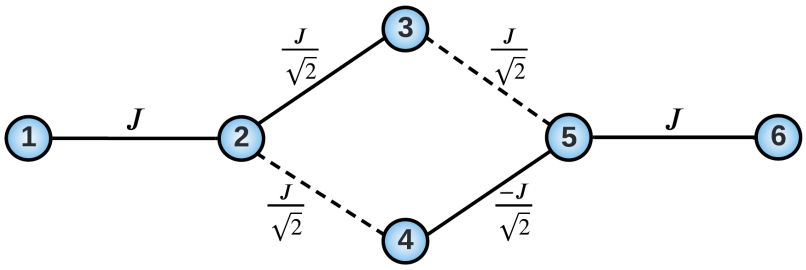

Figure 3.4: Scheme of our two-chain SN, each of three sites. The dashed lines are the new couplings that connect the two USC as a result of the unitary transformation of the USC Hamiltonian. Note that on top of these two additional couplings, the energy associated with some of the already existent couplings has changed[1].

of the USC Hamiltonian, H_{XY}, as the transformation does not change the overall spectrum of the system. This ensures that the PST dynamics observed in the USC system can also be observed in the non-linear SN system. The eigenstates, on the other hand, change under the transformation, which is attributed to the new topology the system acquires after the transformation. A diagram representing this new Hamiltonian, $\mathcal{H}_{XY}$, is given in Fig.3.4. The dashed lines in the SN in Fig.3.4 represent the new couplings that connect the two USC as a result of transforming them. Furthermore, the transformation results in one of the couplings being negative, the coupling between sites 4 and 5.

As shown in Fig.3.4, the Hadamard-like transformation of two USC superposes two sites, each of which belongs to a chain. The first chain is the chain that involves sites 1, 2, and 3. The second chain is the chain that involves sites 4, 5, and 6, as per Fig.3.3. The transformation superposes sites 3 and 4, and so these two sites are now coupled to both chains as a result of the transformation, as shown in Fig.3.4. Since the SN is constructed from two USC, each of three sites, let us name it: two 3-site-chain SN system.

The Hadamard-like unitary shown in Eq.(3.2) is not unique, as a rotation between the two states would work equally (see appendix A for a detailed discussion). Using the rotation unitary instead of the Hadamard-like unitary gives a slightly different transformed Hamiltonian $\mathcal{H}_{XY}$ (with the negative coupling in a different place). Alternatively, a slightly changed initial Hamiltonian H_{XY} can be transformed by the rotation matrix to give the same final $\mathcal{H}_{XY}$, Eq.3.3, as the Hadamard-transformed example. We stress that the transformation of the USC

[1]Note that the numbering of the sites in the second chain of the SN is different to the one shown in Figure 2 in [1].

is a mathematical design step and that the SN shown in Fig.3.4 is the desired structure that should be manufactured experimentally, in order to realise various desirable QIP operations that will be discussed below.

3.2.1 Dynamic

Before discussing the use of this SN for QIP protocols, let us first investigate the dynamics. In order to investigate the dynamics of our two 3-site-chain SN system, we initialise the system such that all sites have a spin down state, $|00\ldots\rangle$. We then start by injecting a single-excitation at site 1 at $t = 0$

$$|\Psi(0)\rangle = |r_1\rangle\,, \tag{3.4}$$

where $|r_1\rangle = |100000\rangle$.

This excitation will then evolve through the system via the system's natural dynamics, and at the mirroring time, t_m, the state will comprise a superposition of the excitation being at sites 3 and 4

$$|\Psi(t_m)\rangle = -\frac{1}{\sqrt{2}}(|r_3\rangle + |r_4\rangle). \tag{3.5}$$

The excitation will then evolve back to site 1 at $2t_m$, regaining its initial state, $|\Psi(2t_m)\rangle = |\Psi(0)\rangle$. As long as the system is assumed to be perfect (the error-free case), this evolutionary cycle will keep repeating itself. A demonstration of the dynamics of the excitation evolution is illustrated in Fig.3.5. For simplicity, we do not write the couplings parameters in the SN shown in Fig.3.5. Moreover, the negative coupling between sites 4 and 5 is now denoted by a horizontal bar, and the couplings that connect the two USC are denoted by the dashed lines. This notation for couplings will be used throughout the thesis.

Note that since we injected the single-excitation at site 1, the excitation evolved only through the first chain of the SN, specifically through sites 1, 2, 3, and 4. Of course, site 4 belongs to the second chain of the SN, but it also shares a coupling with the first chain. The reason the excitation did not evolve through sites 5 and 6 is because of the unitary construction of the SN that superposes only two sites of the two USC, sites 3 and 4.

The above discussion is concerned solely with the single excitation being injected at site 1. Similarly, if instead the single excitation is injected at site 6 at $t = 0$, then the evolution of the excitation would end up in a superposed state

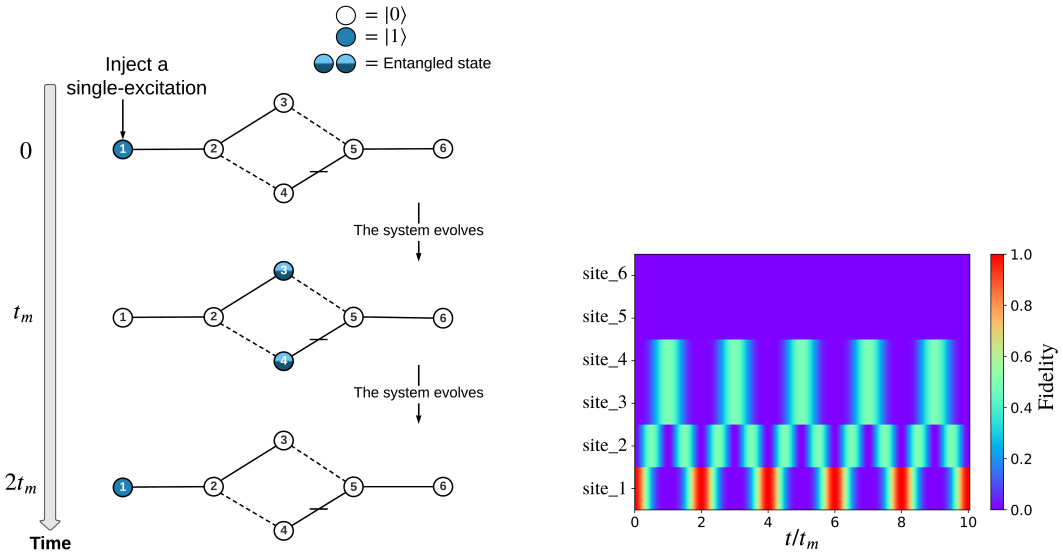

(a) Excitation dynamics **(b)** Fidelity of each site

Figure 3.5: A demonstration of the dynamics of our SN. a) When a single-excitation is injected at site 1 at $t = 0$, the excitation spreads as a superposition between sites 1, 2, 3, and 4 until time t_m where it localises to being in a superposition state between sites 3 and 4. It then starts evolving backward toward site 1, and at $2t_m$ it collapses to being completely at site 1. The excitation will keep repeating this evolutionary cycle. b) The fidelity of each site as a function of the rescaled time, t/t_m.

between sites 3 and 4 at t_m, but with a relative phase of -1

$$|\Psi(t_m)\rangle = -\frac{1}{\sqrt{2}}(|r_3\rangle - |r_4\rangle); \tag{3.6}$$

it would then evolve back to site 6 at $2t_m$. The relative phase arises due to the negative coupling between sites 4 and 5. Here, since we started with a single excitation injected at site 6, the excitation will keep evolving in the second chain of the SN (through sites 3, 4, 5, and 6).

The dynamics of our SN are engineered via the Hadamard-based unitary applied to the USC. Therefore, the dynamics of such SN systems depend on the unitary construction used to form the SN. For example, engineering alternative behaviours/state superpositions can be achieved using a different unitary, one that is based on different gates.

3.3 Spin networks of equal chains

The SN discussed above is made up of two USC, each of three sites. In other words, it is a SN of equal chains. We could, however, design a SN of unequal chains by

coupling together two USC, each of a different number of sites. This will constitute the discussion in Section 3.4; here, though, we will focus on the SN discussed above, the two 3-site-chain SN Fig.3.4. As will be seen in the following, it can be used for routing protocols, generating entanglement, and sensing an unknown phase applied to a site. Furthermore, in order for our results to be realistic, we will consider the effects of various types of disorder on the system.

3.3.1 Routing

Routing can be defined as the transfer of quantum information between distant registers in a spin network, and is an important function in quantum technology. Various methods have been proposed to achieve routing, such as by modulating the on-site energies [148], or controlling the couplings with time-dependent techniques [149, 150]. Our scheme will instead keep the couplings and on-site energies unchanged and will utilise the natural dynamics of the system with a minor control on part of the SN, as will be discussed below.

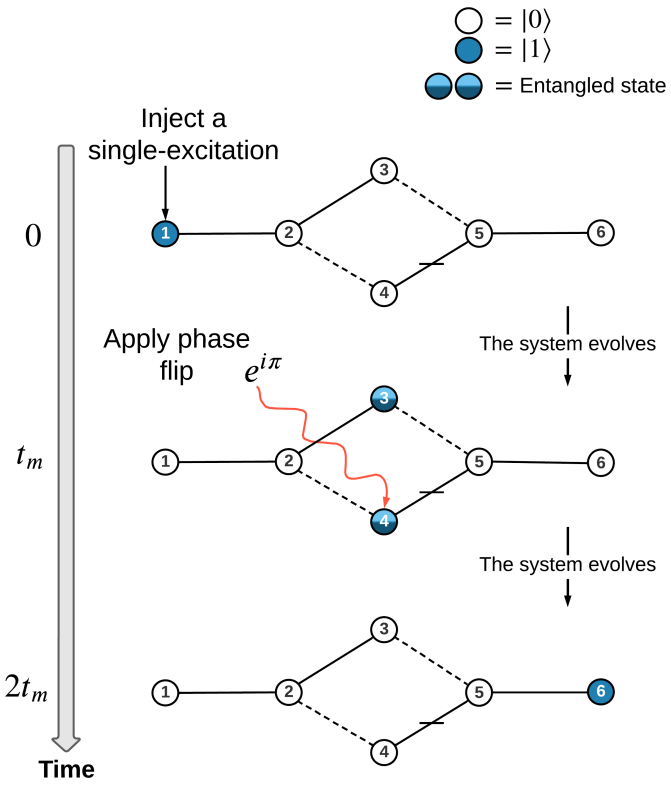

Figure 3.6: Demonstration of the phase-based routing protocol that is achieved via the application of a phase flip at site 4 at t_m.

The goal of routing in our SN is to send a single excitation injected at site 1 all

the way to the other end of the SN, at site 6 (PST from site 1 to site 6). However, we have seen above that when the excitation is injected at site 1 at $t = 0$, it evolves to a superposition state between sites 3 and 4 at t_m, and evolves back to site 1 at $2t_m$. Therefore, we need to perform a sudden operation (on the timescale of the dynamics) at t_m, the time at which the excitation is in a superposed state between sites 3 and 4, to force the excitation to continue evolving toward site 6. This can be achieved via the application of phase flip, as described below.

Phase-based routing protocol

When a single excitation is injected at site 1 at $t = 0$ and evolved for a duration of t_m, it can be distributed as an equal superposition state between sites 3 and 4, as shown in Eq.(3.5). In order to force the excitation to continue evolving forward, a sudden application of a local phase flip of ($e^{i\pi} = -1$) needs to be applied at either sites 3 or 4. This operation needs to be performed very rapidly, on the timescale of the dynamics, and so can be viewed as sudden in the sense of the sudden approximation in quantum mechanics. We choose to apply the phase flip at site 4. Therefore, the state of the system at t_m with the sudden phase flip applied at site 4 is given by

$$|\Psi(t_m)\rangle_\pi = -\frac{1}{\sqrt{2}}(|r_3\rangle + e^{i\pi}|r_4\rangle). \tag{3.7}$$

Experimentally, one can achieve such a local phase application using, for example, a focused laser [126] or microwave pulses [151] applied at site 4. More discussion on the experimental side of the phase application step will be given in Section 3.6.

We now allow the system to evolve, and at time $2t_m$ the excitation will be transferred completely to site 6

$$|\Psi(2t_m)\rangle = |r_6\rangle\,. \tag{3.8}$$

Similarly, if we start by injecting a single-excitation state at site 6 at $t = 0$, we can route it to site 1 following the same protocol.

The effect of applying the phase flip can be thought of as flipping the role of constructive and destructive interference, such that the excitation evolves toward site 6 instead of evolving back to site 1. The excitation will then continue to evolve in the second chain of the SN, between the state Eq. (3.8) and the state Eq. (3.7) unless another phase flip is applied at an odd mirroring time (i.e., $3t_m$,

$5t_m$, etc), which will force the excitation to evolve in the first chain of the SN. The routing protocol in our SN is demonstrated in Fig.3.6. Note that routing any superposition state of zero excitation and one excitation, $|\Psi\rangle = \alpha|0\rangle + \beta|1\rangle$, works in the same way as we can prepare site 1 in this random superposition and let it to evolve to site 6. However, since we are restricting ourselves to the single-excitation subspace, we only consider the evolution of the one excitation state.

An instructive way in which to see how the excitation evolves through the system with time is to plot a colourmap for the fidelity of each site as a function of time. The fidelity, as defined in Chapter 2, measures the closeness of an evolved initial state with a desirable state at a time t. When calculating the fidelity, it is important to take into account the fact that the evolved initial state changes after time t_m due to the application of the relative phase factor to the system. Consequently, two fidelities need to be calculated, i.e., the fidelity before and after the phase factor is applied to the system. Therefore, for our routing protocol above, the case where a single excitation is injected at site 1 at $t = 0$ and a phase flip $e^{i\pi}$ is applied at site 4 at t_m, the fidelity of a desirable state of a single excitation being at site i ($|\Psi_{des}\rangle = |r_i\rangle = |00\ldots1_i00\ldots\rangle$ can be calculated as follows

1. The fidelity for $0 \leq t < t_m$ is calculated as:
   $F(t) = |\langle\Psi_{des}|\exp(-i\mathcal{H}_{XY}t)|\Psi(0)\rangle|^2$, with the initial state being $|\Psi(0)\rangle = |r_1\rangle$.

2. The fidelity for $t \geq t_m$ is calculated as:
   $F(t) = |\langle\Psi_{des}|\exp(-i\mathcal{H}_{XY}t)|\Psi(t_m)\rangle_\pi|^2$, with the new initial state being $|\Psi(t_m)\rangle_\pi = -\frac{1}{\sqrt{2}}(|r_3\rangle + e^{i\pi}|r_4\rangle)$.

A plot of the fidelity against each site as a function of time is shown in Fig.3.7.

Transformation-based routing protocol

The routing protocol discussed above involves a sudden application of a local phase flip at site 4 at time t_m. An equivalent mathematical representation of the phase flip operation is a transformation of the Hamiltonian, a transformation that is achieved via an identity-like matrix $\mathcal{U}$ with phase flip on one of the diagonal elements, specifically $\langle r_4|\mathcal{U}|r_4\rangle = e^{i\pi}$. The unitary transformation is given by

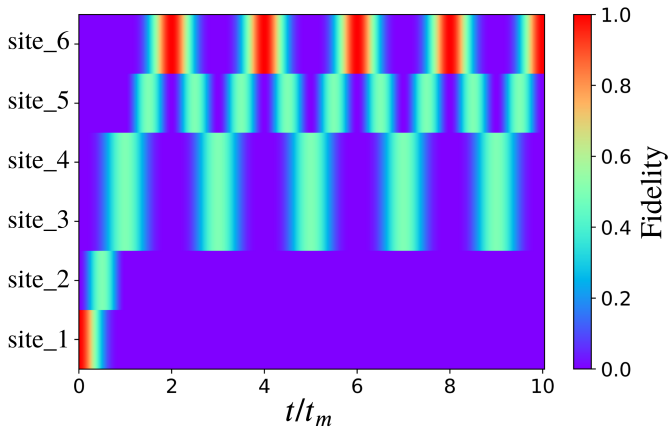

Figure 3.7: The fidelity of an excitation at each of the six sites as a function of the rescaled time, t/t_m. PST can be achieved from site 1 to site 6 when a phase flip is applied at site 4 at t_m.

$$\mathcal{U} = \begin{pmatrix} 1 & 0 & 0 & 0 & 0 & 0 \\ 0 & 1 & 0 & 0 & 0 & 0 \\ 0 & 0 & 1 & 0 & 0 & 0 \\ 0 & 0 & 0 & e^{i\pi} & 0 & 0 \\ 0 & 0 & 0 & 0 & 1 & 0 \\ 0 & 0 & 0 & 0 & 0 & 1 \end{pmatrix}. \tag{3.9}$$

Therefore, when we start with a single-excitation at site 1 at $t = 0$ and let the system evolve until time t_m, where the state of the system is given as a superposed state between sites 3 and 4 (Eq. (3.5)), the routing protocol can be achieved via a sudden transformation of the Hamiltonian: $\mathcal{U}\mathcal{H}_{XY}\mathcal{U}^\dagger$. The excitation at $2t_m$ would then be transferred completely to site 6.

Although each routing protocol (phase-based and transformation-based) has its own unique mathematical formulation, they are nevertheless physically equivalent. Herein, whenever we discuss routing, we will use the phase-based protocol.

3.3.2 Bipartite entanglement generation

Generating quantum entanglement is necessary for various QIP, as previously discussed in Chapter 1. Here, we are interested in generating a bipartite maximally entangled state between the ends of our SN system, between sites 1 and 6 in Fig.3.4. Depending on the initial injected state, a specific protocol is implemented to achieve perfect generation of a bipartite maximally entangled state.

Phase-based bipartite entanglement protocol

When a single excitation is injected at site 1 at $t = 0$ and the system is evolved for a period t_m, the state will be in a superposition between sites 3 and 4, as given in Eq. (3.5). Note that this is, in fact, a bipartite maximally entangled state between sites 3 and 4 generated by natural evolution, and will evolve back to site 1 at $2t_m$ if no operation is performed at t_m. However, we are interested in generating a bipartite maximally entangled state between the ends of the SN. Therefore, a sudden application of a local phase factor to the system at time t_m is needed to force the excitation to evolve through both chains of the SN such that it ends up in a superposition between the ends of the SN.

The phase factor needed in this instance is the phase $e^{i\pi/2}$. When a phase factor of $e^{i\pi/2}$ is injected at site 4 at time t_m and the system is evolved for another duration t_m then the state of the system at $2t_m$ will be in a bipartite maximally entangled state between sites 1 and 6, given as

$$|\Psi(2t_m)\rangle = \frac{1+e^{i\pi/2}}{2}|r_1\rangle + \frac{1-e^{i\pi/2}}{2}|r_6\rangle\,. \tag{3.10}$$

This phase-based protocol for generating the bipartite maximally entangled state is illustrated in Fig.3.8.

Natural generation of bipartite entanglement protocol

Another approach to generate the bipartite maximally entangled state between the ends of the SN can be achieved via a specific initial injection and utilisation of the natural evolution [99]. Instead of initialising the system with a single excitation at site 1, we can start the injection at the central vertex of the diamond, either at site 3 or at site 4 in Fig.3.4.

If we start by injecting a single excitation at site 3 at $t = 0$ and evolve the state of the system for a duration of t_m, then the state of the system at t_m will be given as a bipartite maximally entangled state between sites 1 and 6

$$|\Psi(t_m)\rangle = -\frac{1}{\sqrt{2}}(|r_1\rangle + |r_6\rangle). \tag{3.11}$$

This entanglement is generated by the natural evolution of the system as it does not require an application of a phase in order to occur. It also allows for a faster generation of the entangled state as it is generated at t_m, as compared to

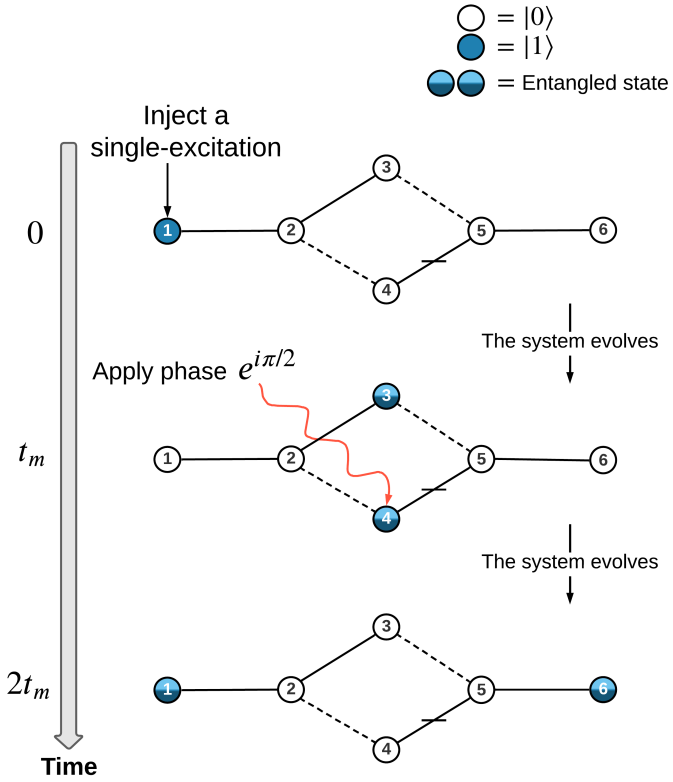

Figure 3.8: Demonstration of the phase-based bipartite entanglement protocol achieved by the application of a phase factor $e^{i\pi/2}$ at site 4 at t_m.

the previous protocol where the entangled state is generated at $2t_m$. Moreover, as will be seen in Section 3.3.4, the entangled state in this protocol is more robust to disorder than the entangled state generated in the previous protocol.

The entangled state generated here is achieved with a single excitation injected at site 3 at $t = 0$, but it can also be generated by injecting the single excitation at site 4 instead. This can be achieved using the same steps: inject a single-excitation at site 4 at $t = 0$ and evolve for a duration t_m. The state at t_m will therefore be a bipartite maximally entangled state between sites 1 and 6, but with a relative phase difference due to the negative coupling between sites 4 and 5

$$|\Psi(t_m)\rangle = -\frac{1}{\sqrt{2}}(|r_1\rangle - |r_6\rangle). \tag{3.12}$$

3.3.3 Phase sensing

The field of quantum sensors is recognised to be one of the most important areas within the whole landscape of quantum technologies [12, 83, 152–157]. High-

precision measurements and ultimate (Heisenberg-limited) sensitivity can be pursued through quantum sensing protocols that use quantum resources. In such applications, in some chosen interferometric system, a phase is imparted to the relevant quantum resource (qubit) by the field or effect being sensed. Thus, measuring this phase through interference allows for the sensing of the field or effect that caused it.

In both the protocols discussed above (routing and phase-based bipartite entanglement), a chosen phase factor is suddenly applied at site 4 at t_m to perform the desired operation. Here, we consider the case where the sudden phase factor applied at site 4 at t_m is unknown, $e^{i\theta}$, where θ is an unknown parameter. This could be the case where the phase is applied to the system by an external field or effect that we do not have access to. Retrieving this unknown phase enables us to sense the field or effect that produced it. The task is then to retrieve this unknown θ (modulo 2π). Investigation of the dynamics of the system with the application of an unknown phase enables us to tailor a protocol that can be used to retrieve the unknown angle, as will be described below.

When the system is first initialised with a single excitation injected at site 1 at $t = 0$ and then allowed to evolve for a duration of t_m where a sudden unknown phase is applied at site 4, the state of the system will be given by

$$|\Psi(t_m)\rangle_\theta = -\frac{1}{\sqrt{2}}(|r_3\rangle + e^{i\theta}|r_4\rangle). \tag{3.13}$$

The excitation at a later time (e.g., $t = 2t_m$) will either evolve back to site 1 or to site 6 or to a superposition state between sites 1 and 6, depending on the unknown phase $e^{i\theta}$. We have derived analytically the state at $2t_m$ when an arbitrary phase $e^{i\theta}$ is applied at site 4 at t_m (see appendix B), and which is given by

$$|\Psi(2t_m)\rangle = \frac{1+e^{i\theta}}{2}|r_1\rangle + \frac{1-e^{i\theta}}{2}|r_6\rangle\,. \tag{3.14}$$

From a practical perspective, let us assume that the only information we have about the unknown phase θ is the value of the measurement of the fidelity at $2t_m$, in particular, the measured fidelity against either a desirable state of an excitation being at site 1 ($|\Psi_{des}\rangle = |r_1\rangle$) or against a desirable state of an excitation being at site 6 ($|\Psi_{des}\rangle = |r_6\rangle$), as the excitation at $2t_m$ (Eq. (3.14)) cannot be found at any other sites. We choose to measure the fidelity against $|r_1\rangle$. It turns out that

the expression for the fidelity against $|r_1\rangle$ at $2t_m$ can be written as

$$F_1 = |\langle r_1|\Psi(2t_m)\rangle|^2 = \frac{1}{2}(1+\cos\theta). \tag{3.15}$$

Further details are given in appendix B. Note that there is no difference in whether we study the case where the unknown phase is applied at site 3 or at site 4, except that the evolved states will have different relative phases that still enable extraction of the unknown applied phase..

Since we now have a formula for the fidelity measurement against $|r_1\rangle$ at $2t_m$ as a function of the unknown θ, we can simply retrieve the unknown angle as $\theta = \cos^{-1}(2F_1 - 1)$. It is crucial to note that this would enable us to obtain any unknown angle in the range 0 to π. However, the range of the unknown angle could be from 0 to 2π; therefore, another separate fidelity, written as a function of $\sin\theta$, along with F_1, is needed to be able to obtain any unknown angle in the range 0 to 2π.

We can see from the above that the expression of the fidelity at $2t_m$ can be rewritten as a function of $\cos\theta$ when an unknown phase θ is applied to site 4 at t_m. In order to have a separate fidelity written as a function of $\sin\theta$, an additional known phase shift needs to be applied at site 4 at the same time as the unknown phase, as described below.

We start with a single excitation injected at site 1 at $t = 0$ and let the system evolve for a time t_m, where a sudden unknown phase is applied to site 4 (as shown in Eq. (3.13)). At this time, we intervene by applying a sudden phase shift of $-\frac{\pi}{2}$, also at site 4. Now, with sudden application of the unknown phase, θ, as well as the known phase shift of $-\frac{\pi}{2}$ at site 4 at t_m, the total sudden phase factor is given as $\exp i(\theta - \frac{\pi}{2})$. As a result, the expression for the fidelity against $|r_1\rangle$ at $2t_m$ can be written as

$$F_2 = \frac{1}{2}(1+\cos(\theta - \frac{\pi}{2})), \tag{3.16}$$

and since $\cos(\theta - \frac{\pi}{2}) = \sin(\theta)$, then

$$F_2 = \frac{1}{2}(1+\sin\theta). \tag{3.17}$$

The fidelity index here is labelled with a subscript '2' in order to distinguish between two fidelities. F_1 represents the measured fidelity against $|r_1\rangle$ at $2t_m$ when an unknown phase is applied to site 6 at t_m, while F_2 represents the measured fidelity against $|r_1\rangle$ at $2t_m$ when the additional phase shift of $-\frac{\pi}{2}$ is added to the

unknown phase. The steps required to generate these two separate fidelities, F_1 and F_2, are shown in Fig.3.9a.

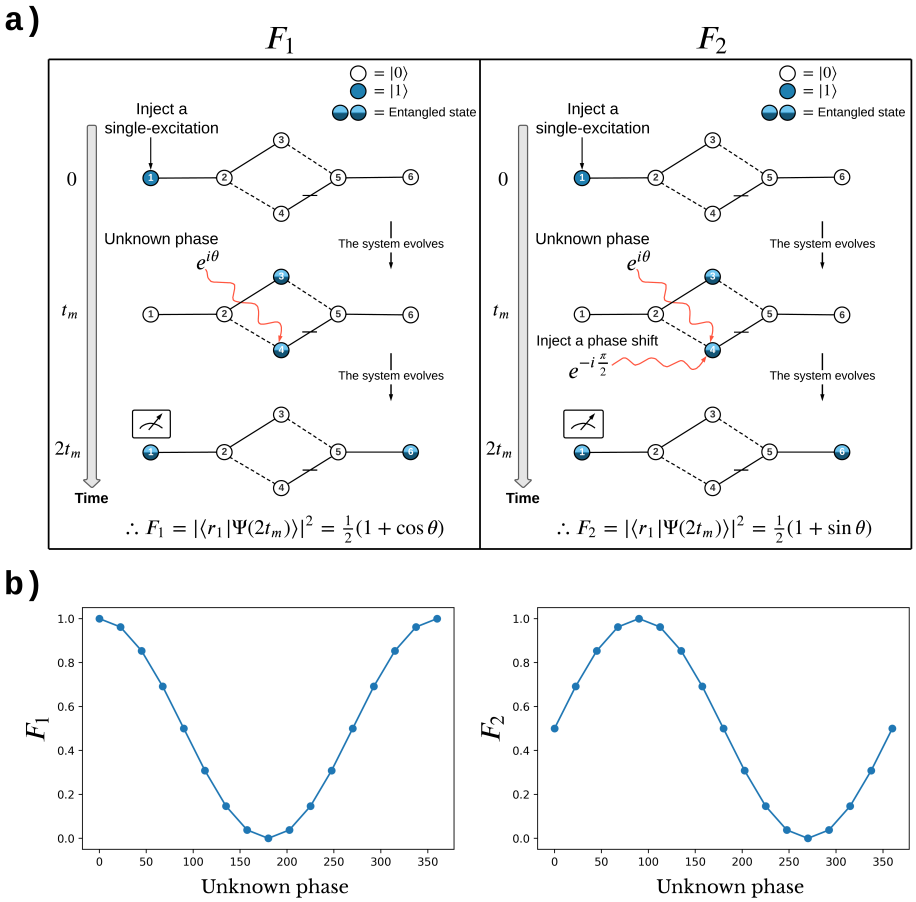

Figure 3.9: a) Demonstration of the two separate experiments used to obtain F_1 (left) and F_2 (right). In both experiments we choose to measure the fidelity against $|r_1\rangle$. **b)** Measurement of F_1 (left) and F_2 (right) for various unknown phases. The angles are given in degrees.

Phase sensing protocol

Our sensing protocol was devised by investigating the behaviour of each fidelity, F_1 and F_2, as a function of various unknown angles in the range 0 to 2π. This is achieved by plotting the fidelities, F_1 and F_2, against various unknown angles, as shown in Fig.3.9b, with angles given in degrees.

Observation of the fidelities F_1 and F_2 in Fig.3.9b reveals that whenever F_2 is greater than 0.5, the unknown angles range from 0° to 180°, and whenever F_2 is less than 0.5, the unknown angles range from 180° to 360°. This is what our sensing protocol is based on. Therefore, if an unknown phase is applied at our SN

(at site 4), we start by first preparing two measurements (F_1 and F_2), and then use the following protocol to retrieve the unknown phase

- Use F_1 to find θ_1 such that $\theta_1 = \cos^{-1}(2F_1 - 1)$
  Then, use F_2 to determine in which range the theta is:
  if $F_2 \geq 0.5$, then $0 \leq \theta_1 \leq \pi$
  if $F_2 < 0.5$, then $\pi \leq \theta_1 \leq 2\pi$

We note that by using this phase-sensing protocol, we can retrieve any unknown phase accurately as we have not yet considered the presence of disorder in the system. However, when we consider the presence of errors in the system, the protocol needs to be adjusted slightly to account for their presence, but will still give a very good estimation of the unknown angles, as will be seen in Section 3.3.4.

3.3.4 Effect of disorder

In order for our results to be realistic, we will now consider the presence of errors in the system and assess how well the applications discussed above perform under such errors. As discussed in Section 2.3, the considered errors are those attributed to manufacturing defects in the SN, where certain parameters have not been engineered as required. These are the on-site energies parameters and coupling interactions parameters. The error in the on-site energies is known as the diagonal error, as it is represented in the diagonal elements of $\mathcal{H}_{XY}$, whereas the error in the coupling interactions is known as the off-diagonal error, as it is represented in the off-diagonal elements of $\mathcal{H}_{XY}$.

Router robustness

The routing of quantum information discussed in Section 3.3.1 is the process of sending a single excitation from site 1 to site 6. Furthermore, because of the periodicity of the system and as long as there are no errors, the excitation is found to be at site 6 at even mirroring times (i.e., $2t_m$, $4t_m$, $6t_m$, etc). As a result, measuring the fidelity of the excitation at site 6 (fidelity against $|r_6\rangle$) at each even t_m will always yield unit fidelity. On the other hand, when the system is subject to errors, then the measurement of this router fidelity would reveal that it is decaying with time and with the strength of the error, E, as will be seen below.

Investigating the effect of disorder on the routing protocol is achieved by first applying the random diagonal or off-diagonal errors to the Hamiltonian $\mathcal{H}_{XY}$ parameters (see Section 2.3 for a discussion of these errors). Once the Hamiltonian contains errors, we perform the routing protocol and then calculate the fidelity against $|r_6\rangle$ at different times $2t_m$, $4t_m$, and $6t_m$. Since the error is random, we calculate $\overline{F}(t)$, which is the average of 1000 realisations of the fidelity, each generated with a random error (see Eq.(2.14)). Therefore, each point in Fig. 3.10 is the average of 1000 realisations of the fidelity.

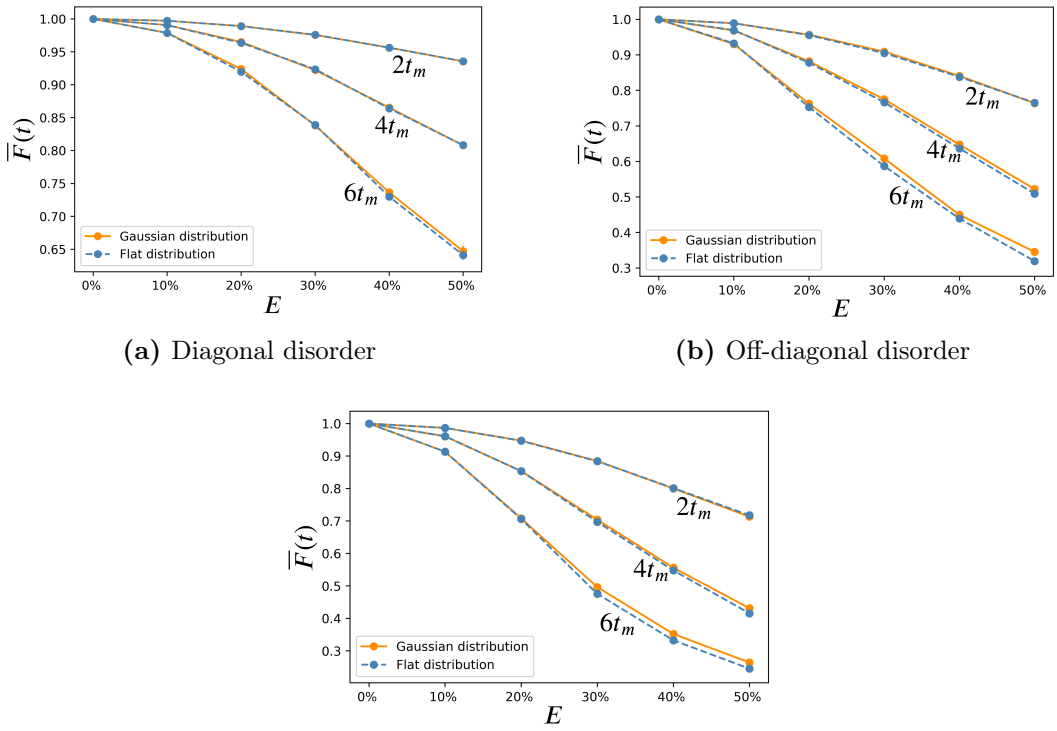

(a) Diagonal disorder

(b) Off-diagonal disorder

(c) Both disorders

Figure 3.10: The robustness of the router fidelity when $\overline{F}(t)$ is measured at $t = 2t_m$, $4t_m$, and $6t_m$ against diagonal disorder (a), off-diagonal disorder (b), and both disorders (c) with different error strengths, E, and for random Gaussian and flat distributions (solid orange and dashed blue lines, respectively). The error bars denoting the standard deviation of the mean $w_{\overline{x}}$, for each point, are also plotted, but are not visible on the plot because they are smaller than the symbol size used for the data points.

It can be observed from Fig.3.10(a) that our routing protocol is very robust against diagonal disorder, as its averaged fidelity remains above 99% at $2t_m$ and $> 95\%$ at a later time, $6t_m$, even with a relatively high error strength of $E = 15\%$. For a significant error strength of $E = 25\%$, the router fidelity remains above 98%, 94%, and 88% at times $2t_m$, $4t_m$, and $6t_m$, respectively. On the other hand,

the robustness of the router fidelity against off-diagonal disorder, Fig.3.10(b), and with an error strength of $E = 15\%$, is observed up to time $4t_m$, where the fidelity is $> 90\%$. However, as the error strength increases, $E \geq 20\%$, there is a clear decay in the fidelity. Therefore, router fidelity is more sensitive to off-diagonal error, particularly for a large error strength, E. The effect of including both types of disorders, Fig.3.10(c), is slightly more damaging but not noticeably different from the case of having only off-diagonal disorder, especially at $2t_m$. This can be attributed to the fact that the error is dominated by off-diagonal disorder.

Furthermore, the standard deviation of the mean, for each point, has also been calculated to assess the accuracy of our data. The formula representing the standard deviation of the mean is given by

$$w_{\overline{\mathrm{x}}} = \frac{\sqrt{\frac{1}{l-1}\sum_{i=1}^{l}(\mathrm{x}_i - \overline{\mathrm{x}})^2}}{\sqrt{l}}, \tag{3.18}$$

where l denotes the sample size that we choose to be $l = 1000$. The standard deviation of the mean, $w_{\overline{\mathrm{x}}}$, turns out to be very small and not visible on the plot, as it is smaller than the symbol size used for the data points. Even with the worst-case scenario (i.e., with both types of disorder and with $E = 50\%$) the standard deviation of the mean is still very small (≈ 0.008) and not visible on the plot. The only exception, where the error bar is hardly discernible on the plot is in the presence of diagonal disorder with $E = 50\%$ and at $6t_m$ Fig.3.10(a). Observing very small standard deviation of the mean emphasises the accuracy and robustness of our results.

Note that the plot also shows that the random number distributions (Gaussian and flat distributions) are essentially indistinguishable on the scale of the plots for an error scale of up to $E = 20\%$; however, for larger error strengths, the flat distribution has slightly more impact on the fidelity than the Gaussian distribution. The discrepancy between these distributions at large error scales may be conjectured to be linked to the fact that the mean for both distributions is zero and therefore that the numbers obtained from the Gaussian distribution are more likely to be close to the mean than to the tails, which is because of the bell-shape the Gaussian distribution has. On the other hand, the flat distribution is rectangular, so any value in the specified range is equally likely to occur.

Once the error strength is $E \leq 10\%$, then the router fidelity against both types of disorder, diagonal or off-diagonal, will be very robust. This is because in the

instance of diagonal disorder, Fig.3.10a, the routing fidelity at three consecutive times ($2t_m$, $4t_m$, and $6t_m$) remains above 97%, whereas in the instance of both types of disorder, Fig.3.10c, the routing fidelity at the same three consecutive times remains above 90%. It is crucial to note that in real physical implementations the error strengths are expected to be reasonable (i.e., much less than $E = 10\%$). Therefore, since our results for router robustness suggest that it is very robust with $E = 10\%$, we highlight the potential of our SN for short-distance routing applications.

Bipartite entanglement robustness

Above, we generated a bipartite maximally entangled state between the ends of the SN system (sites 1 and 6). We proposed two protocols that can be used to generate such an entangled state, the phase-based protocol and the natural generation protocol. Here, we investigate the robustness of the phase-based bipartite entanglement protocol against diagonal and off-diagonal disorder. We will then investigate the robustness of the natural generation protocol of the bipartite entanglement.

Investigating the robustness of the phase-based bipartite entanglement protocol is achieved by applying the error to the $\mathcal{H}_{XY}$ parameters, performing the entanglement protocol and calculating the degree of entanglement between sites 1 and 6 at the relevant time, using the Entanglement of Formation (EOF) tool. The chosen times for the EOF calculations are $2t_m$, $4t_m$, and $6t_m$. These are the times where the system state, for no error, is found to be in a bipartite maximally entangled state. Since the error is random, we calculate the $\overline{EOF}$, which is the average of 1000 realisations of the EOF, each generated with a random error (see Eq.(2.17)). Therefore, each point in Fig.3.11 is the average of 1000 realisations of the EOF.

The bipartite entangled state is very robust against diagonal disorder, Fig.3.11(a), as the $\overline{EOF}$ at $2t_m$ remains above 99% up to a relatively large error strength of $E = 15\%$, and further remains above 95% up to a significant error strength of $E = 25\%$. Moreover, $\overline{EOF}$, at later times up to $6t_m$ and with an error strength of $E = 10\%$, is $> 95\%$. On the other hand, the robustness to off-diagonal disorder, Fig.3.11(b), is observed with an error strength of $E \leq 10\%$, where the $\overline{EOF}$ at $2t_m$ and $4t_m$ remains above 97% and 95%, respectively. In the presence of both disorders and with $E = 10\%$, the entanglement at $2t_m$ and $4t_m$ remains above 97% and 92%, respectively. However, as the error strength increases to $E \geq 20\%$, and

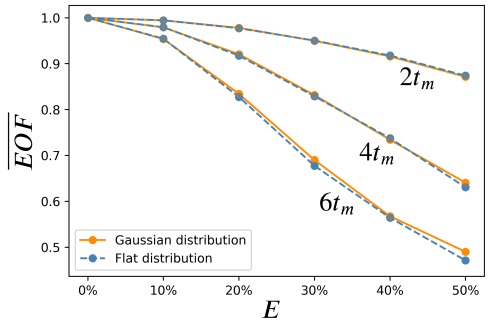

(a) Diagonal disorder

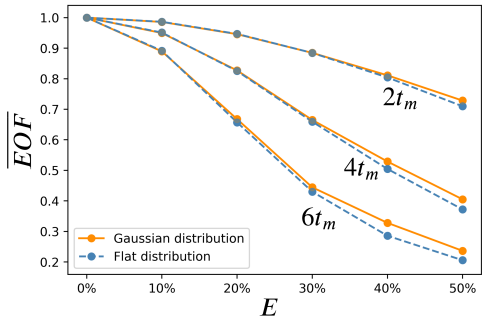

(b) Off-diagonal disorder

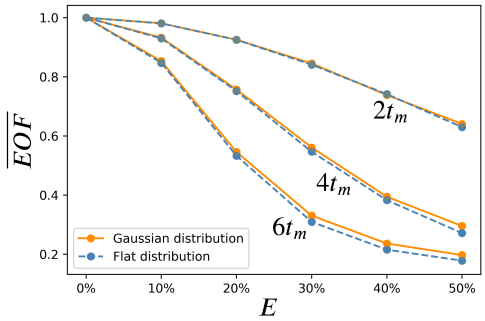

(c) Both disorders

Figure 3.11: The robustness of the bipartite maximally entangled state when the $\overline{EOF}$ is measured at $t = 2t_m$, $4t_m$, and $6t_m$ against diagonal disorder (a), off-diagonal disorder (b), and both disorders (c) with different error strengths E, and for random Gaussian and flat distributions (solid orange and dashed blue lines, respectively). This is for the phase-based entanglement protocol. The error bars denoting the standard deviation of the mean $w_{\overline{x}}$, for each point, are also plotted, but are not visible on the plot because they are smaller than the symbol size used for the data points.

especially at later times ($4t_m$ and $6t_m$), $\overline{EOF}$ decays rapidly. Furthermore, the standard deviation of the mean, for each point, are very small to the point that they are not visible on the plot, as they are smaller than the symbol size. This illustrates the robustness and precision of our results.

The behaviour of $\overline{EOF}$ with respect to the type of random number distribution (Gaussian or flat) in the instance of diagonal disorder at $2t_m$ is indistinguishable on the scale of the plot. In the instance of off-diagonal disorder, the indistinguishability is observed at $2t_m$ up to $E = 40\%$. The effect of the random number distributions become distinguishable at later times and particularly at high error strengths E. Therefore, as long as the error strengths are in the regime of reasonable error strengths (i.e., $E \leq 10\%$), the $\overline{EOF}$ behaviour does not depend on the type of random error distribution used. The robustness of our bipartite entanglement protocol for relatively large error strengths makes it a promising candidate

to be used in real applications.

In the above, we investigated the robustness of the bipartite maximally entangled state that is generated using the first entanglement protocol (the phase-based protocol). On the other hand, the robustness of the bipartite maximally entangled state, when generated using the second entanglement protocol (natural generation protocol), is more robust than the robustness of the entanglement of the phase-based protocol, particularly for $E > 10\%$. This is illustrated in Fig.3.12.

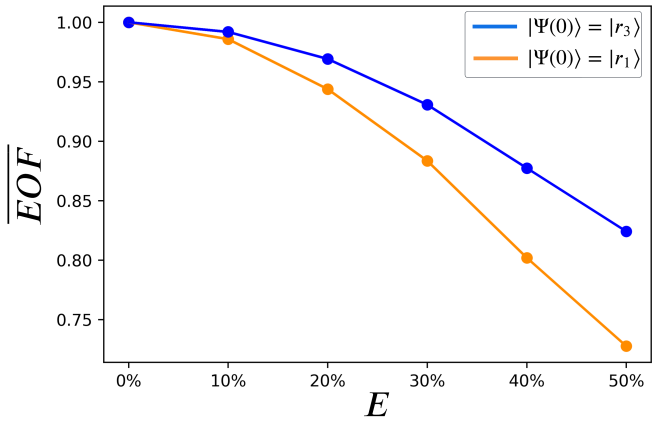

Figure 3.12: Robustness of the bipartite maximally entangled state between site 1 and site 6 for two different entanglement protocols in the presence of off-diagonal disorder. Blue: for the natural generation protocol where the initial state is $|\Psi(0)\rangle = |r_3\rangle$, and the $\overline{EOF}$ is measured at $t = t_m$. Orange: for the phase-based protocol where the initial state is $|\Psi(0)\rangle = |r_1\rangle$, and the $\overline{EOF}$ is measured at $t = 2t_m$.

The reasons why the second entanglement protocol is more robust than the first are attributed to the fact that the second entanglement protocol involves fewer sites with respect to the state evolution and is collected at t_m, whereas the first entanglement protocol involves all sites and is collected at $2t_m$. This is demonstrated in Fig.3.13 where the fidelity against each site as a function of time is plotted in a colormap.

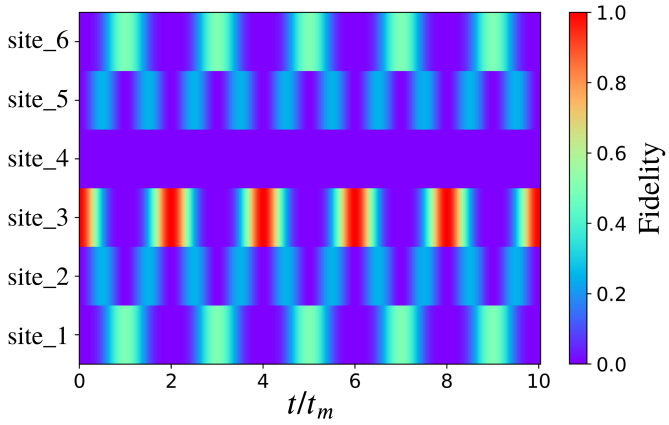

Figure 3.13: Fidelity of each site as a function of the rescaled time, t/t_m, in the second entanglement protocol. It shows that the amplitude at site 4 is always zero.

Gaussian fitting function

More intuition about the system robustness against disorder can be obtained using fitting functions. It also allows the prediction of future data points without the need to redo the numerical calculation for each new parameter. By investigating numerically different fitting functions, we find that the Gaussian fit best describes our system robustness. The form of the Gaussian function is given by

$$f(\mathrm{x}) = a \exp\left(-\frac{(\mathrm{x}-\overline{x})^2}{2w^2}\right), \tag{3.19}$$

where a represents the amplitude of the Gaussian function, $\overline{x}$ denotes the mean of the Gaussian function, and w represents the standard deviation (width) of the Gaussian distribution.

The fitting is done with both routing robustness and entanglement robustness, as shown in Fig.3.14. These results suggest that the behaviour of our SN system against disorder follows a Gaussian distribution. The function $f(\mathrm{x})$ here is a function of the error strengths, $f(E)$. The parameters for the Gaussian fit of routing robustness, Fig.3.14(a), are $a \approx 1.001$, $\overline{x} \approx -0.01$, and $w \approx 0.62$. The parameters for the Gaussian fit of entanglement robustness, Fig.3.14(b), are $a \approx 1.001$, $\overline{x} \approx -0.01$, and $w \approx 0.53$.

Phase-sensing robustness

In practical implementations, the system will be susceptible to disorder and so the phase sensing protocol discussed in Section 3.3.3 is unlikely to work very well. This is because the fidelity, F_1, is reduced in the presence of error and therefore the

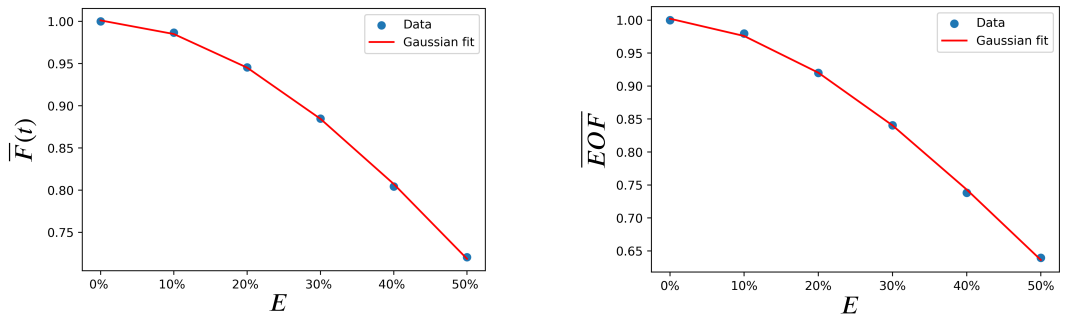

(a) Routing robustness **(b)** Entanglement robustness

Figure 3.14: a) The robustness of the routing protocol against both disorders when its averaged fidelity is measured at $2t_m$ (blue dots) with a Gaussian fit (red line) for various error strengths E. b) The robustness of the entanglement protocol against both disorders when its averaged EOF is measured at $2t_m$ (blue dots) with a Gaussian fit (red line) for various error strengths E.

retrieved angle will deviate considerably from the actual unknown angle. However, the behaviour of the fidelities, F_1 and F_2, under the error inspired us to tailor a suitable phase-sensing protocol that can retrieve the unknown angle in the presence of disorder. The protocol uses both F_1 and F_2 and therefore the application of the unknown phase must be repeatable. The diagonal disorder has only a very weak effect on the fidelities and therefore we will consider the more damaging type of error, off-diagonal disorder, in our sensing protocol.

Measurements of averaged fidelities, $\overline{F_1}$ and $\overline{F_2}$, in the presence of off-diagonal disorder with error strengths of up to $E = 30\%$ are presented in Fig.3.15. The distribution of the random error used here is Gaussian. From now on, we use the Gaussian distribution for the random number error.

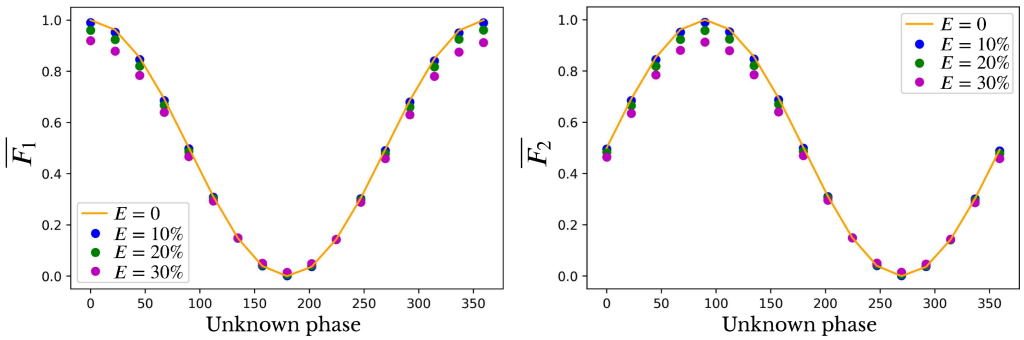

Figure 3.15: Left: Averaged fidelity $\overline{F_1}$ in the presence of off-diagonal disorder for different error strengths, E, and for various unknown phases. **Right:** Averaged fidelity $\overline{F_2}$ in the presence of off-diagonal disorder for different error strengths, E, and for various unknown phases. The orange line corresponds to the ideal case where there is no error. The dots are the averaged fidelity of 1000 fidelity realisations for each unknown phase with error scaled up to $E = 30\%$. Angles are given in degrees.

It can be seen in Fig.3.15 that the fidelities that suffer more from the off-diagonal error are those that are approaching unity. The reason for this is because fidelity is bounded by 1, so the error on fidelity ≈ 1 can only reduce the fidelity, and thus all errors can only act so as to reduce F away from the unique $F = 1$ state. Similarly, fidelities that are close to zero can only be increased by the error because, additionally, the fidelity cannot be less than zero. This, however, is a very small increase and is negligible on the scale of the plot. Small fidelities are clearly not sensitive to the error compared to high fidelities as in the case of fidelities that approach zero, and the error will not guarantee moving the state closer to the desired state. This is because there are numerous different states that are all orthogonal to the desired state and whose occupation probabilities may be increased by the error. As a result, retrieving an unknown angle from a fidelity that approaches unity will be subject to greater error and will deviate more from its actual value. To overcome this issue, a flexible protocol based on the behaviour of $\overline{F_1}$ and $\overline{F_2}$ in Fig.3.15 is proposed.

By observing how the averaged fidelities $\overline{F_1}$ and $\overline{F_2}$ in Fig.3.15 change with respect to the unknown phases and the error strengths, E, an appropriate phase-sensing protocol can be designed. The figure shows that for a given unknown phase, when $\overline{F_1}$ suffers more from the error, $\overline{F_2}$ is less affected, and vice versa. Thus, for our sensing protocol, both F_1 and F_2 are used in order to obtain two angles, θ_1 and θ_2, respectively. This is then repeated over many realisations of the system with random errors. The angle with the lower standard deviation is then

chosen as the best estimate of the unknown angle, as described below.

For a given dataset $\{F_1,F_2\}$ associated with an unknown phase, our sensing protocol works as follows:

1. Use F_1 to find θ_1 such that $\theta_1 = \cos^{-1}(2F_1 - 1)$
   Then, use F_2 to determine the range in which the θ_1 lies:
   if $F_2 \geq 0.5$, then $0 \leq \theta_1 \leq \pi$
   if $F_2 < 0.5$, then $\pi \leq \theta_1 \leq 2\pi$

2. Use F_2 to find θ_2 such that $\theta_2 = \sin^{-1}(2F_2 - 1)$
   Then, use F_1 to determine the range in which θ_2 lies:
   if $F_1 \geq 0.5$, then $-\frac{\pi}{2} \leq \theta_2 \leq \frac{\pi}{2}$
   if $F_1 < 0.5$, then $\frac{\pi}{2} \leq \theta_2 \leq \frac{3\pi}{2}$

In step 2, we set the range of the angle to be from $-\frac{\pi}{2}$ to $\frac{3\pi}{2}$ because with this range the use of F_1 to determine the range of the F_2 angle will then allow us to uniquely distinguish between just two continuous regions of θ_2. This is crucial in order for the angle averaging to work, as described below.

If we use the above protocol on a set of 1000 random realisations of data $\{\{F_1, F_2\}_1, \{F_1, F_2\}_2, \ldots, \{F_1, F_2\}_{1000}\}$, for an unknown phase, we will then obtain $\{\{\theta_1, \theta_2\}_1, \{\theta_1, \theta_2\}_2, \ldots, \{\theta_1, \theta_2\}_{1000}\}$. All the realisations of θ_1 are averaged and all the realisations of θ_2 are averaged as well. It is important to note that when we take the average of all θ_2, for some unknown phases the averaged angle, $\overline{\theta_2}$, could be negative, which is due to the negative ranges employed in step 2 of the protocol. Thus, in order to shift the negative averaged angle to be in the range $3\pi/2$ to 2π, we add 2π to the negative averaged angle. Each of the obtained averaged angles, $\overline{\theta_1}$ and $\overline{\theta_2}$, corresponds to the angle of the unknown phase; however, one of these values will show a greater deviation from the actual unknown angle due to the larger error that perturbs fidelities approaching unity. To determine which of the two, $\overline{\theta_1}$ and $\overline{\theta_2}$, is the closest value to the unknown angle, the standard deviations of these angles are considered, where the angle with a lower standard deviation corresponds to the unknown phase with a higher accuracy.

The robustness of our phase-sensing protocol to off-diagonal disorder and with a relatively high error strength of $E = 20\%$ is demonstrated in Fig.3.16. It is clear

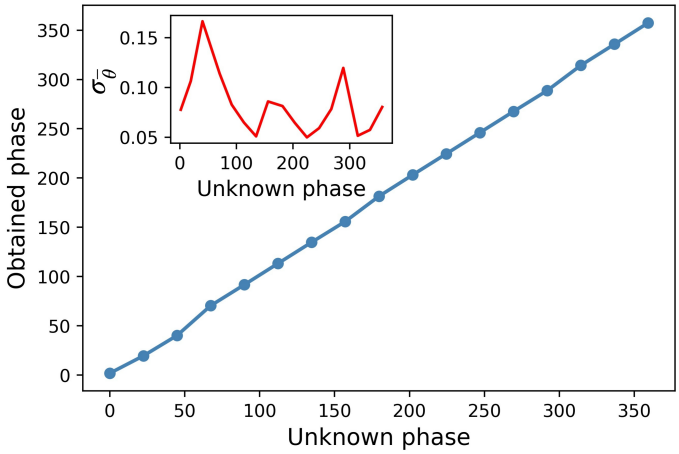

Figure 3.16: The obtained angles vs the unknown angles, in degrees. This is in the presence of off-diagonal disorder with a high error strength of $E = 20\%$ and with angles being averaged over 1000 realisations. Inset: the standard deviation, $\sigma_{\bar{\theta}}$, of the mean of the obtained angles. It is clear that the angle around 45° has the highest standard deviation.

that the angles around 45° have higher standard deviations, which means that they are more subject to the error. With reference to Fig.3.15, this is because both $\overline{F_1}$ and $\overline{F_2}$, for unknown angles around 45°, lie between 0.5 and 1, and therefore suffer more from the error. Even then, the standard deviation for angles around 45° is still small, at around a fraction of one degree.

The performance of our SN in phase sensing, even in the presence of significant errors , that is of the level of $E = 20\%$ of the characteristic energy of the system (see Fig.3.16), makes it a very good potential device for high-precision measurements of unknown phases, which is important for interferometry applications [156, 158], as one can use our device to measure and correct for unknown phases. Furthermore, such precise measurements of unknown phases can be useful in quantum information tasks that require phase factor applications [1, 2, 85, 106], in the sense that it can be integrated into schemes to ensure that the applied phase is the desired one. It is important to note that a simpler version of our sensor device, two 2-site-chain SN, can be used instead for the sensing task. The advantage there would be that fewer qubits in total would be needed with respect to our current device and therefore it would even be more robust to disorder.

Energy spectrum

We now wish to investigate the energy levels of our ideal 6-site SN system. We therefore diagonalise the Hamiltonian $\mathcal{H}_{XY}$ to gain the eigenvalues and plot them

to see how they change when we introduce a diagonal or off-diagonal disorder. Our ideal SN has three doubly degenerate energy levels, one of which is at zero energy. This is shown in Fig.3.17 and Fig.3.18 for instances of off-diagonal and diagonal disorder, respectively.

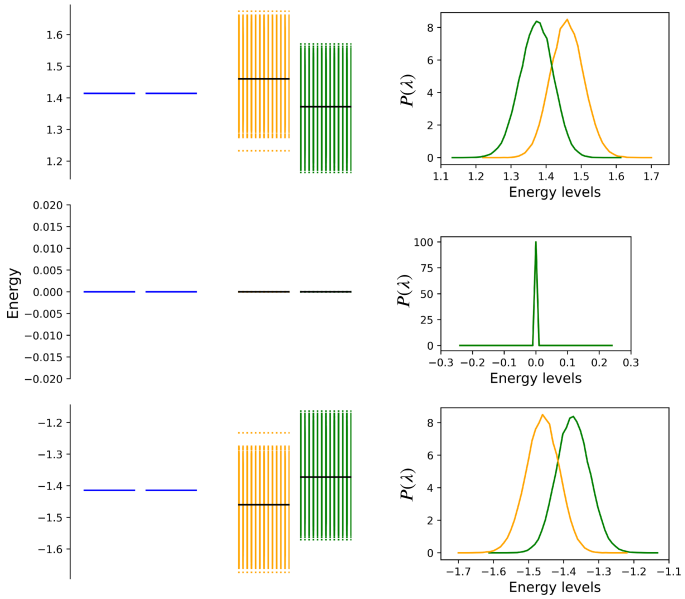

Figure 3.17: Energy spectrum of the 6-site SN. The blue horizontal lines indicate the energy levels in the ideal case with no error. Each of these lines has a degeneracy of two eigenvalues. On the right of the blue lines are 100,000 random realisations of these degenerate energy levels in the presence of off-diagonal disorder and with an error strength of $E = 20\%$. The two degenerate eigenvalues are coloured orange and green, respectively. The black lines are the average of each realisation. The probability density distributions of each energy level realisation are plotted on the right.

.

.

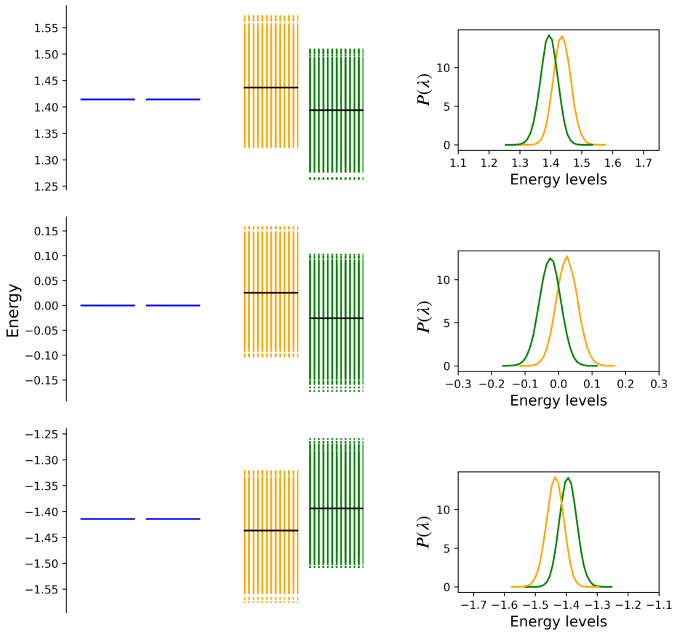

Figure 3.18: Energy spectrum of the 6-site SN. The blue horizontal lines indicate the energy levels in the ideal case with no error. Each of these lines has a degeneracy of two eigenvalues. On the right of the blue lines are 100,000 random realisations of these degenerate energy levels in the presence of diagonal disorder and with an error strength of $E = 20\%$. The two degenerate eigenvalues are coloured orange and green, respectively. The black lines are the average of each realisation. The probability density distributions of each energy level realisation are plotted on the right.

In the ideal case where the system does not have disorder, the three doubly degenerate energy levels are: $-\sqrt{2}, 0, \sqrt{2}$ (the blue horizontal lines in Fig.3.17). These $\pm$ energy levels pairs, alongside the zero energy level, are observed because our Hamiltonian $\mathcal{H}_{XY}$ anticommutes with a unitary operator, $\mathcal{D}$, that satisfies $\mathcal{D}^2 = \mathcal{I}$, as we will describe now. The unitary operator $\mathcal{D}$ that anticommutes with our Hamiltonian ($[\mathcal{D}, \mathcal{H}_{XY}]_+ = \mathcal{D}\mathcal{H}_{XY} + \mathcal{H}_{XY}\mathcal{D} = 0$) is given by

$$\mathcal{D} = \begin{pmatrix} 1 & 0 & 0 & 0 & 0 & 0 \\ 0 & -1 & 0 & 0 & 0 & 0 \\ 0 & 0 & 1 & 0 & 0 & 0 \\ 0 & 0 & 0 & 1 & 0 & 0 \\ 0 & 0 & 0 & 0 & -1 & 0 \\ 0 & 0 & 0 & 0 & 0 & 1 \end{pmatrix}. \tag{3.20}$$

Now, for an eigenstate $|\varphi\rangle$ of the Hamiltonian $\mathcal{H}_{XY}$, the eigenvalue equation is given by

$$\mathcal{H}_{XY} |\varphi\rangle = \lambda |\varphi\rangle . \tag{3.21}$$

Similarly, for an eigenstate $\mathcal{D}|\varphi\rangle$ of the transformed Hamiltonian $\mathcal{D}\mathcal{H}_{XY}$, the eigenvalue equation is given by

$$\mathcal{D}\mathcal{H}_{XY}|\varphi\rangle = \lambda(\mathcal{D}|\varphi\rangle). \tag{3.22}$$

However, we can also write

$$\mathcal{H}_{XY}(\mathcal{D}|\varphi\rangle) = -\lambda(\mathcal{D}|\varphi\rangle), \tag{3.23}$$

as $\mathcal{D}\mathcal{H}_{XY} = -\mathcal{H}_{XY}\mathcal{D}$. Therefore, we can either have $|\varphi\rangle$ and $\mathcal{D}|\varphi\rangle$ as the eigenstates of $\mathcal{H}_{XY}$ with energies λ and $-\lambda$, respectively, or $|\varphi\rangle$ being the eigenstate of $\mathcal{D}$ with energy zero. This property of the energy spectrum is known as "pairing theorem" [159–161].

Since the zero energy level is associated with an eigenstate of the operator $\mathcal{D}$, it does not move from zero even when we include off-diagonal disorder in the Hamiltonian, as observed in Fig.3.17. In this case, the anticommutation with an imperfect Hamiltonian (off-diagonal disorder) still holds. On the other hand, the zero energy level is not protected against diagonal disorder as, in this case, the Hamiltonian does not anticommute with the operator $\mathcal{D}$ (i.e., $[\mathcal{D}, \mathcal{H}_{XY}]_+ \neq 0$). Furthermore, a symmetry of the energy levels with respect to the zero energy level is observed in the presence of off-diagonal disorder, as per Fig.3.17, but is broken in the presence of diagonal disorder, as per Fig.3.18. This is again because the anticommutation condition is not satisfied in the instance of diagonal disorder.

Even though the off-diagonal disorder protects the symmetry of λ around zero and protects the zero energy levels, the results discussed in the previous subsections suggest that the system is more sensitive to off-diagonal disorder than diagonal. This can be explained in terms of the energy scale. The probability density distribution, $P(\lambda)$, for each ensemble of energy levels under disorder shows that the non-zero energy levels are distributed on a wider energy scale in the presence of off-diagonal disorder compared to the diagonal (see the $P(\lambda)$ plots in Fig.3.17 and Fig.3.18), which explain the greater sensitivity of our system to off-diagonal disorder.

Level spacing statistics

The behaviour of the energy levels under the error can also be investigated from another prospective, using level spacing statistics. Level spacing statistics, $P(s)$,

are widely used to investigate classically chaotic quantum systems [162] and complex many-body systems [163]. It is also used to characterise the fidelity behaviour in the presence of error in spin chains [146]. The distribution $P(s)$ gives the probability that the energy gap between two adjacent levels in the presence of error, normalised to the actual spacing in the error-free case, belongs to a specified interval, $[s,s + ds]$. For example, in the error-free case, the energy gap between two adjacent levels for our 6-site SN is $\sqrt{2}$; in the presence of disorder, however, this gap will be different. Therefore, for the $P(s)$ statistics, the energy gap is normalised by dividing it by $\sqrt{2}$, and so for a very small disorder the energy level spacing statistics will form a narrow distribution around 1, as shown in Fig.3.19.

The energy level spacing statistics shown in Fig.3.19 illustrate that for large error strengths of $E > 10\%$, the $P(s)$ gives a wider distribution in the presence of off-diagonal disorder (Fig.3.19a) compared to diagonal disorder (Fig.3.19b). This could also explain the sensitivity of our SN system to off-diagonal disorder, as the $P(s)$ show that the energy gaps are not disturbed by the diagonal disorder to the same extent as by the off-diagonal disorder. We note that the discrete features visible in these plots (as opposed to each being a smooth curve) are due to the fact that the analysis is presented for a 6-site system in order to compare directly with the previous example and discussion. Studies of systems with a much greater number of sites can yield smoother distributions.

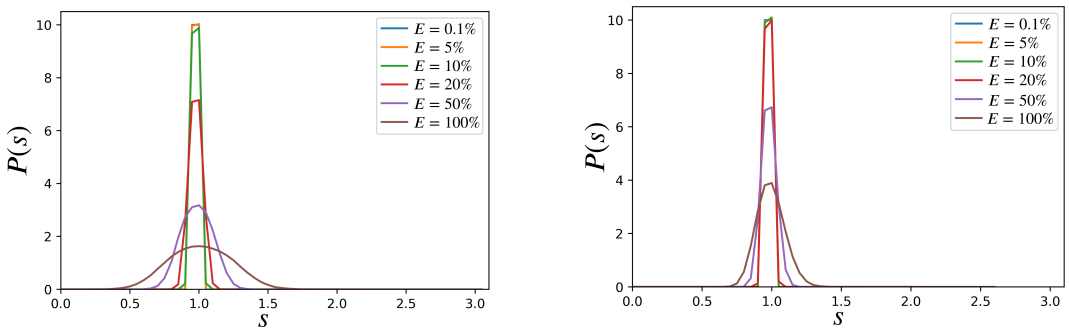

(a) Off-diagonal disorder **(b)** Diagonal disorder

Figure 3.19: Energy level spacing statistics of the 6-site SN with off-diagonal disorder (a) and diagonal disorder (b) for different error strengths, E.

3.4 Spin networks of unequal chains

The SN discussed above is designed by coupling together two PST chains, each of three sites. Here, we investigate a SN designed by coupling together two PST chains, but each of a different number of sites. This is a SN of two PST chains, A and B, of $N_A = 3$ sites and $N_B = 4$ sites, respectively, as shown in Fig.3.20. Since the mirroring time, t_m, of a relevant chain of the SN is given as a function of the length of that chain (see Section 3.1), the time evolution through the chain A is different to that though the chain B. Therefore, we denote the mirroring time for chain A and chain B as $t_{m,A}$ and $t_{m,B}$, respectively.

Routing, bipartite entanglement, and phase sensing protocols can also be generated in this SN. We will discuss below the generation of two of these protocols (routing and bipartite entanglement).

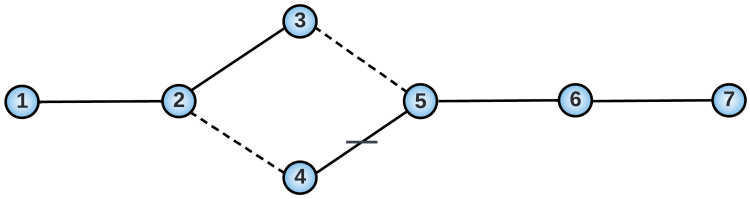

Figure 3.20: Scheme of the SN of unequal chains that is built by coupling together a 3-site PST chain with a 4-site PST chain.

.

3.4.1 Routing

Regardless of the size of the SN and, indeed, regardless of whether the SN is of equal chains or unequal chains, the routing protocol can still be achieved. For instance, in Fig.3.20, routing is achieved by starting with a single excitation injected at site 1 at $t = 0$, and a phase flip applied at site 4 at $t = t_{m,A}$; then, after an evolution period of $t = t_{m,B}$, the excitation would be transferred completely to site 7

$$|\Psi(t_{m,A,B})\rangle = -i\,|r_7\rangle\,, \tag{3.24}$$

where $t_{m,A,B} = t_{m,A} + t_{m,B}$ is the total time for the excitation to evolve from site 1 to site 7.

In the general case, for a longer two-chain SN of arbitrary length $N_A+N_B = N$, the routing protocol will still work in the same way and the routed state will be given by

$$|\Psi(t_{m,A,B})\rangle = e^{-i\gamma(N)}\,|r_N\rangle\,, \tag{3.25}$$

where the global phase factor is $e^{-i\gamma(N)} = (-i)^{N-2}$. This is consistent with previous results for linear chains [89].

3.4.2 Bipartite entanglement generation

As the number of sites for each chain is different, $N_A \neq N_B$, generating a bipartite maximally entangled state between the ends of this SN is not straightforward. The reason for this will be elaborated upon in the following discussion.

Let us apply the phase-based entanglement protocol here and see what happens. We start with a single excitation injected at site 1 at $t = 0$ and we allow the system to evolve for a duration of $t_{m,A}$ (the time the excitation needs to evolve to the central vertex of the diamond, sites 3 and 4), at which point we intervene with a sudden phase factor of $e^{i\pi/2}$ applied at site 4. The application of this phase (as discussed in Section 3.3.2) will result in the excitation propagating through both chains of the SN, which a given amplitude of the excitation evolving through chain A and another evolving through chain B. Therefore, after applying the phase and evolving the system for another period $t_{m,A}$, the state of the system will be given by

$$\begin{aligned}|\Psi(2t_{m,A})\rangle = \frac{1+e^{i\pi/2}}{2}\,|r_1\rangle + a(|r_3\rangle - |r_4\rangle)\\ + b\,|r_5\rangle + c\,|r_6\rangle + f\,|r_7\rangle\end{aligned} \tag{3.26}$$

where numerically we obtain $a \approx -0.031+0.031i$, $b \approx 0.15+0.15i$, $c \approx 0.31-0.31i$, and $f \approx -0.36-0.36i$.

This shows that the amplitude of the excitation that was evolving through chain A is now localised at site 1, whereas the amplitude of the excitation that was evolving through chain B is now delocalised over its sites.

Let us now calculate the fidelity of the system against a desirable state of an excitation being at site 1 (fidelity against $|r_1\rangle$), and the fidelity of the system against a desirable state of an excitation being at site 7 (fidelity against $|r_7\rangle$). Furthermore, in order to determine the degree of entanglement between sites 1 and 7, we calculate the EOF between sites 1 and 7 as a function of time. The

results of these calculations are shown in Fig.3.21.

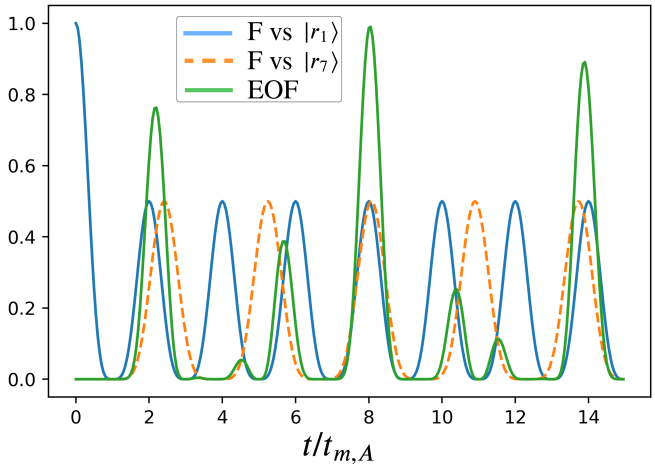

Figure 3.21: The fidelity of the system against site 1 (F vs. $|r_1\rangle$, blue) and against site 7 (F vs. $|r_7\rangle$, orange) and the EOF between them, green, as labelled in the figure.

The figure illustrates that, at $2t_{m,A}$, half of the excitation is localised at site 1, while the other half is in a superposition of states, as stated in Eq.(3.26). Note that after a few oscillations, at $t = 8t_{m,A}$, the excitation ends up in an almost bipartite entangled state between sites 1 and 7 with an EOF approaching 1 Fig.3.21. Nevertheless, this is not a perfect generation of the entangled state, as the time evolution for each chain is different. This can be resolved by utilising the dependence of the mirroring time, t_m, on the maximum coupling, J_{max}, (see Section 2.1.5) and adjusting the J_{max} of one of the SN chains, such that the mirroring times of both chains are equal. The calculations of coupling adjustments presented below are original work.

If we choose to adjust the maximum coupling of the shorter chain ($J_{max,A}$ of chain A) then $J_{max,A}$ will be reduced, which in turn makes the time evolution of chain A slower to match that of chain B ($t_{m,A} = t_{m,B}$). This modification of $J_{max,A}$ is given by

$$J_{max,A} = \frac{\pi N_A}{4t_{m,B}}, \quad \text{if} \quad N_A \quad \text{is even;} \tag{3.27}$$

$$J_{max,A} = \frac{\pi\sqrt{\frac{N_A^2-1}{4}}}{2t_{m,B}}, \quad \text{if} \quad N_A \quad \text{is odd.} \tag{3.28}$$

This is done straightforwardly by equating both mirroring times $t_{m,A} = t_{m,B}$ and rearranging the equation to solve for $J_{max,A}$.

If we instead choose to adjust the maximum coupling of the longer chain ($J_{max,B}$

of chain B) then $J_{max,B}$ will increase, which in turn makes the time evolution of chain B faster to match that of chain A ($t_{m,B} = t_{m,A}$). This modification of $J_{max,B}$ is given by

$$J_{max,B} = \frac{\pi N_B}{4t_{m,A}}, \quad \text{if} \quad N_B \quad \text{is even;} \tag{3.29}$$

$$J_{max,B} = \frac{\pi\sqrt{\frac{N_B^2-1}{4}}}{2t_{m,A}}, \quad \text{if} \quad N_B \quad \text{is odd.} \tag{3.30}$$

We note that either way (that is, adjusting the shorter or the longer chain) will result in the time evolution of both chains being equal. However, since real physical systems may have some form of constraint on the maximum coupling (see Section 2.1.5), it may not be possible to further increase the coupling of the longer chain ($J_{max,B}$). This is because adjusting the maximum coupling of the longer chain results in its couplings being strengthened to magnitudes that might not be practical, specifically when $N_B \gg N_A$, because of the experimental constraint on the maximum coupling. Therefore, we choose to adjust the maximum coupling of the shorter chain, $J_{max,A}$.

Since we have now set the maximum coupling of chain A to be as a function of $t_{m,B}$, the mirroring time of chain A is equal to the mirroring time of chain B ($t_{m,A} = t_{m,B}$). Therefore, perfect generation of the bipartite entangled state can be achieved using either the phase-based protocol or the natural generation protocol. Let us use the latter protocol, where we start with a single excitation at site 3 at $t = 0$ and evolve the system for a duration of $t_{m,A}$, which ends up in a bipartite maximally entangled state between sites 1 and 7

$$|\Psi(t_{m,A})\rangle = \frac{1}{\sqrt{2}}(-|r_1\rangle + i\,|r_7\rangle). \tag{3.31}$$

For a SN of unequal chains of an arbitrary length, injecting a single excitation at the top site of the central vertex of the SN diamond (e.g., site 3 in Fig.3.20) at $t = 0$ will naturally generate a bipartite maximally entangled state between sites 1 and N at $t_{m,A}$, given as

$$|\Psi(t_{m,A})\rangle = \frac{1}{\sqrt{2}}(e^{-i\nu(N_A)}\,|r_1\rangle + e^{-i\nu(N_B)}\,|r_N\rangle)\,, \tag{3.32}$$

where the phase factors $e^{-i\nu(N_j)} = (-i)^{N_j-1}$, $j = A,\ B$ depend on the chain lengths [89]. Note that if instead the single excitation is injected at the bottom site of the central vertex of the SN diamond (e.g., site 4 in Fig.3.20), then the

state given in Eq. (3.32) will have a relative phase of -1 at site $|r_N\rangle$, as one of the couplings in the SN is negative (e.g., the coupling between sites 4 and 5 in Fig.3.20).

3.4.3 Entanglement invariance under local rotations

Here, we discuss the scenario in our SN system where a relative phase change on a qubit q_1 has no effect on a qubit q_2, the two of which are entangled. This occurs if qubit q_1 belongs to a subspace spanned by a certain set of eigenstates of the Hamiltonian, whereas qubit q_2 belongs to a subspace spanned by different eigenstates. Therefore, the evolution of qubit q_2 is independent of qubit q_1, even though they are entangled, as discussed below. Note that the discussion below applies also to the SN of equal chains.

Consider the state at $2t_{m,A}$ where half of the excitation is at site 1 while the other half is shared between sites 3, 4, 5, 6, and 7, as given in Eq.(3.26). We know from Fig.3.21 that there is an entanglement between sites 1 and 7 at this time. There is also a lesser degree of entanglement between sites 1 and each of the sites in Eq.(3.26).

If we now perform a local phase rotation by applying a phase of $e^{i\theta}$ at site 1, the state would be given by

$$\begin{aligned} |\Psi(2t_{m,A})\rangle_\theta = e^{i\theta}\frac{1+e^{i\pi/2}}{2}|r_1\rangle + a(|r_3\rangle - |r_4\rangle) \\ + b\,|r_5\rangle + c\,|r_6\rangle + f\,|r_7\rangle\,. \end{aligned} \tag{3.33}$$

The evolution of this state is obtained by decomposing it into the eigenstates (appendix C) of the Hamiltonian as

$$\begin{aligned} |\Psi(3t_{m,A})\rangle_\theta = e^{i\theta}C_1e^{-i\lambda_1 t_{m,A}}|\varphi_1\rangle \\ + e^{i\theta}C_2e^{-i\lambda_2 t_{m,A}}|\varphi_2\rangle + e^{i\theta}C_3e^{-i\lambda_3 t_{m,A}}|\varphi_3\rangle \\ + C_4e^{-i\lambda_4 t_{m,A}}|\varphi_4\rangle + C_5e^{-i\lambda_5 t_{m,A}}|\varphi_5\rangle \\ + C_6e^{-i\lambda_6 t_{m,A}}|\varphi_6\rangle + C_7e^{-i\lambda_7 t_{m,A}}|\varphi_7\rangle\,, \end{aligned} \tag{3.34}$$

where $|\varphi_j\rangle$ are the eigenstates, λ_j are the eigenvalues, and $C_j = \langle\varphi_j|\Psi(2t_{m,A})\rangle_\theta$ are complex numbers.

It is clear that the phase shift of $e^{i\theta}$ applied at site 1 spans a certain set of eigenstates (i.e., $|\varphi_1\rangle$, $|\varphi_2\rangle$, and $|\varphi_3\rangle$). Moreover, we note that these eigenstates

all have zero at their elements 5, 6, and 7, which correspond to sites 5, 6, and 7 (see appendix C). Therefore, the effect of applying a phase shift at site 1 will not be seen at sites 5, 6, and 7, even though they are entangled with site 1.

We can see from the above that the structure of the eigenstates determines whether the application of a phase on the amplitude of a qubit will affect other qubits or otherwise. This special eigenstate structure is due to the fact that the unitary transformation of the uncoupled chains superposes only two sites (3 and 4 in our SN), and so the eigenstates of the first chain share one site with the eigenstates of the second chain, and vice versa. This can be seen in the eigenstates given in the appendix C, which are expressed in the site basis.

We conclude that the application of a local phase (i.e., rotation) on one qubit does not change the degree of entanglement between this qubit and another qubit that is entangled with it, but it does change the state (and thus there is a corresponding fidelity change). This means that the fidelity of a desirable state given as superposition between sites 1 and 7 will depend on the local phase rotation on site 1, whereas the EOF between sites 1 and 7 does not depend on such a local rotation. This is consistent with the results showing that the local phase rotation in one entangled particle will not affect the degree of entanglement between two entangled particles [13]. For instance, Bell states (given in Eq.(1.7)) can be transformed into each other via local operations, but the degree of entanglement does not change under such operations. In a practical situation, such as teleportation [37,164], where the receiver uses the fidelity to quantify the closeness between the obtained state and the initial state, local phase rotations can be an issue. This is because in this case, even though the degree of entanglement between the entangled qubits is not altered by a local phase rotation, the probability of obtaining a specific desired state (fidelity measurement) changes depending on the local phase rotation. In such a case, if the local phase rotation is unknown, our sensor device could be used to detect and correct the phase error.

3.4.4 Effect of disorder

Router robustness

The router protocol generated in the SN of unequal chains (as shown in Eq. (3.24)) will now be investigated in the presence of disorder to test its robustness. This is achieved by calculating the $\overline{F}(t)$ for the desirable state, $|r_7\rangle$, at the first time it forms, $t_{m,A,B}$, in the presence of both diagonal and off-diagonal disorder, as

shown in Fig.3.22. Its robustness against diagonal disorder shows that the fidelity is $> 99\%$ for a high error strength of $E = 15\%$, whereas in the presence of off-diagonal disorder and with an error strength of $E = 15\%$, the fidelity remains $> 96.5\%$. This shows that the SN remains highly robust to disorder, regardless of whether it is constituted of equal or unequal chains.

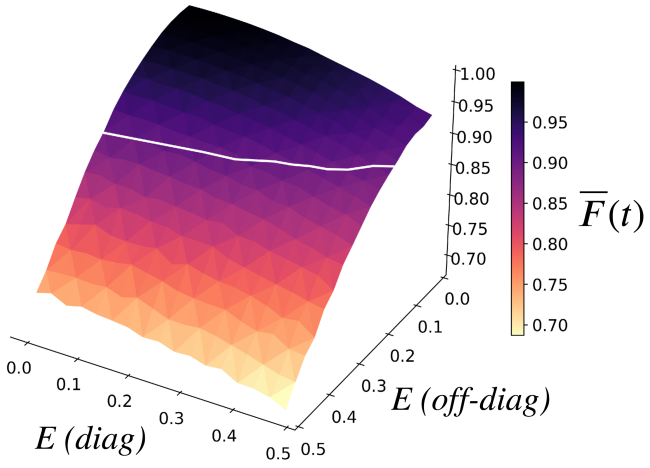

Figure 3.22: The robustness of the router protocol (generated in Eq. (3.24)) is investigated by calculating $\overline{F}(t)$ vs. $|r_7\rangle$ at $t_{m,A,B}$ in the presence of diagonal (*diag*) and off-diagonal disorder (*off-diag*) with different error strengths, E, ranging from 0 to 50%. Each point has been averaged over 1000 realisations. The white line indicates the fidelity 90% threshold ($\pm 1\%$ due to numerical discretisation).

Bipartite entanglement robustness

The bipartite maximally entangled state generated in Eq. (3.31) is now investigated with regard to disorder by calculating the $\overline{EOF}$ between sites 1 and 7 at $t_{m,A}$. This is demonstrated in Fig.3.23. In the presence of diagonal disorder, $\overline{EOF} > 99.8\%$ with an error strength of $E = 10\%$ and $\overline{EOF} > 99\%$ with a significant error strength of $E = 20\%$. In the case where the error is due to off-diagonal disorder and with an error strength $E = 10\%$, we get $\overline{EOF} > 98.5\%$, and $\overline{EOF} > 96\%$ with a significant error strength of $E = 20\%$.

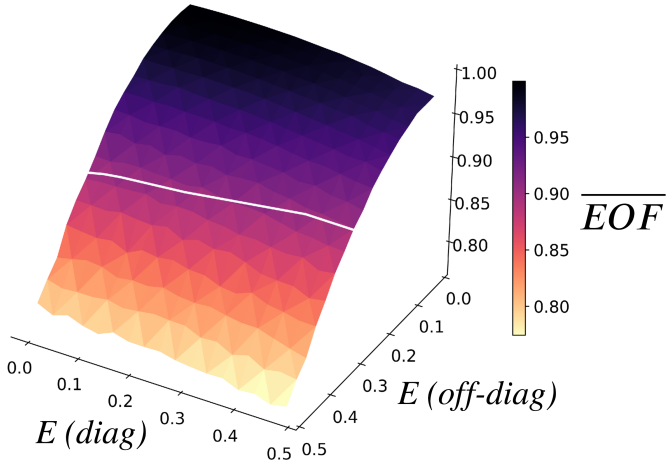

Figure 3.23: The robustness of the bipartite maximally entangled state (generated in Eq. (3.31)) is investigated by calculating the $\overline{EOF}$ at the first time it forms, $t_{m,A}$, in the presence of diagonal (*diag*) and off-diagonal disorder (*off-diag*) with different error strengths, E, ranging from 0 to 50%. Each point has been averaged over 1000 realisations . The white line has same meaning as in Fig. 3.22 but for the $\overline{EOF}$.

.

3.5 Scalability and applications

The first of DiVincenzo's requirements (see Section 1.1.2) for a reliable quantum device is the ability of the system to be scalable. This means that the system should have the ability to be scaled up by adding more qubits. We therefore study the scalability by building a larger two-chain SN system and investigating its ability to realise the desired phenomena that have been achieved in the small two-chain SN above.

In order to scale the two-chain SN we couple two longer USC. This is achieved using the same method discussed in Section 3.2, that is, by applying a Hadamard-like unitary on the Hamiltonian of two large USC to build an arbitrarily large SN system. An example of such a SN, as formed by coupling together two chains each of length $N/2$, is shown in Fig.3.24.

This SN can then be used for quantum communication over a longer distance, as opposed to the shorter distance protocols discussed above. It can also be used for generating a longer-range entanglement than the short-range entanglement discussed above. Moreover, the phase-sensing protocol discussed for the 6-site SN above will now be investigated for a larger SN system.

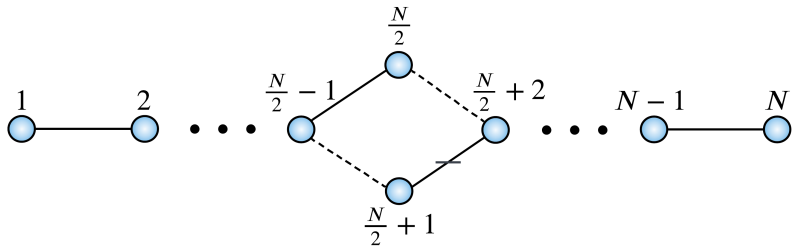

Figure 3.24: Diagram of a large two-chain SN system of size N (even).

3.5.1 Routing

The SN shown in Fig.3.24 of size N, where N is even, can be operated as a router (PST from site 1 to site N) following the same method used for the smaller 6-site SN discussed in Section 3.3.1. After initialising the system such that all sites have a spin down state, we start by injecting a single excitation at site 1 at $t = 0$. The system is then left to evolve for a duration t_m, which is the time where the excitation is found to be in the central vertices of the diamond (i.e., a superposed state between sites $\frac{N}{2}$ and $\frac{N}{2}+1$), given as

$$|\Psi(t_m)\rangle = \frac{e^{-i\varphi(N)}}{\sqrt{2}}(|r_{\frac{N}{2}}\rangle + |r_{\frac{N}{2}+1}\rangle). \tag{3.35}$$

The global phase factor for this evolution period is given by $e^{-i\varphi(N)} = (-i)^{\frac{N}{2}-1}$, which is consistent with previous results for spin chains [78]. If we do nothing, the state will then evolve back to site 1 at $2t_m$; instead, however, we intervene by applying a phase flip at site $\frac{N}{2}+1$ at t_m that flips the role of constructive and destructive interference, resulting in the excitation evolving towards site N. Therefore, after application of the phase flip and a further evolution of t_m, the excitation will be transferred completely to site N at a time $2t_m$

$$|\Psi(2t_m)\rangle = e^{-i\gamma(N)}\,|r_N\rangle\ , \tag{3.36}$$

The routing protocol is described in Fig.3.25 and is confirmed by our numerical simulations.

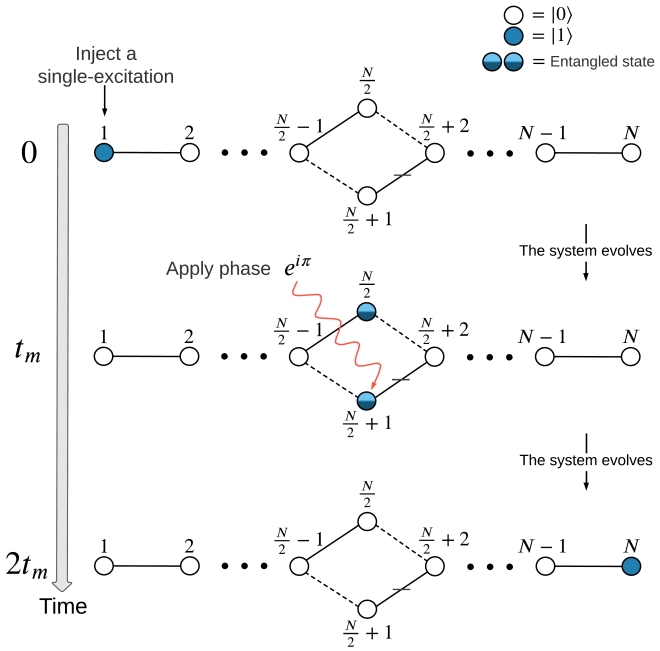

Figure 3.25: The routing protocol is achieved by injecting a single excitation at site 1 at $t = 0$ and a phase flip at site $\frac{N}{2} + 1$ at $t = t_m$.

3.5.2 Bipartite entanglement generation

A bipartite maximally entangled state between the ends of the SN shown in Fig.3.24 can be generated using either the phase-based entanglement protocol or the natural generation entanglement protocol. We will show below that perfect generation of a bipartite maximally entangled state between sites 1 and N can be achieved in the same way as for the smaller SN discussed above.

Using the phase-based entanglement protocol, we start by initialising the system with a single excitation injected at site 1 at $t = 0$ and evolving the system for t_m, where the state will be as given in Eq. (3.35). We now intervene by applying a sudden phase factor of $e^{i\pi/2}$ at site $\frac{N}{2} + 1$ at t_m. Then, after a further evolution of t_m, the state of the system will be given as a bipartite maximally entangled state between sites 1 and N at $2t_m$

$$|\Psi(2t_m)\rangle = e^{-i\delta(N)}\left(\frac{1 + e^{i\pi/2}}{2}|r_1\rangle + \frac{1 - e^{i\pi/2}}{2}|r_N\rangle\right), \tag{3.37}$$

with a global phase given by $e^{-i\delta(N)} = (-1)^{\frac{N}{2}-1}$. This entanglement generation protocol is shown in Fig.3.26.

Using the natural generation entanglement protocol, we start by injecting a

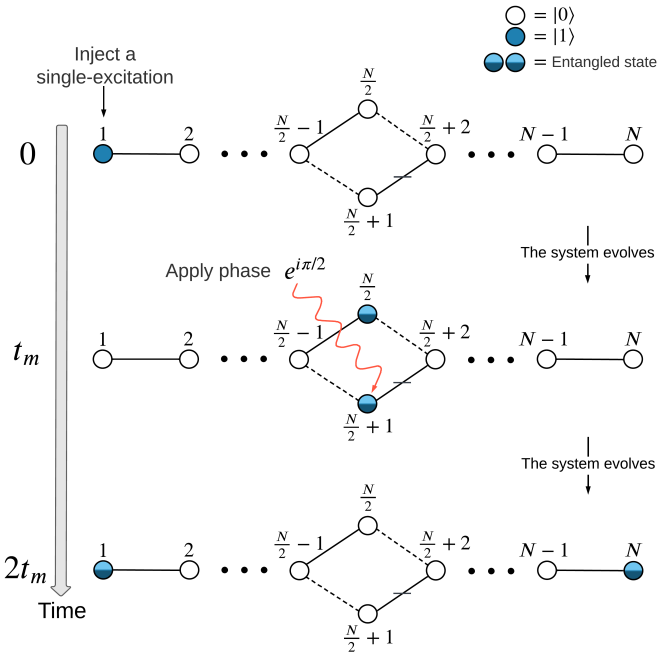

Figure 3.26: The phase-based entanglement protocol used to generate a bipartite maximally entangled state between sites 1 and N at $2t_m$.

single excitation at site $\frac{N}{2}$ at $t = 0$

$$|\Psi(0)\rangle = |r_{\frac{N}{2}}\rangle\,. \tag{3.38}$$

We then let the system to evolve for a duration t_m which will result in a bipartite maximally entangled state between sites 1 and N at t_m, given by

$$|\Psi(t_m)\rangle = \frac{e^{-i\varphi(N)}}{\sqrt{2}}(|r_1\rangle + |r_N\rangle). \tag{3.39}$$

As discussed in Section 2.2.2, knowing the entangled state and not just the information about the extent to which the two qubits are entangled (EOF) is important for certain protocols, such as teleportation [109].

3.5.3 Phase sensing

We now wish to investigate the phase-sensing protocol when scalability is considered. As discussed in Section 3.3.3, the objective is to retrieve an unknown phase of $e^{i\theta}$ applied at a site $\frac{N}{2}+1$ of the SN, Fig.3.24. Following the same protocol discussed in Section 3.3.3, the unknown phase can be retrieved for any two-chain SN of arbitrary size, N. However, the presence of error in the system requires the

use of a more complex protocol that takes into account the presence of error, as already discussed in Section 3.3.4 for the 6-site SN and as will be discussed below for larger SN systems.

3.5.4 Effect of disorder

Router robustness

We now investigate the robustness of the routing protocol to disorder for various SN sizes, N, with N being even. For each SN, we perform the routing protocol and calculate the fidelity against site $|r_N\rangle$ at the first point in time that the routing protocol forms, $2t_m$. This is performed 1000 times, and we then take the average of these 1000 realisations of the fidelity, $\overline{F}(t)$.

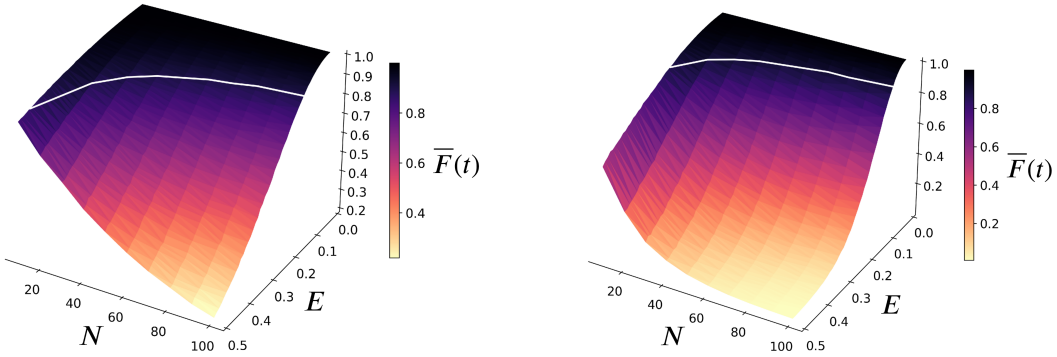

(a) Diagonal disorder **(b)** Off-diagonal disorder

Figure 3.27: The robustness of the routing protocol when $\overline{F}(t)$ is measured at $t = 2t_m$ in the presence of diagonal (a) and off-diagonal (b) disorder. This is performed for different N values and for different error strengths, E. White lines have the same meaning as in Fig. 3.22.

Interestingly, the routing protocol is very robust, even when scalability is considered. This is observed in Fig.3.27, where in the presence of diagonal disorder the averaged fidelity, $\overline{F}(t)$, at $2t_m$ remains greater than 98% up to $N = 100$ with an error strength of $E \leq 5\%$. For a relatively high error strength of $E = 10\%$, $\overline{F}(t) > 97\%$ up to $N = 40$ and $\overline{F}(t) > 92\%$ up to $N = 100$. In the presence of the more damaging type of disorder, off-diagonal disorder, and with an error strength of $E \leq 10\%$, the $\overline{F}(t) > 90\%$ up to $N = 40$ and $\overline{F}(t) > 75\%$ up to $N = 100$. Then, as E and N increase, the averaged fidelity $\overline{F}(t)$ decays. The robustness of the routing protocol observed, even with large SN sizes, gives our SN the potential to be used for quantum communications within the scale of a quantum processing device.

We now investigate the presence of different types of error that might occur in the system. The routing protocol, as discussed in Section 3.3.1, requires the application of a phase flip at a specific site at a given time. Two possible errors that can be considered here are when the phase application time is not perfect (i.e., the phase is not applied at the right time (see Eq.(2.19))) and when the angle of the applied phase is not perfect (see Eq.(2.21)).

Investigation of the former shows that the routing is very sensitive to this error, Fig.3.28a. This is because for a SN size of $N = 10$ with a timing error of $D = 10\%$, the fidelity is found to be $\approx 82\%$. High fidelities of $F(t) > 98\%$ are observed with very small error scales: $D = 3\%$, $D = 2\%$, and $D = 1\%$ for $N = 10$, $N = 20$, and $N = 80$, respectively, as per Fig.3.28a. We note that the robustness is independent of whether the scale of the phase timing error is $D > 0$ (delayed operation) or $D < 0$ (earlier operation).

On the other hand, the system is very robust to phase angle error, ξ_D (Fig.3.28b), as the fidelity is observed to be $> 97\%$ for any SN size with a high error scale of $D = 10\%$. For a smaller error scale of $D = 5\%$, the fidelity is found to be $> 99\%$, as per Fig.3.28b. Note that the routing robustness to phase error is independent of N and rather is dependent only on the error scale, D, due to the PST nature of our SN.

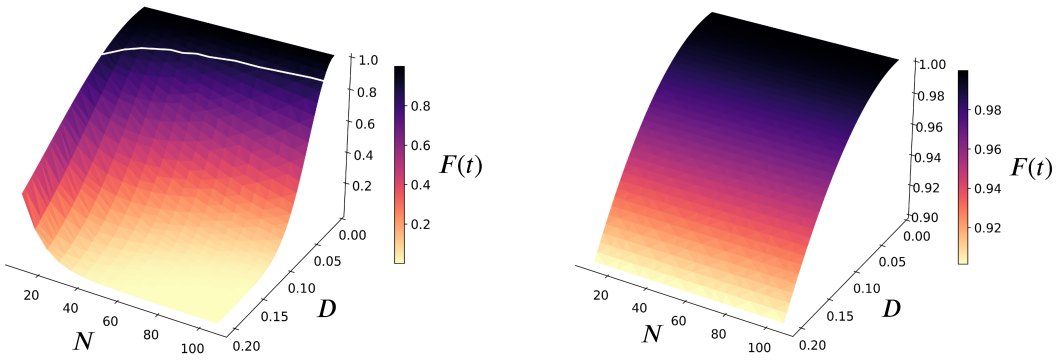

(a) $t_{d,\xi}$ **(b)** ξ_D

Figure 3.28: The robustness of the routing protocol when $F(t)$ is measured at $t = 2t_m$ in the presence of an error in the phase application time, $t_{d,\xi}$ (a), and an error in the angle of the applied phase, ξ_D (b). This is performed for various N values and error scales, D. The white line has the same meaning as in Fig. 3.22 but for the $F(t)$.

The design of our SN allows the routing of quantum information (here, single excitation) between distant qubits to be performed very well, even in the presence of high strengths of disorder. More importantly, the SN can be scaled up by cou-

pling together longer PST chains and still be used for routing. The robustness and scalability of our SN system is of potential utility in future quantum technologies. Specifically, our SN device could represent a promising candidate for future solid-state-based or matter-based quantum processes (e.g., trapped ions) that rely on the routing of quantum information between distant quantum resources.

Gaussian fitting function

We have seen in Section 3.3.4 that our SN system, when including diagonal and off-diagonal disorder, follows a Gaussian distribution as a function of the error strength E. We now investigate this in the case where the error is due to phase timing error and due to phase angle error.

The results shown in Fig.3.29 are for the routing robustness of a 6-site SN against phase timing error, Fig.3.29(a), and phase angle error, Fig.3.29(b). These clearly indicate that our SN behaviour against such errors also follows a Gaussian distribution, Eq.(3.19). The function $f(\mathrm{x})$ here is a function of the error scale, $f(D)$. The parameters for the Gaussian fit with phase timing error, Fig.3.29(a), are $a \approx 1$, $\overline{x} \approx 0.0013$, and $w \approx 0.22$. The parameters for the Gaussian fit with phase angle error, Fig.3.29(b) are $a \approx 1$, $\overline{x} \approx 0.0015$, and $w \approx 0.44$.

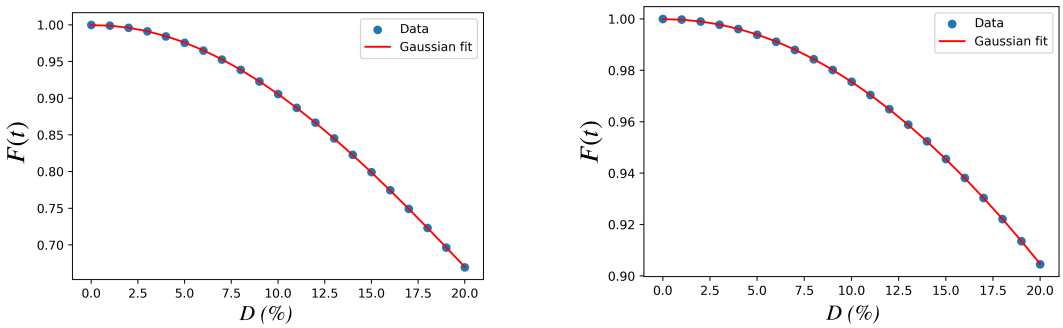

(a) $t_{d,\xi}$ **(b)** ξ_D

Figure 3.29: a) The robustness of the routing protocol against phase timing error when its fidelity is measured at $2t_m$ (blue dots) with a Gaussian fit (red line) for various error strengths D. b) The robustness of the routing protocol against phase angle error when its fidelity is measured at $2t_m$ (blue dots) with a Gaussian fit (red line) for various error strengths D.

Bipartite entanglement robustness

Similarly, we now investigate the robustness of the phase-based bipartite maximally entangled state between sites 1 and N for various sizes of SN. This is

achieved by computing $\overline{EOF}$ between sites 1 and N at $2t_m$ in the presence of both types of disorder, as shown in Fig.3.30.

In the presence of diagonal disorder, the $\overline{EOF}$ remains above 96% up to $N = 100$ with an error strength of $E = 5\%$, whereas it remains above 94% up to $N = 50$ with a larger error strength of $E = 10\%$. On the other hand, the robustness of the bipartite maximally entangled state to off-diagonal disorder shows that the $\overline{EOF} \gtrsim 92\%$ up to $N = 20$ with $E = 10\%$. For $N = 100$ and with smaller error strength of $E = 5\%$, we get $\overline{EOF} \approx 89\%$. This decays as N and E increase.

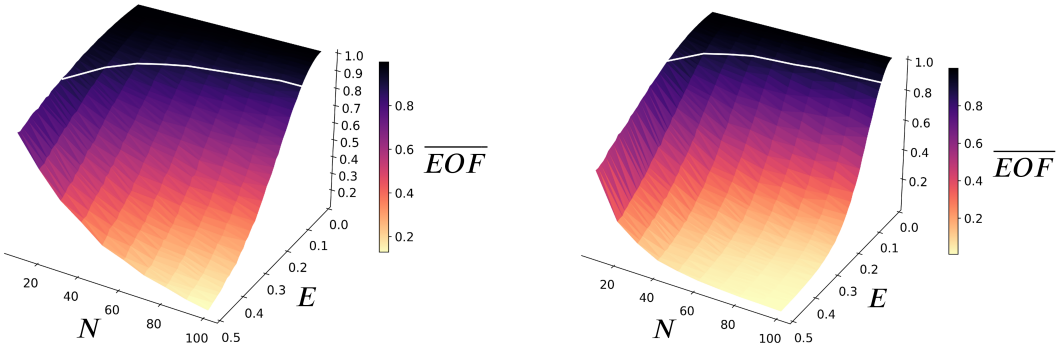

(a) Diagonal disorder **(b)** Off-diagonal disorder

Figure 3.30: The $\overline{EOF}$ between sites 1 and N at $t = 2t_m$ for different sizes of SN in the presence of diagonal (a) and off-diagonal (b) disorder with different error strengths, E. The white lines have the same meaning as in Fig. 3.23.

We now investigate the effects of the presence of phase timing error and phase angle error. In the presence of a phase application time error, Eq.(2.19), as per Fig.3.31a, the entanglement is found to be $EOF \approx 84\%$ for a relatively large timing error of $D = 10\%$ and with $N = 10$. High entanglement of $EOF > 98\%$ is observed for very small error scales: $D = 3\%$, $D = 2\%$, and $D = 1\%$ for $N = 10$, $N = 30$, and $N = 100$, respectively. In the presence of a phase angle error, Eq. (2.21), as per Fig.3.31b, the system is very robust, with the entanglement found to be $> 98\%$ with a relatively large error scale of $D = 10\%$ and $> 99.5\%$ with a smaller error of $D = 5\%$. Since the error is on the phase angle the EOF will always be the same, regardless of the SN size, N (see Fig.3.31b) as our SN achieve PST in the ideal case for any size of SN.

The ability of our SN to generate a bipartite maximally entangled state that is robust against disorder and with scalability (increasing N) makes it a potential candidate for quantum technology, potentially in applications relating to quantum networks where such an entangled state between the ends of the network is

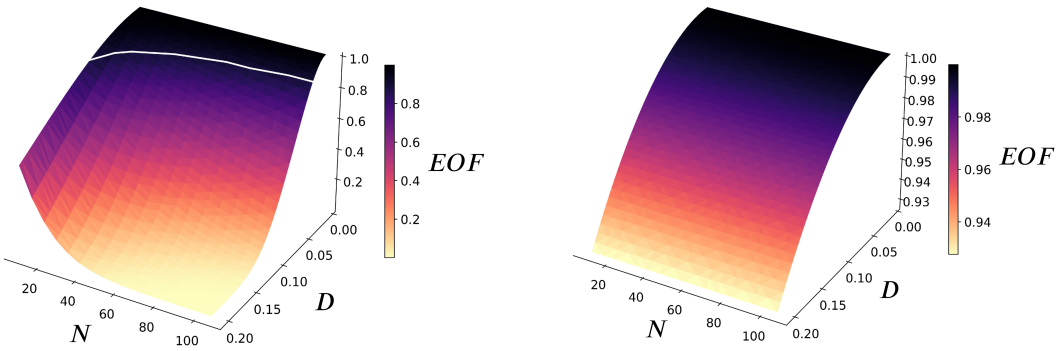

(a) $t_{d,\xi}$ **(b)** ξ_D

Figure 3.31: The robustness of the bipartite entanglement protocol when EOF is measured at $t = 2t_m$ in the presence of an error in the phase application time, $t_{d,\xi}$ (a), and an error in the angle of the applied phase ξ_D (b). This is performed for different values of N and for different error scales, D. The white line has the same meaning as in Fig. 3.23 but for the EOF.

required. This network of qubits should, of course, be a solid-state-type qubit.

Phase sensing robustness

In the presence of disorder, we use the phase sensing protocol proposed in Section 3.3.4 to investigate the robustness of sensing unknown phases in larger SN systems. Robustness is investigated with regard to diagonal and off-diagonal disorder and with large error strengths of $E = 5\%$ and $E = 10\%$, and for different SN sizes. A demonstration of the phase-sensing performance for a range of unknown angles from $0°$ to $360°$ in the presence of disorder, and for two SN systems of $N = 20$ and $N = 50$ is shown in Fig.3.32.

Interestingly, phase sensing is also robust against disorder in larger SN systems, particularly against diagonal disorder. For example, the retrieved angles in the presence of diagonal disorder remain very close to the angles obtained in the ideal case where there is no error. In the presence of off-diagonal disorder and with an error strength of $E = 5\%$, as per Fig.3.32(a,c), most of the retrieved angles are very close to their ideal case counterparts, with the exception of angles around $45°$, which show slight deviations from the ideal case, particularly for $N = 50$. In the case where $E = 10\%$ and in the presence of off-diagonal disorder, the retrieved angles slightly deviate from the actual unknown angles for $N = 20$, as per Fig.3.32(b), and deviate more for $N = 50$, as per Fig.3.32(d). These results can be understood by examining the standard deviation of the mean, $\sigma_{\overline{\theta}}$, which illustrates that $\sigma_{\overline{\theta}}$ fluctuates at a lower rate in the presence of diagonal disorder,

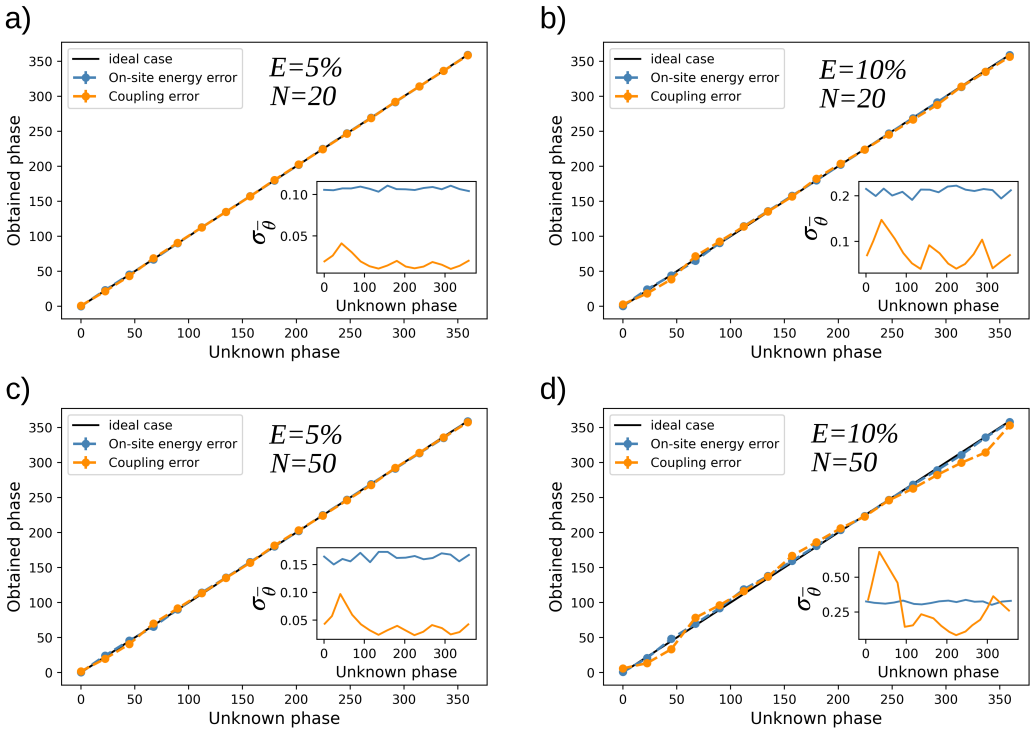

Figure 3.32: The obtained angles vs. the unknown angles, in degrees, with an error strength of $E = 5\%$ and SN of $N = 20$ (a), with an error strength of $E = 10\%$ and SN of $N = 20$ (b), with an error strength of $E = 5\%$ and SN of $N = 50$ (c), and with an error strength of $E = 10\%$ and SN of $N = 50$ (d). The results shown here are for: the error-free case (black line), the diagonal disorder case (blue line), and the off-diagonal disorder case (orange line). Inset: the mean standard deviation, $\sigma_{\bar{\theta}}$, of the retrieved angles.

.

while fluctuating at a higher rate with off-diagonal disorder.

The very good performance observed for both types of disorder with $E \leq 5\%$ implies that our SN has the potential to be used as a phase sensor device, even when the SN is scaled up to $N = 50$. For example, it can be used to obtain an unknown phase that is applied from a black box or from an uncontrolled source, so that the retrieved phase can be corrected. With respect to the effect of the scalability of our SN (increasing N) and the effect of increasing the error strength, E, it is clear that the latter has considerable impact on the system; a detailed discussion of such will be given below.

Analysis of the effect of error and scalability on the system

As observed above, the performance of the QIP protocols degrades as the error strength and system size (E and N, respectively) increase. This is because the SN

system is designed to deliver these protocols by exploiting the quantum interference amongst various amplitudes in the system, and therefore the presence of errors disturbs the interference, which in turn affects the quality of the desired task. For most protocols considered in this thesis, the value of the desired calculation (e.g., the fidelity) is at its maximum, in the error-free case. Consequently, small errors in the system parameters will result in the performance metric being affected only to second order, after the fidelity is expanded in a Taylor series with respect to the time around its maximum. This indicates that the effect on system performance when we scale the system by increasing the number of spins, N, while keeping the average amount of error small, is less than when we keep N constant and increase the average amount of error. Further increases in the error disturb the quantum interference and coherence in the system, which are responsible for delivering the desired operation. Ultimately, a significant amount of error can even lead to the case where excitations do not move, a process known as localisation [141]. For large N, the system becomes more susceptible to error, as the quantum interference that delivers the desired process involves more amplitudes. This description of how the performance of the protocols degrades with E and N applies to all the protocols in this thesis.

3.6 Summary

In this chapter, we have proposed a SN of equal chain lengths designed by coupling together two identical PST spin chains via a Hadamard-like unitary transformation. Useful QIP protocols, such as routing quantum information, bipartite entanglement generation, and quantum sensing have been realised in this SN. We then studied another SN of unequal chain lengths that was constructed by coupling together two PST spin chains, each of a different number of spins. Finally, we have also considered the scalability of our two-chain SN system (i.e., building larger two-chain SN systems by coupling together two long PST chains) and investigating its ability to generate the QIP protocols.

For the routing protocol, we showed that this can be achieved with a sudden phase flip operation at a given site and at a specific time. The physical representation of the phase application step depends on the system, as it could be performed by applying a focused laser (or magnetic field). In a system of superconducting transmon qubits, for example, this can be achieved using microwave pulses [151].

In Rydberg Cesium (Cs) atoms, on the other hand, the phase flip operation can be performed by applying a 459 nm laser [126].

For bipartite entanglement, we proposed two methods: the phase-based protocol and the natural generation protocol. The latter is straightforward and does not require intervention and is also more robust against disorder, so we suggest that it is advisable to use it for the generation of the bipartite entangled state. Both protocols (sudden phase, or natural evolution) result in a single excitation being shared between two sites, a sharing that is analogous to a beam splitter for a photon, which generates mode entanglement for a quantum optical system containing just a single photon [165–168].

Some of the QIP protocols shown here require the application of a phase factor at a specific site. However, when this is performed experimentally, neighbouring sites may also be affected by the phase application. Fortunately, there are advanced optical addressing technologies that indicate that the effect of the phase application on neighbouring sites can be significantly reduced [169,170]. These are implemented on ions-based systems, making them potentially useful for phase application protocols. High addressable single-site operations have also been demonstrated in Rydberg atoms [126,171–173].

In any practical realisation of these QIP protocols, the presence of disorder is inevitable, so we have therefore investigated the effects of disorder on them. The types of disorder considered here are diagonal disorder (on-site energy disorder), off-diagonal disorder (coupling disorder), phase timing error, and phase angle error. The phase timing error turns out to be the most damaging type of disorder and whose reduction should thus be the focus of experimentalists in physical systems. The reason that the phase timing error is most damaging is because the phase application step needs to be a sudden operation and an error on that should have much impact on the desired state. For other types of disorder, our SN seems highly robust, even when scalability is considered, for error strengths up to $E = 10\%$; it should be noted that useful devices are expected to have error strengths considerably lower than 10%. Moreover, the random errors generated from either Gaussian or flat distributions give results which are basically indistinguishable on the scale of the plot, when the performance metric (e.g., fidelity) is calculated for the first time the desired state forms. Furthermore, system robustness against phase angle error is independent of system size, N, as our SN is designed to deliver PST for any N in the ideal case. Finally, further investigation of the SN robustness

against these types of disorder shows that our SN behaviour follows a Gaussian distribution as a function of error scale parameter.

Chapter 4

Multi-chain spin networks

In this chapter, we construct and investigate another SN structure, that is, a SN system designed by coupling together multiple PST chains using our Hadamard-like transformation. We show that scaling the SN by connecting together multiple chains has advantages over an equivalent long spin chain. Moreover, we show that such complex structures of the SN allow the generation of different types of entangled states, together with the QIP protocols discussed in the previous chapter. All these applications are investigated against disorder.

Part of the work in this chapter has been published in [2]

To this point, we have examined a two-chain SN. A more general method of constructing the SN is by coupling together a large number of PST chains. The concept of connecting together multiple systems is known as modularisation, and has previously been used for modular entanglement [174] and high-fidelity QST [175]. Let us now proceed to a discussion of a multi-chain SN designed via unitary transformation of many USC.

Scaling the SN by connecting together multiple identical spin chains has an advantage over an equivalent long spin chain for the following reasons. It could be more accessible experimentally, depending on hardware, to prepare a system where the energy difference between the largest and the smallest coupling is small, and which is ultimately what multi-chain SN systems offer. This is because the energy difference between the largest and the smallest coupling for a multi-chain SN of size N is smaller than the energy difference for an equivalent long spin chain of size N. Another advantage that a multi-chain SN offers, at least for certain types of implementation, is that there are fewer different coupling values that need to be experimentally engineered. Moreover, the richer topology involved in such complex multi-chain SN systems allows us to generate multipartite maximally entangled states, along with the QIP protocols discussed in the previous chapter.

4.1 Three 3-site-chain SN

An example of a multi-chain SN is a SN designed by coupling together three PST chains, each consisting of three sites. This SN is constructed by applying a unitary transformation on the Hamiltonian of the three USC. The unitary used for this transformation is again a Hadamard-like unitary transformation that superposes two pairs of sites, specifically sites 3 and 4, and sites 6 and 7, which is given in the single-excitation basis as

$$U = \begin{pmatrix} 1 & 0 & 0 & 0 & 0 & 0 & 0 & 0 & 0 \\ 0 & 1 & 0 & 0 & 0 & 0 & 0 & 0 & 0 \\ 0 & 0 & \frac{1}{\sqrt{2}} & \frac{1}{\sqrt{2}} & 0 & 0 & 0 & 0 & 0 \\ 0 & 0 & \frac{1}{\sqrt{2}} & \frac{-1}{\sqrt{2}} & 0 & 0 & 0 & 0 & 0 \\ 0 & 0 & 0 & 0 & 1 & 0 & 0 & 0 & 0 \\ 0 & 0 & 0 & 0 & 0 & \frac{1}{\sqrt{2}} & \frac{1}{\sqrt{2}} & 0 & 0 \\ 0 & 0 & 0 & 0 & 0 & \frac{1}{\sqrt{2}} & \frac{-1}{\sqrt{2}} & 0 & 0 \\ 0 & 0 & 0 & 0 & 0 & 0 & 0 & 1 & 0 \\ 0 & 0 & 0 & 0 & 0 & 0 & 0 & 0 & 1 \end{pmatrix}. \tag{4.1}$$

The application of the unitary transformation on the three-USC Hamiltonian will therefore result in a Hamiltonian that represents the three 3-site-chain SN. The diagram that represents this SN is shown in Fig.4.1. We will now discuss how we can use this SN in various QIP applications.

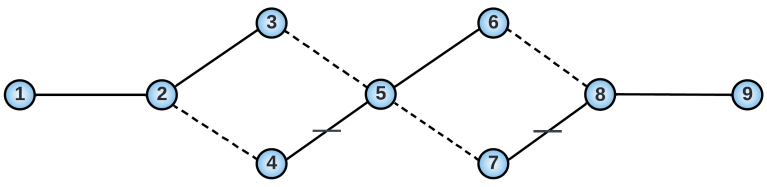

Figure 4.1: Diagram of the three-chain SN where each chain consists of three sites. The first chain (chain A) includes sites 1, 2, and 3. The second chain (chain B) includes sites 4, 5, and 6. The third chain (chain C) includes sites 7, 8, and 9.

.

4.1.1 Routing

Routing a single excitation from one end of the SN to the other, as discussed in the two-chain SN, only requires the application of a phase flip and natural evolution. This protocol can be applied in the three-chain SN. We start by injecting a single excitation at site 1 at $t = 0$ and evolve for a duration t_m. At this time, a sudden phase flip of $e^{i\pi} = -1$ is applied at site 4. The system is then left to evolve for another evolution of t_m, when another sudden phase flip is applied at site 7, at time $2t_m$. Then, with further evolution t_m, the excitation will be transferred completely to site 9 at $3t_m$. This is demonstrated in Fig.4.2.

Similarly, if we start by injecting a single-excitation state at site 9 at $t = 0$, we can route to site 1 following the same protocol.

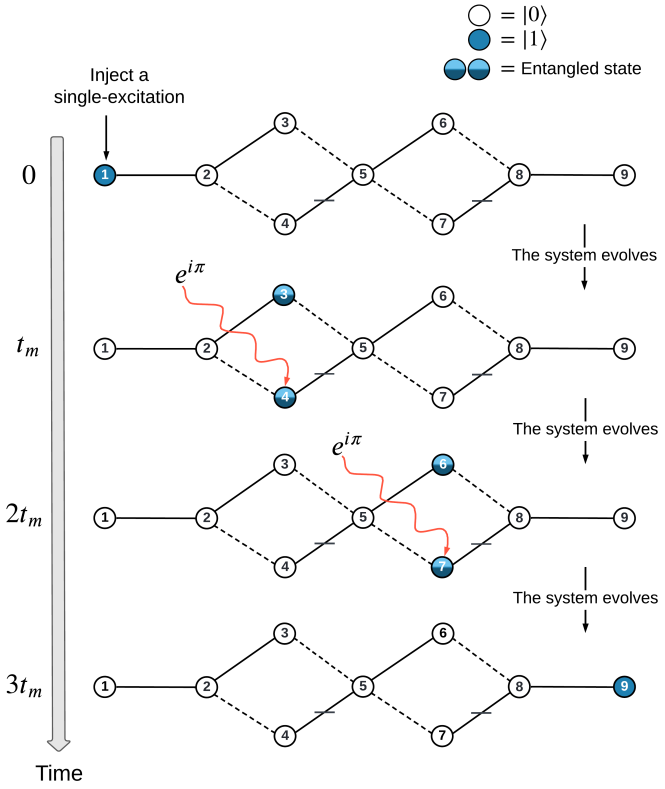

Figure 4.2: Demonstration of the routing protocol used to send a single-excitation from site 1 to site 9.

.

4.1.2 Tripartite entanglement generation

The quantum entangled state that represents an equally shared entanglement between three qubits is generally called W-state entanglement [102,103]. Let us refer

to this herein as Tripartite W-type State (TWS) entanglement to distinguish it from the various other types of W-state entanglement that will be discussed later.

This type of entangled state has various applications in quantum non-locality protocols [107], superdense coding [108], quantum teleportation protocols [109], and quantum secure direct communication [110]. Such TWS entanglement can be generated in our SN, as per Fig.4.1, as follows.

Starting with a single excitation injected at site 1 at $t = 0$ and evolving the system for a duration t_m, the excitation will be in a superposed state at sites 3 and 4. If a sudden phase of $e^{i\theta}$ is now injected at site 4, and the system is evolved for another duration t_m, the system state at $2t_m$ will be given by

$$|\Psi(2t_m)\rangle = \frac{1+e^{i\theta}}{2}|r_1\rangle + \frac{1-e^{i\theta}}{2\sqrt{2}}(|r_6\rangle + |r_7\rangle). \tag{4.2}$$

If the applied phase factor is $e^{i\phi}$, where $\phi = \arccos(-1/3)$, then the amplitudes of sites 1, 6, and 7 would be equal, which means a TWS entanglement has been formed between these sites.

Evolving the system further shows that the TWS entanglement will keep forming at each even t_m (i.e., $2t_m$, $4t_m$, $6t_m$, ...), as shown in Fig.4.3. A demonstration of the steps used to generate this entangled state is given in Fig.4.4.

The rich topology of the SN also allows us to generate the TWS entanglement between different sites, specifically sites 3, 4, and 9. This can be achieved following a protocol similar to that used above, in which we start by injecting a single excitation at site 9 at $t = 0$ and a sudden phase factor of $e^{i\phi}$ at site 7 at t_m.

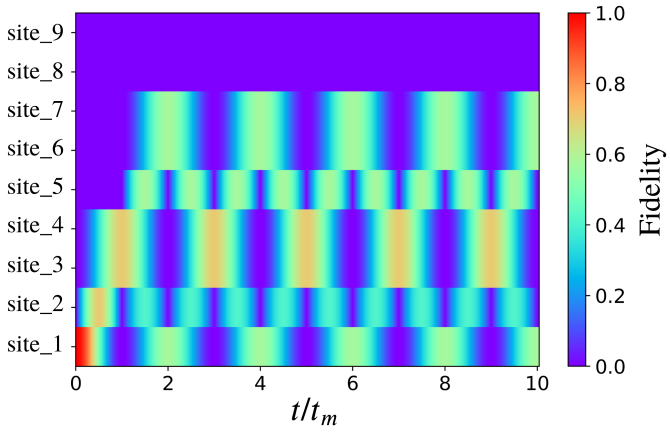

Figure 4.3: Fidelity of the system against each site as a function of the rescaled time t/t_m.

.

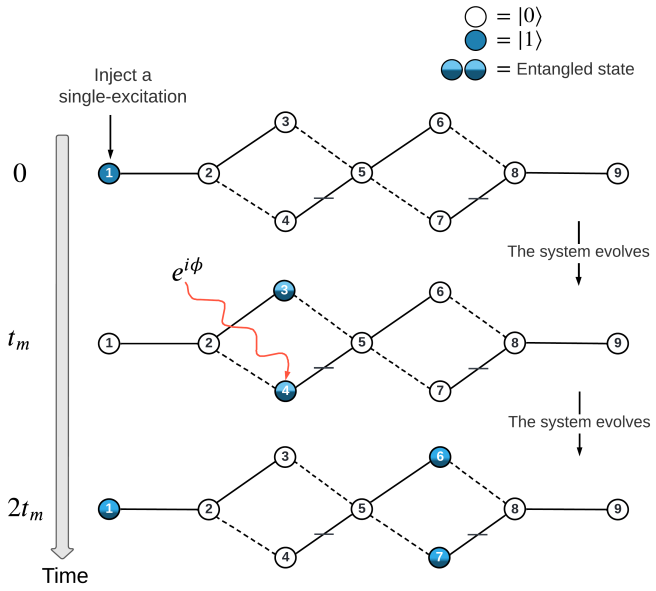

Figure 4.4: Demonstration of the TWS entanglement protocol. The phase applied at site 4 is $\phi = \cos^{-1}(-1/3)$.

.

4.1.3 Multipartite entanglement generation

The quantum-entangled state that represents an equally shared entanglement between four or more qubits is called Multipartite W-type State (MWS) entanglement [176]. Due to the topology involved in the three 3-site-chain SN, Fig.4.1, generating an example of MWS entanglement is straightforward and does not require application of a phase factor, as discussed below.

We can see in the SN that site 5 is directly coupled to the central vertices of the diamonds (i.e., sites 3, 4, 6, and 7). Therefore, a MWS entanglement can be generated between these sites simply by injecting a single excitation at site 5 at $t = 0$,

$$|\Psi(0)\rangle = |r_5\rangle\,, \tag{4.3}$$

and evolving the system for duration $t_m/2$. The resultant state will be a MWS entanglement, given as

$$|\Psi(t_m/2)\rangle = \frac{i}{2}(-|r_3\rangle + |r_4\rangle) - \frac{i}{2}(|r_6\rangle + |r_7\rangle)\,. \tag{4.4}$$

A demonstration of the steps used to generate the MWS entanglement is given in Fig.4.5. Evolving the system for further duration $t_m/2$ will return the excitation

to site 5. Thus, the excitation keeps evolving between Eq. (4.3) and Eq. (4.4) due to the periodicity of the system. The excitation evolution pattern can be changed with the application of a phase factor and can result in a different entangled state, as explained below.

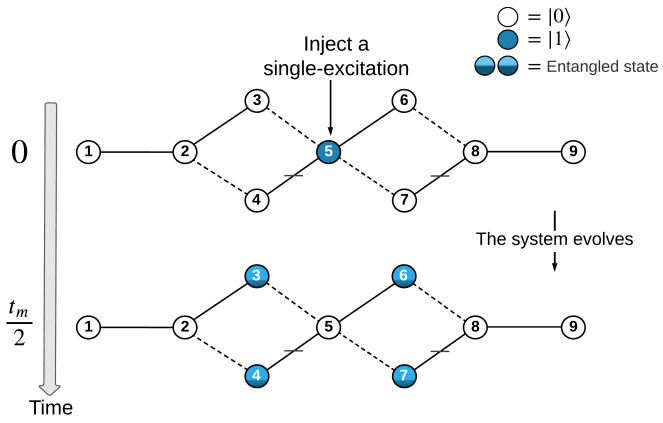

Figure 4.5: A simple injection of a single excitation at site 5 at $t = 0$ results in a MWS entanglement at $t_m/2$.

.

4.1.4 Bipartite entanglement generation

When the state is given as a MWS entanglement, Eq. (4.4), we can intervene by simultaneously applying two sudden phase flips at sites 4 and 7 at time $t_m/2$. This will flip the direction of the excitation evolution. Therefore, evolving the system for another duration of $t_m/2$ will result in a bipartite maximally entangled state between sites 1 and 9 at time $3t_m/2$

$$|\Psi(3t_m/2)\rangle = \frac{i}{\sqrt{2}}(|r_1\rangle + |r_9\rangle) \ . \tag{4.5}$$

The protocol used to generate the bipartite entanglement is shown in Fig.4.6.

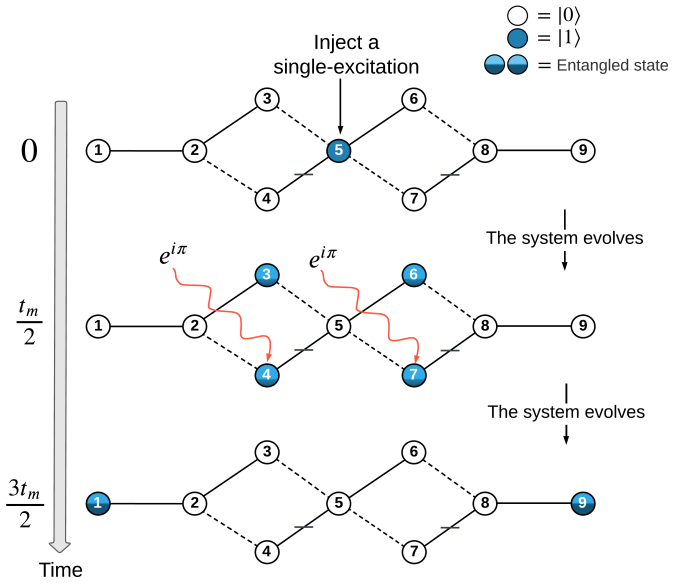

Figure 4.6: Bipartite entanglement is achieved by injecting a single excitation at site 5 at $t = 0$ and with sudden phase flips applied simultaneously at sites 4 and 7 at time $t_m/2$.

.

4.1.5 Effect of disorder

We will now consider the generation of the above protocols in the presence of disorder. This is achieved by applying the disorder type, diagonal or off-diagonal errors, to the Hamiltonian of the SN. We then perform the desired protocol for several realisations and calculate its performance metric (e.g., fidelity) under error. We also consider the errors that might arise in the protocols that are used to generate the desired states, such as phase timing error and phase angle error.

Router robustness

The router protocol is highly robust against diagonal disorder, where Fig.4.7 shows the averaged fidelity $\overline{F}(t) > 99.5\%$ with an error strength of $E = 10\%$, and $\overline{F}(t) > 98\%$ with a significant error strength of $E = 20\%$. A slightly lower robustness is observed for off-diagonal disorder, where the $\overline{F}(t) > 98\%$ with an error strength of $E = 10\%$, and $\overline{F}(t) > 93\%$ with a significant error strength of $E = 20\%$. This suggests that routing in the multi-chain SN is highly robust to both types of disorder and therefore has the potential for use in future technologies.

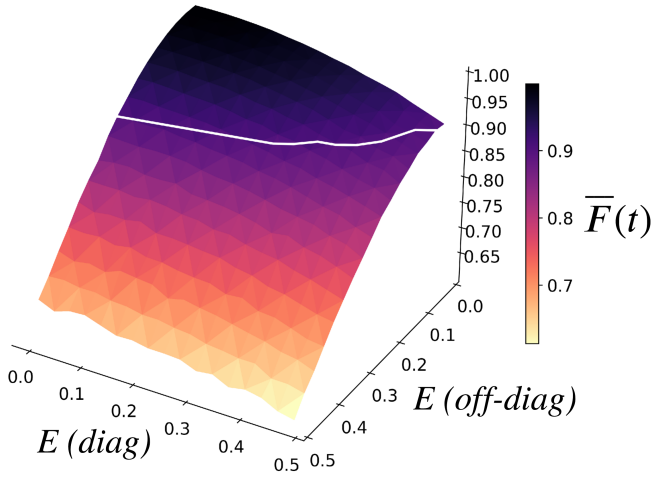

Figure 4.7: The robustness of the router protocol is investigated by calculating $\overline{F}(t)$ vs. $|r_9\rangle$ at time $3t_m$ in the presence of diagonal disorder (*diag*) and off-diagonal disorder (*off-diag*) with different error strengths, E, ranging from 0 to 50%. Each point has been averaged over 1000 realisations. The white line has the same meaning as in Fig. 3.22.

.

Investigation of the effects of another type of disorder, phase timing error, Eq.(2.19), shows that the system is very sensitive to this type of error, as per Fig.4.8a, as the fidelity was found to be $< 75\%$ with a timing error of $D = 10\%$. A high fidelity of $F(t) >= 95\%$ can be observed even with a very small timing error of $D <= 3.8\%$. The effect of the phase angle error, Eq.(2.21), on the other hand, as per Fig.4.8b, is much less damaging to the system, as the fidelity was found to be $> 95\%$ for an error scale of $D = 10\%$. For a smaller error of $D = 5\%$, the fidelity was observed to be $\approx 98.7\%$,.

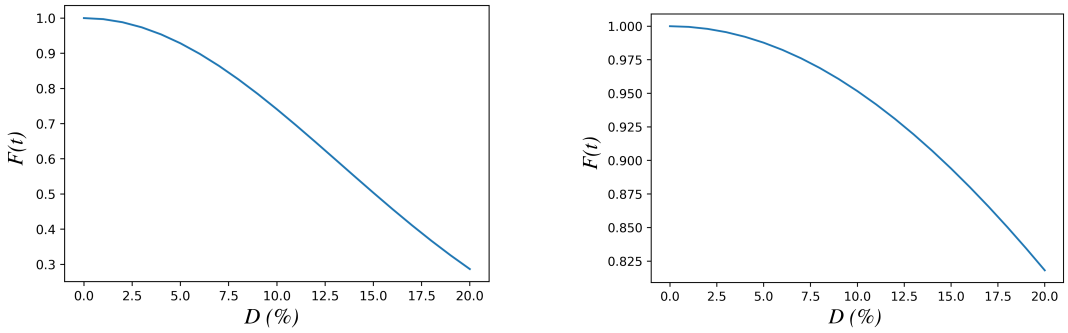

(a) $t_{d,\xi}$ **(b)** ξ_D

Figure 4.8: The robustness of the routing protocol when $F(t)$ is measured at time $3t_m$ in the presence of an error on the phase application at time $t_{d,\xi}$ (a) and an error of the angle of the applied phase, ξ_D (b). This was performed for various error scales, D, with a step size of 0.01.

TWS entanglement robustness

The robustness of the TWS entanglement was investigated by calculating the fidelity of the system at time $2t_m$ for a desirable state represented by a TWS entanglement between sites 1, 6, and 7, as per Fig.4.9. In the presence of diagonal disorder, the TWS entanglement is, in fact, very robust as $\overline{F}(t) > 99.6\%$ with an error strength of $E = 10\%$, and $\overline{F}(t) > 98\%$ with a relatively large error strength of $E = 20\%$. In the presence of a the more damaging type of disorder, that is, off-diagonal disorder, TWS entanglement was still robust as $\overline{F}(t) > 98.5\%$ with an error strength of $E = 10\%$. For a higher error strength of $E = 20\%$, the fidelity was observed to be $\overline{F}(t) > 95.5\%$, but which then decays rapidly as E increases.

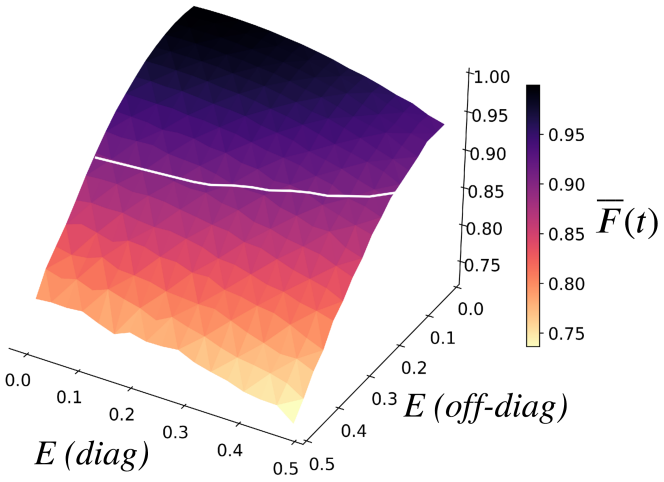

Figure 4.9: The robustness of the TWS entanglement at time $2t_m$ (the first time the TWS is formed) against diagonal disorder (*diag*) and off-diagonal disorder (*off-diag*) with various error strengths, E, ranging from 0 to 50%. Each point has been averaged over 1000 realisations. The white line has same meaning as in Fig. 3.22

..

The robustness of the TWS entanglement to phase timing error, Eq.(2.19), as per Fig.4.10a, was found to be $> 97.5\%$ for a timing error of $D = 5\%$, and $\approx 93.5\%$ for a higher timing error of $D = 10\%$. In the presence of phase angle error, Eq.(2.21), as per Fig.4.10b, TWS entanglement was found to be $> 99.7\%$ for a timing error of $D = 5\%$, and $> 99\%$ for a higher timing error of $D = 10\%$.

Bipartite entanglement robustness

The robustness of the bipartite maximally entangled state generated between sites 1 and 9 was investigated by calculating the $\overline{EOF}$ between these sites, as per Fig.4.11. Excellent robustness was observed to diagonal disorder, where the

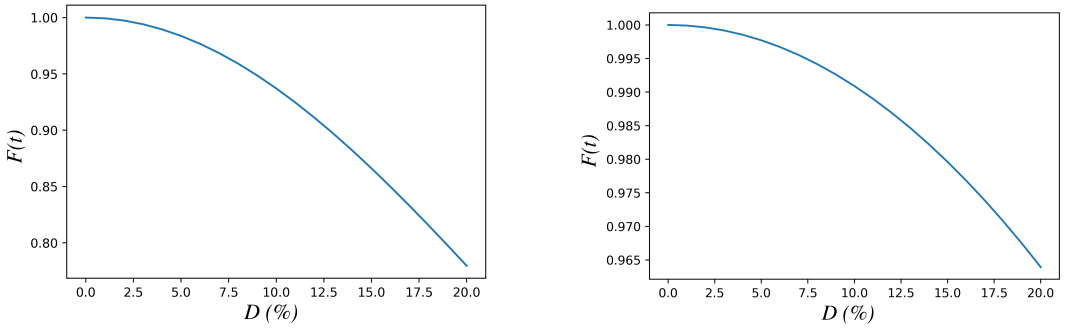

(a) $t_{d,\xi}$ **(b)** ξ_D

Figure 4.10: The robustness of the TWS entanglement at time $2t_m$ in the presence of an error on the phase application time, $t_{d,\xi}$ (a), and an error on the angle of the applied phase, ξ_D (b). This was performed for different error scales, D, with a step size of 0.01.

$\overline{EOF} > 99.6\%$ with an error strength of $E = 10\%$, and the $\overline{EOF} \approx 99\%$ with significant error strength of $E = 20\%$. The robustness to off-diagonal disorder with an error strength of $E \leq 10\%$ is observed to have entanglement of $\overline{EOF} > 98.7\%$, whereas for the higher error strength of $E = 20\%$ we get $\overline{EOF} \approx 95\%$. The strong robustness observed in the three 3-site-chain SN for generating various QIP protocols makes our SN a promising platform for future solid state-based quantum devices.

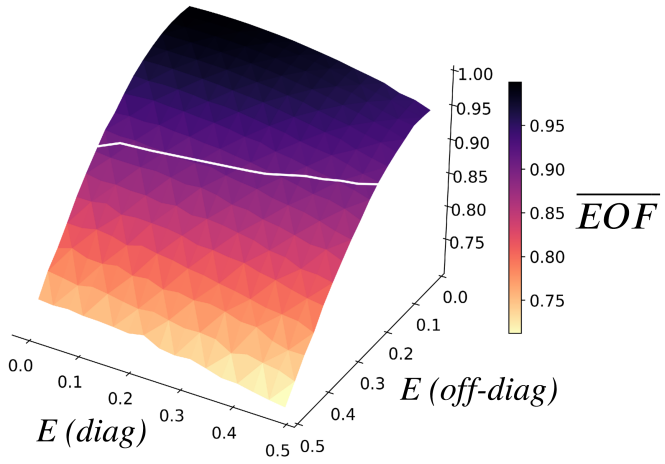

Figure 4.11: The robustness of the bipartite maximally entangled state at $3t_m/2$ (the first time it forms) against diagonal (*diag*) and off-diagonal disorder (*off-diag*) with various error strengths, E, ranging from 0 to 50%. Each point has been averaged over 1000 realisations. The white line has the same meaning as in Fig. 3.23

. .

The robustness of bipartite entanglement against phase timing error, Eq.(2.19), as illustrated in Fig.4.12a, was found to be $\approx 98\%$ for a timing error of $D = 5\%$,

and $> 94\%$ for a larger timing error of $D = 10\%$. In the presence of a phase angle error, Eq.(2.21), as seen in Fig.4.12b, the bipartite entanglement was found to be $> 99\%$ for a timing error of $D = 5\%$, and $> 96\%$ for a larger timing error of $D = 10\%$.

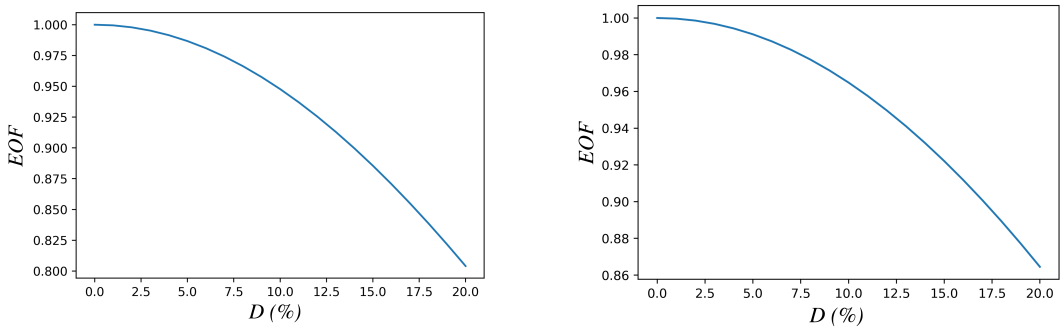

(a) $t_{d,\xi}$ **(b)** ξ_D

Figure 4.12: The robustness of bipartite entanglement at time $3t_m/2$ in the presence of an error in the phase application time, $t_{d,\xi}$ (a), and an error in the angle of the applied phase, ξ_D (b). This was performed for various error scales, D, with a step size of 0.01.

4.2 Three 4-site-chain SN

The multi-chain SN discussed above can be formed by coupling together three chains, each of an odd number of sites (three sites). Let us now construct and investigate another SN system where the number of sites in each chain is even. Using the same unitary construction method discussed above, we couple three USC, each of four sites. Let us label the three USC chains with letters: chain A consists of sites 1, 2, 3, and 4; chain B consists of sites 5, 6, 7, and 8, and chain C consists of sites 9, 10, 11, and 12. The Hadamard-like unitary used to connect these chains superposes sites 4 and 5 as well as sites 8 and 9. The resultant SN is the three 4-site-chain SN shown in Fig.4.13.

Operating this SN as a router can be achieved using the routing protocol discussed in Section 4.1.1. We start by injecting a single excitation at site 1 at $t = 0$ and applying the phase flip $e^{i\pi}$ at site 5 at t_m, and a further phase flip at site 9 at $2t_m$. The excitation will then be transferred completely to site 12 at $3t_m$. We can also use this SN to realise various entangled state, as we describe below.

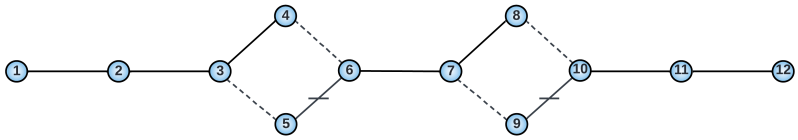

Figure 4.13: Diagram of a three 4-site-chain SN.

.

4.2.1 Tripartite entanglement generation

TWS entanglement can also be generated in this SN by applying the protocol shown in Fig.4.4. We start with a single excitation at site 1 at $t = 0$ and evolve the system for a duration of t_m. At this time, a sudden phase factor $e^{i\phi}$ is applied at site 5 and the system is evolved for another duration of t_m. The state of the system at $2t_m$ will thus be given by

$$|\Psi(2t_m)\rangle = -\frac{1+e^{i\phi}}{2}|r_1\rangle - \frac{1-e^{i\phi}}{2\sqrt{2}}(|r_8\rangle + |r_9\rangle). \tag{4.6}$$

This is an equal superposition between sites 1, 8, and 9, which represents a TWS entanglement. Similarly, a TWS entanglement can also be generated between sites 4, 5, and 12 by injecting a single excitation at site 12 at $t = 0$ and a sudden phase factor of $e^{i\phi}$ at site 9 at t_m.

4.2.2 Multipartite entanglement generation

We have seen that generating an example of MWS entanglement in the three 3-site-chain SN (Fig.4.1) can be achieved by a simple initial injection at a given site (site 5 in Fig.4.1) that shares direct couplings with four sites. However, this is not the case in the three 4-site-chain SN (Fig.4.13) as there is no site that is coupled with four sites. As a result, we propose another protocol that can be used to generate the MWS entanglement in the three 4-site-chain SN.

The MWS entanglement we seek to generate is an equally shared entanglement between sites 4, 5, 8, and 9 in the SN shown in Fig.4.13. In order to do so, we need to adjust the maximum coupling of chain B ($J_{max,B}$) such that the excitation evolution time through chain B is slower by half compared to the excitation evolution time through chain A. This can be achieved by setting $J_{max,B} = 1/2$. As a result, the relation between the mirroring times of chains A and B is given

by $t_{m,B} = 2t_{m,A}$. The reason for making $t_{m,B}$ slower by half, compared to $t_{m,A}$ or $t_{m,C}$, will be made clear below.

We now start with a single excitation injected at site 5 at $t = 0$

$$|\Psi(0)\rangle = |r_5\rangle\,, \tag{4.7}$$

and let the system to evolve. The excitation will evolve through chain A and chain B. Over a period of $2t_{m,A}$, the excitation amplitude that evolves through A would have evolved to site 1 and returned back to a superposed state between sites 4 and 5, whereas the other excitation amplitude that evolves through B would have evolved to being in a superposed state between sites 8 and 9. This is because of the fact that $2t_{m,A} = t_{m,B}$. The resultant state at $2t_{m,A}$ is therefore a MWS entanglement between sites 4, 5, 8, and 9

$$|\Psi(2t_{m,A})\rangle = -\frac{1}{2}(|r_4\rangle + |r_5\rangle) - \frac{i}{2}(|r_8\rangle + |r_9\rangle). \tag{4.8}$$

Evolving the system for further duration of $2t_{m,A}$ shows that the excitation collapses to being entirely localised at site 4 at a time $4t_{m,A}$

$$|\Psi(4t_{m,A})\rangle = |r_4\rangle\,. \tag{4.9}$$

Note that the excitation does not return to its initial state (i.e., being localised at site 5) at $4t_{m,A}$. The reason for this is attributed to the time difference of the excitation amplitude evolution through chains A and B. This difference in the evolution time through each chain leads to different phases, which in turn results in destructive interference (see appendix D).

Evolving the system for a further duration $2t_{m,A}$, the state of the system at $6t_{m,A}$ will be given as a MWS entanglement but with a relative phase difference compared to the one given in Eq. (4.8)

$$|\Psi(6t_{m,A})\rangle = -\frac{1}{2}(|r_4\rangle + |r_5\rangle) + \frac{i}{2}(|r_8\rangle + |r_9\rangle). \tag{4.10}$$

Under a further evolution of $2t_{m,A}$, the excitation will finally evolve back to its initial state, at a time $8t_{m,A}$

$$|\Psi(8t_{m,A})\rangle = |r_5\rangle\,. \tag{4.11}$$

The detailed evolution of the dynamics of this excitation as a function of time through the SN can be seen from a colourmap showing the fidelity of the system against each site as a function of time; see Fig.4.14.

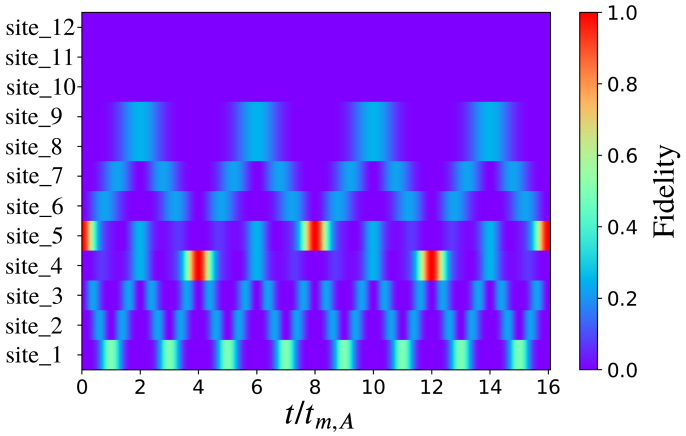

Figure 4.14: The fidelity of the system against each site vs. the rescaled time, $t/t_{m,A}$, shows that the MWS entanglement is periodic.

.

4.2.3 Bipartite entanglement generation

We now wish to generate a bipartite maximally entangled state between the ends of the three 4-site-chain SN shown in Fig.4.13. With the maximum couplings for all the chain being equal (i.e., $J_{max,A} = J_{max,B} = J_{max,C}$), it is not possible to achieve the bipartite maximally entangled state. Therefore, we need to first adjust the maximum coupling of chain B to be $J_{max,B} = 1/2$. As a result, the mirroring times of each chain are given by $t_{m,B} = 2t_{m,A} = 2t_{m,C}$.

Having established this, we now inject a single excitation at site 5 at $t = 0$ and let the system evolve for a duration $2t_{m,A}$. The state will therefore be given in Eq. (4.8). If a sudden phase flip is applied at site 9 and the system is evolved for a time $t = t_{m,A}$, a bipartite maximally entangled state will be formed between sites 1 and 12 at time $3t_{m,A}$

$$|\Psi(3t_{m,A})\rangle = \frac{-1}{\sqrt{2}}(i\,|r_1\rangle - |r_{12}\rangle)\,. \tag{4.12}$$

This illustrates how changing the J_{max} of one of the chains of the SN allows timing evolution to be appropriately controlled in order to deliver a desired operation.

4.2.4 Effects of disorder

TWS entanglement robustness

The robustness of the TWS entanglement against diagonal and off-diagonal disorder is shown in Fig.4.15. A very strong robustness is observed in the presence of diagonal disorder, where the average fidelity, $\overline{F}(t)$, at $2t_m$ remains $> 99.5\%$, and $> 98\%$ with error strengths of $E = 10\%$ and $E = 20\%$, respectively. In the presence of off-diagonal disorder and with an error strength of $E \leq 10\%$, the averaged fidelity $\overline{F}(t)$ remains $> 98\%$, while for a higher error strength of $E = 20\%$, the average fidelity remains $> 92\%$, but which decays as E increases. Overall, strong robustness of the TWS entanglement is observed as long as $E \leq 10\%$, giving our SN the potential to be used for practical TWS entanglement generation.

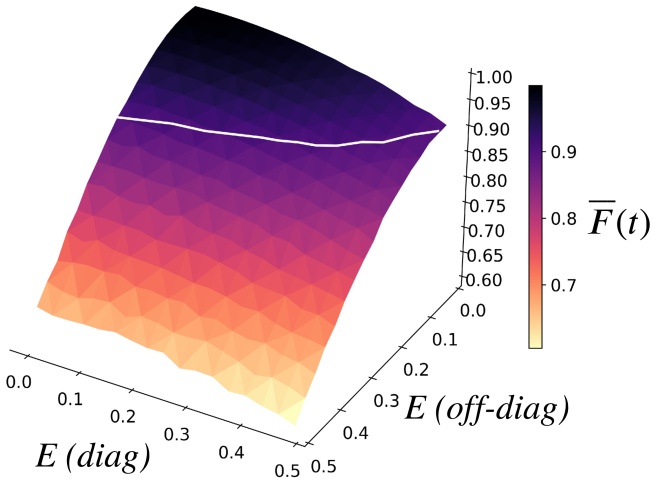

Figure 4.15: The robustness of the TWS entanglement against diagonal (*diag*) and off-diagonal disorder (*off-diag*) with various error strengths, E, ranging from 0 to 50%. Each point has been averaged over 1000 realisations. The white line has the same meaning as in Fig. 3.22.

The robustness of the TWS entanglement against phase timing error, Eq.(2.19), as per Fig.4.16a, was found to be $\approx 97.5\%$ for a timing error of $D = 5\%$, and $> 90\%$ for a larger timing error of $D = 10\%$. In the presence of phase angle error, Eq. (2.21), as per Fig.4.16b, the TWS entanglement robustness was found to be very strong, with $F(t) > 99.75\%$ for a timing error of $D = 5\%$, and $> 99\%$ for a larger timing error of $D = 10\%$.

We now investigate the case where the error on the TWS entanglement is attributed to the measurement-time error. This means that the TWS entanglement is measured (calculated) at a different time, so instead of measuring the TWS at

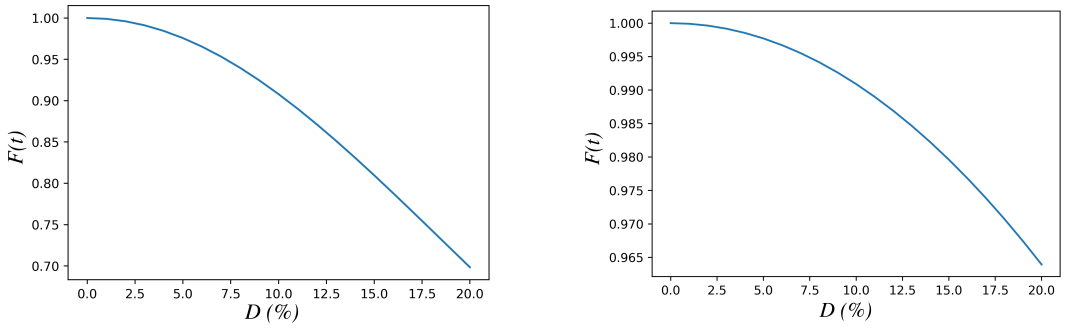

(a) $t_{d,\xi}$ **(b)** ξ_D

Figure 4.16: The robustness of the TWS entanglement at time $2t_m$ in the presence of an error in the phase application time, $t_{d,\xi}$ (a), and an error in the angle of the applied phase, ξ_D (b). This is performed for different error scales, D, with a step size of 0.01.

$2t_m$, it is now measured at $2t_m + D2t_m$, where D, as defined in Section 2.3.3, represents a dimensionless error scale ($-0.2 \leq D \leq 0.2$).

The robustness of the TWS entanglement against measurement-time error is shown in Fig.4.17. Excellent robustness of $> 97.5\%$ is observed with a measurement-time error of $D = 5\%$, while for $D = 10\%$, the robustness is observed to be $\approx 92.5\%$. This result shows that the effect of the measurement-time error is less damaging compared to the effect of the phase timing error.

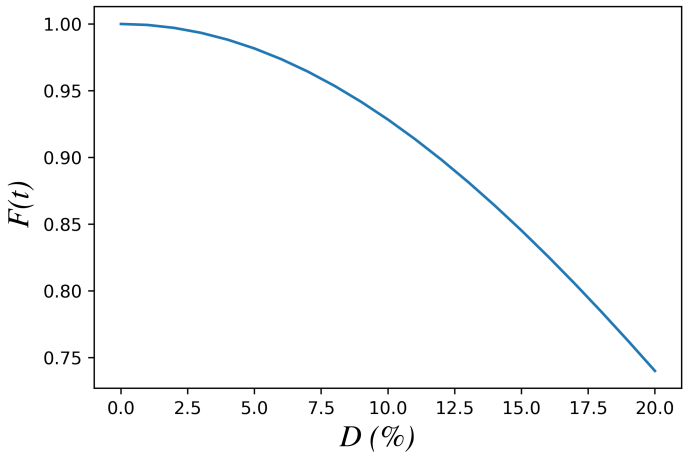

Figure 4.17: The robustness of TWS entanglement against measurement-time error. This was performed for different error scales, D, with a step size of 0.01.

.

MWS entanglement robustness

The robustness of the MWS entanglement generated at time $2t_{m,A}$, as per Eq.(4.8), against diagonal and off-diagonal disorder is shown in Fig.4.18. We note that the MWS entanglement was also very robust, as the average fidelity $\overline{F}(t)$ against the

diagonal disorder and with $E = 10\%$ remained $> 99.5\%$, whereas it remained $> 98\%$ with a larger error strength of $E = 20\%$. A reduced robustness was observed against off-diagonal disorder where the average fidelity remained $> 98.3\%$ and $\approx 94\%$ with error strengths of $E = 10\%$ and $E = 20\%$, respectively.

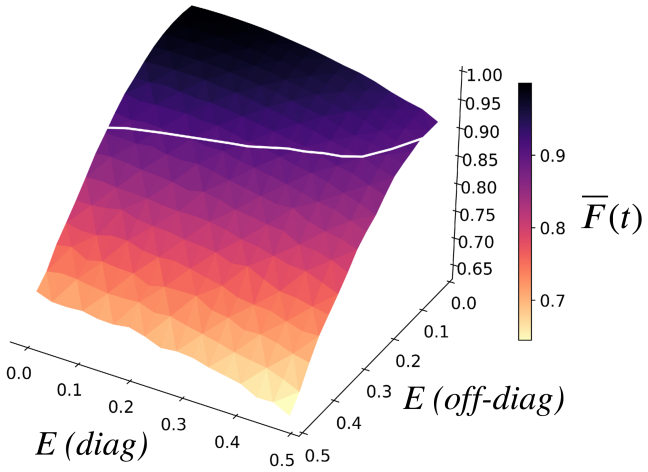

Figure 4.18: Robustness of MWS entanglement against diagonal (*diag*) and off-diagonal disorder (*off-diag*) with various error strengths, E, ranging from 0 to 50%. Each point has been averaged over 1000 realisations. The white line has same meaning as in Fig. 3.22.

.

The robustness of the MWS entanglement against measurement-time error is shown in Fig.4.19. With a measurement-time error of $D = 5\%$, the MWS entanglement is found to be $\approx 95\%$, whereas lower robustness of $\approx 82\%$ is observed for an error of $D = 10\%$.

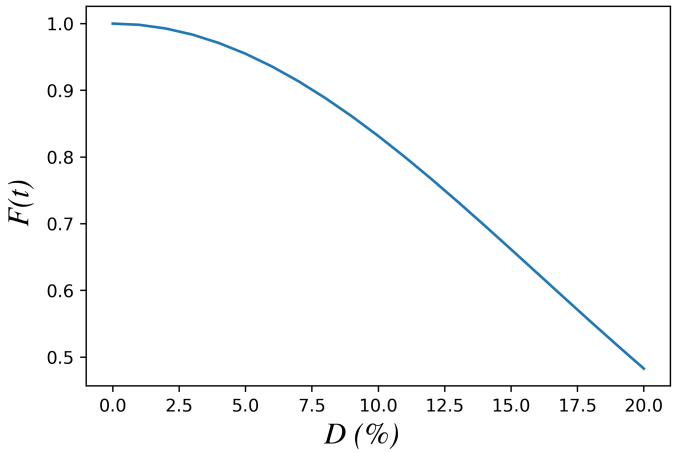

Figure 4.19: The robustness of MWS entanglement against measurement-time error. This was performed for different error scales, D, with a step size of 0.01.

.

Bipartite entanglement robustness

The robustness of the bipartite entanglement generated at time $3t_{m,A}$, Eq.(4.12), against diagonal and off-diagonal disorder is shown in Fig.4.20. The bipartite entanglement was very robust against diagonal disorder as $\overline{EOF} > 99\%$ with an error strength of $E = 10\%$ and $\overline{EOF} > 96\%$ with a significant error strength of $E = 20\%$. A lower robustness was observed in the presence of off-diagonal disorder as $\overline{EOF} > 95\%$ with an error strength of $E = 10\%$ and $\overline{EOF} \approx 82\%$ with a larger error strength of $E = 20\%$.

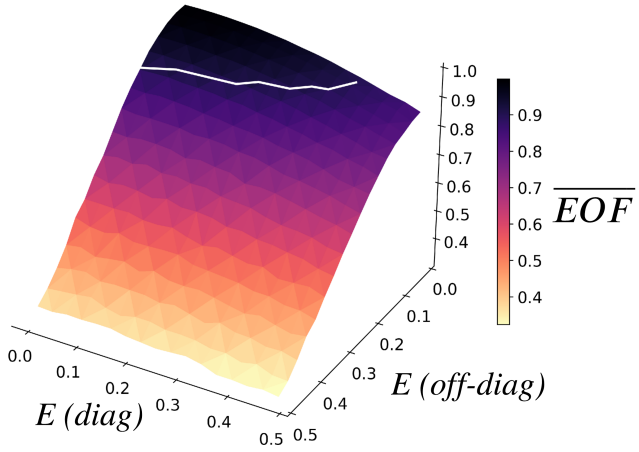

Figure 4.20: The robustness of the bipartite maximally entangled state generated at time $3t_{m,A}$ against diagonal (*diag*) and off-diagonal disorder (*off-diag*) with various error strengths, E, ranging from 0 to 50%. Each point has been averaged over 1000 realisations. The white line has the same meaning as in Fig. 3.23.

The robustness of the bipartite entanglement against phase timing error, Eq.(2.19), as per Fig.4.21a, was found to be $> 93\%$ for a timing error of $D = 5\%$, and $> 75\%$ for a larger timing error of $D = 10\%$. In the presence of phase angle error, Eq. (2.21), as per Fig.4.21b, the bipartite entanglement was found to be $> 99.5\%$ for a timing error of $D = 5\%$, and $> 98\%$ for a larger timing error of $D = 10\%$.

The robustness of the bipartite entanglement against measurement-time error is shown in Fig.4.22. With a measurement-time error of $D = 5\%$, the bipartite entanglement is found to be $\approx 97.5\%$, while for an error of $D = 10\%$, the bipartite entanglement is found to be $\approx 90\%$.

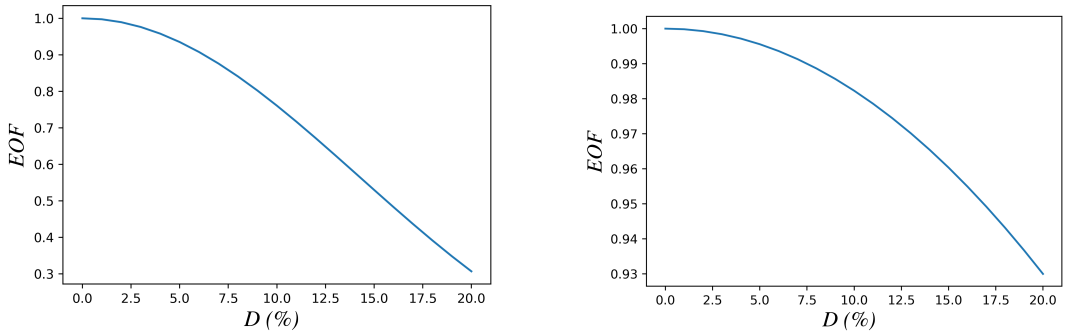

(a) $t_{d,\xi}$ **(b)** ξ_D

Figure 4.21: The robustness of the bipartite entanglement at time $3t_{m,A}$ in the presence of an error in the phase application time, $t_{d,\xi}$ (a), and an error in the angle of the applied phase, ξ_D (b). This is performed for different error scales, D, with a step size of 0.01.

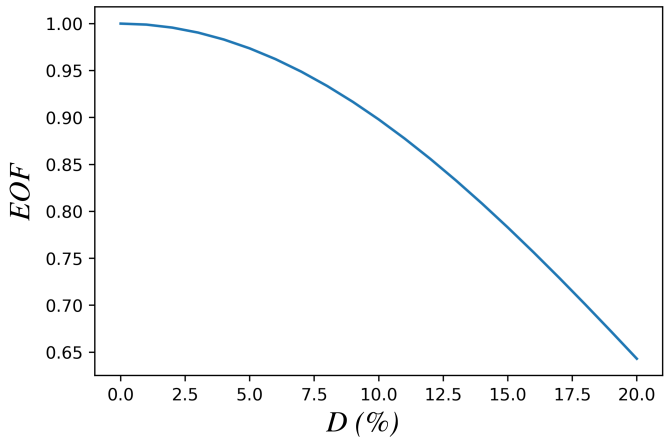

Figure 4.22: The robustness of bipartite entanglement against measurement-time error. This was performed for different error scales, D, with a step size of 0.01.

.

4.3 M 3-site-chain SN

Thus far, we have investigated the SN of three chains. Here, we demonstrate the possibility of generalising the results to even more complex and larger SN systems. Constructing such SN system is again achieved by coupling together M USC using the Hadamard-like unitary transformation. An example of an M-chain SN, where each chain constitutes three sites, is shown in Fig.4.23 for the case of $M = 5$.

Routing here (i.e., sending a single excitation from site 1 to site 15, or vice versa) can be achieved using an extension of the router protocol discussed above. If we start by injecting a single excitation at site 1 at $t = 0$, the excitation will evolve to the central vertices of the first diamond (i.e., superposition between sites

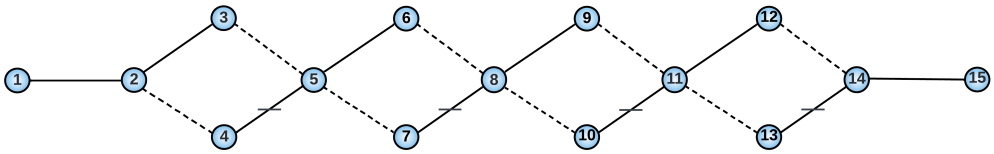

Figure 4.23: Diagram of a SN of five chains, each constituting three sites.

.

3 and 4) at time t_m, then it will evolve back to site 1 at time $2t_m$. Therefore, in order to route the excitation, we intervene at time t_m (the time at which the excitation is in a superposed state between sites 3 and 4) by injecting a sudden phase flip at site 4, which forces the excitation to continue evolving forward. The application of the phase must be repeated at different sites and at different times, as it is required to route the excitation each time the excitation is located at the central vertices of a diamond: at site 7 at time $2t_m$, at site 10 at time $3t_m$, and at site 13 at time $4t_m$.

TWS entanglement can also be generated in this SN between sites 1, 6, and 7 following the protocol shown in Fig.4.4. This is achieved by starting with the injection of a single excitation at site 1 at time $t = 0$ and a phase factor of $e^{i\phi}$ at site 4 at time t_m. Similarly, we can generate the TWS entanglement between sites 9, 10, and 15 by injecting a single excitation at site 15 at time $t = 0$ and a phase factor of $e^{i\phi}$ at site 13 at time t_m.

4.3.1 Multipartite entanglement generation

Generating a MWS entanglement in this SN is straightforward and can be achieved between any four sites at the vertices of the diamonds. This is due to the rich topology involved in the SN, as per Fig.4.23. We will now illustrate every achievable MWS entanglement that can be generated here. These methods of generating MWS entanglement are applicable to longer 3-site-chain SN systems in the same way.

We start by injecting a single excitation at site 5 at time $t = 0$ and evolve the system for a duration of $t_m/2$, where a MWS entanglement will be formed between sites 3, 4, 6, and 7, which is given by

$$|\Psi(t_m/2)\rangle = \frac{-i}{2}(|r_3\rangle - |r_4\rangle + |r_6\rangle + |r_7\rangle). \tag{4.13}$$

Similarly, if we start by injecting a single excitation at site 8 and evolve the system for a duration of $t_m/2$, a MWS entanglement will be formed between sites 6, 7, 9, and 10. a MWS entanglement between sites 9, 10, 12, and 13 can also be generated by starting injecting a single excitation at site 11 at time $t = 0$ and evolving for a duration $t_m/2$. These are all the achievable MWS entanglements that can be generated by injecting a single excitation at sites that are coupled with four other sites. Note that because of the periodicity of our SN, any MWS will evolve back to its initial state and keep oscillating back and forth.

In addition to generating MWS entanglement between close sites (e.g., sites 3, 4, 6, and 7), we can also generate MWS entanglement between distant sites. For example, when a single excitation is injected at site 6 at time $t = 0$ and the system is allowed to evolve for a duration t_m then a MWS entanglement between sites 3, 4, 9, and 10 will be formed, which is given by

$$|\Psi(t_m)\rangle = \frac{-1}{2}(|r_3\rangle - |r_4\rangle + |r_9\rangle + |r_{10}\rangle). \tag{4.14}$$

Note that we can instead inject the excitation at site 7 and still achieve the MWS entanglement but with different phases for the MWS components. Similarly, MWS entanglement between sites 6, 7, 12, and 13 can be generated by injecting a single excitation at either site 9 or 10 at time $t = 0$ and evolving the system for a duration t_m.

4.3.2 Multipartite entanglement transfer

The complex structure of the SN allows us to generate and transfer a MWS entanglement through the SN, forming a MWS entanglement between distant sites (sites 3, 4, 12, and 13). This can be achieved by exploiting the application of a phase flip, as described below.

We start by injecting a single excitation at site 8 at time $t = 0$ and evolve the system for a duration $t_m/2$. We then apply two simultaneous phase flips at sites 7 and 10 which, allowing for a further evolution of t_m, will result in the MWS entanglement between sites 3, 4, 12, and 13, given by

$$|\Psi(3t_m/2)\rangle = \frac{i}{2}(|r_3\rangle - |r_4\rangle + |r_{12}\rangle + |r_{13}\rangle). \tag{4.15}$$

The steps used to generate this entangled state are illustrated in Fig.4.24. The system will then keep evolving between MWS entanglement of sites 3, 4, 12, and

13 and MWS entanglement of sites 6, 7, 9, and 10, as shown in the plot of the fidelity of each site, Fig.4.25. A table summarising all the types of entanglement generated in this SN is given in Fig.4.26.

Note that when the state of the system is as given at time $3t_m/2$ in Fig.4.24, then an application of two simultaneous phase flips at sites 4 and 13 will result in a bipartite maximally entangled state between sites 1 and 15 at time $2t_m$.

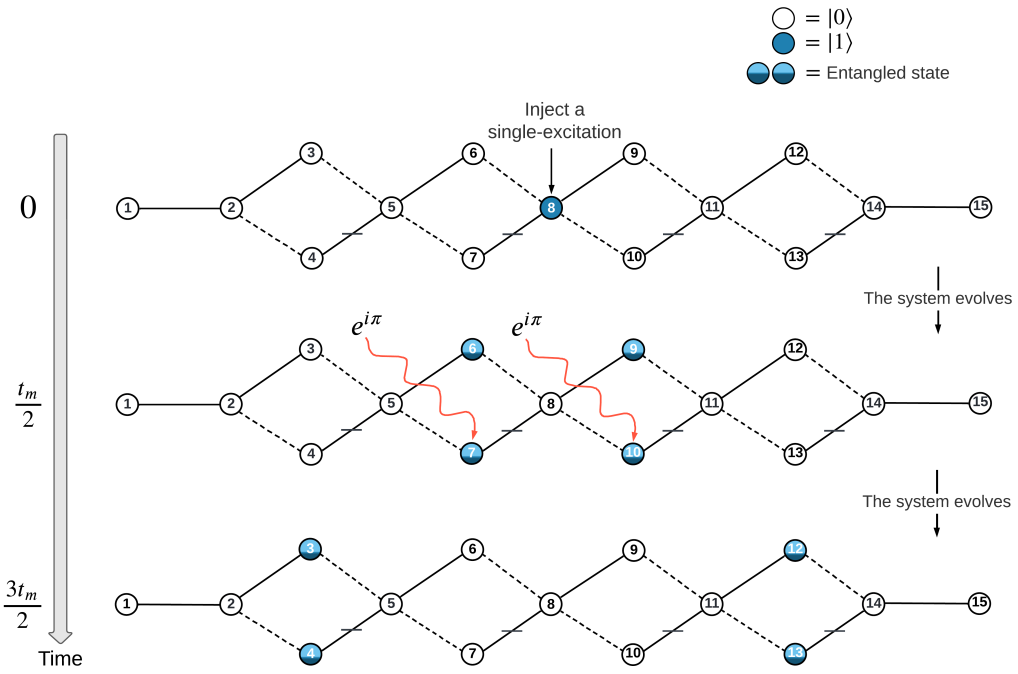

Figure 4.24: Demonstration of the steps used to generate the MWS entanglement between further sites. Note that if, at time $3t_m/2$, two simultaneous phase flips are applied at sites 4 and 13, then a bipartite maximally entangled state will be formed between sites 1 and 15.

.

4.3.3 Effect of disorder

MWS entanglement robustness

We now investigate the performance with regard to generating and transferring MWS entanglement in the presence of both types of disorder. This is achieved by calculating the fidelity of the system at time $3t_m/2$ against a desirable state chosen as a MWS entanglement between sites 3, 4, 12, and 13, as illustrated in Fig.4.27.

A very robust MWS entanglement is observed in the presence of diagonal disorder, with fidelity being $> 99\%$ for a high error strength of $E <= 15\%$. For the

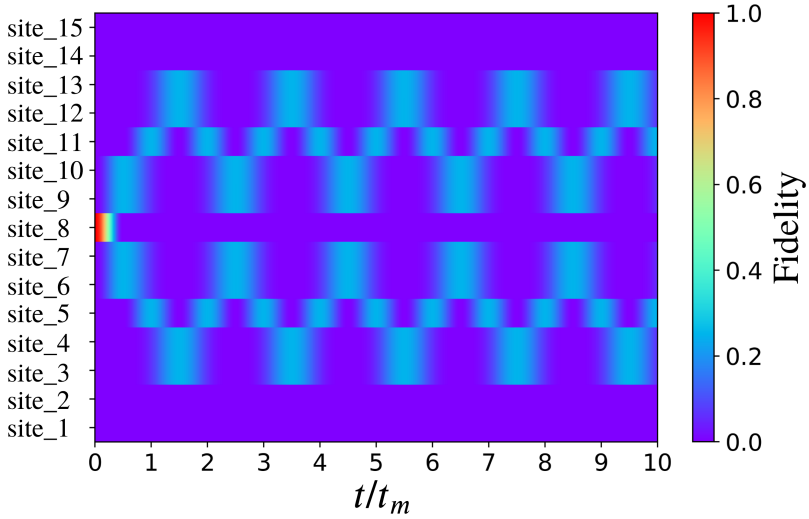

Figure 4.25: The fidelity of the system against the desirable states of an excitation being at each site as a function of the rescaled time, t/t_m. Due to the periodicity of the SN, the state keeps evolving from a MWS entanglement (between sites 6, 7, 9, and 10) to another MWS entanglement (between sites 3, 4, 12, and 13), and vice versa.

.

same error strength but in the presence of off-diagonal disorder, the fidelity remains above 97.5%. We note that since in real experiments the error is expected to be much less than 10%, and that we observed very good robustness up to $E = 15\%$, our SN thus represents a promising platform for MWS entanglement generation.

The robustness of the MWS entanglement against phase timing error, Eq.(2.19), as per Fig.4.28a, was found to be $\approx 98.5\%$ for a timing error of $D = 5\%$, and $> 96\%$ for a larger timing error of $D = 10\%$. In the presence of phase angle error, Eq. (2.21), as per Fig.4.28b, the MWS entanglement was found to be $> 99\%$ for a timing error of $D = 5\%$, and $> 97\%$ for a larger timing error of $D = 10\%$.

Entanglement type	Excitation injection $t = 0$	Evolve for	Phase injection	Evolve for
TWS {1,6,7}	at site 1	t_m	$e^{i\phi}$ at site 4	t_m
TWS {9,10,15}	at site 15	t_m	$e^{i\phi}$ at site 13	t_m
MWS {3,4,6,7}	at site 5	$\frac{t_m}{2}$	-	-
MWS {6,7,9,10}	at site 8	$\frac{t_m}{2}$	-	-
MWS {9,10,12,13}	at site 11	$\frac{t_m}{2}$	-	-
MWS {3,4,9,10}	at site 6	t_m	-	-
MWS {6,7,12,13}	at site 9	t_m	-	-
MWS {3,4,12,13}	at site 8	$\frac{t_m}{2}$	$e^{i\pi}$ at sites 7 & 10	t_m

Figure 4.26: Table demonstrating the steps used to generate various entangled states in the five 3-site-chain SN.

.

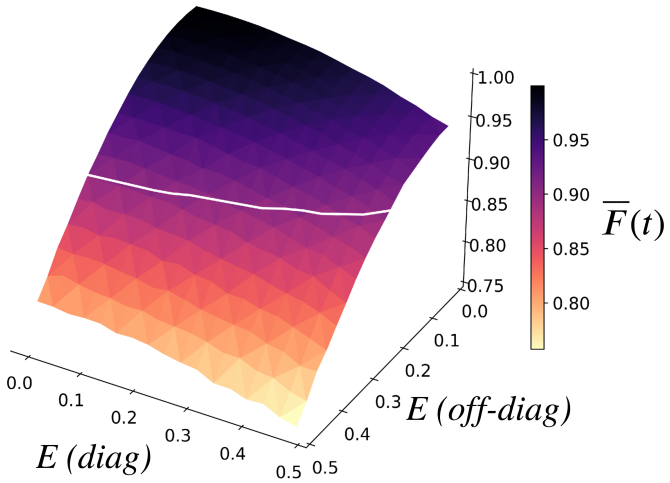

Figure 4.27: The robustness of the MWS entanglement generated at time $3t_m/2$ against diagonal (*diag*) and off-diagonal disorder (*off-diag*) with various error strengths, E, ranging from 0 to 50%. Each point has been averaged over 1000 realisations. The white line has the same meaning as in Fig. 3.22.

.

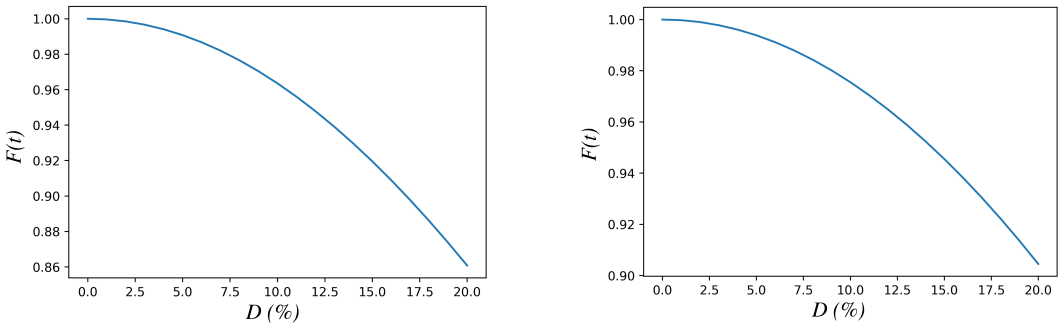

(a) $t_{d,\xi}$ **(b)** ξ_D

Figure 4.28: The robustness of the MWS entanglement at time $3t_m/2$ in the presence of an error in the phase application time, $t_{d,\xi}$ (a), and an error in the angle of the applied phase, ξ_D (b). This is performed for different error scales, D, with a step size of 0.01.

4.4 M N_j-site-chain SN

We can see from the above that the SN system can be scaled up either by increasing the number of sites, N_j, per chain while keeping the number of chains, M, fixed (as shown in Section 3.5), or vice versa (as shown in Section 4.3). We wish now to compare the robustness of the QIP protocol against disorder for both scaling approaches.

We compare the robustness of the router protocol in the two-chain and four-chain SN systems for two examples of N (i.e., $N = 12$, Fig.4.29(a,c), and $N = 24$, Fig.4.29(b,d)). As can be seen from these figures below, both scaling approaches (two-chain SN or four-chain SN) show very similar robustness against disorder up to $E = 10\%$. For larger error strengths, $E > 10\%$, we can see that each approach differs slightly. However, this only occurs for large error strengths, well above those we would generally expect in useful and practical realisations.

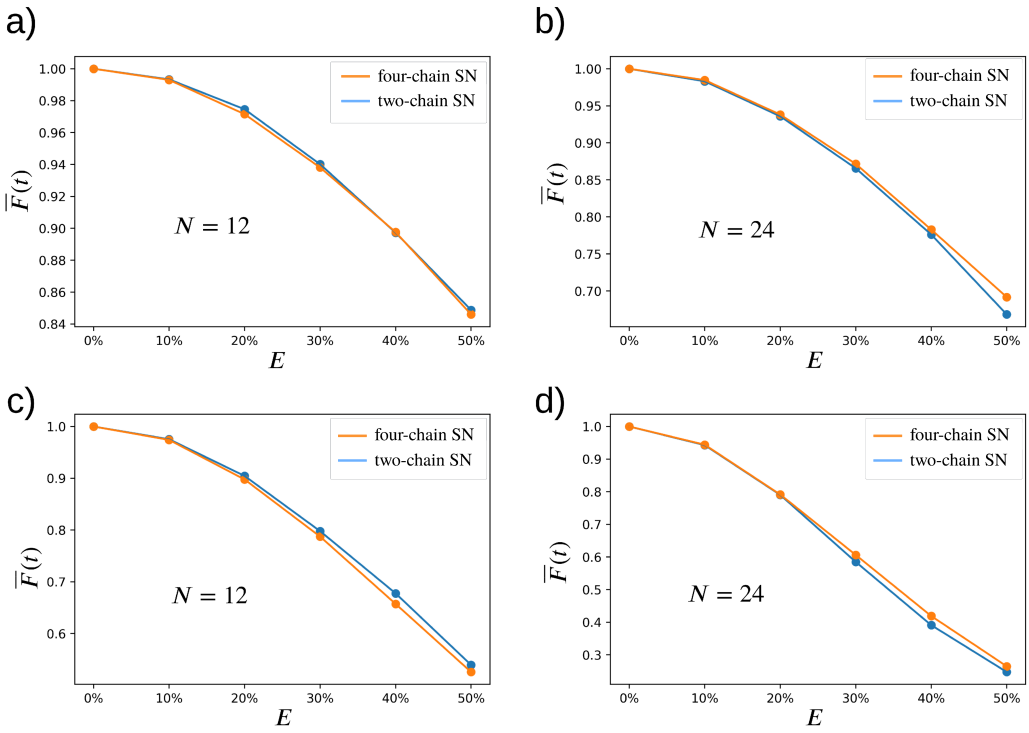

Figure 4.29: The robustness of the averaged router fidelity at time t_m ($\overline{F}(t)$ vs. $|r_N\rangle$) in the two-chain and four-chain SN systems to diagonal disorder (a) and (b) and off-diagonal disorder (c) and (d). This is for two examples of N ((a) and (c) for $N = 12$, and (b) and (d) for $N = 24$).

.

4.5 Three unequal-chain SN

We have so far investigated multi-chain SN systems, where each chain has the same number of sites. We will now investigate the case where the chains in a multi-chain SN are of different lengths[1]. Specifically, we consider a SN designed by coupling together three unequal PST chains, A, B, and C, where $N_A = 3$, $N_B = 4$, and $N_C = 5$. An illustration of such a SN is shown in Fig.4.30.

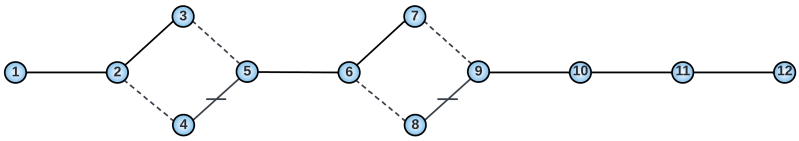

Figure 4.30: Diagram of a SN with three unequal chains.

.

As discussed in Section 3.4, since the chains of the SN are of different lengths,

[1]this additional result is not included in the second paper [2].

the time evolution of the excitation through each chain is different. The mirroring times for chains A, B, and C are $t_{m,A} = \frac{\pi}{2J_{0,A}}$, $t_{m,B} = \frac{\pi}{2J_{0,B}}$, and $t_{m,C} = \frac{\pi}{2J_{0,C}}$, respectively, where $J_{0,j} = f(N_j, J_{max,j})$, $j = A, B, C$ (see Section 2.1.5).

4.5.1 Routing

Routing can be achieved in this SN by starting with a single excitation injected at site 1 at time $t = 0$ and the application of a sudden phase flip, $e^{i\pi}$, at site 4 at time $t_{m,A}$; after a further evolution of duration $t_{m,B}$, another phase flip is applied at site 8. The state at $t_{m,A,B,C}$ will therefore be given by

$$|\Psi(t_{m,A,B,C})\rangle = -i\,|r_{12}\rangle\,, \tag{4.16}$$

where $t_{m,A,B,C} = t_{m,A} + t_{m,B} + t_{m,C}$ (the time the excitation takes to evolve from site 1 to site 12).

4.5.2 Tripartite entanglement generation

As can be seen above, any type of entangled state that we generate in our SN systems is distributed between different sites that belong to different chains (e.g., TWS entanglement between sites 1, 7, and 8). However, since the chains of the SN are different in length, an entangled state will not be distributed between the desired sites at the same given time. This, however, can be resolved by exploiting the adjustment of J_{max}, as discussed in Section 3.4.2, which we describe below.

The method of adjusting J_{max} is used to equate the mirroring times of the chains that are different in length. We note that the excitation in the TWS entanglement protocol only evolves through two chains of the SN. This is also true with the SN system shown here, Fig.4.30, so when we apply the TWS entanglement protocol to generate TWS entanglement between sites 1, 7, and 8, the excitation will only evolve through chains A and B. Therefore, we can only equate the mirroring times of the chains related to our TWS entanglement protocol (chains A and B); this can be achieved by adjusting the maximum coupling of chain A to be

$$J_{max,A} = \frac{\pi\sqrt{\frac{N_A^2-1}{4}}}{2t_{m,B}}, \tag{4.17}$$

which results in both chains mirroring times being equal, $(t_{m,A} = t_{m,B})$.

Now, since the mirroring times for each chain, A and B, are equal, we can apply the TWS entanglement here as follows. We start with a single excitation at site 1 at time $t = 0$ and evolve the system for a duration $t_{m,A}$, and then apply a sudden phase of $e^{i\phi}$ at site 4. After a further evolution of $t_{m,A}$, the state can be given as

$$|\Psi(2t_{m,A}\rangle = \frac{1+e^{i\phi}}{2}|r_1\rangle - i\frac{1-e^{i\phi}}{2\sqrt{2}}(|r_7\rangle + |r_8\rangle). \tag{4.18}$$

If instead we want to generate TWS entanglement between sites 3, 4, and 12, which in this case means that the excitation will only evolve through chains B and C, we need to make the mirroring times of chains B and C to be equal, that is $t_{m,B} = t_{m,C}$. This is achieved by adjusting the maximum coupling of chain B to $J_{max,B} = \frac{\pi N_B}{4t_{m,C}}$ (see Section 3.4.2). We then enact the TWS entanglement protocol by injecting a single excitation at site 12 at time $t = 0$ and a phase factor of $e^{i\phi}$ at site 8 at time $t_{m,C}$.

4.5.3 Multipartite entanglement generation

Our MWS entanglement protocol (discussed in Section 4.2.2) can be used here to distribute MWS entanglement between sites 3, 4, 7, and 8. The protocol requires that the mirroring time of chain B is equal to twice the mirroring time of chain A ($t_{m,B} = 2t_{m,A}$). We cannot satisfy this condition by simply setting $J_{max,B} = 1/2$ as the chain lengths are different, $N_A \neq N_B$. Instead, we will first utilise the method used in Section 3.4.2 to equate the mirroring times of chains A and B by setting their maximum couplings, $J_{max,A}$ and $J_{max,B}$, as a function of $t_{m,C}$. Then, a further adjustment to $J_{max,B}$ is performed by dividing it by half. These modifications of $J_{max,A}$ and $J_{max,B}$ are given by

$$J_{max,A} = \frac{\pi\sqrt{\frac{N_A^2-1}{4}}}{2t_{m,C}}, \qquad J_{max,B} = \frac{1}{2}\frac{\pi N_B}{4t_{m,C}}. \tag{4.19}$$

The relationship between the chains' mirroring times is now given by $t_{m,A} = \frac{1}{2}t_{m,B} = t_{m,C}$. Since we have achieved $t_{m,B} = 2t_{m,A}$, we can apply the MWS entanglement protocol as follows: we inject a single excitation at site 4 at time $t = 0$ and allow the system to evolve for a duration $2t_{m,A}$. Over this period of time, some of the excitation amplitudes would have evolved to site 1 and returned back to being in a superposition between sites 3 and 4, while other excitation

amplitudes will have evolved to being in a superposition between sites 7 and 8. The resulting state at $2t_{m,A}$ is a MWS entanglement between sites 3, 4, 7, and 8

$$|\Psi(2t_{m,A})\rangle = \frac{1}{2}(|r_3\rangle + |r_4\rangle) - \frac{i}{2}(|r_7\rangle + |r_8\rangle). \tag{4.20}$$

4.5.4 Bipartite entanglement generation

We can also generate a bipartite maximally entangled state between sites 1 and 12 using the same adjustment method described above, Eq.(4.19). We start with a single excitation injected at site 4 at time $t = 0$ and evolve the system for a duration of $2t_{m,A}$, where the state will be given as a MWS entanglement as shown in Eq.(4.20). At this time, a sudden phase flip of $e^{i\pi}$ is injected at site 8 and the system is allowed to evolve for a further duration $t_{m,A}$, which will generate a bipartite maximally entangled state between the ends of the SN, given as

$$|\Psi(3t_{m,A})\rangle = \frac{-1}{\sqrt{2}}(|r_1\rangle + i\,|r_{12}\rangle). \tag{4.21}$$

4.5.5 Effect of disorder

Routing robustness

The robustness of the router protocol generated in Eq.(4.16) was investigated by calculating $\overline{F}(t)$ against a desirable state of a single excitation at site 12 at time $3t_{m,A,B,C}$ (the first time the routing protocol is achieved). This is shown in Fig.4.31 for diagonal and off-diagonal disorder. The fidelity in the presence of diagonal disorder with an error strength of $E = 10\%$ was $> 99\%$, while for a significant error strength of $E = 20\%$ the fidelity was $> 97\%$. A reduced robustness was observed in the presence of off-diagonal disorder where the fidelity remained above 97% for an error strength of $E = 10\%$, and above 90% for a significant error strength of $E = 20\%$.

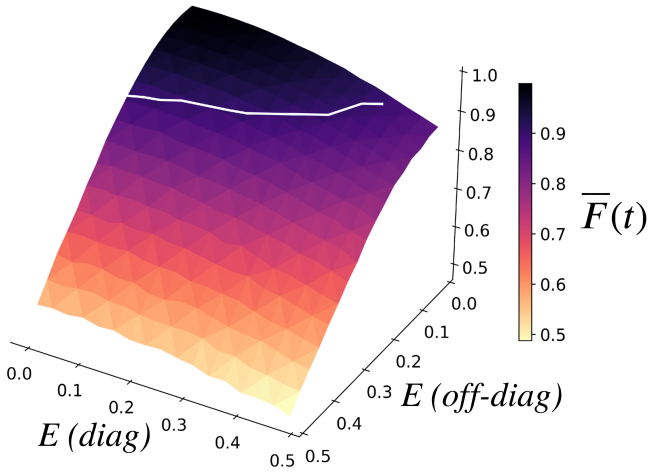

Figure 4.31: The robustness of the router protocol when $\overline{F}(t)$ is calculated at time $3t_{m,A,B,C}$ in the presence of diagonal (*diag*) and off-diagonal disorder (*off-diag*) with different error strengths, E, ranging from 0 to 50%. Each point has been averaged over 1000 realisations. The white line has the same meaning as in Fig. 3.22.

The robustness of the routing against phase timing error, Eq.(2.19), as per Fig.4.32a, was found to be $\approx 97.5\%$ for a timing error of $D = 5\%$, and $> 92\%$ for a larger timing error of $D = 10\%$. In the presence of phase angle error, Eq. (2.21), as per Fig.4.32b, the routing fidelity was found to be $\approx 98\%$ for a timing error of $D = 5\%$, and $> 95\%$ for a larger timing error of $D = 10\%$.

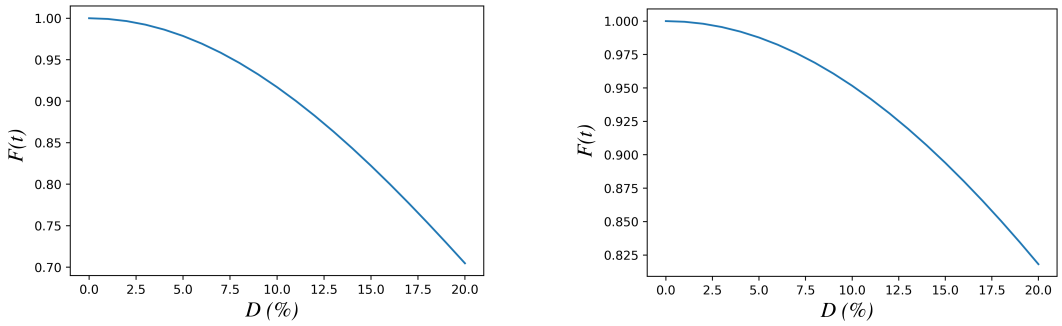

(a) $t_{d,\xi}$ **(b)** ξ_D

Figure 4.32: The robustness of the routing fidelity when $F(t)$ is calculated at time $3t_{m,A,B,C}$ in the presence of an error in the phase application time, $t_{d,\xi}$ (a), and an error in the angle of the applied phase, ξ_D (b). This is performed for different error scales, D, with a step size of 0.01.

TWS entanglement robustness

The robustness of the TWS entanglement generated in Eq.(4.18) is very robust as

shown in Fig.4.33. In the presence of diagonal disorder, the fidelity of the TWS entanglement remained above 99.5% and 98% for error strengths of $E = 10\%$ and $E = 20\%$, respectively. In the presence of off-diagonal disorder with an error strength of $E = 10\%$, the fidelity remained above 98.6%. For significant error strength of $E = 20\%$, the fidelity was found to be $\approx 95\%$.

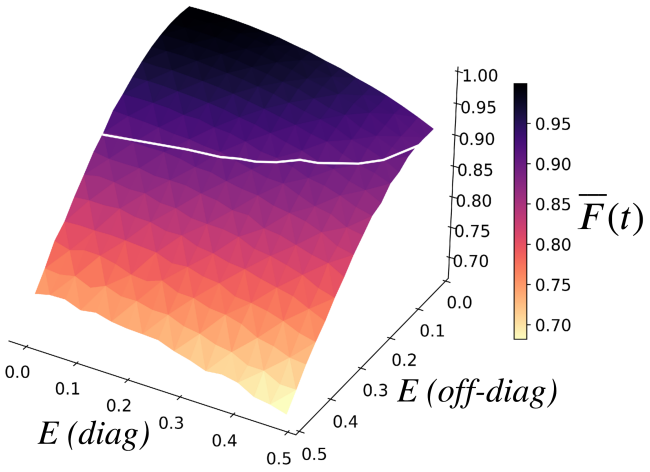

Figure 4.33: The robustness of the TWS entanglement against diagonal (*diag*) and off-diagonal disorder (*off-diag*) with various error strengths, E, ranging from 0 to 50%. Each point has been averaged over 1000 realisations. The white line has the same meaning as in Fig. 3.22.

The robustness of the TWS entanglement to phase timing error, Eq.(2.19), as per Fig.4.34a, was found to be $\approx 97.5\%$ for a timing error of $D = 5\%$, and $> 93\%$ for a higher timing error of $D = 10\%$. Excellent robustness is observed in the presence of phase angle error, Eq. (2.21)), as per Fig.4.34b, the TWS entanglement was found to be $\approx 99.75\%$ for a timing error of $D = 5\%$, and $> 99\%$ for a higher timing error of $D = 10\%$.

MWS entanglement robustness

The robustness of the MWS entanglement generated in Eq.(4.20) is shown in Fig.4.35. In the presence of diagonal disorder, the fidelity of the MWS entanglement remained above 99.6% and 98.5% for error strengths of $E = 10\%$ and $E = 20\%$, respectively. In the presence of off-diagonal disorder with an error strength of $E = 10\%$, the fidelity remained above 99%. For the significant error strength of $E = 20\%$, the fidelity remained above 96%.

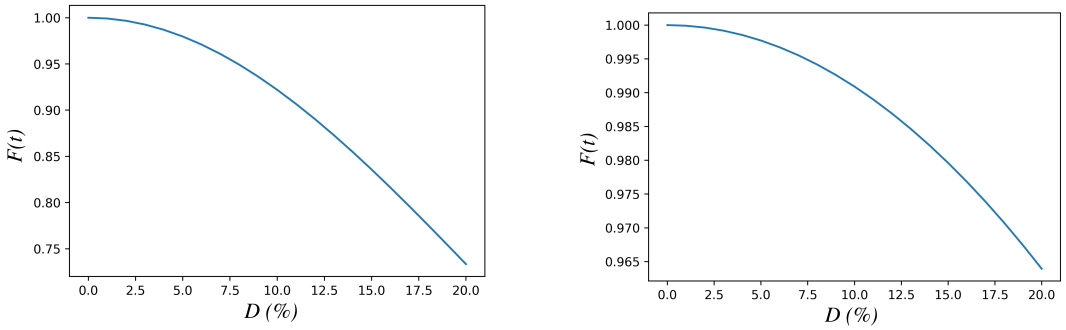

(a) $t_{d,\xi}$ **(b)** ξ_D

Figure 4.34: The robustness of the TWS entanglement in the presence of an error in the phase application time, $t_{d,\xi}$ (a), and an error in the angle of the applied phase, ξ_D (b). This is performed for different error scales, D, with a step size of 0.01.

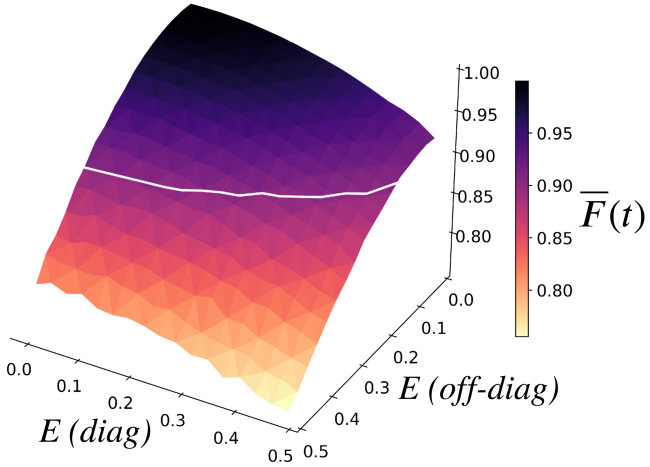

Figure 4.35: The robustness of the MWS entanglement generated at $2t_{m,A}$ against diagonal (*diag*) and off-diagonal disorder (*off-diag*) with various error strengths, E, ranging from 0 to 50%. Each point has been averaged over 1000 realisations. The white line has the same meaning as in Fig. 3.22.

Bipartite entanglement robustness

The robustness of the bipartite maximally entangled state generated in Eq.(4.21) is shown in Fig.4.36. The $\overline{EOF}$ in the presence of diagonal disorder and with an error strength of $E = 10\%$ remained above 99%, and further remained above 97% for a larger error strength of $E = 20\%$. In the presence of off-diagonal disorder, the $\overline{EOF} \approx 97\%$ for an error strength of $E = 10\%$, whereas for a significant error strength of $E = 20\%$, it was found to be $> 88\%$.

The robustness of the bipartite entanglement against phase timing error, Eq.(2.19), as per Fig.4.37a, was found to be $> 90\%$ for a timing error of $D = 5\%$,and $> 70\%$

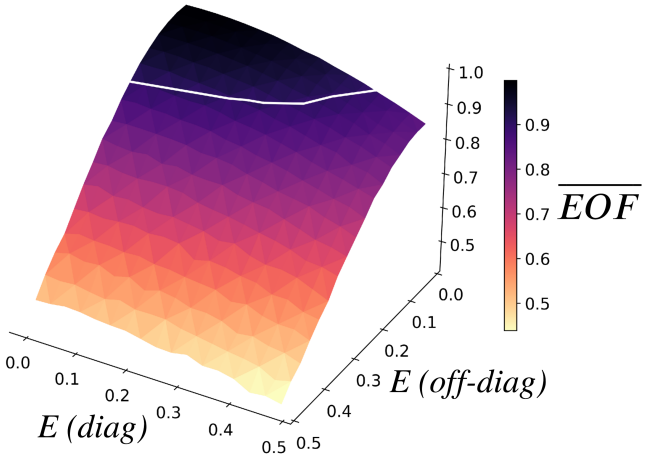

Figure 4.36: The robustness of the bipartite maximally entangled state at time $3t_{m,A}$ against diagonal (*diag*) and off-diagonal disorder (*off-diag*) with various error strengths, E, ranging from 0 to 50%. Each point has been averaged over 1000 realisations. The white line has the same meaning as in Fig. 3.23.

for a higher timing error of $D = 10\%$. In the presence of phase angle error, Eq. (2.21), as per Fig.4.37b, the bipartite entanglement was found to be $> 99.5\%$ for a timing error of $D = 5\%$, and $> 98\%$ for a larger timing error of $D = 10\%$.

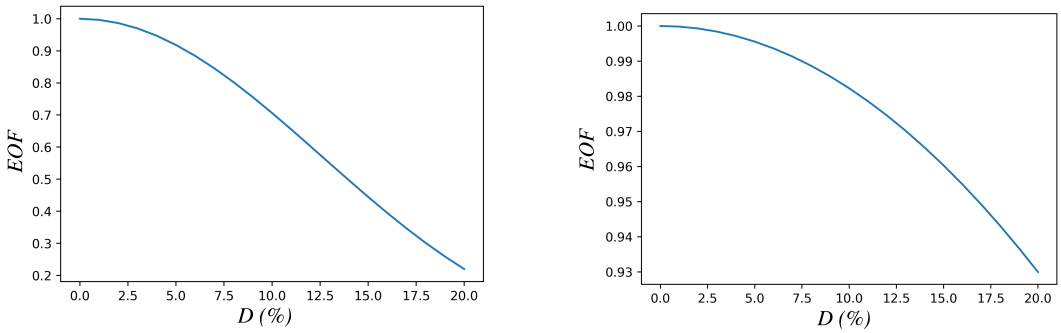

(a) $t_{d,\xi}$ **(b)** ξ_D

Figure 4.37: The robustness of the bipartite entanglement at time $3t_{m,A}$ in the presence of an error in the phase application time, $t_{d,\xi}$ (a), and an error in the angle of the applied phase, ξ_D (b). This was performed for different error scales, D, with a step size of 0.01.

4.6 Summary

In this chapter, we used the Hadamard unitary transformation to couple multiple PST chains. The resultant multi-chain SN systems were then investigated with regard to various QIP protocols. We have shown various multi-chain SN systems

starting from a three-chain SN up to an M-chain SN. In addition to operating the system as a router or generating bipartite maximally entangled states, the complex topology involved in the multi-chain SN system allows us to generate different multipartite entangled states (e.g., TWS and MWS entanglement). We have also proposed a method that can be used to generate and distribute a MWS entanglement between distant qubits using a larger multi-chain SN system.

We have shown that routing is straightforward and can be generated for any of these SN systems. With regard to bipartite and multipartite entangles states, we have proposed protocols that can be used to generate such states. Depending on the target state and the topology of the SN, these protocols may involve adjustment of some of the chains' J_{max} in order to control the excitation evolution time through them. For instance, in the three 4-site-chain SN, the protocol for MWS entanglement requires the maximum coupling of the middle chain to be reduced by half.

We have also constructed and investigated a SN of multiple unequal chains. As the chains' lengths in this SN are not equal, some of the QIP protocol requires there to be an adjustment to some of the chains' J_{max} in order to equate the excitation evolution time through them. This adjustment is required in order to generate the bipartite and multipartite entangled states. On the other hand, routing can be generated here without the need to equate the mirroring times of the SN chains.

All results have been investigated with regard to various types of disorder. For all SN systems we studied, we have observed very good robustness in all QIP protocols against diagonal and off-diagonal disorder. In general, strong robustness (e.g., fidelity $> 97\%$) was observed up to a typical error strength of $E = 10\%$ for both types of disorder for SN systems of size $N \leq 15$. Even with a significant error strength of $E = 20\%$ and against the more damaging type of disorder (that is, off-diagonal disorder), some protocols still show strong robustness. For example, in the three 3-site-chain SN, the robustness of the TWS entanglement remains $> 95\%$, and in the three unequal-chain SN, the robustness of the MWS entanglement remains $> 96\%$. The phase timing error, on the other hand, seems to be more damaging to the system than any of the other types of error we considered, which suggests that it is the form of error that should generally be kept small in real-world implementations of our SN systems. The results we obtain for the effect of measurement-time error, on one example of our SN systems, are indication of the error effect and show that it is not as damaging as the phase timing error. We

have also shown that both approaches to scaling the SN (increasing the number of chains whilst keeping the number of sites per chain fixed, or vice versa) show similar robustness against disorder.

Multi-chain SN systems may be more experimentally friendly than spin chain systems with respect to the difference between the largest and the smallest energy couplings (C_{max} and C_{min}, respectively). This is because the difference between C_{max} and C_{min} for a spin chain of size N is larger than the difference between C_{max} and C_{min} in a multi-chain SN of an equivalent size N (see appendix E). This difference between the largest and the smallest energy couplings is given by

$$J_{\text{diff}} = |C_{max} - C_{min}| / J_{max}. \tag{4.22}$$

It is important to note the distinction between the largest coupling value, C_{max}, and the maximum constraint on the couplings, J_{max}, which has been defined in Section 2.1.5. Moreover, in a multi-chain SN system, there is a smaller number of different coupling values that need to be experimentally engineered compared to an equivalent long spin chain, which could be useful in certain types of implementation.

Finally, we wish to discuss the optimal number of chains/diamonds in an SN to deliver desired tasks with the best robustness against fabrication errors and phase timing errors, taking into account the difference between C_{max} and C_{min}, Eq.(4.22). This is done by testing the routing fidelity for various SN systems (three-chain SN, four-chain SN, and six-chain SN), each having $N = 12$ number of sites. Using a figure of merit of the ratio between the J_{diff} and the fidelity, we find that the six-chain SN could be the optimal SN. On the other hand, trading off between the fidelity and J_{diff} may also depend on experimental limitations/preferences (see appendix F) for more details.

Chapter 5

Two-excitation consideration

In this chapter we introduce an alternative method to construct our SN system using an operator-based transformation instead of the matrix-based transformation, which has been discussed in the previous chapters. We show that this method is necessary when considering two- or higher-excitation subspace. Working on higher-excitation subspaces allows us to generate cluster state, which is a useful phenomena for quantum technology. The effect of various types of disorder is considered to investigate the robustness of the system in higher-excitation subspaces.

The work in this chapter is in preparation for publication.

Thus far, we have considered only the single-excitation subspace (e.g., $|r_i\rangle$) and so we will now investigate the case where the system can have multiple excitations (e.g., $|r_{i,j}\rangle = |001_i00\ldots1_j00\ldots\rangle$). The time-independent Hamiltonian H_{XY} given in Eq.(2.1) can be written in ladder operators form as

$$H_{XY} = \sum_{i=1}^{N-1} J_{i,i+1}(\sigma_i^+\sigma_{i+1}^- + \sigma_{i+1}^+\sigma_i^-) + \sum_{i=1}^{N} \frac{\epsilon_i}{2}(\sigma_i^+\sigma_i^- - \sigma_i^-\sigma_i^+), \tag{5.1}$$

with $\sigma^\pm = \frac{\sigma^x \pm i\sigma^y}{2}$. Excitations at different sites are distinguished by the site labelling, and therefore, exchanging two excitations, for $i \neq j$, follows the rule of commutation (i.e., $[\sigma_i^\pm, \sigma_j^\pm]_- = \sigma_i^\pm\sigma_j^\pm - \sigma_j^\pm\sigma_i^\pm = 0$).

5.1 Construction of two-chain spin network

As we have seen in previous chapters, our two-chain SN systems are designed with the application of a matrix-based unitary transformation on the Hamiltonian of two USC. Such transformation couples sites not previously connected by superposing the definitions of the sites. This unitary transformation matrix is given

in the single-excitation basis, Eq.(3.2), and so it can only be used when we are restricted to the single-excitation subspace. The state space dimension for an $\mathcal{N}$-excitation subspace grows as $\frac{N!}{\mathcal{N}!(N-\mathcal{N})!}$ (with N and $\mathcal{N}$ being the number of sites and excitation number, respectively). Consequently, the unitary transformation must be extended to the cases of multiple excitations. However, a direct intuitive construction of the matrices becomes more difficult for multiple excitations. Therefore, putting the unitary transformation into operator form means that it can then be applied to any number of excitations (by taking matrix elements with the appropriate basis). In this new approach, the two USC are coupled together with a general unitary transformation.

Let us first define a set of operators [177] that will be used for our unitary transformation:

- $n^{\uparrow} = \sigma^{+}\sigma^{-}$
- $n^{\downarrow} = \sigma^{-}\sigma^{+}$
- $n^{\uparrow} + n^{\downarrow} = \mathcal{I}$
- $\Sigma_{\pm} = \sigma^{+}_{N_j}\sigma^{-}_{N_j+1} \pm \sigma^{+}_{N_j+1}\sigma^{-}_{N_j}$
- $P = n^{\uparrow}_{N_j} n^{\downarrow}_{N_j+1} + n^{\downarrow}_{N_j} n^{\uparrow}_{N_j+1}$,

where N_j and $N_j + 1$ denote the sites that we choose to superpose (e.g., in the two 3-site-chain SN, Fig.3.4, $N_j = 3$ and $N_j + 1 = 4$). The unitary operator that superposes two sites is of the form $e^{\pm\vartheta\Sigma_-}$, and ϑ here is a parameter in the unitary transformation. This matrix exponential can be derived by expanding it in the infinite series. We choose $e^{-\vartheta\Sigma_-}$ to be our unitary, which can be expanded as

$$e^{-\vartheta\Sigma_-} = \sum_{i=0}^{\infty} \frac{(-\vartheta\Sigma_-)^i}{i!} = 1 - \vartheta\Sigma_- + \frac{(\vartheta\Sigma_-)^2}{2!} - \frac{(\vartheta\Sigma_-)^3}{3!} + \frac{(\vartheta\Sigma_-)^4}{4!} - \frac{(\vartheta\Sigma_-)^5}{5!} + \dots . \tag{5.2}$$

Note that we have not used the imaginary number i in the power of the exponent as Σ_- is anti-Hermitian and so no i is needed to make this unitary. Alternatively, if instead we use Σ_+, which is Hermitian, then i is required in the exponent.

With the fact that $\Sigma_-^2 = -P$ and $\pm P(\Sigma_-) = \pm\Sigma_-$ we can rewrite the equation as

$$e^{-\vartheta\Sigma_-} = 1 - \vartheta\Sigma_- - \frac{(\vartheta)^2 P}{2!} + \frac{(\vartheta)^3\Sigma_-}{3!} + \frac{(\vartheta)^4 P}{4!} - \frac{(\vartheta)^5\Sigma_-}{5!} - \dots . \tag{5.3}$$

By arranging the cosine and sine terms, the matrix exponential can be expressed as

$$e^{-\vartheta\Sigma_-} = 1 - P + P\cos(\vartheta) - \Sigma_- \sin(\vartheta), \tag{5.4}$$

The Hamiltonian of two identical USC, each of N_j number of sites, is given by

$$\begin{aligned} H_{XY} = &\sum_{i=1}^{N_j-1} J_{i,i+1}(\sigma_i^+\sigma_{i+1}^- + \sigma_{i+1}^+\sigma_i^-) - J_{1,2}(\sigma_{N_j+1}^+\sigma_{N_j+2}^- + \sigma_{N_j+2}^+\sigma_{N_j+1}^-) \\ &+ \sum_{i=2}^{N_j-1} J_{i,i+1}(\sigma_{i+N_j}^+\sigma_{i+N_j+1}^- + \sigma_{i+N_j+1}^+\sigma_{i+N_j}^-). \end{aligned} \tag{5.5}$$

As discussed in Section 3.2, since the unitary being used here is effectively of rotation matrix form and we want to design the same SN that we designed using the Hadamard-like unitary, we started here with a slightly changed initial Hamiltonian H_{XY}.

Let us now design a two 2-site-chain SN using the unitary operator shown in Eq.(5.4). First we use Eq.(5.5) to write down the Hamiltonian of the two USC, each of length $N_j = 2$, which is represented as

$$H_{XY} = \sigma_1^+\sigma_2^- + \sigma_2^+\sigma_1^- - \sigma_3^+\sigma_4^- - \sigma_4^+\sigma_3^-. \tag{5.6}$$

We can now apply the unitary operator Eq.(5.4) on this Hamiltonian to superpose sites 2 and 3. This is done by $\mathcal{H}_{XY} = (e^{-\vartheta\Sigma_-})H_{XY}(e^{\vartheta\Sigma_-})$. Through a rigorous calculation (see appendix G), we obtain the Hamiltonian that represents the SN system that is suitable for any excitation-subspace, which is given by

$$\begin{aligned} \mathcal{H}_{XY} = &\cos(\vartheta)[\sigma_1^+\sigma_2^- + \sigma_2^+\sigma_1^- - \sigma_3^+\sigma_4^- - \sigma_4^+\sigma_3^-] \\ &+ \sin(\vartheta)[(\sigma_1^+\sigma_3^- + \sigma_3^+\sigma_1^-)(n_2^\downarrow - n_2^\uparrow) + (\sigma_2^+\sigma_4^- + \sigma_4^+\sigma_2^-)(n_3^\downarrow - n_3^\uparrow)]. \end{aligned} \tag{5.7}$$

The matrix of this SN for the two-excitation subspace can be obtained by taking matrix elements in the two-excitation site basis ($|r_{1,2}\rangle$, $|r_{1,3}\rangle$, $|r_{2,3}\rangle$, $|r_{1,4}\rangle$,

$|r_{2,4}\rangle$, $|r_{3,4}\rangle$) and is given by

$$\mathcal{H}_{XY} = \begin{pmatrix} 0 & 0 & -\sin(\vartheta) & \sin(\vartheta) & 0 & 0 \\ 0 & 0 & \cos(\vartheta) & -\cos(\vartheta) & 0 & 0 \\ -\sin(\vartheta) & \cos(\vartheta) & 0 & 0 & -\cos(\vartheta) & -\sin(\vartheta) \\ \sin(\vartheta) & -\cos(\vartheta) & 0 & 0 & \cos(\vartheta) & \sin(\vartheta) \\ 0 & 0 & -\cos(\vartheta) & \cos(\vartheta) & 0 & 0 \\ 0 & 0 & -\sin(\vartheta) & \sin(\vartheta) & 0 & 0. \end{pmatrix} \tag{5.8}$$

As we discussed in Chapter 3, the unitary transformation preserves the energy spectrum, as the eigenvalues are not changed under the transformation. This should also be true here, as we are performing the same transformation (i.e., a rotation that superposes two sites) but in a different approach. Indeed, by calculating the eigenvalues of the USC Hamiltonian (Eq.(5.6)) and the eigenvalues of the SN Hamiltonian (Eq.(5.8)), for the two-excitation matrix basis, they turn out to be the same.

Generalising the Hamiltonian to any two identical N_j-site-chain SN, with N_j being the number of sites in each chain, Eq.(5.7) becomes

$$\begin{aligned} \mathcal{H}_{XY} = & \sum_{i=1}^{N_j-2} J_{i,i+1}(\sigma_i^+\sigma_{i+1}^- + \sigma_{i+1}^+\sigma_i^-) + J_{N_j-1,N_j}(\sigma_{N_j-1}^+\sigma_{N_j}^- + \sigma_{N_j}^+\sigma_{N_j-1}^-)\cos(\vartheta) \\ & + J_{N_j-1,N_j}(\sigma_{N_j-1}^+\sigma_{N_j+1}^- + \sigma_{N_j+1}^+\sigma_{N_j-1}^-)(n_{N_j}^{\downarrow} - n_{N_j}^{\uparrow})\sin(\vartheta) \\ & + J_{1,2}(\sigma_{N_j}^+\sigma_{N_j+2}^- + \sigma_{N_j+2}^+\sigma_{N_j}^-)(n_{N_j+1}^{\downarrow} - n_{N_j+1}^{\uparrow})\sin(\vartheta) \\ & - J_{1,2}(\sigma_{N_j+1}^+\sigma_{N_j+2}^- + \sigma_{N_j+2}^+\sigma_{N_j+1}^-)\cos(\vartheta) \\ & + \sum_{i=2}^{N_j-1} J_{i,i+1}(\sigma_{i+N_j}^+\sigma_{i+N_j+1}^- + \sigma_{i+N_j+1}^+\sigma_{i+N_j}^-), \end{aligned} \tag{5.9}$$

where sites N_j and N_j+1 are the sites that we choose to superpose. In Eq.(5.9), the first two terms represent the couplings of chain A of the SN, the second two terms represent the additional couplings imposed by the transformation, and the last two terms represent the couplings of chain B of the SN. It is clear that the couplings that connect the two chains in the SN (i.e., the third and fourth terms) will always be positive in the single-excitation subspace, which is consistent with the findings presented in Chapter 3. In higher-excitation subspace, the sign of these couplings can be negative if another excitation is at a nearby site.

By setting $\vartheta = \frac{\pi}{4}$ we can design the exact same SN that we designed Chapter .3 except that now it is not only restricted to a single-excitation subspace, as it can be used for higher-excitation subspace. It still conserves the number of excitations and so if we start by injecting two-excitations, the system will only evolve in this excitation-subspace. Furthermore, the unitary here is also not unique as we can use different rotation of the unitary and still get the same SN. However, as noted in Section 3.2, one of the four diamond-shaped couplings will have a different sign depending on the unitary used for the SN construction.

5.1.1 Dynamics of two 3-site-chain SN

We wish now to investigate the dynamics of our two 3-site-chain SN, shown in Fig.3.4, in the two-excitation subspace. We start by initialising the system with two excitations being injected at the ends of the SN

$$|\Psi(0)\rangle = |r_{1,6}\rangle\,, \tag{5.10}$$

where $|r_{1,6}\rangle = |100001\rangle$. As discussed in Chapter 3, the design of the SN allows an excitation, injected at one end of the SN, to evolve only to the central vertices of the diamond and back to its initial site. This is also true in the two excitation subspace, as when we evolve the two excitations $|r_{1,6}\rangle$ for a duration of t_m, they will end up being localised in the central vertices of the diamond, given by

$$|\Psi(t_m)\rangle = |r_{3,4}\rangle\,, \tag{5.11}$$

and evolves back to the initial state, Eq.(5.10). This is demonstrated in Fig.5.1 where the fidelity of each basis is plotted as a function of time.

5.1.2 Two-qubit cluster state

A cluster state is a maximally entangled state that is used particularly in the measurement-based quantum computer (or one-way quantum computer) [178–184]. This is a different approach to quantum computing, which is based on a sequence of measurements applied to a large initial entangled state (usually a cluster state). It is equivalent to the gate approach, discussed in Chapter 1, but relies on measurements to effect, or drive, the computation, whereas the gate model used gates to derive the computation and only measurements at the end to extract the

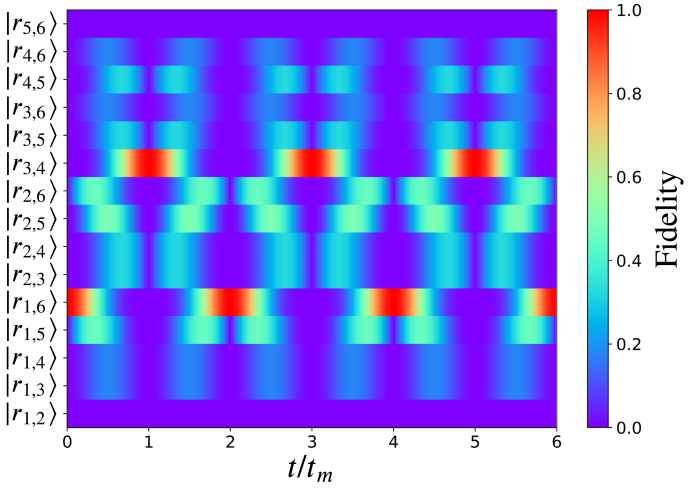

Figure 5.1: Dynamics of the SN system with the initial excitation being injected at both ends of the SN.

results. Cluster entangled states differ from the W-type entangled states presented in Chapter 4 in the sense that the entanglement does not easily get destroyed by projective measurements as well as its usefulness in measurement-based quantum computer.

The generation of cluster states in SN systems can be achieved via the injection of the state $|+\rangle = \frac{1}{\sqrt{2}}(|0\rangle + |1\rangle)$ at the first and last spin of the system [185, 186]. Cluster-state generation is equivalent to a two-qubit entangling gate and together with appropriate single-qubit gates (see Section 1.1.1), they form a universal set of quantum gates [187]. We are interested in generating this in our non-linear two 3-site-chain SN (Fig.3.4 in Chapter 3).

If we start by injecting the plus state $|+\rangle$ at both ends of the SN, for example by applying a Hadamard gate to each of site 1 and site 6, the state of the system will be given by

$$\begin{aligned} |\Psi(0)\rangle &= |+\rangle_1 \otimes |0\rangle_2 \otimes |0\rangle_3 \otimes |0\rangle_4 \otimes |0\rangle_5 \otimes |+\rangle_6 \\ &= \frac{1}{2}(|r_0\rangle + |r_6\rangle + |r_1\rangle + |r_{1,6}\rangle). \end{aligned} \tag{5.12}$$

The system now is in the zero- single- and two-excitation subspace. By letting the system to evolve for a duration of t_m, the resulting evolved state at t_m will be given by

$$|\Psi(t_m)\rangle = \frac{1}{2}|r_0\rangle - \frac{1}{\sqrt{2}}|r_3\rangle - \frac{1}{2}|r_{3,4}\rangle\,, \tag{5.13}$$

We note that the single-excitation basis combined to be at site 3, which is because

of the negative coupling between sites 4 and 5 that induces a destructive interference at site 4. This and the following dynamics are obtained from our numerical calculations. If we now evolve the system again for another duration of t_m, the system will regain its initial state, $|\Psi(2t_m)\rangle = |\Psi(0)\rangle$. This is in contrast to linear SN systems, where the cluster state is generated simply by injecting $|+\rangle$ states and evolving the system. The reason for that is because our SN is designed such that it does not allow the excitation to hop from one chain of the SN to another chain of the SN, unless a phase factor is applied (see Section 3.2.1).

Therefore, in order to force the excitation to keep evolving, crossing each other to end up forming a maximally entangled state between the first and the last spin of the SN, a sudden phase flip $e^{i\pi}$ needs to be applied at site 3 at t_m where the state of the system is given as shown in Eq.(5.13). This is done by applying the phase flip at any basis that involves an excitation at site 3

$$|\Psi(t_m)\rangle_\pi = \frac{1}{2}|r_0\rangle - e^{i\pi}\frac{1}{\sqrt{2}}|r_3\rangle - e^{i\pi}\frac{1}{2}|r_{3,4}\rangle\,. \tag{5.14}$$

By letting the system to evolve for another duration of t_m, the state of the system at $2t_m$ will be given as

$$|\Psi(2t_m)\rangle = \frac{1}{2}(|r_0\rangle - |r_6\rangle - |r_1\rangle - |r_{1,6}\rangle). \tag{5.15}$$

The overall phase factor for the single-excitation basis for any SN of two chains, each of length N_j, is -1^{N_j}, whereas the overall phase factor for the two-excitation basis is always -1. EOF between sites 1 and 6 as a function of time, plotted in Fig.5.2, shows that they are maximally entangled. We can express the operation as an effective two-qubit gate G

$$G = \begin{pmatrix} -1 & 0 & 0 & 0 \\ 0 & 0 & -1^{N_j} & 0 \\ 0 & -1^{N_j} & 0 & 0 \\ 0 & 0 & 0 & 1 \end{pmatrix}, \tag{5.16}$$

using the basis $\{|1\rangle_1|1\rangle_N, |1\rangle_1|0\rangle_N, |0\rangle_1|1\rangle_N, |0\rangle_1|0\rangle_N\}$. Note that this maximally entangled state occurs for any two N_j-site-chain SN.

The state given in Eq. (5.15) can be considered as a *minimal* two-qubit cluster state, as it has the entanglement required for a cluster state and is generated in a similar way to the generation of cluster states [183, 186, 188], which involves injec-

tion of $|+\rangle$ states. Note that the cluster state generation protocol in other systems can involve the application of a controlled-Z gate between nearest-neighbouring qubits, in addition to applying the $|+\rangle$ states [183]. On the other hand, the protocol we used here, to generate the two-qubit cluster state, requires injection of $|+\rangle$ states, natural evolution of the system, and a local phase flip operation. This could indicate that the natural dynamics of the system and the local phase flip operation simulate the effect of a controlled-Z gate.

Therefore, by the injection of $|+\rangle$ states at the ends of the SN, we obtain this effective two-qubit entangling gate that has also been achieved in linear SN systems [185,186,188]. The minimal cluster state generated here can be thought of as a starting point or building block of more spatially extended two-qubit cluster states, as one can increase the site number of the chains within the SN in order to realise a two-qubit cluster state between qubits that are further apart (this will be discussed in Section 5.2.1). Two-qubit cluster states can be used to implement a one-way quantum computation by appropriately measuring one qubit in a specific chosen basis, which results in a rotation of the second qubit [189]. However, it is crucial to note that the two-qubit cluster states are not a universal resource for one-way quantum computing, as it is a linear or minimal cluster state and is locally equivalent to a maximally entangled Bell state [190]. There is potential for building cluster states containing a larger number of qubits in our SN, for example, following ideas from [186], which would be an interesting future work.

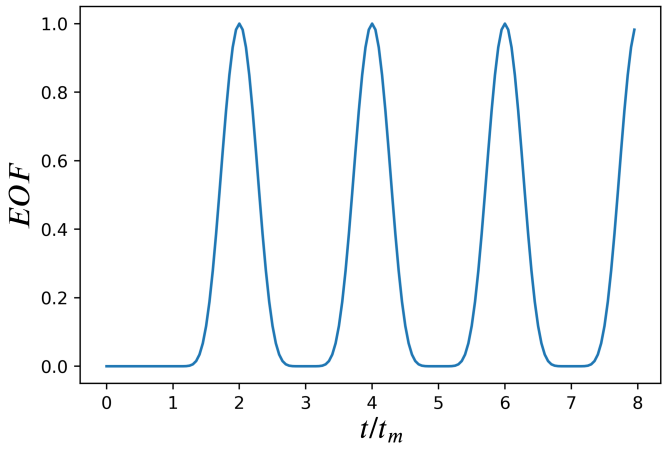

Figure 5.2: The EOF between sites 1 and 6 as a function of rescaled time t/t_m.

Similarly, we can generate two-qubit entangling gate between sites 3 and 4 by

starting injecting the $|+\rangle$ states at sites 3 and 4

$$|\Psi(0)\rangle = \frac{1}{2}(|r_0\rangle + |r_4\rangle + |r_3\rangle + |r_{3,4}\rangle), \tag{5.17}$$

and evolving the system for t_m where the state will be given by

$$|\Psi(t_m)\rangle = \frac{1}{2}|r_0\rangle - \frac{1}{\sqrt{2}}|r_1\rangle - \frac{1}{2}|r_{1,6}\rangle . \tag{5.18}$$

With the application of a phase flip at site 1 at t_m and evolving the system for a duration of t_m, a cluster state will be formed at $2t_m$, given as

$$|\Psi(2t_m)\rangle = \frac{1}{2}(|r_0\rangle - |r_4\rangle - |r_3\rangle - |r_{3,4}\rangle), \tag{5.19}$$

which by investigating the phases of the elements of the basis for different SN size, turns out to be generated by the same effective gate G.

5.1.3 Effect of disorder

We will now investigate the robustness of the two-qubit entangling gate between sites 1 and 6 in the presence of various types of disorder. We will consider the diagonal and off-diagonal disorder. Another type of disorder that will be considered is the excitation-excitation interaction. In addition, timing error and phase error will also be considered.

Diagonal and off-diagonal disorder

When we include the diagonal disorder in the SN, the cluster state robustness remains $\overline{EOF} > 99.6\%$ with error strength up to $E = 10\%$, and $EOF > 98.5\%$ with significant error strength of up to $E = 20\%$. In the presence of off-diagonal disorder and with error strengths of up to $E = 10\%$ and $E = 20\%$, the cluster state robustness remains $\overline{EOF} > 98.6\%$ and $\overline{EOF} > 94\%$, respectively, Fig.5.3.

Excitation-excitation interactions

When the system has multiple excitations, a type of perturbation known as excitation-excitation interaction can occur. This represents an unwanted interaction between nearby excitations and an example of this is the exciton-exciton interaction in quantum dots [191, 192]. Therefore, excitation-excitation interactions can be pre-

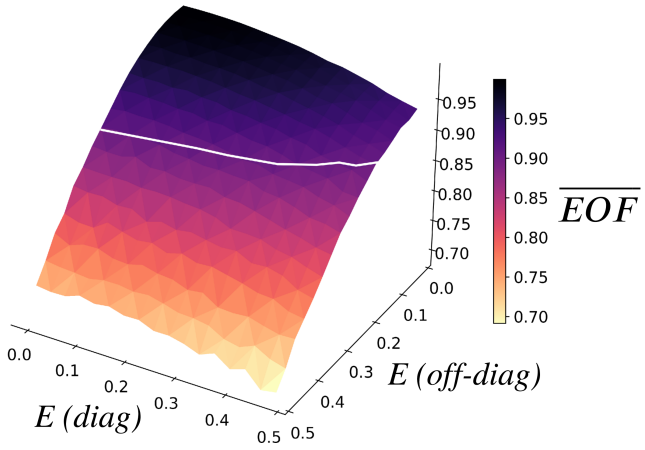

Figure 5.3: The robustness of the $\overline{EOF}$ between sites 1 and 6 at $t = 2t_m$ in the presence of diagonal and off-diagonal disorder with different error strength E. White lines have same meaning as in Fig. 3.23.

sented as an additional term in the Hamiltonian

$$H_e = \sum_{i=1}^{N-1} EJ_0[|1\rangle\langle 1|_i \otimes |1\rangle\langle 1|_{i+1}]. \tag{5.20}$$

The effect of excitation-excitation interaction on the cluster state is very week even when the cluster state is calculated at the third time it forms, $6t_m$, as shown in Fig.5.4. The cluster state first peak is around 99.9% and 99.6% for $E = 10\%$ and $E = 20\%$, respectively.

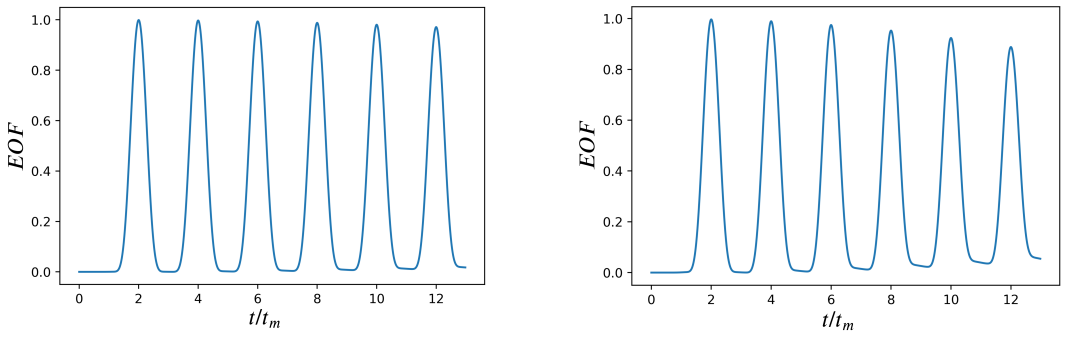

(a) $E = 10\%$ **(b)** $E = 20\%$

Figure 5.4: The robustness of the cluster state in the presence of excitation-excitation interaction of two different strengths. $E = 10\%$ (a) and $E = 20\%$ (b).

Time delays

As we have seen above, the protocol of generating the entangled cluster state involves application of a phase flip at a site at t_m. We wish to consider now the case where there is a delay in the phase application, a delay that is specified by the strength D (see Eq.(2.19)). We have investigated this scenario and as shown in Fig.5.5a it turns out that the robustness of the cluster state is very sensitive to the phase time delay. For a small delay scale of $D = 5\%$, the cluster state is observed to have entanglement of $EOF = 93\%$ and decays fast as D increases. This could be because of the fact that the protocol of generating the cluster state requires the sudden application of the phase. Thus, an error on that phase application time will have greater impact to the cluster state. Note that the robustness is independent of whether the phase time error is $D > 0$ (delayed operation) or $D < 0$ (earlier operation).

Another type of time delay error that we wish to investigate is the case where the initial injected $|+\rangle$ states at sites 1 and 6 are not performed in a synchronous way (see Eq.(2.20)). This type of delay is not as damaging to the cluster state as much as the damage caused by the above phase timing error. As shown in Fig.5.5b, the cluster state remains very robust with $EOF > 99\%$ when the delay strength is of $D = 5\%$ and $EOF > 96\%$ when $D = 10\%$.

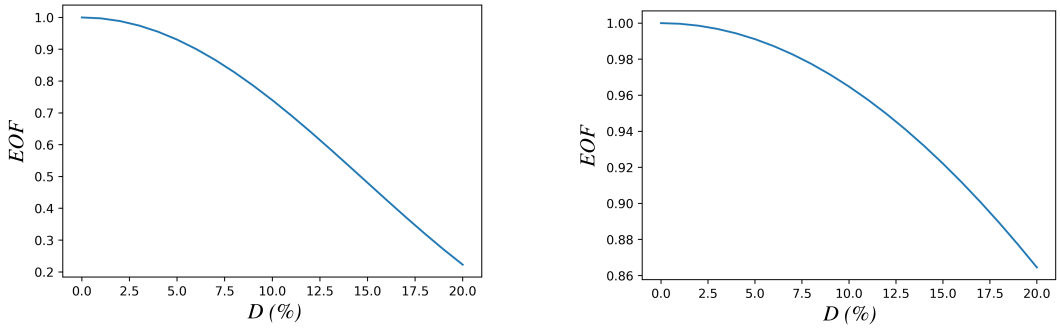

(a) $t_{d,\xi}$ **(b)** $t_{d,|+\rangle}$

Figure 5.5: The robustness of the $\overline{EOF}$ between sites 1 and 6 at $t = 2t_m$ against a time delay on the phase application, $t_{d,\xi}$, (a) and against a time delay on the initial injected $|+\rangle$ states, $t_{d,|+\rangle}$ (b). This is performed for different error scales, D, with a step size of 0.01.

Phase disorder

We will now investigate the case where the error is due to a phase angle disorder (see Eq. (2.21)). In this case, the phase factor $e^{i\pi}$ required for our cluster state generation is not accurate (i.e., $e^{i(\pi+D\pi)}$). This has a very weak effect on the cluster state robustness, as we can see in Fig.5.6 that the $EOF > 98\%$ with $D = 10\%$.

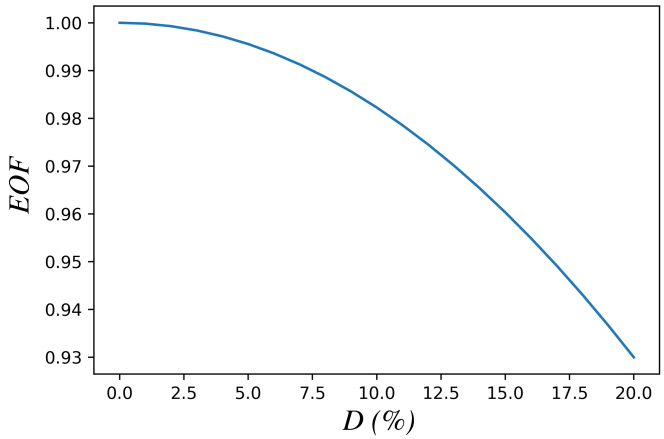

Figure 5.6: The robustness of the $\overline{EOF}$ between sites 1 and 6 at $t = 2t_m$. This is performed for different error scales, D, with a step size of 0.01.

5.2 Construction of multi-chain spin network

Construction of multi-chain SN systems, as discussed in Chapter 4, is done by applying a unitary transformation, that superposes $M - 1$ pair of sites, on the Hamiltonian of the M USC. For example, for the case of $M = 3$ (three USC), the unitary transformation is chosen such that it superposes two pair of sites in order to form the three-chain SN.

Solving the transformation using the operator-based unitary can be a cumbersome task, but we can instead write the transformed Hamiltonian straightforwardly given that we already know, from the two-chain SN Hamiltonian, Eq.(5.9), where the negative couplings should be. Therefore, we can just expand Eq.(5.9) by adding additional terms that correspond to the additional chains. A representation of the Hamiltonian of a three-chain SN, where each chain is of N_j number

of sites, is given by

$$
\begin{aligned}
\mathcal{H}_{XY} = & \sum_{i=1}^{N_j-2} J_{i,i+1}(\sigma_i^+\sigma_{i+1}^- + \sigma_{i+1}^+\sigma_i^-) + J_{N_j-1,N_j}(\sigma_{N_j-1}^+\sigma_{N_j}^- + \sigma_{N_j}^+\sigma_{N_j-1}^-)\cos(\vartheta) \\
& + J_{N_j-1,N_j}(\sigma_{N_j-1}^+\sigma_{N_j+1}^- + \sigma_{N_j+1}^+\sigma_{N_j-1}^-)(n_{N_j}^{\downarrow} - n_{N_j}^{\uparrow})\sin(\vartheta) \\
& - J_{1,2}(\sigma_{N_j+1}^+\sigma_{N_j+2}^- + \sigma_{N_j+2}^+\sigma_{N_j+1}^-)\cos(\vartheta) \\
& + J_{1,2}(\sigma_{N_j}^+\sigma_{N_j+2}^- + \sigma_{N_j+2}^+\sigma_{N_j}^-)(n_{N_j+1}^{\downarrow} - n_{N_j+1}^{\uparrow})\sin(\vartheta) \\
& + \sum_{i=2}^{N_j-2} J_{i,i+1}(\sigma_{i+N_j}^+\sigma_{i+N_j+1}^- + \sigma_{i+N_j+1}^+\sigma_{i+N_j}^-) \\
& + J_{N_j-1,N_j}(\sigma_{2N_j-1}^+\sigma_{2N_j}^- + \sigma_{2N_j}^+\sigma_{2N_j-1}^-)\cos(\vartheta) \\
& + J_{N_j-1,N_j}(\sigma_{2N_j-1}^+\sigma_{2N_j+1}^- + \sigma_{2N_j+1}^+\sigma_{2N_j-1}^-)(n_{2N_j}^{\downarrow} - n_{2N_j}^{\uparrow})\sin(\vartheta) \\
& - J_{1,2}(\sigma_{2N_j+1}^+\sigma_{2N_j+2}^- + \sigma_{2N_j+2}^+\sigma_{2N_j+1}^-)\cos(\vartheta) \\
& + J_{1,2}(\sigma_{2N_j}^+\sigma_{2N_j+2}^- + \sigma_{2N_j+2}^+\sigma_{2N_j}^-)(n_{2N_j+1}^{\downarrow} - n_{2N_j+1}^{\uparrow})\sin(\vartheta) \\
& + \sum_{i=2}^{N_j-1} J_{i,i+1}(\sigma_{i+2N_j}^+\sigma_{i+2N_j+1}^- + \sigma_{i+2N_j+1}^+\sigma_{i+2N_j}^-)
\end{aligned}
\tag{5.21}
$$

A layout of this Hamiltonian SN is shown in Fig.4.13. Note that this Hamiltonian describes any three N_j-site-chain SN, for $N_j > 2$. A special case of $N_j = 2$ cannot be described by this Hamiltonian. This is because this simplest example of three-chain SN (three 2-site-chain SN) has additional coupling between distant sites (sites 2 and 5), which is the result of superposing two nearby pair of sites (sites 2 and 3 as well as sites 4 and 5). This special example is not considered here as we are interested in larger SN systems.

As discussed in Chapter 3, the figure of merit that can be used to check whether our SN Hamiltonian is correct or not is the eigenvalues conservation. We therefore used numerical methods to build the matrix of this three-chain SN Hamiltonian for N size and compute its eigenvalues to see if they are the same as the eigenvalues of the 3 USC of the same N size. This has been confirmed numerically.

5.2.1 Two-qubit cluster state

We wish to generate now the two-qubit entangling gate in the three 4-site-chain SN (Fig.4.13). We start by injecting a plus state, $|+\rangle$, at both ends of the SN, so

our initial state is given by

$$\begin{aligned} |\Psi(0)\rangle &= |+\rangle_1 \otimes |0\rangle_2 \otimes \ldots \otimes |0\rangle_{11} \otimes |+\rangle_{12} \\ &= \frac{1}{2}(|r_0\rangle + |r_1\rangle + |r_{12}\rangle + |r_{1,12}\rangle). \end{aligned} \tag{5.22}$$

Evolving this initial state for a duration of t_m, the excitations will now be in a superposition between sites 4, 5, 8, and 9 in the single-excitation subspace and the two-excitations subspace, given by

$$|\Psi(t_m)\rangle = \frac{1}{2}|r_0\rangle + \frac{i}{2\sqrt{2}}(|r_4\rangle + |r_5\rangle + |r_8\rangle - |r_9\rangle) + \frac{1}{4}(-|r_{4,8}\rangle + |r_{4,9}\rangle - |r_{5,8}\rangle + |r_{5,9}\rangle). \tag{5.23}$$

Application of a phase flip is required now in order to force the excitations to keep evolving forward and crossing each other, which is a condition for the entangling gate formation (see Section 5.1.2). The phase flip $e^{i\pi}$ is applied at sites 5 and 9 as

$$\begin{aligned} |\Psi(t_m)\rangle_\pi = \frac{1}{2}|r_0\rangle + \frac{i}{2\sqrt{2}}(|r_4\rangle + e^{i\pi}|r_5\rangle + |r_8\rangle - e^{i\pi}|r_9\rangle) \\ + \frac{1}{4}(-|r_{4,8}\rangle + e^{i\pi}|r_{4,9}\rangle - e^{i\pi}|r_{5,8}\rangle + e^{i\pi}e^{i\pi}|r_{5,9}\rangle). \end{aligned} \tag{5.24}$$

Now, we let the system to evolve for t_m where the state of the system would be given by

$$|\Psi(2t_m)\rangle = \frac{1}{2}|r_0\rangle + \frac{1}{2\sqrt{2}}(-|r_4\rangle + |r_5\rangle - |r_8\rangle - |r_9\rangle) + \frac{1}{4}(-|r_{4,8}\rangle - |r_{4,9}\rangle + |r_{5,8}\rangle + |r_{5,9}\rangle). \tag{5.25}$$

With another application of phase flips at the same sites and another evolution of t_m, the two-qubit entangling gate will be formed between the sites 1 and 12, given as

$$|\Psi(3t_m)\rangle = \frac{1}{2}(|r_0\rangle - i|r_{12}\rangle - i|r_1\rangle + |r_{1,12}\rangle). \tag{5.26}$$

The state generated at $3t_m$ is therefore a two-qubit entangling gate that effect the following G gate

$$G = \begin{pmatrix} -1^{N_j} & 0 & 0 & 0 \\ 0 & 0 & i^{N_j-1} & 0 \\ 0 & i^{N_j-1} & 0 & 0 \\ 0 & 0 & 0 & 1 \end{pmatrix}, \tag{5.27}$$

expressed using the two-qubit basis $\{|1\rangle_1 |1\rangle_N, |1\rangle_1 |0\rangle_N, |0\rangle_1 |1\rangle_N, |0\rangle_1 |0\rangle_N\}$. The N_j is the length of a single chain in the three-chain SN, as we are assuming that all the three chains are of equal lengths. The expressions of the global phases have been obtained by investigating the two-qubit entangling gate for various N sizes. The maximally entangled state occurs for any three N_j-site-chain SN, with $N_j > 2$. This is because our Hamiltonian, Eq.(5.21), can not describe three 2-site-chain SN (see Section 5.2).

5.2.2 Effect of disorder

We will now investigate the robustness of the two-qubit entangling gate between sites 1 and 12 in the presence of diagonal and off-diagonal disorder, excitation-excitation interaction, time delay errors, and phase error.

Diagonal and off-diagonal disorder

In the presence of diagonal disorder, the cluster state generated at $3t_m$ gives $\overline{EOF} \approx 99\%$ for error strength of $E = 10\%$ and $\overline{EOF} > 95\%$ for significant error strength of $E = 20\%$. The robustness is reduced in the presence of off-diagonal disorder, as the $\overline{EOF} = 96\%$ and $\overline{EOF} = 85\%$ for error strengths of $E = 10\%$ and $E = 20\%$, respectively, Fig.5.7.

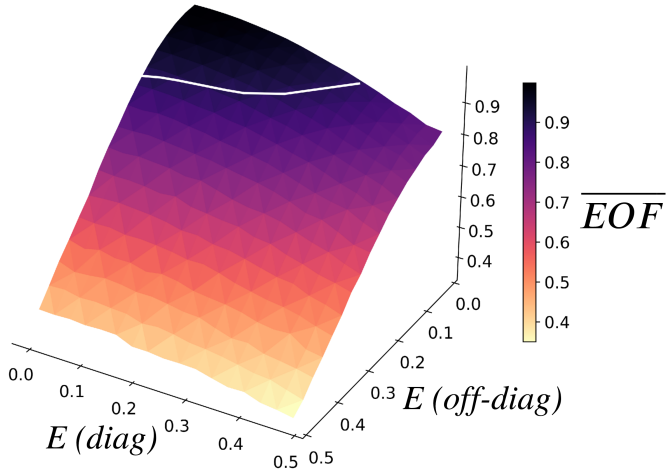

Figure 5.7: The robustness of the $\overline{EOF}$ between sites 1 and 12 at $t = 3t_m$ in the presence of diagonal and off-diagonal disorder with different error strength E. The white line indicates the $\overline{EOF}$ 90% threshold ($\pm 2\%$ due to numerical discretization).

Excitation-excitation interactions

The robustness of the cluster state in the presence of excitation-excitation interaction, with large error strength of $E = 20\%$, is found to be $EOF = 99.7\%$. It is clear from Fig.5.8 that the three-chain SN system is more robust against excitation-excitation interaction when it is compared to the two-chain SN (see Section 5.1.3). This is because the system configurations of the three-chain SN system involves very few basis vectors that have two neighbouring excitations compared to the total number of basis vectors in the system (i.e., there are only 13 basis vectors of two nearby excitations out of 79 basis vectors that do not have two nearby excitations). This suggest that as the SN size increases, the system will be even more robust against excitation-excitation interaction, as the discrepancy between the number of basis vectors that do not have two neighbouring excitations and those having two neighbouring excitations will be larger, which in turn makes the excitation-excitation interaction less effective. To put this in another perspective, the two excitations spend very little time in adjacent network sites and the model interaction is zero whenever they are further apart, which is mostly the case.

Another interesting thing we note from the figure is that the EOF does not decay with time, which can be attributed to the fact that the excitation-excitation error is fixed and the two plus states interacted only once, when they are exchanged by the phase flip at t_m (see Eq.(5.24)). Therefore, since there is no interaction between the plus states and the error does not increase with time, the EOF keeps forming at each odd t_m (i.e., $3t_m$, $5t_m$, etc) with extremely close values, Fig.5.8.

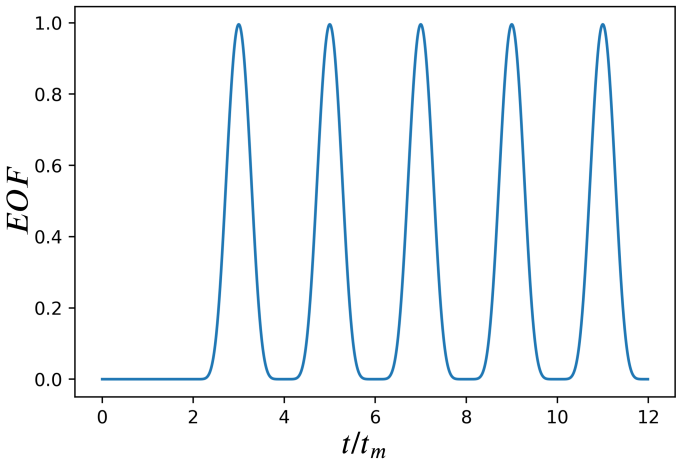

Figure 5.8: The robustness of the cluster state in the presence of excitation-excitation interaction with strength of $E = 20\%$.

Time delays

Let us now investigate the case where the error is due to a time delay in applying the required phases, Eq.(2.19), for the cluster state protocol to work. The cluster state generation protocol involves applying phase flips at sites 5 and 9 at two different times, at t_m and $2t_m$, respectively. Therefore, we will simulate the case where the application of the phases are not performed exactly at the right time.

The robustness of the two-qubit cluster state is very sensitive to the time delay in the phase application, as the entanglement is observed to have $EOF \approx 85\%$ for a small delay scale of $D = 5\%$ and $EOF \approx 51\%$ for a larger delay of $D = 10\%$, Fig.5.9a.

We wish to investigate the case where the time error is in the initial injection of the $|+\rangle$ states, Eq. (2.20). This error does not have much effect on the cluster state, as the entanglement is observed to have $EOF > 98\%$ for $D = 5\%$ and $EOF \approx 95\%$ for a larger delay of $D = 10\%$, Fig.5.9b.

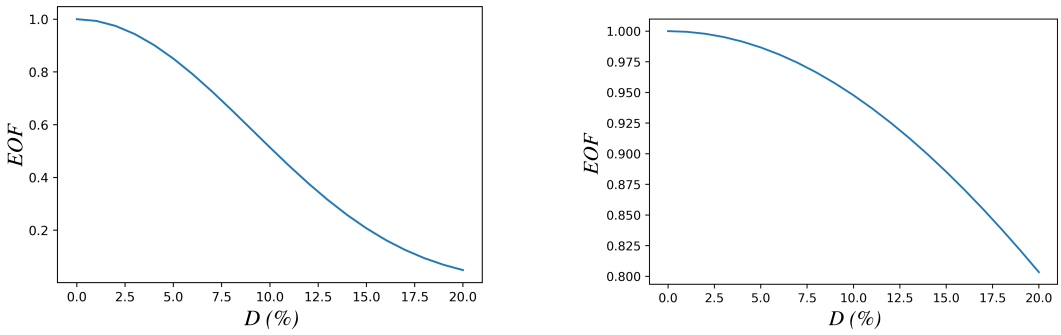

(a) $t_{d,\xi}$ **(b)** $t_{d,|+\rangle}$

Figure 5.9: The robustness of the $\overline{EOF}$ between sites 1 and 12 at $t = 3t_m$ against a time delay on the phase application, $t_{d,\xi}$, (a) and against a time delay on the initial injected $|+\rangle$ states, $t_{d,|+\rangle}$ (b). This is performed for different error scales, D, with a step size of 0.01.

Phase disorder

We will now investigate the effect of the phase angle disorder (see Eq. (2.21)) and in such a case, the phase flips $e^{i\pi}$ required for our cluster state generation is not accurate (i.e., $e^{i(\pi+D\pi)}$). With an error strength of $D = 5\%$ the robustness of the two-qubit cluster state is observed with entanglement of $EOF > 97.5\%$, while for a larger error of $D = 10\%$, the $EOF > 92.5\%$, Fig.5.10 .

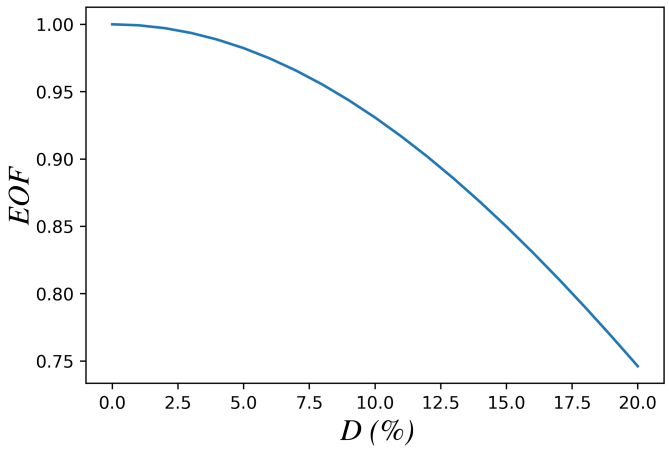

Figure 5.10: The robustness of the $\overline{EOF}$ between sites 1 and 12 at $t = 3t_m$. This is performed for different error scales, D, with a step size of 0.01.

5.3 Summary

In this chapter, we propose a different approach to design our SN system using a general unitary transformation, as opposed to the matrix-based unitary transformation discussed in the previous chapters. This approach allows us to build a SN that works for any-excitation subspace. We have then presented the generation of two-qubit entangling gate with a protocol that uses $|+\rangle$ states injection and phase flips application, in which the system evolves in the zero- single- and two-excitation subspace. Such a two-qubit entangling gate can be used in measurement-based quantum computers [178–181, 189].

Different types of disorder have been considered in order to investigate the robustness of the two-qubit entangling gate: diagonal and off-diagonal disorder, excitation-excitation interaction, time delay in the initial injected $|+\rangle$ states, time delay in the phase application time, and error in the applied phase angle. We note that in both, time error and phase error, the robustness is independent of whether $D > 0$ or $D < 0$. The results suggest that the excitation-excitation interaction has a very weak effect on the system, and it becomes even weaker in larger SN systems, as this effect only results when the two excitations are actual nearest neighbours, which generally only occurs in a small fraction of the amplitudes that comprise the total state. On the other hand, the most damaging type of error is the time error in the phase application. The reason that the phase timing error has a much impact on the system can be attributed to the fact that the desired state that we need to achieve requires the sudden application of the phase and therefore applying the phase even at a slightly different time will have a much impact on

the amplitude of the desired state. Therefore, the error from the phase application time is the one that the experimentalists should focus on reducing.

Chapter 6

Conclusion

This thesis presents complex quantum spin networks that are designed by unitarily transforming uncoupled spin chains and that have the potential to be used in various QIP protocols with excellent robustness to errors. We used PST spin chains, which have been proven to be useful for routing quantum information and entanglement generation [11,74,82,88,99–101,185,193], as the basic building blocks of our SN systems. We will summarise below the unitary construction method we used to design our spin-chain-based SN systems, the applications of such systems in quantum technology, their robustness to disorder and the scalability, the operation times vs coherence times, the physical realisations and advantages of SN systems, and will conclude with a number of suggestions for future work.

6.1 Unitary transformation method

In order to design a SN system by coupling together spin chain systems, one can utilise the transformation method, which can be used to mathematically expand (transform) an USC into a complex SN system. Such a transformation ensures that the resultant SN system will have the same features (i.e., PST) as the original system (spin chains). The unitary transformation we use is a Hadamard-like unitary, which can be implemented with two different but otherwise equivalent methods.

A simple method to design the SN system is to apply a matrix-based Hadamard-like unitary to the Hamiltonian matrix of the USC systems. This unitary matrix is given in the single-excitation basis and therefore is only used when we are restricted to the single-excitation subspace. An equivalent method to design the SN is to apply a general unitary transformation to the Hamiltonian of the USC systems. This is useful when we are considering a multi-excitation subspace. Such

unitary transformation is designed to couple a site from one chain to a site from another chain. Additional transformations can be used to couple further chains to the system.

The resultant SN system will have $M-1$ diamond shapes of four couplings (for a SN constructed from M chains), with one of these couplings having a negative sign for each diamond which is induced by the transformation (see Fig.3.4 for example). The important point here is that the transformation step is a mathematical step that is used to ensure that the SN generated has the same features (i.e., PST) that the original spin chains have. The Hadamard-like unitary we used is only one specific example, but clearly there are many other unitaries to choose from. We emphasise that the flexibility and power of the unitary design approach allows us to choose a different unitary (i.e., rotation unitary) that results in a SN with the negative coupling being between different sites than the one labeled in this thesis (that results from the Hadamard unitary). Therefore, when realising this SN experimentally, one can choose any of the four diamond-shaped couplings to be negative. Note that in this case, i.e., choosing a different unitary to design the SN, the desired states and global phases one can obtain for a specific quantum information task will be different to those we obtained in the examples given in this thesis. This is not a problem, but rather a crucial consideration when implementing our SN systems. The final important point, designing a SN with a rotation matrix type of approach, it is also possible to use an angle, ϑ, that is not $\pi/4$ which would change the weights.

6.2 Applications of our SN systems

We have shown in this thesis that many possible quantum information tasks can be achieved using our SN systems. These useful tasks are necessary for current quantum technology (e.g., quantum sensing or fundamental quantum mechanics investigations) and future quantum technology (e.g., quantum devices). For instance, routing quantum information (here, single-excitation or a superposition state of zero and one excitation) from one end of the SN system to the other end can be used to connect quantum registers in a quantum device. Therefore, they are suitable for short-range quantum communications. We have shown that routing can be generated in any of our SN systems, as it only requires single-excitation injection or preparation of the initial site state as a superposition of zero and one

excitation, Hamiltonian evolution, and a phase flip operation.

Our SN can also be used in quantum sensing related to retrieving an unknown phase applied at a qubit. This is, for example, useful in cases where a black box in an experiment injects an unknown phase factor of $e^{i\theta}$ at a qubit. Measuring the fidelity of a site at a later time and using our phase-sensing protocol, we can retrieve the unknown phase with very good accuracy, even with high fabrication error in the SN.

Entanglement generation is another useful quantum information task that has in fact been achieved in our SN systems. We have shown that various entangled states can be achieved in multi-chain SN systems. If one needs a bipartite maximally entangled state, then the use of the two-chain SN system is sufficient to achieve this. Generating a TWS or MWS entanglement, on the other hand, requires a SN of at least three chains (two diamonds). This is because each diamond can evolve an excitation through two paths, and therefore an excitation, in a SN of two diamonds, can be distributed between three (TWS) or four (MWS) qubits, depending on the injection protocol used (see Fig.4.4 and Fig.4.5, for examples). A generalisation of how many chains would be needed for N-qubit W state (with $N > 4$) could be made by investigating how such states can be generated, which is an interesting future work. One can also use our SN system to generate the MWS entanglement between distant qubits by first generating it between nearby qubits and then moving the entanglement apart with the application of phase flip and Hamiltonian evolution. Such entangled states can be useful for quantum teleportation, quantum secure direct communication, superdense coding, and Bell inequality tests for demonstrating quantum non locality [107–110]. We have also demonstrated the generation of a two-qubit entangling gate in our SN systems via injection of $|+\rangle$ states at sites 1 and N.

6.3 Advantages of our SN systems

Our SN systems have an advantage over spin chain systems with respect to the versatility of the SN, without the need to re-engineer its coupling parameters for each quantum information task. This is because a possible downside of spin chains is that while routing a single-excitation can be achieved with a specific coupling arrangement (symmetrically distributed around the centre of the chain), the same coupling arrangement does not allow entanglement generation using the

single-excitation. This is because the couplings now need to be re-engineered in another arrangement (e.g., using weak/strong couplings technique [99]). Our SN, on the other hand, can generate the routing, entanglement, and many other useful quantum information tasks without the need to re-engineer the coupling parameters. The only cases where adjustment of the couplings is required in our SN systems are where the chains of the SN are of different lengths. Therefore, in a SN of equal chains, one can route a single-excitation and re-initialise the system such that all sites have a spin down state, using the relevant initialisation technique of the relevant physical system, then use another QIP protocol (e.g., generation of bipartite or TWS entanglement) in the same SN system. The versatility of our SN system in generating various QIP protocols in the same SN system could be an experimentally-friendly feature and therefore might potentially be useful in future QIP technologies that aim to provide various QIP in a single device.

Another advantage of our SN systems compared to an equivalent long spin chain is that multi-chain SN could be more accessible experimentally, depending on hardware. The reason for this is because the energy difference between the maximum coupling interaction and the minimum coupling interaction (J_{diff}, Eq.(4.22)) is larger in a spin chain of size N compared to an equivalent long multi-chain SN of size N. With larger spin chain and larger multi-chain SN, the J_{diff} becomes much larger in the spin chain compared to the SN (this is illustrated in the appendix E).

6.4 Disorder and scalability effects

We have investigated the effects of various types of disorder in the system. One type of disorder is that arising due to an imperfect construction of the SN (coupling errors or on-site energy errors). We acknowledge that there may be other forms of error, specific to particular realisations of the SN systems, but we are considering generic errors that could apply to a wide range of realisations. The effects of the errors on the Hamiltonian (diagonal or off-diagonal disorder) turn out to be distinguishable, as diagonal disorder has only a weak effect compared to off-diagonal disorder. We have shown that the high sensitivity of the system to off-diagonal disorder can be attributed to the fact that the non-zero energies are distributed on wider energy scale in the presence of off-diagonal disorder, compared to the case of diagonal disorder. This suggests that experimentalists should focus on reducing the off-diagonal disorder in the physical implementation of our SN systems.

We note that our investigations of the effect of fabrication errors illustrate that the averaged fidelity/EOF, of a desired task, decays over time. This, as we explained in Section 2.3, is due to the averaging procedure we employ. Nevertheless, our model, through the averaging procedure we apply, can also be viewed as a simplified example of an open system. This is because it mimics the expected dynamic behavior of a single device interacting with an environment, exhibiting decay of a desired operation due to decoherence and relaxation. As a result, one could tune our disorder model in order to compare the typical decoherence and relaxation times, of a specific physical system, with our error strength E.

Other forms of error include those arising in the protocols that one uses to generate a specific quantum information task. For example, generation of the routing protocol or an entangled state protocol requires application of a phase factor at a specific site at a specific time. However, such an operation might not be perfect in experiment as there might be a timing error in the phase application, and/or an error in the angle of the phase, and/or measurement-time error. These possibilities have been considered in our investigations, from which it turns out that error in the phase application time is the most damaging type of error. This is because the phase application step needs to be a sudden operation in order to deliver the desired state, and so a timing error in the phase will have a considerable impact on the desired state. Therefore, phase time error is another type of error that one should keep as small as possible in physical realisations of our SN systems. We also found that our SN behaviour against fabrication errors (diagonal and off-diagonal errors) or protocols errors (timing and phase angle errors) follows a Gaussian distribution as a function of error scale parameter.

In all the QIP protocols investigated in this thesis, the scalability (increasing the SN size) seems to have a lower impact on the system performance compared to the increase in the error strength. Furthermore, we have shown that scaling the SN by connecting a larger number, M, of spin chains, while keeping the number of sites, N_j, per chain fixed, shows similar robustness against disorder to the case of scaling the SN by increasing N_j for the chain while keeping M fixed.

6.5 Decoherence vs Operation times

According to the DiVincenzo criteria (Section 1.1.2), it is necessary that the time required to perform a quantum information processing protocol is significantly

shorter than the decoherence time of the relevant system. We examine this criterion in our system by investigating the operation time of the two-qubit entangling gate (Eq. (5.26)) generated in the SN system (Fig.4.13) against the coherence time for various physical systems.

The two-qubit entangling gate is generated at $3t_m$ and this time is given as $3t_m = \frac{3\pi}{2J_0}$, where $J_0 = \frac{2J_{max}}{N_j}$ with $N_j = 4$, which is the number of sites in each chain of the SN (see Section 2.1.5). Thus, $3t_m = \frac{3\pi}{J_{max}}$. We now compare the entangling gate time and coherence time for different physical systems. Using the values of characteristic energy J_{max} and coherence time T_c, given in Section 1.2.4 for various physical systems, we construct a table showing this comparison (see Fig.6.1).

Entangling times vs. Decoherence			
Platform	**Characteristic energy, J_{max}**	**Entangling time**	**Coherence time, T_c**
Silicon QDs	900 MHz	10 ns	8.3 μs
Trapped $^{171}YB^{+}$ ions	0.6 kHz	0.02 s	0.5 s
Superconducting qubits	50 MHz	0.18 μs	10 μs
Rydberg atoms	685 MHz	13.7 ns	1.3 μs

Figure 6.1: Comparison of the entangling gate time ($3t_m$) against the coherence time (T_c) for various physical systems.

Note that we have considered a relatively large SN system (see Fig.4.13) to quantify the operation time of the two-qubit entangling gate against the coherence time, from which we found that the entangling time remains much shorter than the coherence time for all the physical systems considered here. Particularly, for Silicon QDs and Rydberg atoms, the entangling time is found to be many orders of magnitude shorter than the coherence time.

6.6 Physical realisations of our SN systems

The building blocks of our spin-chain-based SN systems, as the name suggests, are systems of PST spin chains. A spin chain, as already introduced in Chapter 1, is a generic model that represents a chain of spin-1/2 like particles and can be

realised in various physical systems. Examples include trapped ions, quantum dots, superconducting qubits, Rydberg atoms, and NMR-based processors. A detailed discussion on each platform is given in Section 1.2.4.

Realising our SN systems physically requires preparation of systems of spin chains with additional couplings that connect these chains in order to form the SN. The spin chains need to be connected in a way that form a diamond-like shape of four couplings connecting the spin chain. The energy of these four couplings needs to be rescaled by $\frac{1}{\sqrt{2}}$, with one of them being negative. This ensures that the resultant SN system will be exactly identical to the one designed in this thesis, with the condition that the negative coupling need to be at the bottom right coupling of the diamond couplings. Building a SN with these conditions, one can use any QIP protocol illustrated in this thesis.

Clearly, as discussed in the unitary section above, we could choose another unitary transformation to place the negative coupling on any one of the four diamond-shaped couplings, as the SN will still be capable of delivering useful quantum information tasks. Therefore, experimentalists may choose the most suitable coupling to be assigned as negative in their physical realisation of the SN, as long as it is assigned to one of the four diamond-shaped couplings. Theory and modelling can then determine the precise form of the entangled states generated, or the phase injection required (and at which site) to perform the desired routing.

Realising Our SN systems experimentally can be done using various physical systems, as discussed in Section 1.2.4. Particularly, systems that are experimentally realised in a two-dimensional structure, which is important as our SN systems has couplings prepared in a two-dimensional structure (the diamond-like shape). Examples include qubits of Rydberg atoms, which have been experimentally realised in a two-dimensional structure, and such platform can therefore be used to realise our SN systems [64, 65, 124–127]. Superconducting transmon qubits have also been used to experimentally implement a two-dimensional tight-binding lattice [60], which resembles our Hamiltonian model and could be adapted to resemble our SN topology. Trapped ions have also been used to experimentally realise a two-dimensional SN system [194–196]. The reference [196] also shows that the sign of the coupling interaction between two sites can be tuned to be negative using Raman detunings. The four diamond-shaped couplings, one of which being negative, have indeed been investigated in [80] and it has also been shown that such negative coupling is realisable using Feshbach resonances in optical lattices [80, 197–199].

6.7 Future work

With respect to the SN design, we have used a Hadamard-like unitary, but clearly there are many unitaries to choose from. One can design and investigate a SN built using a unitary that differs from our own by a rotation. Moreover, one can choose a different angle for the unitary such that it will result in the SN being biased, with respect to the excitation evolution, toward a specific direction. Note that such a biased evolution can be achieved in our SN with the application of a specific phase factor. However, instead, this can be achieved from the construction step of the SN itself by using the appropriate unitary. Further investigation of unitary construction would be to use various random unitaries and investigate their resulted SN systems. Another interesting future work is to explore and investigate how N-partite entanglement (with $N > 4$) can be achieved in our SN systems.

Our investigation of disorder is general and can be applied to various physical systems. However, each physical system has its own particular types of disorder. For example, the errors that might arise in quantum dots may be different from those arising in superconducting qubits. Therefore, one can model a specific realisation by further adapting our SN modelling to include a specific form of error. Investigation of the effect of imperfect addressing of phase factor applications (i.e., when the applied phase at a site also affects neighbouring sites) is also an interesting area for further research.

Finally, our investigation of the multiple-excitation subspace included investigating a two-chain SN and a three-chain SN. A further step would be to investigate cases where the chains of the SN are of different lengths or have a larger number of excitations. Furthermore, more complicated topologies of connected chains could represent another significant research direction.

Appendix A

Rotation unitary

We used a Hadamard-like unitary transformation to couple together USC systems. However, this is not the only way to do it; instead, we can use a rotation matrix. For example, to couple together two USC, each of 3-site, we can apply a rotation matrix of the form

$$U_\vartheta = \begin{pmatrix} 1 & 0 & 0 & 0 & 0 & 0 \\ 0 & 1 & 0 & 0 & 0 & 0 \\ 0 & 0 & \cos(\vartheta) & -\sin(\vartheta) & 0 & 0 \\ 0 & 0 & \sin(\vartheta) & \cos(\vartheta) & 0 & 0 \\ 0 & 0 & 0 & 0 & 1 & 0 \\ 0 & 0 & 0 & 0 & 0 & 1 \end{pmatrix} \tag{A.1}$$

Here, $U_\vartheta^\dagger \neq U_\vartheta$ and with $\vartheta = \frac{\pi}{4}$.

When we use this to transform the USC Hamiltonian, we will still get a similar SN system to that we designed before (Fig.3.4), but with a minus coupling being between sites 3 and 5. Previously, where we used the Hadamard-like transformation, the negative coupling was between sites 4 and 5. With a different unitary transformation, we can choose where the negative coupling in the SN can be. It basically can be at any coupling in the SN diamond depending on the unitary rotation. Therefore, experimentalists can choose which coupling of the SN diamond is negative. Note that using a SN that has a negative coupling in a different place than where we set the negative coupling in our SN (e.g., between sites 2 and 4) will mean that the desired states and the global phases that one can obtain will be different than what we obtained in the examples given in thesis. This should not be an issue but rather an important point to take into account when physically realising our SN system.

Appendix B

Derivation of F_1

B.1 Eigenvalues and Eigenvectors of the Hamiltonian

The eigenvalues and eigenvectors of the Hamiltonian $\mathcal{H}_{XY}$ are given in table B.1. They are expressed in the site basis as labelled in Fig.(3.4).

Eigenvalues	Eigenvectors
$\lambda_1 = -\sqrt{2}J$	$\lvert\varphi_1\rangle = \frac{1}{2\sqrt{2}} \begin{pmatrix} \sqrt{2} \\ -2 \\ 1 \\ 1 \\ 0 \\ 0 \end{pmatrix}$
$\lambda_2 = -\sqrt{2}J$	$\lvert\varphi_2\rangle = \frac{1}{2\sqrt{2}} \begin{pmatrix} 0 \\ 0 \\ -1 \\ 1 \\ 2 \\ -\sqrt{2} \end{pmatrix}$
$\lambda_3 = \sqrt{2}J$	$\lvert\varphi_3\rangle = \frac{1}{2\sqrt{2}} \begin{pmatrix} \sqrt{2} \\ 2 \\ 1 \\ 1 \\ 0 \\ 0 \end{pmatrix}$
$\lambda_4 = \sqrt{2}J$	$\lvert\varphi_4\rangle = \frac{1}{2\sqrt{2}} \begin{pmatrix} 0 \\ 0 \\ 1 \\ -1 \\ 2 \\ \sqrt{2} \end{pmatrix}$
$\lambda_5 = 0$	$\lvert\varphi_5\rangle = \frac{1}{2} \begin{pmatrix} -\sqrt{2} \\ 0 \\ 1 \\ 1 \\ 0 \\ 0 \end{pmatrix}$
$\lambda_6 = 0$	$\lvert\varphi_6\rangle = \frac{1}{2} \begin{pmatrix} 0 \\ 0 \\ -1 \\ 1 \\ 0 \\ \sqrt{2} \end{pmatrix}$

Table B.1: Eigenvalues (left) and eigenvectors (right) of the Hamiltonian $\mathcal{H}_{XY}$

B.2 Analytical Calculation of Relevant System Evolution and Related Fidelities

Our two 3-site-chain SN is first prepared such that all sites have spin down $|00\ldots\rangle$. Since the Hamiltonian of our system preserves the number of spin up (down), the system will not evolve unless an excitation is injected to the system. Therefore, when a single-excitation is injected at site 1 at $t = 0$

$$|\Psi(0)\rangle = |r_1\rangle \tag{B.1}$$

the system will start evolving within the single-excitation (single spin-up) subspace. We can find the system state at later time by decomposing the initial state $|\Psi(0)\rangle$ into the eigenvectors of the Hamiltonian (table B.1) using the following decomposition equation

$$|\Psi(t)\rangle = \sum_{j=1}^{N} \langle\varphi_j|\psi_1(0)\rangle\, e^{-i\lambda_j t}\, |\varphi_j\rangle\,, \tag{B.2}$$

where $|\varphi_j\rangle$ are the eigenvectors, and λ_j are the eigenvalues. Therefore, the state of the system at t_m will be

$$|\Psi(t_m)\rangle = -\frac{1}{\sqrt{2}}(|r_3\rangle + |r_4\rangle). \tag{B.3}$$

If now an unknown phase $e^{i\theta}$ is instantaneously applied at site 4, the state of the system becomes

$$|\Psi(t_m)\rangle_\theta = -\frac{1}{\sqrt{2}}(|r_3\rangle + e^{i\theta}\,|r_4\rangle). \tag{B.4}$$

By decomposing the state Eq. (B.4) into the eigenvectors of the Hamiltonian, using Eq. (B.2), and then evolving the system for an additional time $t = t_m$, the state of the system at $2t_m$ can be found to be

$$|\Psi(2t_m)\rangle = \frac{1 + e^{i\theta}}{2}\,|r_1\rangle + \frac{1 - e^{i\theta}}{2}\,|r_6\rangle\,. \tag{B.5}$$

Therefore, Eq. (B.5) determines the occupation of site 1 and site 6 depending on the unknown phase θ.

The fidelity against $|r_1\rangle$ at $2t_m$ is then

$$\begin{aligned} |\langle r_1|\Psi(2t_m)\rangle|^2 &= |\frac{1+e^{i\theta}}{2}\langle r_1|r_1\rangle + \frac{1-e^{i\theta}}{2}\langle r_1|r_6\rangle|^2 \\ &= |\frac{1+e^{i\theta}}{2}|^2 = |e^{i\frac{\theta}{2}}(\frac{e^{-i\frac{\theta}{2}}+e^{i\frac{\theta}{2}}}{2})|^2 \\ &= \cos^2\frac{\theta}{2} = \frac{1+\cos(\theta)}{2} \\ &= \frac{1}{2}(1+\cos\theta) = F_1. \end{aligned} \tag{B.6}$$

We now have the fidelity against $|r_1\rangle$ at $2t_m$ as a function of θ which can be used in our sensing protocol by measuring the fidelity against $|r_1\rangle$. However, if we choose to measure the fidelity against $|r_6\rangle$ instead, then the sensing protocol will still work with a slight modification as the fidelity against $|r_6\rangle$ differs from the fidelity against $|r_1\rangle$, and can be calculated in a similar way.

Appendix C

Eigenvalues and Eigenstates of the Hamiltonian of the SN shown in Fig.(3.20)

The eigenvalues and Eigenstates of the Hamiltonian $\mathcal{H}_{XY}$ are given in table C.1. They are expressed in the site basis as labelled in Fig.(3.20).

Eigenvalues	Eigenstates
$\lambda_1 = -\sqrt{2}$	$\|\varphi_1\rangle = \begin{pmatrix} 1/2 \\ -1/\sqrt{2} \\ 1/2\sqrt{2} \\ 1/2\sqrt{2} \\ 0 \\ 0 \\ 0 \end{pmatrix}$
$\lambda_2 = 0$	$\|\varphi_2\rangle = \begin{pmatrix} -1/\sqrt{2} \\ 0 \\ 1/2 \\ 1/2 \\ 0 \\ 0 \\ 0 \end{pmatrix}$
$\lambda_3 = \sqrt{2}$	$\|\varphi_3\rangle = \begin{pmatrix} 1/2 \\ 1/\sqrt{2} \\ 1/2\sqrt{2} \\ 1/2\sqrt{2} \\ 0 \\ 0 \\ 0 \end{pmatrix}$
$\lambda_4 = \frac{3}{2}$	$\|\varphi_4\rangle = \begin{pmatrix} 0 \\ 0 \\ 1/4 \\ 1/2\sqrt{2} \\ \sqrt{3}/2\sqrt{2} \\ \sqrt{3}/2\sqrt{2} \\ -1/4 \end{pmatrix}$
$\lambda_5 = \frac{1}{2}$	$\|\varphi_5\rangle = \begin{pmatrix} 0 \\ 0 \\ \sqrt{3}/4 \\ -\sqrt{3}/2\sqrt{2} \\ -1/2\sqrt{2} \\ 1/2\sqrt{2} \\ -\sqrt{3}/4 \end{pmatrix}$
$\lambda_6 = \frac{-1}{2}$	$\|\varphi_6\rangle = \begin{pmatrix} 0 \\ 0 \\ -\sqrt{3}/4 \\ -\sqrt{3}/2\sqrt{2} \\ 1/2\sqrt{2} \\ 1/2\sqrt{2} \\ \sqrt{3}/4 \end{pmatrix}$
$\lambda_7 = \frac{3}{2}$	$\|\varphi_7\rangle = \begin{pmatrix} 0 \\ 0 \\ -1/4 \\ 1/2\sqrt{2} \\ -\sqrt{3}/2\sqrt{2} \\ \sqrt{3}/2\sqrt{2} \\ 1/4 \end{pmatrix}$

Table C.1: Eigenvalues (left) and Eigenstates (right) of the Hamiltonian $\mathcal{H}_{XY}$

Appendix D

Excitation amplitudes evolving different phases

In the SN system shown in Fig.4.13, injecting a single-excitation at site 5 at $t = 0$ will result in the excitation being evolving through both chains of the SN. An excitation amplitude evolves through the chain A of length N_A and another amplitude evolves through the chain B of length N_B. The state at later time is determined by the different phases that result from the excitation amplitudes evolving through A and B, as we now describe.

Consider the excitation amplitude that evolves through A. This will evolve to site 1 at $t_{m,A}$ with an overall phase factor of $e^{-i\alpha(N_A)} = (-i)^{N_A-1} = i$, as $N_A = 4$. Thus, the excitation amplitude at site 1 at $t_{m,A}$ will be given by

$$|site_1(t_{m,A})\rangle = \frac{i}{\sqrt{2}} |r_1\rangle \,. \tag{D.1}$$

Then, this excitation amplitude evolves back from site 1 to being in a superposition state between sites 4 and 5, acquiring another overall phase of i, so the amplitude at $2t_{m,A}$ will now be given with an overall phase of -1,

$$|site_{4,5}(2t_{m,A})\rangle = -\frac{1}{2}(|r_4\rangle + |r_5\rangle). \tag{D.2}$$

Evolving the system for another duration of $2t_{m,A}$, the amplitude at $4t_{m,A}$ will be given by

$$|site_{4,5}(4t_{m,A})\rangle = \frac{1}{2}(|r_4\rangle + |r_5\rangle). \tag{D.3}$$

Consider now the other amplitude of the excitation, that evolves through chain B, which by design has weaker couplings. This will therefore take twice the time that the excitation amplitudes take to evolve through chain A, so $t_{m,B} = 2t_{m,A}$.

The amplitude of the single excitation injected at site 5 that evolves through the chain B ends up in a superposition state between sites 8 and 9 at $t_{m,B}$, with an overall phase factor of $(-i)^{N_B-1} = i$, but in addition because the coupling between sites 5 and 6 is negative, the overall phase is $-i$,

$$|site_{8,9}(t_{m,B})\rangle = -i\frac{1}{2}(|r_8\rangle + |r_9\rangle). \tag{D.4}$$

Following this, the excitation amplitude will evolve back to being in a superposition state between sites 4 and 5 at $2t_{m,B}$, with another overall phase of i and a further relative phase of -1 at site 5 because of the negative coupling between sites 5 and 6. Thus, the amplitude at $2t_{m,B}$ will be given by

$$|site_{4,5}(2t_{m,B})\rangle = \frac{1}{2}(|r_4\rangle - |r_5\rangle). \tag{D.5}$$

We have seen how the excitation amplitudes evolve through each chain. These can be combined to give the state of the system at $2t_{m,B}$, which will simply be the sum of equations Eq.(D.3) and Eq.(D.5), as $2t_{m,B} = 4t_{m,A}$, so the state of the system at $2t_{m,B}$ is given as

$$|\psi(2t_{m,B}\rangle = \frac{1}{2}(|r_4\rangle + |r_5\rangle + |r_4\rangle - |r_5\rangle) = |r_4\rangle\,. \tag{D.6}$$

It is now clear that if there is no difference in the excitation time through each chain (i.e., $t_{m,A} = t_{m,B}$), then the state of the system at $2t_{m,B}$ will simply be the sum of Eq.(D.2) and Eq.(D.5), as $2t_{m,B} = 2t_{m,A}$, so the state would be given as

$$|\psi(2t_{m,B}\rangle = \frac{1}{2}(-|r_4\rangle - |r_5\rangle + |r_4\rangle - |r_5\rangle) = -|r_5\rangle\,. \tag{D.7}$$

We note that if we evolve for another $2t_{m,B}$, then both equations (Eq.(D.6) and Eq.(D.7)) will evolve back to $|r_5\rangle$, demonstrating periodicity with period $4t_{m,B}$.

Appendix E

Difference between C_{max} and C_{min} for multi-chain SN and spin chain systems

We show the difference between C_{max} and C_{min} (J_{diff}, Eq. (4.22)), for a spin chain system and a multi-chain SN system, both of the same size N. This is done for various N and various multi-chain SN systems (three-chain SN, four-chain SN, five-chain SN, and six-chain SN). The plots demonstrate that J_{diff} is larger in spin chain systems and increases as the number of chains in the multi-chain SN increases, Fig.E.1.

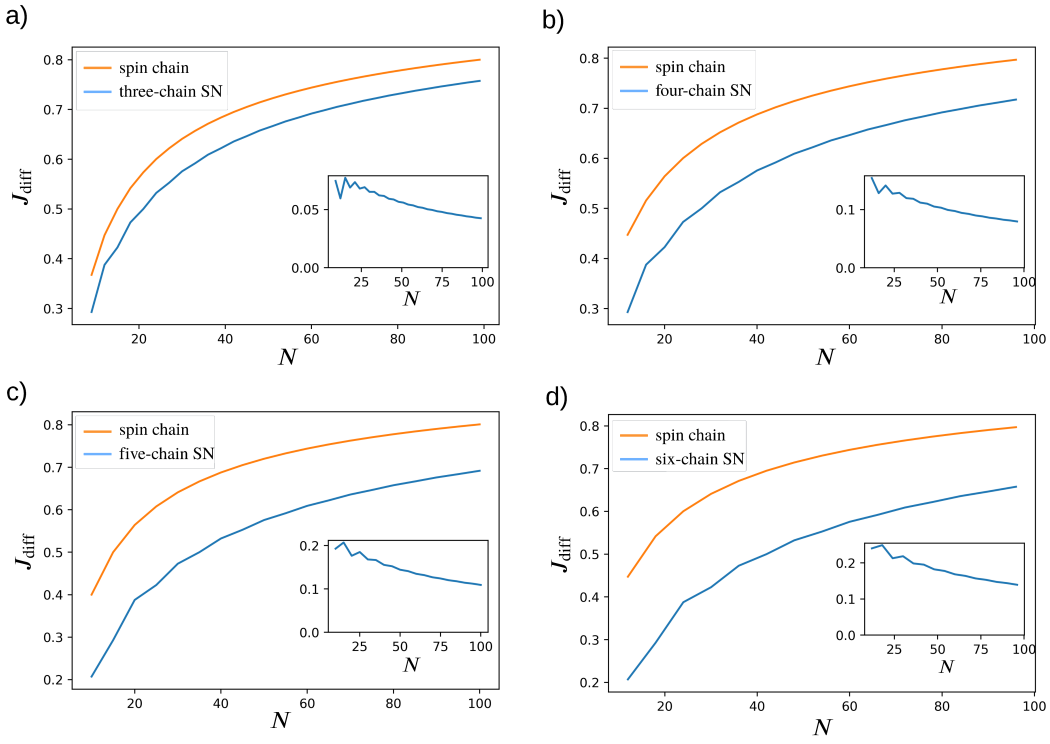

Figure E.1: The difference between the largest coupling C_{max} and the smallest coupling C_{min} (J_{diff}, Eq. (4.22)) for a spin chain of size N and a multi-chain SN of the same size N. This is done for various N and for various multi-chain SN. a) three-chain SN, b) four-chain SN, (c) five-chain SN, and (d) six-chain SN. Inset: the difference between the values obtained from spin chains and the values obtained from multi-chain SN.

Appendix F

Optimal number of chains in an SN

The plot shown in Fig.F.1 (blue line) illustrates that the effect of fabrication errors (coupling and on-site energy errors), on the averaged routing fidelity, is similar for all the different SN systems, which is in agreement with what has been shown previously in Fig.4.29. On the other hand, the effect of phase timing errors becomes more damaging to the fidelity as the SN contains more chains, Fig.F.1 (orange line). This is expected, as a SN with more chains contains more diamonds, and so the effect of the phase timing error (that occurs with each diamond) becomes more dominant. The plot also shows that J_{diff} (Eq.(4.22)) becomes smaller as the SN contains more chains, Fig.F.1 (green line).

It can be observed from Fig.F.1 that there is a trade-off between the phase timing error (which becomes more damaging with SN containing more chains) and the value of J_{diff}, Eq. (4.22), (which is better, at least for some implementations, with SN containing more chains). The highest fidelity observed, in the presence of phase timing errors, is $\approx 89\%$ for the three-chain SN, from which the J_{diff} is observed to be ≈ 0.39. Smaller values of J_{diff} can be observed for SN systems containing more chains, but this comes at the cost of smaller fidelity. Therefore, we can find the optimal SN by considering the figure of merit $\text{Opt}_{\text{SN}} = J_{\text{diff}}/\overline{F}(t)$ and determine its minimum. This is because for the perfect case, $J_{\text{diff}} = 0$ and $\overline{F}(t) = 1$, the figure of merit $\text{Opt}_{\text{SN}} = 0$, while for the worst case, $J_{\text{diff}} = 1$ and $\overline{F}(t) = 0$, the figure of merit $\text{Opt}_{\text{SN}} = \infty$. The averaged fidelity $\overline{F}(t)$ used in the figure of merit is the orange dotted line shown in Fig.F.1(a). By analysing each SN with the Opt_{SN} figure of merit we find that the six-chain SN might be the optimal SN, as it has the lowest Opt_{SN} of ≈ 0.25.

From another perspective, choosing which SN is the optimal SN might depend

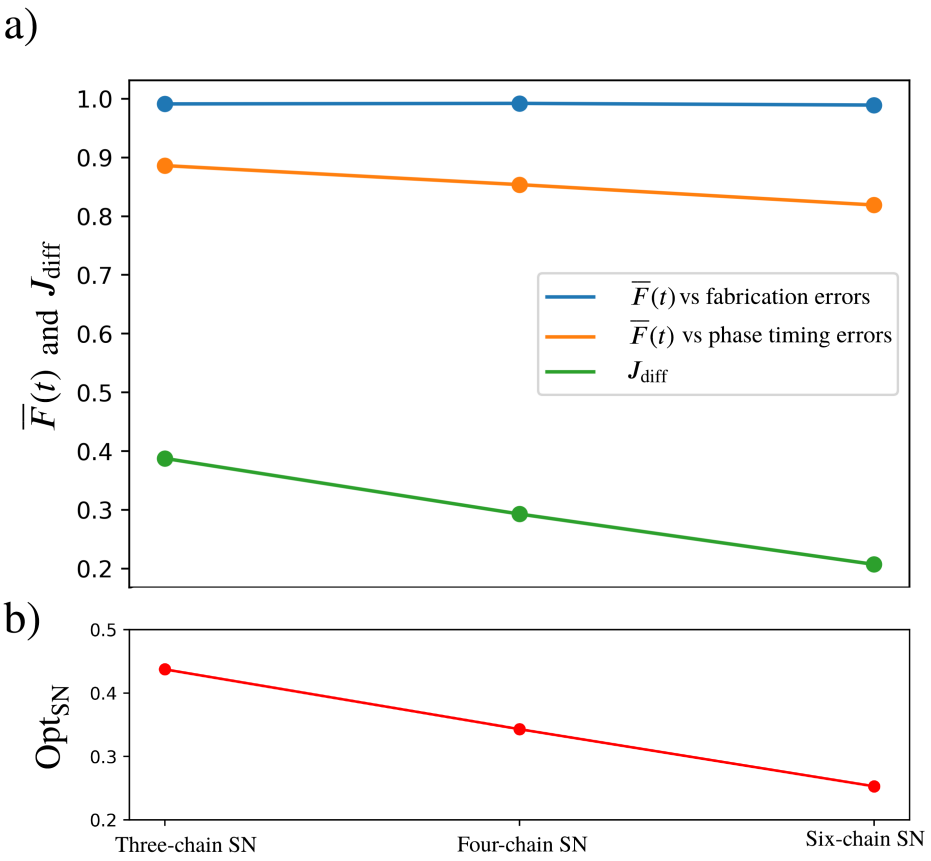

Figure F.1: a) The averaged routing fidelity $\overline{F}(t)$, when it is measured at the first time it forms, in the presence of fabrication errors (blue) and phase timing error (orange), with error strength of 5%. The difference between the maximum and minimum couplings, J_{diff}, for each SN is also plotted (green). b) The figure of merit Opt_{SN}. The total number of sites in each SN is $N = 12$.

on experimental preferences. For example, if in a practical situation, the value of J_{diff} is not an issue, meaning that the system can be built regardless of the value of J_{diff}, then one could use the three-chain SN, as it has the highest fidelity in the presence of phase timing error, Fig.F.1 (orange line). On the other hand, if the effect of the phase timing error is controlled and kept very small, then one may use SN containing more chains (e.g., six-chain SN) because it has smaller J_{diff}. Therefore, with more details of the physical preferences, on whether J_{diff} is not a constraint (i.e., the system can be easily built even when J_{diff} is large), or whether the phase timing error can be kept small. One can choose the optimal SN by trading off between the two.

Appendix G

Derivation of Eq.(5.7)

Since we want to superpose sites 2 and 3, the operators that we need for the unitary transformaction are $\Sigma_- = \sigma_2^+\sigma_3^- - \sigma_3^+\sigma_2^-$ and $P = n_2^\uparrow n_3^\downarrow + n_2^\downarrow n_3^\uparrow$. Applying the transformation unitary, Eq.(5.4), on the Hamiltonian of two USC, Eq.(5.6), as $(e^{-\vartheta\Sigma_-})H_{XY}(e^{\vartheta\Sigma_-})$ will give us the transformed Hamiltonian $\mathcal{H}_{XY}$ that represents the SN. We will now solve this transformation step by step.

First, we will solve $H_{XY}e^{\vartheta\Sigma_-}$. This is expanded as

$$H_{XY}e^{\vartheta\Sigma_-} = H_{XY} - H_{XY}P + H_{XY}P\cos(\vartheta) + H_{XY}\Sigma_-\sin(\vartheta). \tag{G.1}$$

The second term of Eq.(G.1) is expanded as

$$\begin{aligned} -H_{XY}P = &-\sigma_1^+\sigma_2^-n_2^\uparrow n_3^\downarrow - \sigma_1^+\sigma_2^-n_2^\downarrow n_3^\uparrow - \sigma_2^+\sigma_1^-n_2^\uparrow n_3^\downarrow - \sigma_2^+\sigma_1^-n_2^\downarrow n_3^\uparrow \\ &+ \sigma_3^+\sigma_4^-n_2^\uparrow n_3^\downarrow + \sigma_3^+\sigma_4^-n_2^\downarrow n_3^\uparrow + \sigma_4^+\sigma_3^-n_2^\uparrow n_3^\downarrow + \sigma_4^+\sigma_3^-n_2^\downarrow n_3^\uparrow, \end{aligned} \tag{G.2}$$

but since the operators at different sites commute and $\sigma_i^+n_i^\uparrow = (\sigma_i^+)^2\sigma_i^- = 0$ and $\sigma_i^-n_i^\downarrow = (\sigma_i^-)^2\sigma_i^+ = 0$, the 2nd, 3rd, 6th, and 7th terms vanish, so Eq.(G.2) is given by

$$-H_{XY}P = -\sigma_1^+\sigma_2^-n_2^\uparrow n_3^\downarrow - \sigma_2^+\sigma_1^-n_2^\downarrow n_3^\uparrow + \sigma_3^+\sigma_4^-n_2^\uparrow n_3^\downarrow + \sigma_4^+\sigma_3^-n_2^\downarrow n_3^\uparrow. \tag{G.3}$$

Similarly, the third term of Eq.(G.1) is expanded as

$$H_{XY}P\cos(\vartheta) = \cos(\vartheta)\left[\sigma_1^+\sigma_2^-n_2^\uparrow n_3^\downarrow + \sigma_2^+\sigma_1^-n_2^\downarrow n_3^\uparrow - \sigma_3^+\sigma_4^-n_2^\uparrow n_3^\downarrow - \sigma_4^+\sigma_3^-n_2^\downarrow n_3^\uparrow\right]. \tag{G.4}$$

With the fact that $\sigma_i^+\sigma_i^- = n_i^\uparrow$ and $\sigma_i^-\sigma_i^+ = n_i^\downarrow$, the last term of Eq.(G.1) is expanded as

$$H_{XY}\Sigma_-\sin(\vartheta) = \sin(\vartheta)\left[\sigma_1^+\sigma_3^-n_2^\downarrow - \sigma_1^-\sigma_3^+n_2^\uparrow - \sigma_4^-\sigma_2^+n_3^\uparrow + \sigma_4^+\sigma_2^-n_3^\downarrow\right]. \tag{G.5}$$

Therefore, Eq.(G.1) is written as

$$\begin{aligned} H_{XY}e^{\vartheta\Sigma_-} &= \sigma_1^+\sigma_2^- + \sigma_2^+\sigma_1^- - \sigma_3^+\sigma_4^- - \sigma_4^+\sigma_3^- \\ &+ \left[-\sigma_1^+\sigma_2^- n_2^\uparrow n_3^\downarrow - \sigma_2^+\sigma_1^- n_2^\downarrow n_3^\uparrow + \sigma_3^+\sigma_4^- n_2^\uparrow n_3^\downarrow + \sigma_4^+\sigma_3^- n_2^\downarrow n_3^\uparrow\right] \\ &+ \cos(\vartheta)\left[\sigma_1^+\sigma_2^- n_2^\uparrow n_3^\downarrow + \sigma_2^+\sigma_1^- n_2^\downarrow n_3^\uparrow - \sigma_3^+\sigma_4^- n_2^\uparrow n_3^\downarrow - \sigma_4^+\sigma_3^- n_2^\downarrow n_3^\uparrow\right] \\ &+ \sin(\vartheta)\left[\sigma_1^+\sigma_3^- n_2^\downarrow - \sigma_1^-\sigma_3^+ n_2^\uparrow - \sigma_4^-\sigma_2^+ n_3^\uparrow + \sigma_4^+\sigma_2^- n_3^\downarrow\right]. \end{aligned} \tag{G.6}$$

Now, we will calculate $e^{-\vartheta\Sigma_-}\left[H_{XY}e^{\vartheta\Sigma_-}\right]$, which is expanded as

$$\begin{aligned} e^{-\vartheta\Sigma_-}\left[H_{XY}e^{\vartheta\Sigma_-}\right] &= H_{XY}e^{\vartheta\Sigma_-} - P\left[H_{XY}e^{\vartheta\Sigma_-}\right] \\ &+ P\cos(\vartheta)\left[H_{XY}e^{\vartheta\Sigma_-}\right] - \Sigma_-\sin(\vartheta)\left[H_{XY}e^{\vartheta\Sigma_-}\right]. \end{aligned} \tag{G.7}$$

The second term of Eq.(G.7) is expanded as

$$\begin{aligned} -P\left[H_{XY}e^{\vartheta\Sigma_-}\right] &= -P\left[\sigma_1^+\sigma_2^- + \sigma_2^+\sigma_1^- - \sigma_3^+\sigma_4^- - \sigma_4^+\sigma_3^-\right] \\ &- P\left[-\sigma_1^+\sigma_2^- n_2^\uparrow n_3^\downarrow - \sigma_2^+\sigma_1^- n_2^\downarrow n_3^\uparrow + \sigma_3^+\sigma_4^- n_2^\uparrow n_3^\downarrow + \sigma_4^+\sigma_3^- n_2^\downarrow n_3^\uparrow\right] \\ &- P\cos(\vartheta)\left[\sigma_1^+\sigma_2^- n_2^\uparrow n_3^\downarrow + \sigma_2^+\sigma_1^- n_2^\downarrow n_3^\uparrow - \sigma_3^+\sigma_4^- n_2^\uparrow n_3^\downarrow - \sigma_4^+\sigma_3^- n_2^\downarrow n_3^\uparrow\right] \\ &- P\sin(\vartheta)\left[\sigma_1^+\sigma_3^- n_2^\downarrow - \sigma_1^-\sigma_3^+ n_2^\uparrow - \sigma_4^-\sigma_2^+ n_3^\uparrow + \sigma_4^+\sigma_2^- n_3^\downarrow\right]. \end{aligned} \tag{G.8}$$

Since $n_i^\uparrow\sigma_i^- = \sigma_i^+(\sigma_i^-)^2 = 0$ and $n_i^\downarrow\sigma_i^+ = \sigma_i^-(\sigma_i^+)^2 = 0$, only the first term of Eq.(G.8) survive and the remaining terms vanish, so Eq.(G.8) is given by

$$\begin{aligned} -P\left[H_{XY}e^{\vartheta\Sigma_-}\right] &= -P\left[\sigma_1^+\sigma_2^- + \sigma_2^+\sigma_1^- - \sigma_3^+\sigma_4^- - \sigma_4^+\sigma_3^-\right] \\ &= -n_2^\uparrow n_3^\downarrow\sigma_2^+\sigma_1^- + n_2^\uparrow n_3^\downarrow\sigma_4^+\sigma_3^- - n_2^\downarrow n_3^\uparrow\sigma_1^+\sigma_2^- + n_2^\downarrow n_3^\uparrow\sigma_3^+\sigma_4^-, \end{aligned} \tag{G.9}$$

and similarly the third term of Eq.(G.7) is now given by

$$P\cos(\vartheta)\left[H_{XY}e^{\vartheta\Sigma_-}\right] = \cos(\vartheta)\left[n_2^\uparrow n_3^\downarrow\sigma_2^+\sigma_1^- - n_2^\uparrow n_3^\downarrow\sigma_4^+\sigma_3^- + n_2^\downarrow n_3^\uparrow\sigma_1^+\sigma_2^- - n_2^\downarrow n_3^\uparrow\sigma_3^+\sigma_4^-\right]. \tag{G.10}$$

The last term of Eq.(G.7) is expanded as

$$\begin{aligned}
&-\Sigma_- \sin(\vartheta)\left[H_{XY}e^{\vartheta\Sigma_-}\right] = \\
&-\Sigma_- \sin(\vartheta)\left[\sigma_1^+\sigma_2^- + \sigma_2^+\sigma_1^- - \sigma_3^+\sigma_4^- - \sigma_4^+\sigma_3^-\right] \\
&-\Sigma_- \sin(\vartheta)\left[-\sigma_1^+\sigma_2^- n_2^\uparrow n_3^\downarrow - \sigma_2^+\sigma_1^- n_2^\downarrow n_3^\uparrow + \sigma_3^+\sigma_4^- n_2^\uparrow n_3^\downarrow + \sigma_4^+\sigma_3^- n_2^\downarrow n_3^\uparrow\right] \\
&-\Sigma_- \sin(\vartheta)\cos(\vartheta)\left[\sigma_1^+\sigma_2^- n_2^\uparrow n_3^\downarrow + \sigma_2^+\sigma_1^- n_2^\downarrow n_3^\uparrow - \sigma_3^+\sigma_4^- n_2^\uparrow n_3^\downarrow - \sigma_4^+\sigma_3^- n_2^\downarrow n_3^\uparrow\right] \\
&-\Sigma_- \sin(\vartheta)\sin(\vartheta)\left[\sigma_1^+\sigma_3^- n_2^\downarrow - \sigma_1^-\sigma_3^+ n_2^\uparrow - \sigma_4^-\sigma_2^+ n_3^\uparrow + \sigma_4^+\sigma_2^- n_3^\downarrow\right].
\end{aligned} \tag{G.11}$$

Here, all terms vanish except the first term, and so this equation is now given by

$$\begin{aligned}
&-\Sigma_- \sin(\vartheta)\left[H_{XY}e^{\vartheta\Sigma_-}\right] = -\Sigma_- \sin(\vartheta)\left[\sigma_1^+\sigma_2^- + \sigma_2^+\sigma_1^- - \sigma_3^+\sigma_4^- - \sigma_4^+\sigma_3^-\right] \\
&= \sin(\vartheta)\left[-\sigma_1^+\sigma_3^- n_2^\uparrow + \sigma_2^+\sigma_4^- n_3^\downarrow + \sigma_3^+\sigma_1^- n_2^\downarrow - \sigma_2^-\sigma_4^+ n_3^\uparrow\right].
\end{aligned} \tag{G.12}$$

Therefore, the transformed Hamiltonian is now given by

$$\begin{aligned}
\mathcal{H}_{XY} &= \sigma_1^+\sigma_2^- + \sigma_2^+\sigma_1^- - \sigma_3^+\sigma_4^- - \sigma_4^+\sigma_3^- \\
&+ \left[-\sigma_1^+\sigma_2^- n_2^\uparrow n_3^\downarrow - \sigma_2^+\sigma_1^- n_2^\downarrow n_3^\uparrow + \sigma_3^+\sigma_4^- n_2^\uparrow n_3^\downarrow + \sigma_4^+\sigma_3^- n_2^\downarrow n_3^\uparrow\right] \\
&+ \cos(\vartheta)\left[\sigma_1^+\sigma_2^- n_2^\uparrow n_3^\downarrow + \sigma_2^+\sigma_1^- n_2^\downarrow n_3^\uparrow - \sigma_3^+\sigma_4^- n_2^\uparrow n_3^\downarrow - \sigma_4^+\sigma_3^- n_2^\downarrow n_3^\uparrow\right] \\
&+ \sin(\vartheta)\left[\sigma_1^+\sigma_3^- n_2^\downarrow - \sigma_1^-\sigma_3^+ n_2^\uparrow - \sigma_4^-\sigma_2^+ n_3^\uparrow + \sigma_4^+\sigma_2^- n_3^\downarrow\right] \\
&+ \left[-n_2^\uparrow n_3^\downarrow\sigma_2^+\sigma_1^- + n_2^\uparrow n_3^\downarrow\sigma_4^+\sigma_3^- - n_2^\downarrow n_3^\uparrow\sigma_1^+\sigma_2^- + n_2^\downarrow n_3^\uparrow\sigma_3^+\sigma_4^-\right] \\
&+ \cos(\vartheta)\left[n_2^\uparrow n_3^\downarrow\sigma_2^+\sigma_1^- - n_2^\uparrow n_3^\downarrow\sigma_4^+\sigma_3^- + n_2^\downarrow n_3^\uparrow\sigma_1^+\sigma_2^- - n_2^\downarrow n_3^\uparrow\sigma_3^+\sigma_4^-\right] \\
&+ \sin(\vartheta)\left[-\sigma_1^+\sigma_3^- n_2^\uparrow + \sigma_2^+\sigma_4^- n_3^\downarrow + \sigma_3^+\sigma_1^- n_2^\downarrow - \sigma_2^-\sigma_4^+ n_3^\uparrow\right].
\end{aligned} \tag{G.13}$$

Now, we can simplify the equation by summing together the similar terms. The sum of the 2nd and 5th terms is given by

$$(-\sigma_1^+\sigma_2^- - \sigma_2^+\sigma_1^- + \sigma_3^+\sigma_4^- + \sigma_4^+\sigma_3^-)(n_2^\uparrow n_3^\downarrow + n_2^\downarrow n_3^\uparrow), \tag{G.14}$$

which with the fact that $n_2^\uparrow n_3^\downarrow + n_2^\downarrow n_3^\uparrow = \mathcal{I}$, becomes equal to $-H_{XY}$, and when summed with the 1st term, it gives 0, as the 1st term is equal to H_{XY}.

Similarly, the sum of the two cosine terms (3rd and 6th terms) results in: $\cos(\vartheta)H_{XY}$. The sum of the sine terms (4th and last terms) is given by

$$\sin(\vartheta)\left[(\sigma_1^+\sigma_3^- + \sigma_3^+\sigma_1^-)(n_2^\downarrow - n_2^\uparrow) + (\sigma_2^+\sigma_4^- + \sigma_4^+\sigma_2^-)(n_3^\downarrow - n_3^\uparrow)\right], \tag{G.15}$$

and so the transformed Hamiltonian is now given by

$$\begin{aligned}\mathcal{H}_{XY} =& e^{-\vartheta\Sigma_-}\left[H_{XY}e^{\vartheta\Sigma_-}\right] = \\ & \cos(\vartheta)\left[\sigma_1^+\sigma_2^- + \sigma_2^+\sigma_1^- - \sigma_3^+\sigma_4^- - \sigma_4^+\sigma_3^-\right] \\ & + \sin(\vartheta)\left[(\sigma_1^+\sigma_3^- + \sigma_3^+\sigma_1^-)(n_2^\downarrow - n_2^\uparrow) + (\sigma_2^+\sigma_4^- + \sigma_4^+\sigma_2^-)(n_3^\downarrow - n_3^\uparrow)\right].\end{aligned} \tag{G.16}$$

Bibliography

[1] A. H. Alsulami, I. D'Amico, M. P. Estarellas, and T. P. Spiller, "Unitary design of quantum spin networks for robust routing, entanglement generation, and phase sensing," *Advanced Quantum Technologies*, vol. 5, no. 8, p. 2200013, 2022.

[2] A. H. Alsulami, I. D'Amico, M. P. Estarellas, and T. P. Spiller, "Scalable quantum spin networks from unitary construction," *Advanced Quantum Technologies*, vol. 7, no. 2, p. 2300238, 2024.

[3] R. P. Feynman, "Simulating physics with computers," *Int. J. Theor. Phys*, vol. 21, no. 6/7, 1982.

[4] P. W. Shor, "Polynomial-time algorithms for prime factorization and discrete logarithms on a quantum computer," *SIAM review*, vol. 41, no. 2, pp. 303–332, 1999.

[5] A. Montanaro, "Quantum algorithms: an overview," *npj Quantum Information*, vol. 2, no. 1, pp. 1–8, 2016.

[6] I. Bloch, J. Dalibard, and S. Nascimbene, "Quantum simulations with ultracold quantum gases," *Nature Physics*, vol. 8, no. 4, pp. 267–276, 2012.

[7] A. Aspuru-Guzik and P. Walther, "Photonic quantum simulators," *Nature physics*, vol. 8, no. 4, pp. 285–291, 2012.

[8] F. Arute, K. Arya, R. Babbush, D. Bacon, J. C. Bardin, R. Barends, R. Biswas, S. Boixo, F. G. Brandao, D. A. Buell, *et al.*, "Quantum supremacy using a programmable superconducting processor," *Nature*, vol. 574, no. 7779, pp. 505–510, 2019.

[9] H.-S. Zhong, H. Wang, Y.-H. Deng, M.-C. Chen, L.-C. Peng, Y.-H. Luo, J. Qin, D. Wu, X. Ding, Y. Hu, *et al.*, "Quantum computational advantage using photons," *Science*, vol. 370, no. 6523, pp. 1460–1463, 2020.

[10] N. Gisin, G. Ribordy, W. Tittel, and H. Zbinden, "Quantum cryptography," *Reviews of modern physics*, vol. 74, no. 1, p. 145, 2002.

[11] S. Bose, "Quantum communication through spin chain dynamics: an introductory overview," *Contemporary Physics*, vol. 48, no. 1, pp. 13–30, 2007.

[12] C. L. Degen, F. Reinhard, and P. Cappellaro, "Quantum sensing," *Reviews of modern physics*, vol. 89, no. 3, p. 035002, 2017.

[13] M. A. Nielsen and I. Chuang, "Quantum computation and quantum information," 2002.

[14] A. Uhlmann, "The "transition probability" in the state space of a $*$-algebra," *Reports on Mathematical Physics*, vol. 9, no. 2, pp. 273–279, 1976.

[15] R. Jozsa, "Fidelity for mixed quantum states," *Journal of modern optics*, vol. 41, no. 12, pp. 2315–2323, 1994.

[16] Y.-C. Liang, Y.-H. Yeh, P. E. Mendonça, R. Y. Teh, M. D. Reid, and P. D. Drummond, "Quantum fidelity measures for mixed states," *Reports on Progress in Physics*, vol. 82, no. 7, p. 076001, 2019.

[17] V. Krutyanskiy, M. Galli, V. Krcmarsky, S. Baier, D. Fioretto, Y. Pu, A. Mazloom, P. Sekatski, M. Canteri, M. Teller, *et al.*, "Entanglement of trapped-ion qubits separated by 230 meters," *Physical Review Letters*, vol. 130, no. 5, p. 050803, 2023.

[18] D. L. Moehring, P. Maunz, S. Olmschenk, K. C. Younge, D. N. Matsukevich, L.-M. Duan, and C. Monroe, "Entanglement of single-atom quantum bits at a distance," *Nature*, vol. 449, no. 7158, pp. 68–71, 2007.

[19] L. J. Stephenson, D. P. Nadlinger, B. C. Nichol, S. An, P. Drmota, T. G. Ballance, K. Thirumalai, J. F. Goodwin, D. M. Lucas, and C. J. Ballance, "High-rate, high-fidelity entanglement of qubits across an elementary quantum network," *Physical review letters*, vol. 124, no. 11, p. 110501, 2020.

[20] C. Couteau, "Spontaneous parametric down-conversion," *Contemporary Physics*, vol. 59, no. 3, pp. 291–304, 2018.

[21] W. K. Wootters, "Entanglement of formation and concurrence.," *Quantum Inf. Comput.*, vol. 1, no. 1, pp. 27–44, 2001.

[22] A. Einstein, B. Podolsky, and N. Rosen, "Can quantum-mechanical description of physical reality be considered complete?," *Physical review*, vol. 47, no. 10, p. 777, 1935.

[23] J. S. Bell, "On the einstein podolsky rosen paradox," *Physics Physique Fizika*, vol. 1, no. 3, p. 195, 1964.

[24] S. J. Freedman and J. F. Clauser, "Experimental test of local hidden-variable theories," *Physical Review Letters*, vol. 28, no. 14, p. 938, 1972.

[25] A. Aspect, P. Grangier, and G. Roger, "Experimental realization of einstein-podolsky-rosen-bohm gedankenexperiment: A new violation of bell's inequalities," *Physical review letters*, vol. 49, no. 2, p. 91, 1982.

[26] J.-Å. Larsson, "Loopholes in bell inequality tests of local realism," *Journal of Physics A: Mathematical and Theoretical*, vol. 47, no. 42, p. 424003, 2014.

[27] B. Hensen, H. Bernien, A. E. Dréau, A. Reiserer, N. Kalb, M. S. Blok, J. Ruitenberg, R. F. Vermeulen, R. N. Schouten, C. Abellán, *et al.*, "Loophole-free bell inequality violation using electron spins separated by 1.3 kilometres," *Nature*, vol. 526, no. 7575, pp. 682–686, 2015.

[28] S. Storz, J. Schär, A. Kulikov, P. Magnard, P. Kurpiers, J. Lütolf, T. Walter, A. Copetudo, K. Reuer, A. Akin, *et al.*, "Loophole-free bell inequality violation with superconducting circuits," *Nature*, vol. 617, no. 7960, pp. 265–270, 2023.

[29] G. Ribordy, J. Brendel, J.-D. Gautier, N. Gisin, and H. Zbinden, "Long-distance entanglement-based quantum key distribution," *Physical Review A*, vol. 63, no. 1, p. 012309, 2000.

[30] M. Curty, M. Lewenstein, and N. Lütkenhaus, "Entanglement as a precondition for secure quantum key distribution," *Physical review letters*, vol. 92, no. 21, p. 217903, 2004.

[31] J. Yin, Y. Cao, Y.-H. Li, J.-G. Ren, S.-K. Liao, L. Zhang, W.-Q. Cai, W.-Y. Liu, B. Li, H. Dai, *et al.*, "Satellite-to-ground entanglement-based quantum key distribution," *Physical review letters*, vol. 119, no. 20, p. 200501, 2017.

[32] J. Yin, Y.-H. Li, S.-K. Liao, M. Yang, Y. Cao, L. Zhang, J.-G. Ren, W.-Q. Cai, W.-Y. Liu, S.-L. Li, *et al.*, "Entanglement-based secure quantum cryptography over 1,120 kilometres," *Nature*, vol. 582, no. 7813, pp. 501–505, 2020.

[33] D. Bouwmeester, J.-W. Pan, K. Mattle, M. Eibl, H. Weinfurter, and A. Zeilinger, "Experimental quantum teleportation," *Nature*, vol. 390, no. 6660, pp. 575–579, 1997.

[34] A. Karlsson and M. Bourennane, "Quantum teleportation using three-particle entanglement," *Physical Review A*, vol. 58, no. 6, p. 4394, 1998.

[35] S. G. Hofer, W. Wieczorek, M. Aspelmeyer, and K. Hammerer, "Quantum entanglement and teleportation in pulsed cavity optomechanics," *Physical Review A*, vol. 84, no. 5, p. 052327, 2011.

[36] S. Pirandola, J. Eisert, C. Weedbrook, A. Furusawa, and S. L. Braunstein, "Advances in quantum teleportation," *Nature photonics*, vol. 9, no. 10, pp. 641–652, 2015.

[37] T. J. Apollaro, G. M. Almeida, S. Lorenzo, A. Ferraro, and S. Paganelli, "Spin chains for two-qubit teleportation," *Physical Review A*, vol. 100, no. 5, p. 052308, 2019.

[38] J. I. Cirac and P. Zoller, "Quantum computations with cold trapped ions," *Physical review letters*, vol. 74, no. 20, p. 4091, 1995.

[39] A. Barenco, C. H. Bennett, R. Cleve, D. P. DiVincenzo, N. Margolus, P. Shor, T. Sleator, J. A. Smolin, and H. Weinfurter, "Elementary gates for quantum computation," *Physical review A*, vol. 52, no. 5, p. 3457, 1995.

[40] D. P. DiVincenzo, "The physical implementation of quantum computation," *Fortschritte der Physik: Progress of Physics*, vol. 48, no. 9-11, pp. 771–783, 2000.

[41] S. Lloyd, "Almost any quantum logic gate is universal," *Physical Review Letters*, vol. 75, no. 2, p. 346, 1995.

[42] I. Usmani, M. Afzelius, H. De Riedmatten, and N. Gisin, "Mapping multiple photonic qubits into and out of one solid-state atomic ensemble," *Nature Communications*, vol. 1, no. 1, p. 12, 2010.

[43] A. Delteil, Z. Sun, S. Fält, and A. Imamoğlu, "Realization of a cascaded quantum system: Heralded absorption of a single photon qubit by a single-electron charged quantum dot," *Physical review letters*, vol. 118, no. 17, p. 177401, 2017.

[44] Z. Luo, S. Sun, A. Karasahin, A. S. Bracker, S. G. Carter, M. K. Yakes, D. Gammon, and E. Waks, "A spin–photon interface using charge-tunable quantum dots strongly coupled to a cavity," *Nano letters*, vol. 19, no. 10, pp. 7072–7077, 2019.

[45] N. Gisin and R. Thew, "Quantum communication," *Nature photonics*, vol. 1, no. 3, pp. 165–171, 2007.

[46] K. Azuma, K. Tamaki, and H.-K. Lo, "All-photonic quantum repeaters," *Nature communications*, vol. 6, no. 1, p. 6787, 2015.

[47] H. De Riedmatten, I. Marcikic, W. Tittel, H. Zbinden, D. Collins, and N. Gisin, "Long distance quantum teleportation in a quantum relay configuration," *Physical Review Letters*, vol. 92, no. 4, p. 047904, 2004.

[48] T. E. Northup and R. Blatt, "Quantum information transfer using photons," *Nature photonics*, vol. 8, no. 5, pp. 356–363, 2014.

[49] T. Honjo, S. W. Nam, H. Takesue, Q. Zhang, H. Kamada, Y. Nishida, O. Tadanaga, M. Asobe, B. Baek, R. Hadfield, *et al.*, "Long-distance entanglement-based quantum key distribution over optical fiber," *Optics Express*, vol. 16, no. 23, pp. 19118–19126, 2008.

[50] Q. D. Xuan, Z. Zhang, and P. L. Voss, "A 24 km fiber-based discretely signaled continuous variable quantum key distribution system," *Optics express*, vol. 17, no. 26, pp. 24244–24249, 2009.

[51] J.-P. Chen, C. Zhang, Y. Liu, C. Jiang, D.-F. Zhao, W.-J. Zhang, F.-X. Chen, H. Li, L.-X. You, Z. Wang, *et al.*, "Quantum key distribution over 658 km fiber with distributed vibration sensing," *Physical Review Letters*, vol. 128, no. 18, p. 180502, 2022.

[52] Y. Liu, W.-J. Zhang, C. Jiang, J.-P. Chen, C. Zhang, W.-X. Pan, D. Ma, H. Dong, J.-M. Xiong, C.-J. Zhang, *et al.*, "Experimental twin-field quantum key distribution over 1000 km fiber distance," *Physical Review Letters*, vol. 130, no. 21, p. 210801, 2023.

[53] S.-K. Liao, W.-Q. Cai, W.-Y. Liu, L. Zhang, Y. Li, J.-G. Ren, J. Yin, Q. Shen, Y. Cao, Z.-P. Li, *et al.*, "Satellite-to-ground quantum key distribution," *Nature*, vol. 549, no. 7670, pp. 43–47, 2017.

[54] S. Ecker, B. Liu, J. Handsteiner, M. Fink, D. Rauch, F. Steinlechner, T. Scheidl, A. Zeilinger, and R. Ursin, "Strategies for achieving high key rates in satellite-based qkd," *npj Quantum Information*, vol. 7, no. 1, p. 5, 2021.

[55] J. Poyatos, J. I. Cirac, and P. Zoller, "Schemes of quantum computations with trapped ions," *Fortschritte der Physik: Progress of Physics*, vol. 48, no. 9-11, pp. 785–799, 2000.

[56] A. E. Webb, S. C. Webster, S. Collingbourne, D. Bretaud, A. M. Lawrence, S. Weidt, F. Mintert, and W. K. Hensinger, "Resilient entangling gates for trapped ions," *Physical review letters*, vol. 121, no. 18, p. 180501, 2018.

[57] S. Hawaldar, P. Shahi, A. L. Carter, A. M. Rey, J. J. Bollinger, and A. Shankar, "Bilayer crystals of trapped ions for quantum information processing," *arXiv preprint arXiv:2312.10681*, 2023.

[58] M. Kjaergaard, M. E. Schwartz, J. Braumüller, P. Krantz, J. I.-J. Wang, S. Gustavsson, and W. D. Oliver, "Superconducting qubits: Current state of play," *Annual Review of Condensed Matter Physics*, vol. 11, pp. 369–395, 2020.

[59] R. Yousefjani and A. Bayat, "Parallel entangling gate operations and two-way quantum communication in spin chains," *Quantum*, vol. 5, p. 460, 2021.

[60] A. H. Karamlou, J. Braumüller, Y. Yanay, A. Di Paolo, P. M. Harrington, B. Kannan, D. Kim, M. Kjaergaard, A. Melville, S. Muschinske, *et al.*, "Quantum transport and localization in 1d and 2d tight-binding lattices," *npj Quantum Information*, vol. 8, no. 1, p. 35, 2022.

[61] D. Loss and D. P. DiVincenzo, "Quantum computation with quantum dots," *Physical Review A*, vol. 57, no. 1, p. 120, 1998.

[62] K. W. Chan, H. Sahasrabudhe, W. Huang, Y. Wang, H. C. Yang, M. Veldhorst, J. C. Hwang, F. A. Mohiyaddin, F. E. Hudson, K. M. Itoh, *et al.*, "Exchange coupling in a linear chain of three quantum-dot spin qubits in silicon," *Nano Letters*, vol. 21, no. 3, pp. 1517–1522, 2021.

[63] F. Borsoi, N. W. Hendrickx, V. John, M. Meyer, S. Motz, F. van Riggelen, A. Sammak, S. L. de Snoo, G. Scappucci, and M. Veldhorst, "Shared control of a 16 semiconductor quantum dot crossbar array," *Nature Nanotechnology*, pp. 1–7, 2023.

[64] C. S. Adams, J. D. Pritchard, and J. P. Shaffer, "Rydberg atom quantum technologies," *Journal of Physics B: Atomic, Molecular and Optical Physics*, vol. 53, no. 1, p. 012002, 2019.

[65] G. Bornet, G. Emperauger, C. Chen, B. Ye, M. Block, M. Bintz, J. A. Boyd, D. Barredo, T. Comparin, F. Mezzacapo, *et al.*, "Scalable spin squeezing in a dipolar rydberg atom array," *Nature*, vol. 621, no. 7980, pp. 728–733, 2023.

[66] P. L. Ocola, I. Dimitrova, B. Grinkemeyer, E. Guardado-Sanchez, T. Đorđević, P. Samutpraphoot, V. Vuletić, and M. D. Lukin, "Control and entanglement of individual rydberg atoms near a nanoscale device," *Physical Review Letters*, vol. 132, no. 11, p. 113601, 2024.

[67] J. I. Cirac, P. Zoller, H. J. Kimble, and H. Mabuchi, "Quantum state transfer and entanglement distribution among distant nodes in a quantum network," *Physical Review Letters*, vol. 78, no. 16, p. 3221, 1997.

[68] R. Vrijen and E. Yablonovitch, "A spin-coherent semiconductor photodetector for quantum communication," *Physica E: Low-dimensional Systems and Nanostructures*, vol. 10, no. 4, pp. 569–575, 2001.

[69] W. Yao, R.-B. Liu, and L. Sham, "Theory of control of the spin-photon interface for quantum networks," *Physical review letters*, vol. 95, no. 3, p. 030504, 2005.

[70] R. Uppu, L. Midolo, X. Zhou, J. Carolan, and P. Lodahl, "Quantum-dot-based deterministic photon–emitter interfaces for scalable photonic quantum technology," *Nature nanotechnology*, vol. 16, no. 12, pp. 1308–1317, 2021.

[71] C. F. Schuck, R. Boutelle, K. Silverman, G. Moody, and P. J. Simmonds, "Single-photon generation from self-assembled gaas/inalas (111) a quantum dots with ultrasmall fine-structure splitting," *Journal of Physics: Photonics*, vol. 3, no. 2, p. 024012, 2021.

[72] P. Kok, *A First Introduction to Quantum Physics*. Springer Nature, 2018.

[73] G. M. Nikolopoulos, I. Jex, *et al.*, *Quantum state transfer and network engineering*. Springer, 2014.

[74] S. Bose, "Quantum communication through an unmodulated spin chain," *Physical review letters*, vol. 91, no. 20, p. 207901, 2003.

[75] S. C. Benjamin and S. Bose, "Quantum computing with an always-on heisenberg interaction," *Physical review letters*, vol. 90, no. 24, p. 247901, 2003.

[76] X. Zhou, Z.-W. Zhou, G.-C. Guo, and M. J. Feldman, "Quantum computation with untunable couplings," *Phys. Rev. Lett.*, vol. 89, p. 197903, 2002.

[77] R. Yousefjani and A. Bayat, "Simultaneous multiple-user quantum communication across a spin-chain channel," *Physical Review A*, vol. 102, no. 1, p. 012418, 2020.

[78] M. Christandl, N. Datta, T. C. Dorlas, A. Ekert, A. Kay, and A. J. Landahl, "Perfect transfer of arbitrary states in quantum spin networks," *Phys. Rev. A*, vol. 71, p. 032312, 2005.

[79] A. Kay, "Basics of perfect communication through quantum networks," *Physical Review A*, vol. 84, no. 2, p. 022337, 2011.

[80] P. J. Pemberton-Ross and A. Kay, "Perfect quantum routing in regular spin networks," *Physical Review Letters*, vol. 106, no. 2, p. 020503, 2011.

[81] S. S. Roy, H. S. Dhar, D. Rakshit, A. Sen, U. Sen, *et al.*, "Response to defects in multipartite and bipartite entanglement of isotropic quantum spin networks," *Physical Review A*, vol. 97, no. 5, p. 052325, 2018.

[82] J. Riegelmeyer, D. Wignall, M. P. Estarellas, I. D'Amico, and T. P. Spiller, "Generation and robustness of quantum entanglement in spin graphs," *Quantum Information Processing*, vol. 20, no. 1, p. 2, 2021.

[83] S. Pirandola, B. R. Bardhan, T. Gehring, C. Weedbrook, and S. Lloyd, "Advances in photonic quantum sensing," *Nature Photonics*, vol. 12, no. 12, pp. 724–733, 2018.

[84] S. Lorenzo, T. J. G. Apollaro, A. Sindona, and F. Plastina, "Quantum-state transfer via resonant tunneling through local-field-induced barriers," *Physical Review A*, vol. 87, no. 4, p. 042313, 2013.

[85] T. Tufarelli and V. Giovannetti, "High-fidelity state transfer in binary-tree spin networks," *Physical Review A*, vol. 79, no. 2, p. 022313, 2009.

[86] K. Eckert, O. Romero-Isart, and A. Sanpera, "Efficient quantum state transfer in spin chains via adiabatic passage," *New journal of physics*, vol. 9, no. 5, p. 155, 2007.

[87] M. Christandl, N. Datta, A. Ekert, and A. J. Landahl, "Perfect state transfer in quantum spin networks," *Physical review letters*, vol. 92, no. 18, p. 187902, 2004.

[88] G. M. Nikolopoulos, D. Petrosyan, and P. Lambropoulos, "Electron wavepacket propagation in a chain of coupled quantum dots," *Journal of Physics: Condensed Matter*, vol. 16, no. 28, p. 4991, 2004.

[89] M. Christandl, N. Datta, T. C. Dorlas, A. Ekert, A. Kay, and A. J. Landahl, "Perfect transfer of arbitrary states in quantum spin networks," *Physical Review A*, vol. 71, no. 3, p. 032312, 2005.

[90] D. Burgarth and S. Bose, "Conclusive and arbitrarily perfect quantum-state transfer using parallel spin-chain channels," *Physical Review A*, vol. 71, no. 5, p. 052315, 2005.

[91] D. Burgarth and S. Bose, "Perfect quantum state transfer with randomly coupled quantum chains," *New journal of physics*, vol. 7, no. 1, p. 135, 2005.

[92] H. L. Haselgrove, "Optimal state encoding for quantum walks and quantum communication over spin systems," *Physical Review A*, vol. 72, no. 6, p. 062326, 2005.

[93] H. Yadsan-Appleby and T. J. Osborne, "Achievable qubit rates for quantum-information wires," *Physical Review A*, vol. 85, no. 1, p. 012310, 2012.

[94] X.-Q. Liu, J. Liu, and Z.-Y. Xue, "Robust and fast quantum state transfer on superconducting circuits," *JETP Letters*, pp. 1–6, 2023.

[95] J. Majer, J. Chow, J. Gambetta, J. Koch, B. Johnson, J. Schreier, L. Frunzio, D. Schuster, A. A. Houck, A. Wallraff, *et al.*, "Coupling superconducting qubits via a cavity bus," *Nature*, vol. 449, no. 7161, pp. 443–447, 2007.

[96] G. Ciaramicoli, I. Marzoli, and P. Tombesi, "Spin chains with electrons in penning traps," *Physical Review A*, vol. 75, no. 3, p. 032348, 2007.

[97] J. Zhang, G. L. Long, W. Zhang, Z. Deng, W. Liu, and Z. Lu, "Simulation of heisenberg x y interactions and realization of a perfect state transfer in spin chains using liquid nuclear magnetic resonance," *Physical Review A*, vol. 72, no. 1, p. 012331, 2005.

[98] X. Li, Y. Ma, J. Han, T. Chen, Y. Xu, W. Cai, H. Wang, Y. Song, Z.-Y. Xue, Z.-q. Yin, *et al.*, "Perfect quantum state transfer in a superconducting qubit chain with parametrically tunable couplings," *Physical Review Applied*, vol. 10, no. 5, p. 054009, 2018.

[99] K. N. Wilkinson, M. P. Estarellas, T. P. Spiller, and I. D'amico, "Rapid and robust generation of einstein–podolsky–rosen pairs with spin chains," *Quantum Information & Computation*, vol. 18, no. 3-4, pp. 247–264, 2018.

[100] M. P. Estarellas, I. D'Amico, and T. P. Spiller, "Robust quantum entanglement generation and generation-plus-storage protocols with spin chains," *Physical Review A*, vol. 95, no. 4, p. 042335, 2017.

[101] I. D'Amico, B. W. Lovett, and T. P. Spiller, "Freezing distributed entanglement in spin chains," *Physical Review A*, vol. 76, no. 3, p. 030302, 2007.

[102] O. Gühne and G. Tóth, "Entanglement detection," *Physics Reports*, vol. 474, no. 1-6, pp. 1–75, 2009.

[103] M. M. Cunha, A. Fonseca, and E. O. Silva, "Tripartite entanglement: Foundations and applications," *Universe*, vol. 5, no. 10, p. 209, 2019.

[104] D. Bruß, N. Datta, A. Ekert, L. C. Kwek, and C. Macchiavello, "Multipartite entanglement in quantum spin chains," *Physical Review A*, vol. 72, no. 1, p. 014301, 2005.

[105] I. D'Amico, B. W. Lovett, and T. P. Spiller, "Creating and preserving multipartite entanglement with spin chains," *physica status solidi c*, vol. 5, no. 7, pp. 2481–2485, 2008.

[106] K. R. K. Rao and A. Kumar, "Entanglement in a 3-spin heisenberg-xy chain with nearest-neighbor interactions, simulated in an nmr quantum simulator," *International Journal of Quantum Information*, vol. 10, no. 04, p. 1250039, 2012.

[107] C. Zhang, C.-J. Zhang, Y.-F. Huang, Z.-B. Hou, B.-H. Liu, C.-F. Li, and G.-C. Guo, "Experimental test of genuine multipartite nonlocality under the no-signalling principle," *Scientific reports*, vol. 6, no. 1, p. 39327, 2016.

[108] Y.-S. Zhou, F. Wang, and M.-X. Luo, "Efficient superdense coding with w states," *International Journal of Theoretical Physics*, vol. 57, pp. 1935–1941, 2018.

[109] B.-S. Shi and A. Tomita, "Teleportation of an unknown state by w state," *Physics Letters A*, vol. 296, no. 4-5, pp. 161–164, 2002.

[110] X.-B. Chen, Q.-Y. Wen, F.-Z. Guo, Y. Sun, G. Xu, and F.-C. Zhu, "Controlled quantum secure direct communication with w state," *International Journal of Quantum Information*, vol. 6, no. 04, pp. 899–906, 2008.

[111] E. Knill, R. Laflamme, and G. J. Milburn, "A scheme for efficient quantum computation with linear optics," *nature*, vol. 409, no. 6816, pp. 46–52, 2001.

[112] S. Bartolucci, P. Birchall, H. Bombin, H. Cable, C. Dawson, M. Gimeno-Segovia, E. Johnston, K. Kieling, N. Nickerson, M. Pant, *et al.*, "Fusion-based quantum computation," *Nature Communications*, vol. 14, no. 1, p. 912, 2023.

[113] H. Kamada and H. Gotoh, "Quantum computation with quantum dot excitons," *Semiconductor science and technology*, vol. 19, no. 4, p. S392, 2004.

[114] I. D'Amico, "Quantum buses and quantum computer architecture based on quantum dots," *arXiv preprint cond-mat/0511470*, 2005.

[115] T. P. Spiller, I. D'Amico, and B. W. Lovett, "Entanglement distribution for a practical quantum-dot-based quantum processor architecture," *New Journal of Physics*, vol. 9, no. 1, p. 20, 2007.

[116] M. Veldhorst, C. Yang, J. Hwang, W. Huang, J. Dehollain, J. Muhonen, S. Simmons, A. Laucht, F. Hudson, K. M. Itoh, *et al.*, "A two-qubit logic gate in silicon," *Nature*, vol. 526, no. 7573, pp. 410–414, 2015.

[117] Z.-L. Xiang, S. Ashhab, J. You, and F. Nori, "Hybrid quantum circuits: Superconducting circuits interacting with other quantum systems," *arXiv preprint arXiv:1204.2137*, 2012.

[118] B. B. Blinov, D. Leibfried, C. Monroe, and D. J. Wineland, "Quantum computing with trapped ion hyperfine qubits," *Quantum Information Processing*, vol. 3, no. 1, pp. 45–59, 2004.

[119] C. Monroe and J. Kim, "Scaling the ion trap quantum processor," *Science*, vol. 339, no. 6124, pp. 1164–1169, 2013.

[120] L. Feng, O. Katz, C. Haack, M. Maghrebi, A. V. Gorshkov, Z. Gong, M. Cetina, and C. Monroe, "Continuous symmetry breaking in a trapped-ion spin chain," *Nature*, vol. 623, no. 7988, pp. 713–717, 2023.

[121] G. Wendin, "Quantum information processing with superconducting circuits: a review," *Reports on Progress in Physics*, vol. 80, no. 10, p. 106001, 2017.

[122] A. Acín, I. Bloch, H. Buhrman, T. Calarco, C. Eichler, J. Eisert, D. Esteve, N. Gisin, S. J. Glaser, F. Jelezko, *et al.*, "The quantum technologies roadmap: a european community view," *New Journal of Physics*, vol. 20, no. 8, p. 080201, 2018.

[123] M. Roth, N. Moll, G. Salis, M. Ganzhorn, D. J. Egger, S. Filipp, and S. Schmidt, "Adiabatic quantum simulations with driven superconducting qubits," *Physical Review A*, vol. 99, no. 2, p. 022323, 2019.

[124] S. Ebadi, T. T. Wang, H. Levine, A. Keesling, G. Semeghini, A. Omran, D. Bluvstein, R. Samajdar, H. Pichler, W. W. Ho, *et al.*, "Quantum phases of matter on a 256-atom programmable quantum simulator," *Nature*, vol. 595, no. 7866, pp. 227–232, 2021.

[125] I. Cong, H. Levine, A. Keesling, D. Bluvstein, S.-T. Wang, and M. D. Lukin, "Hardware-efficient, fault-tolerant quantum computation with rydberg atoms," *Physical Review X*, vol. 12, no. 2, p. 021049, 2022.

[126] T. Graham, Y. Song, J. Scott, C. Poole, L. Phuttitarn, K. Jooya, P. Eichler, X. Jiang, A. Marra, B. Grinkemeyer, *et al.*, "Multi-qubit entanglement and algorithms on a neutral-atom quantum computer," *Nature*, vol. 604, no. 7906, pp. 457–462, 2022.

[127] I. Frérot, M. Fadel, and M. Lewenstein, "Probing quantum correlations in many-body systems: a review of scalable methods," *Reports on Progress in Physics*, 2023.

[128] D. G. Cory, R. Laflamme, E. Knill, L. Viola, T. Havel, N. Boulant, G. Boutis, E. Fortunato, S. Lloyd, R. Martinez, *et al.*, "Nmr based quantum information processing: Achievements and prospects," *Fortschritte der Physik: Progress of Physics*, vol. 48, no. 9-11, pp. 875–907, 2000.

[129] C. Negrevergne, T. Mahesh, C. Ryan, M. Ditty, F. Cyr-Racine, W. Power, N. Boulant, T. Havel, D. Cory, and R. Laflamme, "Benchmarking quantum control methods on a 12-qubit system," *Physical review letters*, vol. 96, no. 17, p. 170501, 2006.

[130] P. Cappellaro, "Implementation of state transfer hamiltonians in spin chains with magnetic resonance techniques," in *Quantum state transfer and network engineering*, pp. 183–222, Springer, 2013.

[131] E. Schrödinger, "An undulatory theory of the mechanics of atoms and molecules," *Physical review*, vol. 28, no. 6, p. 1049, 1926.

[132] R. Shankar, *Principles of Quantum Mechanics*. Springer Nature, 2012.

[133] C. Di Franco, M. Paternostro, and M. Kim, "Perfect state transfer on a spin chain without state initialization," *Physical review letters*, vol. 101, no. 23, p. 230502, 2008.

[134] A. Kay, "Perfect, efficient, state transfer and its application as a constructive tool," *International Journal of Quantum Information*, vol. 8, no. 04, pp. 641–676, 2010.

[135] P. Karbach and J. Stolze, "Spin chains as perfect quantum state mirrors," *Physical Review A*, vol. 72, no. 3, p. 030301, 2005.

[136] V. Kostak, G. Nikolopoulos, and I. Jex, "Perfect state transfer in networks of arbitrary topology and coupling configuration," *Physical Review A*, vol. 75, no. 4, p. 042319, 2007.

[137] A. Wojcik, T. Luczak, P. Kurzynski, A. Grudka, T. Gdala, and M. Bednarska, "Unmodulated spin chains as universal quantum wires," *Physical Review A*, vol. 72, no. 3, p. 034303, 2005.

[138] S. Oh, Y.-P. Shim, J. Fei, M. Friesen, and X. Hu, "Effect of randomness on quantum data buses of heisenberg spin chains," *Physical Review B*, vol. 85, no. 22, p. 224418, 2012.

[139] L. Banchi, T. J. G. Apollaro, A. Cuccoli, R. Vaia, and P. Verrucchi, "Optimal dynamics for quantum-state and entanglement transfer through homogeneous quantum systems," *Physical Review A*, vol. 82, no. 5, p. 052321, 2010.

[140] L. Banchi, A. Bayat, P. Verrucchi, and S. Bose, "Nonperturbative entangling gates between distant qubits using uniform cold atom chains," *Physical review letters*, vol. 106, no. 14, p. 140501, 2011.

[141] R. Ronke, M. P. Estarellas, I. D'Amico, T. P. Spiller, and T. Miyadera, "Anderson localisation in spin chains for perfect state transfer," *The European Physical Journal D*, vol. 70, pp. 1–8, 2016.

[142] L. Amico, A. Osterloh, F. Plastina, R. Fazio, and G. M. Palma, "Dynamics of entanglement in one-dimensional spin systems," *Physical Review A*, vol. 69, no. 2, p. 022304, 2004.

[143] P. Jain and S. Mahapatra, "Mixed state entanglement measures as probe for confinement," *Physical Review D*, vol. 102, no. 12, p. 126022, 2020.

[144] M. Bina, A. Mandarino, S. Olivares, and M. G. Paris, "Drawbacks of the use of fidelity to assess quantum resources," *Physical Review A*, vol. 89, no. 1, p. 012305, 2014.

[145] A. Shimizu and T. Miyadera, "Stability of quantum states of finite macroscopic systems against classical noises, perturbations from environments, and local measurements," *Physical review letters*, vol. 89, no. 27, p. 270403, 2002.

[146] G. De Chiara, D. Rossini, S. Montangero, and R. Fazio, "From perfect to fractal transmission in spin chains," *Physical Review A*, vol. 72, no. 1, p. 012323, 2005.

[147] A. Kay, "The perfect state transfer graph limbo," *arXiv preprint arXiv:1808.00696*, 2018.

[148] D. Zueco, F. Galve, S. Kohler, and P. Hänggi, "Quantum router based on ac control of qubit chains," *Physical Review A*, vol. 80, no. 4, p. 042303, 2009.

[149] A. Bayat, S. Bose, and P. Sodano, "Entanglement routers using macroscopic singlets," *Physical review letters*, vol. 105, no. 18, p. 187204, 2010.

[150] S. Paganelli, S. Lorenzo, T. J. Apollaro, F. Plastina, and G. L. Giorgi, "Routing quantum information in spin chains," *Physical Review A*, vol. 87, no. 6, p. 062309, 2013.

[151] H. S. Ku, J. Long, X. Wu, M. Bal, R. Lake, E. Barnes, S. E. Economou, and D. P. Pappas, "Single qubit operations using microwave hyperbolic secant pulses," *Physical Review A*, vol. 96, no. 4, p. 042339, 2017.

[152] V. Giovannetti, S. Lloyd, and L. Maccone, "Advances in quantum metrology," *Nature photonics*, vol. 5, no. 4, pp. 222–229, 2011.

[153] L.-Z. Liu, Y.-Z. Zhang, Z.-D. Li, R. Zhang, X.-F. Yin, Y.-Y. Fei, L. Li, N.-L. Liu, F. Xu, Y.-A. Chen, *et al.*, "Distributed quantum phase estimation with entangled photons," *Nature Photonics*, vol. 15, no. 2, pp. 137–142, 2021.

[154] L. Pezzè and A. Smerzi, "Quantum phase estimation algorithm with gaussian spin states," *PRX Quantum*, vol. 2, no. 4, p. 040301, 2021.

[155] Y. Maleki and M. S. Zubairy, "Distributed phase estimation and networked quantum sensors with w-type quantum probes," *Physical Review A*, vol. 105, no. 3, p. 032428, 2022.

[156] U. Dorner, R. Demkowicz-Dobrzanski, B. J. Smith, J. S. Lundeen, W. Wasilewski, K. Banaszek, and I. A. Walmsley, "Optimal quantum phase estimation," *Physical review letters*, vol. 102, no. 4, p. 040403, 2009.

[157] Q. Zhuang, Z. Zhang, and J. H. Shapiro, "Distributed quantum sensing using continuous-variable multipartite entanglement," *Physical Review A*, vol. 97, no. 3, p. 032329, 2018.

[158] D. Brivio, S. Cialdi, S. Vezzoli, B. T. Gebrehiwot, M. G. Genoni, S. Olivares, and M. G. Paris, "Experimental estimation of one-parameter qubit gates in the presence of phase diffusion," *Physical Review A—Atomic, Molecular, and Optical Physics*, vol. 81, no. 1, p. 012305, 2010.

[159] C. Coulson and G. Rushbrooke, "Note on the method of molecular orbitals," in *Mathematical Proceedings of the Cambridge Philosophical Society*, vol. 36, pp. 193–200, Cambridge University Press, 1940.

[160] K. Ruedenberg and C. W. Scherr, "Free-electron network model for conjugated systems. i. theory," *The Journal of Chemical Physics*, vol. 21, no. 9, pp. 1565–1581, 1953.

[161] M. Shen, "Pairing theorem of graph eigenvalues: Its new proof and a generalization," *International journal of quantum chemistry*, vol. 37, no. 2, pp. 121–123, 1990.

[162] F. M. Izrailev, "Simple models of quantum chaos: Spectrum and eigenfunctions," *Physics Reports*, vol. 196, no. 5-6, pp. 299–392, 1990.

[163] F. Haake, "Quantum signatures of chaos," in *Quantum Coherence in Mesoscopic Systems*, pp. 583–595, Springer, 1991.

[164] S. Harraz, J.-Y. Zhang, and S. Cong, "High-fidelity quantum teleportation through noisy channels via weak measurement and environment-assisted measurement," *Results in Physics*, vol. 55, p. 107164, 2023.

[165] S. Tan, D. Walls, and M. Collett, "Nonlocality of a single photon," *Physical review letters*, vol. 66, no. 3, p. 252, 1991.

[166] H.-W. Lee and J. Kim, "Quantum teleportation and Bell's inequality using single-particle entanglement," *Physical Review A*, vol. 63, no. 1, p. 012305, 2000.

[167] M. O. T. Cunha, J. A. Dunningham, and V. Vedral, "Entanglement in single-particle systems," *Proceedings of the Royal Society A: Mathematical, Physical and Engineering Sciences*, vol. 463, no. 2085, pp. 2277–2286, 2007.

[168] W. Li, L. Wang, and S. Zhao, "Phase matching quantum key distribution based on single-photon entanglement," *Scientific Reports*, vol. 9, no. 1, p. 15466, 2019.

[169] Y. Wang, S. Crain, C. Fang, B. Zhang, S. Huang, Q. Liang, P. H. Leung, K. R. Brown, and J. Kim, "High-fidelity two-qubit gates using a microelectromechanical-system-based beam steering system for individual qubit addressing," *Physical Review Letters*, vol. 125, no. 15, p. 150505, 2020.

[170] I. Pogorelov, T. Feldker, C. D. Marciniak, L. Postler, G. Jacob, O. Krieglsteiner, V. Podlesnic, M. Meth, V. Negnevitsky, M. Stadler, *et al.*, "Compact ion-trap quantum computing demonstrator," *PRX Quantum*, vol. 2, no. 2, p. 020343, 2021.

[171] H. Labuhn, S. Ravets, D. Barredo, L. Béguin, F. Nogrette, T. Lahaye, and A. Browaeys, "Single-atom addressing in microtraps for quantum-state engineering using rydberg atoms," *Physical Review A*, vol. 90, no. 2, p. 023415, 2014.

[172] X.-F. Shi, "Fast, accurate, and realizable two-qubit entangling gates by quantum interference in detuned rabi cycles of rydberg atoms," *Physical Review Applied*, vol. 11, no. 4, p. 044035, 2019.

[173] X.-F. Shi, "Single-site rydberg addressing in 3d atomic arrays for quantum computing with neutral atoms," *Journal of Physics B: Atomic, Molecular and Optical Physics*, vol. 53, no. 5, p. 054002, 2020.

[174] G. Gualdi, S. M. Giampaolo, and F. Illuminati, "Modular entanglement," *Physical Review Letters*, vol. 106, no. 5, p. 050501, 2011.

[175] G. M. Almeida, F. Ciccarello, T. J. Apollaro, and A. M. Souza, "Quantum-state transfer in staggered coupled-cavity arrays," *Physical Review A*, vol. 93, no. 3, p. 032310, 2016.

[176] M. Walter, D. Gross, and J. Eisert *Quantum Information: From Foundations to Quantum Technology Applications*, pp. 293–330, 2016.

[177] T. P. Spiller, "unpublished notes.".

[178] R. Raussendorf and H. J. Briegel, "A one-way quantum computer," *Physical review letters*, vol. 86, no. 22, p. 5188, 2001.

[179] R. Raussendorf, D. E. Browne, and H. J. Briegel, "Measurement-based quantum computation on cluster states," *Physical review A*, vol. 68, no. 2, p. 022312, 2003.

[180] H. J. Briegel, D. E. Browne, W. Dür, R. Raussendorf, and M. Van den Nest, "Measurement-based quantum computation," *Nature Physics*, vol. 5, no. 1, pp. 19–26, 2009.

[181] M. A. Nielsen, "Cluster-state quantum computation," *Reports on Mathematical Physics*, vol. 57, no. 1, pp. 147–161, 2006.

[182] C. Reimer, S. Sciara, P. Roztocki, M. Islam, L. Romero Cortes, Y. Zhang, B. Fischer, S. Loranger, R. Kashyap, A. Cino, *et al.*, "High-dimensional one-way quantum processing implemented on d-level cluster states," *Nature Physics*, vol. 15, no. 2, pp. 148–153, 2019.

[183] M. Gong, M.-C. Chen, Y. Zheng, S. Wang, C. Zha, H. Deng, Z. Yan, H. Rong, Y. Wu, S. Li, *et al.*, "Genuine 12-qubit entanglement on a superconducting quantum processor," *Physical review letters*, vol. 122, no. 11, p. 110501, 2019.

[184] R. T. Chepuri and I. A. Kovács, "Complex quantum network models from spin clusters," *Communications Physics*, vol. 6, no. 1, p. 271, 2023.

[185] M.-H. Yung and S. Bose, "Perfect state transfer, effective gates, and entanglement generation in engineered bosonic and fermionic networks," *Physical Review A*, vol. 71, no. 3, p. 032310, 2005.

[186] R. Ronke, I. D'Amico, and T. Spiller, "Knitting distributed cluster-state ladders with spin chains," *Physical Review A*, vol. 84, no. 3, p. 032308, 2011.

[187] M. J. Bremner, C. M. Dawson, J. L. Dodd, A. Gilchrist, A. W. Harrow, D. Mortimer, M. A. Nielsen, and T. J. Osborne, "Practical scheme for quantum computation with any two-qubit entangling gate," *Physical review letters*, vol. 89, no. 24, p. 247902, 2002.

[188] S. Clark, C. M. Alves, and D. Jaksch, "Efficient generation of graph states for quantum computation," *New Journal of Physics*, vol. 7, no. 1, p. 124, 2005.

[189] J. K. Pachos, *Introduction to topological quantum computation*. Cambridge University Press, 2012.

[190] P. Walther, K. J. Resch, T. Rudolph, E. Schenck, H. Weinfurter, V. Vedral, M. Aspelmeyer, and A. Zeilinger, "Experimental one-way quantum computing," *Nature*, vol. 434, no. 7030, pp. 169–176, 2005.

[191] I. D'Amico and F. Rossi, "Field-induced coulomb coupling in semiconductor macroatoms: Application to single-electron quantum devices," *Applied Physics Letters*, vol. 79, no. 11, pp. 1676–1678, 2001.

[192] S. De Rinaldis, I. D'Amico, and F. Rossi, "Exciton–exciton interaction engineering in coupled gan quantum dots," *Applied physics letters*, vol. 81, no. 22, pp. 4236–4238, 2002.

[193] L. C. Venuti, C. D. E. Boschi, and M. Roncaglia, "Long-distance entanglement in spin systems," *Physical review letters*, vol. 96, no. 24, p. 247206, 2006.

[194] J. W. Britton, B. C. Sawyer, A. C. Keith, C.-C. J. Wang, J. K. Freericks, H. Uys, M. J. Biercuk, and J. J. Bollinger, "Engineered two-dimensional ising interactions in a trapped-ion quantum simulator with hundreds of spins," *Nature*, vol. 484, no. 7395, pp. 489–492, 2012.

[195] K. A. Gilmore, M. Affolter, R. J. Lewis-Swan, D. Barberena, E. Jordan, A. M. Rey, and J. J. Bollinger, "Quantum-enhanced sensing of displacements and electric fields with two-dimensional trapped-ion crystals," *Science*, vol. 373, no. 6555, pp. 673–678, 2021.

[196] M. Qiao, Z. Cai, Y. Wang, B. Du, N. Jin, W. Chen, P. Wang, C. Luan, E. Gao, X. Sun, *et al.*, "Tunable quantum simulation of spin models with a two-dimensional ion crystal," *Nature Physics*, pp. 1–8, 2024.

[197] S. Inouye, M. Andrews, J. Stenger, H.-J. Miesner, D. M. Stamper-Kurn, and W. Ketterle, "Observation of feshbach resonances in a bose–einstein condensate," *Nature*, vol. 392, no. 6672, pp. 151–154, 1998.

[198] E. A. Donley, N. R. Claussen, S. L. Cornish, J. L. Roberts, E. A. Cornell, and C. E. Wieman, "Dynamics of collapsing and exploding bose–einstein condensates," *Nature*, vol. 412, no. 6844, pp. 295–299, 2001.

[199] A. Kay and J. K. Pachos, "Quantum computation in optical lattices via global laser addressing," *New Journal of Physics*, vol. 6, no. 1, p. 126, 2004.